ENGINEERING DEFECTS IN HEXAGONAL BORON NITRIDE TO ADVANCE ELECTROCHEMICAL ENERGY STORAGE IN SUPERCAPACITOR DEVICES

by
MOHAMAD HASAN ALEINAWI

Submitted to the Graduate School of Engineering and Natural Sciences
in partial fulfillment of
the requirements for the degree of Doctor of Philosophy

Sabancı University

July 2025

ENGINEERING DEFECTS IN HEXAGONAL BORON NITRIDE TO ADVANCE ELECTROCHEMICAL ENERGY STORAGE IN SUPERCAPACITOR DEVICES

Approved By:

Prof. EMRE ERDEM……...
(Dissertation Supervisor)

Assoc. Prof. FERAY BAKAN MISIRLIOĞLU……..…….

Prof. NURDAN DEMİRCİ SANKIR……..…….

Assoc. Prof. MUSTAFA KEMAL BAYAZIT……..……...

Asst. Prof. SÜLEYMAN GÖKHAN ÇOLAK……..……...

Date of Approval: July 21, 2025

ABSTRACT

ENGINEERING DEFECTS IN HEXAGONAL BORON NITRIDE TO ADVANCE ELECTROCHEMICAL ENERGY STORAGE IN SUPERCAPACITOR DEVICES

MOHAMAD HASAN ALEINAWI

Materials Science and Nanoengineering, Ph.D. Dissertation, July 2025

Dissertation Supervisor: Prof. EMRE ERDEM

Keywords: h-BN - defect engineering - Mn-doping - nanocomposites - supercapacitors - advanced characterization - EPR - PL - specific capacitance - energy density – power density.

Hexagonal boron nitride (h-BN), a wide-bandgap two-dimensional material, has recently garnered attention for energy storage applications due to its chemical inertness and thermal stability. However, its intrinsically low electrical conductivity and limited surface reactivity hinder its electrochemical performance in supercapacitor devices. This thesis explores a comprehensive defect-engineering approach to overcome these limitations by inducing structural and chemical modifications in h-BN through high-temperature annealing, high-energy ball milling, and transition metal doping, specifically with manganese (Mn). Systematic structural, optical, and electronic characterizations were conducted using X-ray diffraction (XRD), Raman, photoluminescence (PL), and electron paramagnetic resonance (EPR) spectroscopy. Results revealed that controlled nitrogen vacancy formation and carbon substitution enhanced defect density, leading to significant improvements in charge transport

and pseudocapacitive behavior. Mn doping was successfully achieved through a multi-step synthesis involving mechanochemical activation, chemical doping, and thermal annealing. EPR confirmed the substitutional incorporation of Mn^{2+}, and PL spectra showed defect-mediated blue emissions with increasing Mn content. Additionally, Tauc analysis revealed bandgap narrowing, indicating improved electronic conductivity. The investigation was extended to Mn-doped ZnO and Mn:ZnO-hBN nanocomposites, revealing a synergistic interaction that further enhanced electrochemical properties. Electrochemical tests conducted in symmetric two-electrode supercapacitor configurations demonstrated substantial performance improvements. Ball-milled nitrogen-deficient h-BN ($NHBN_{bm}$) showed a 3× enhancement in specific capacitance, reaching ~615 F/g at 10 mV/s. Mn-doped h-BN samples heat-treated at 800 °C delivered the highest stability and specific capacitance of ~566 F/g at 1 A/g, with >92% capacitance retention over 5000 cycles. The Mn:ZnO-hBN nanocomposites exhibited the best overall performance, achieving a maximum specific capacitance of ~795 F/g, energy density of 110 Wh/kg, and power density of 41.8 kW/kg. These findings highlight the critical role of defect engineering and composite design in activating h-BN as a high-performance electrode material, paving the way for its practical implementation in next-generation supercapacitor technologies.

ÖZET

ALTIGEN BOR NİTRÜRDEKİ KUSURLARIN MÜHENDİSLİĞİ İLE SÜPERKAPASİTÖR CİHAZLARINDA ELEKTROKİMYASAL ENERJİ DEPOLAMANIN İYİLEŞTİRİLMESİ

MOHAMAD HASAN ALEİNAWİ

Malzeme Bilimi ve Nano Mühendislik, Doktora Tezi, Temmuz 2025

Tez Danışman: Prof. Dr. EMRE ERDEM

Anahtar Kelimeler: h-BN – defekt mühendisliği – Mn katkılama – nanokompozitler – süperkapasitörler – gelişmiş karakterizasyon – EPR – PL – özgül kapasitans – enerji yoğunluğu – güç yoğunluğu

Altıgen bor nitrür (h-BN), geniş bant aralığına sahip iki boyutlu bir malzeme olarak kimyasal kararlılığı ve termal dayanıklılığı sayesinde enerji depolama uygulamaları için son yıllarda ilgi görmektedir. Ancak, h-BN'in doğası gereği düşük elektriksel iletkenliği ve sınırlı yüzey reaktivitesi, süperkapasitör cihazlarındaki elektrokimyasal performansını ciddi şekilde kısıtlamaktadır. Bu tezde, bu sınırlamaların üstesinden gelmek amacıyla, h-BN'in yüksek sıcaklıkta tavlama, yüksek enerjili bilyalı öğütme ve geçiş metali katkılaması (özellikle manganez, Mn) gibi yöntemlerle yapısal ve kimyasal olarak modifiye edilmesine dayalı kapsamlı bir defekt mühendisliği yaklaşımı sunulmuştur.Yapılan sistematik yapısal, optik ve elektronik karakterizasyonlar; X-ışını kırınımı (XRD), Raman, fotolüminesans (PL) ve elektron paramanyetik rezonans (EPR) spektroskopileri ile gerçekleştirilmiştir. Elde edilen bulgular, kontrollü azot boşluğu (VN) oluşumunun ve karbon sübstitüsyonunun defekt yoğunluğunu artırarak yük taşıma kapasitesinde ve psödokapasitif davranışta belirgin

iyileşmeler sağladığını ortaya koymuştur. Mn katkılaması, mekanokimyasal aktivasyon, kimyasal katkılama ve termal tavlama adımlarını içeren çok aşamalı bir sentez yöntemi ile başarıyla gerçekleştirilmiştir. EPR analizleri Mn^{2+} iyonlarının yer değiştirme (substitüsyonel) olarak h-BN kafesine dahil olduğunu doğrulamış, PL spektrumları ise artan Mn içeriğiyle birlikte defekt kaynaklı mavi ışık emisyonlarının belirginleştiğini göstermiştir. Ayrıca, Tauc analizleri bant aralığında daralma olduğunu göstermiş ve bu durumun elektriksel iletkenlikte artışa işaret ettiği belirlenmiştir. Çalışma, Mn katkılı ZnO ve Mn:ZnO–hBN nanokompozitlerinin sentezini de kapsamış ve bu malzemelerin sinerjik etkileşim yoluyla elektrokimyasal özellikleri daha da artırdığı tespit edilmiştir. Simetrik iki elektrotlu süperkapasitör konfigürasyonlarında yapılan elektrokimyasal testler, performansta önemli iyileşmeleri ortaya koymuştur. Özellikle bilyalı öğütmeye tabi tutulan azot açısından zenginleştirilmiş h-BN ($NHBN_{bm}$) örnekleri, özgül kapasitans değerinde 3 kat artışla yaklaşık 615 F/g seviyesine ulaşmıştır (10 mV/s tarama hızında). 800 °C'de tavlanan Mn katkılı h-BN örnekleri, 1 A/g akım yoğunluğunda ~566 F/g özgül kapasitans ve %92'nin üzerinde döngüsel stabilite (5000 çevrim sonrası) göstermiştir. En iyi genel performans ise Mn:ZnO-hBN nanokompozitlerinde gözlemlenmiş ve bu malzemeler ~795 F/g özgül kapasitans, 110 Wh/kg enerji yoğunluğu ve 41.8 kW/kg güç yoğunluğu değerlerine ulaşmıştır. Bu bulgular, defekt mühendisliği ve kompozit tasarımının h-BN'i yüksek performanslı bir elektrot malzemesi haline getirmedeki kilit rolünü vurgulamakta ve bu malzemenin yeni nesil süperkapasitör teknolojilerinde pratik uygulamaları için umut vadeden bir yol sunduğunu göstermektedir

ACKNOWLEDGMENTS

First and foremost, I would like to express my deepest gratitude to my supervisor, Prof. Dr. Emre Erdem, and his family whom I consider my second family in Istanbul, for his invaluable guidance, continuous support, and constructive feedback throughout my PhD journey. His passion for research, patience, and commitment to scientific excellence have been a constant source of inspiration. I am sincerely thankful to the members of my thesis committee Prof. Dr. Nurdan Demirci Sankır, Assoc. Prof. Dr. Feray Bakan Misirlioğlu, Assoc. Prof. Dr. Mustafa Kemal Bayazıt, and Asst. Prof. Dr. Süleyman Gökhan Çolak, for their insightful comments, valuable suggestions, and kind encouragement, all of which have significantly enriched the quality of this work. I would also like to extend my gratitude to Prof. Dr. Steven Suib and Mohamad Khairul from the University of Connecticut for the opportunity to collaborate and learn from their expertise in materials chemistry, as well as all the team members involved in this joint project.

Special thanks go to Dr. Arpad Mihai Rostas and Dr. Ameen Uddin Ammar from Romania for their unwavering support and invaluable partnership throughout this journey. I also wish to express my appreciation to Dr. Ahmet Güngör, İpek Deniz Yıldırım, Oluwatosin Johnson Ajala, Berfu Akgöl, Kamil Kiraz, and my fellow researchers and colleagues at Sabancı University and our partner institutions for the stimulating discussions, technical assistance, and collaborative spirit

I am deeply grateful to the Faculty of Engineering and Natural Sciences (FENS) and the Nanotechnology Research and Application Center (SUNUM) at Sabancı University for providing access to state-of-the-art research facilities that were instrumental to the success of this work. I would also like to sincerely thank Bilge Esenkal, Cansu Yılmaz Baker, and Anıl Tez for their tireless support and dedication to ensuring a safe and well-equipped laboratory environment.

On a personal note, I am profoundly thankful to my family for their unconditional love, sacrifices, and unwavering belief in me. Your support has been my strength through every

challenge. A heartfelt thank you goes to Farah, although entering my life only recently, her presence and unwavering support during this critical period have meant more than words can express.

Lastly, I would like to thank all my friends and lab mates who have made this journey more meaningful with their friendship, encouragement, and shared passion for science.

TABLE OF CONTENTS

LIST OF FIGURES

LIST OF TABLES

1. ABOUT THE STRUCTURAL DEFECTS IN h-BN

1.1. Introduction

Hexagonal Boron Nitride (h-BN) has emerged as a promising material for advanced energy storage technologies due to its exceptional thermal stability, high surface area, and chemical inertness. However, its inherently low electrical conductivity and limited surface activity pose substantial challenges for its direct application in electrochemical devices such as supercapacitors. To overcome these limitations, the present thesis explores a comprehensive strategy that combines defect engineering, transition metal doping, and composite formation to enhance the electrochemical performance of h-BN-based electrode materials.

The overarching goal of this research is to develop structurally and chemically modified h-BN systems tailored for supercapacitor applications by systematically investigating the role of intrinsic and extrinsic defects, including nitrogen vacancies, carbon impurities, and manganese (Mn) dopants. The thesis is organized into four interrelated chapters, each focusing on a different dimension of this goal:

Chapter 1 investigates the influence of intrinsic and extrinsic point defects in h-BN, including nitrogen vacancies, carbon impurities, and Mn doping. The chapter introduces a multi-step synthetic route combining thermal annealing, ball milling, and Mn incorporation via mechanochemical and thermal treatment. Advanced characterization techniques such as X-ray Diffraction (XRD), Raman Spectroscopy, photoluminescence (PL), and electron paramagnetic resonance (EPR) are used to evaluate defect types and their impact on structural, electronic, and optical properties. This chapter establishes the role of each defect

type, including Mn^{2+} substitution, in modulating charge carrier density and facilitating pseudocapacitive behavior.

Chapter 2 shifts the focus to ZnO and Mn-doped ZnO, examining the intrinsic and extrinsic defect landscape of this complementary material system. Using microwave-assisted hydrothermal synthesis, ZnO nanostructures with varying Mn doping levels were fabricated and characterized to assess how structural modifications affect electronic behavior, crystallinity, and surface area, and the effect of the microwave power on the defective structure of Mn-doped ZnO. All crucial factors in enhancing electrode performance.

Chapter 3 builds upon the findings of the previous chapters by integrating Mn-doped ZnO with h-BN to form Mn:ZnO-hBN nanocomposites. The rationale behind this composite design is to synergistically combine the defect-mediated conductivity and redox activity of ZnO:Mn with the high surface area and mechanical robustness of h-BN. Structural, optical, and magnetic characterizations provide evidence of successful hybridization and enhanced functional behavior.

Chapter 4 presents a detailed electrochemical evaluation of all prepared materials using cyclic voltammetry (CV), galvanostatic charge-discharge (GCPL), electrochemical impedance spectroscopy (EIS), and Dunn method analysis. The study highlights the improvement in specific capacitance, energy density, and power density for each material system, showing how each modification step, be it defect engineering, doping, or composite formation, contributes to the performance enhancement.

Together, these chapters converge on the central hypothesis that rational defect and composite engineering can transform insulating h-BN into a viable high-performance material for supercapacitor electrodes. The insights gained from this work offer new directions for defect-activated 2D materials and demonstrate the value of multi-step synthesis and comprehensive characterization in materials optimization.

Throughout this thesis, the sample nomenclature will adhere to the designations outlined in Table 1 below. These labels are used consistently in all subsequent discussions, figures, and analyses for clarity and uniformity.

Table 1: Samples nomenclature used throughout the thesis

Sample nomenclature	Description
HBN	h-BN with carbon impurities
NHBN	h-BN with nitrogen vacancies
Mn:hBN	Mn-doped h-BN
ZnO:Mn	Mn-doped ZnO
Mn:ZnO-hBN	Nanocomposite material of Mn doped ZnO and h-BN

h-BN, a two-dimensional material known for its excellent chemical stability (Chen, Lee, et al. 2015), wide bandgap of ~6 eV at room temperature (Cassabois, Valvin, and Gil 2016), and robust mechanical properties (Zembilgotov et al. 2005, Arenal et al. 2006), has attracted considerable attention in fields ranging from nanoelectronics (Thirumurugan et al. 2024, Dean et al. 2010, Chernozatonskii, Demin, and Bellucci 2016) to energy storage (Zheng et al. 2018, Wang et al. 2021, Liu et al. 2020). Recent studies have highlighted the role of defect engineering in h-BN, where the controlled introduction of defects can significantly alter its electronic (Toledo et al. 2018, Guo et al. 2014), optical (Cheng et al. 2024, Behzad and Chegel 2024), and mechanical (Shen and Zhu 2023, Mousavi and Montazeri 2023) properties. This tunability makes h-BN a promising candidate for advanced applications such as electrode materials in supercapacitors.

The layered structure of h-BN allows for various types of defects, including (Wong et al. 2015, Liu, Zou, and Yakobson 2012, Ponce et al. 2024) :

- Point defects such as nitrogen vacancies (V_N) and boron vacancies (V_B).
- Antisite defects where nitrogen occupies a boron site (N_B) or vice versa (B_N).
- 1D defects like grain boundaries and dislocations.

Additionally, carbon impurities may substitute either nitrogen (C_N) or boron (C_B) sites. These extrinsic defects can be introduced during synthesis or via environmental exposure (Maciaszek, Razinkovas, and Alkauskas 2022). Importantly, carbon substitution is known to

reduce the bandgap energy of h-BN, thereby enhancing its electrical and thermal conductivity. Among various strategies to further modulate the physicochemical properties of h-BN, transition metal doping has emerged as a powerful approach. Manganese (Mn), in particular, has attracted interest due to its multiple oxidation states (Mn^{2+}, Mn^{3+}, Mn^{4+}) and ability to introduce localized states within the bandgap of wide-bandgap semiconductors (Xu et al. 2022, Ruf et al. 2016b, Aleinawi et al. 2022). Incorporating Mn into the h-BN lattice can potentially induce electronic, and electrochemical activity, which are otherwise absent in pristine h-BN. First-principles studies have shown that Mn atoms can substitute boron or nitrogen sites and create mid-gap states that enhance carrier density and modulate spin polarization.

From an electrochemical perspective, Mn-doping is particularly appealing for supercapacitor applications. The introduction of Mn can improve electrical conductivity, surface redox activity, and pseudocapacitive behavior, thereby enhancing the charge storage capability of the host material (Alaş et al. 2019). In layered materials like h-BN, such dopants may also facilitate interlayer charge transfer and improve ionic accessibility through defect-induced channels.

Recent experimental works have reported the successful incorporation of Mn into various 2D materials, such as graphene and MoS_2, demonstrating improved specific capacitance, cycling stability, and rate capability (Singha et al. 2020, Ahmed, Singh, and Arya 2025). However, the controlled doping of Mn into h-BN remains underexplored, particularly with respect to understanding the relationship between dopant-induced defect structures, local bonding environments, and electrochemical performance.

The remarkable thermal and chemical stability of h-BN makes it a highly desirable material for applications in harsh environments. With decomposition temperatures exceeding 1000 °C in air and exceptional oxidation resistance up to 850–900 °C, making it suitable for applications in extreme environments such as aerospace, high-power electronics, and thermal coatings (Wu and Han 2020, Jaffe et al. 2023). However, this very stability also presents significant challenges when it comes to doping. Unlike more reactive materials, h-BN resists the incorporation of foreign atoms due to its strong in-plane B–N covalent bonds and its wide bandgap, which result in low defect formation energies only under extreme synthesis

conditions such as high temperature or plasma-assisted environments. Conventional doping methods often lead to low dopant solubility, clustering, or unwanted phase segregation, limiting the effectiveness of electronic and optical property modulation. Furthermore, maintaining structural integrity while introducing substitutional or interstitial dopants without inducing excessive defects remains difficult. These challenges necessitate the use of advanced strategies, including high-energy ball milling, complex chemical processes, recrystallization, and high temperature heat treatment.

In this chapter, the structural, optical, and electronic characteristics h-BN are systematically examined, with particular emphasis on the role of intrinsic point defects - those naturally present within the lattice - and extrinsic defects introduced through intentional doping. The discussion provides a foundational understanding of how such defect types influence the material's fundamental properties. This chapter also establishes a critical context for the subsequent chapters, which explore various defect-engineering strategies aimed at enhancing the functional performance of h-BN, particularly in relation to its electrochemical behavior.

1.2. Literature Review

1.2.1. General Properties of h-BN

h-BN is composed of alternating boron and nitrogen atoms arranged in a honeycomb lattice, structurally analogous to graphite. It was first synthesized in 1842 by W. H. Balmain through a reaction between molten boric oxide (H_3BO_3) and potassium cyanide (KCN), although its layered structure was not clearly identified until the advent of modern crystallographic techniques in the mid-20th century (Pakdel, Bando, and Golberg 2014). Over the years, h-BN evolved from a relatively obscure ceramic material to a subject of intense research due to its unique combination of chemical stability, high thermal conductivity, excellent insulating behavior, and atomically smooth surface. The crystal structure of h-BN is governed by sp^2 hybridized B–N bonds forming a hexagonal arrangement within each layer.

These layers are stacked via weak van der Waals interactions along the c-axis, with the most thermodynamically stable configuration being the AA′ stacking, where boron atoms in one layer align with nitrogen atoms in adjacent layers. The in-plane lattice constant is approximately 2.50 Å, and the interlayer distance is around 3.33 Å, closely resembling the parameters of graphite (Watanabe, Taniguchi, and Kanda 2004). BN exists in various crystalline forms. The hexagonal form h-BN is analogous to that or graphite, packing a layered structure. There is also the cubic form c-BN which is similar to diamond, and it is the second hardest material known.

The stability of the material is mainly governed by purity, average grains size, and defects concentration. Similar to different carbon-based variants, BN also can exist in different nanomorphologies. Figure 1 below shows the different morphologies of BN.

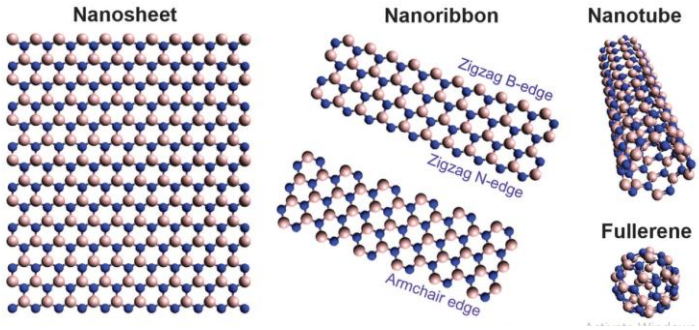

Figure 1: Various modes of 2D, 1D, and 0D BN, showing the versatility of the atoms arrangement in the structure, adapted from (Pakdel, Bando, and Golberg 2014)

From a physical properties standpoint, h-BN is classified as a deep-ultraviolet insulator (Watanabe, Taniguchi, and Kanda 2004). This bandgap can, however, be tuned through defect engineering and doping, which has significant implications for optoelectronic applications. The material demonstrates high thermal conductivity (up to 400 $W \cdot m^{-1}.K^{-1}$ in-plane), excellent resistance to oxidation (stable up to 1000 °C in air), and chemical inertness in both acidic and basic environments (Paszkowicz et al. 2002). Unlike graphene, which is metallic or semimetallic, the ionic character of the B–N bond imparts intrinsic electrical insulation to h-BN, making it a complementary 2D material in van der Waals heterostructures. Its atomically flat, charge-neutral surface also supports defect-free epitaxial growth of 2D semiconductors, thus positioning h-BN as a critical platform in the emerging fields of nanoelectronics and quantum devices (Tran et al. 2016). Despite its structural

simplicity, h-BN hosts a variety of defects and dopants that significantly modify its physical and electronic properties, such as single-photon emission, modulated bandgap, and enhanced electrochemical activity. These aspects have become central to recent research, particularly in the context of catalysis and supercapacitor applications.

1.2.2. Intrinsic point defects in h-BN

Although pristine h-BN is often described as a structurally perfect material, real-world samples frequently contain a variety of intrinsic point defects that strongly influence its electronic, optical, and electrochemical behavior. These defects arise naturally during synthesis, especially under high temperatures or non-stoichiometric growth conditions, and include vacancies, antisite defects, and interstitials.

1.2.2.1. Nitrogen and Boron Vacancies

The most common intrinsic defects in h-BN are V_N and V_B, which correspond to the absence of a nitrogen or boron atom from the lattice, respectively. First-principles calculations have shown that V_N defects are more thermodynamically favorable than V_B under nitrogen-poor or boron-rich growth conditions, owing to the lower formation energy (Attaccalite et al. 2011). These defects introduce localized states within the bandgap and are often responsible for optical transitions observed in photoluminescence (PL) and paramagnetic signals detected via electron paramagnetic resonance (EPR) spectroscopy (Toledo et al. 2018). V_N defects, in particular, have been identified as likely candidates for single-photon emitters due to their characteristic zero-phonon lines in the visible range (Jungwirth and Fuchs 2017). Moreover, V_N centers are paramagnetic and have been successfully simulated and identified in X-band EPR studies with g-values around 2.003–2.006 (Cassabois, Valvin, and Gil 2016).

1.2.2.2. Nitrogen and Boron Interstitials

Interstitial defects in h-BN refer to the presence of additional nitrogen (N_i) or boron (B_i) atoms occupying positions in the lattice that are not normally host sites. These atoms can become embedded in the lattice during non-equilibrium processes such as high-energy ball milling, ion irradiation, or plasma-assisted synthesis. Compared to vacancies, interstitials generally exhibit higher formation energies, making them less likely to form under thermodynamic equilibrium but increasingly probable under high-energy conditions or in the presence of defect clustering . Density functional theory (DFT) calculations reveal that N_i atoms often stabilize in a dumbbell-like configuration, forming bonds with neighboring nitrogen atoms out of the basal plane. This geometry introduces shallow donor states and enhances n-type conductivity. In contrast, B_i atoms tend to create deeper electronic states within the bandgap due to the mismatch in atomic size and electronegativity, leading to significant lattice distortions (Li et al. 2023, Azevedo et al. 2009).

1.2.2.3. Antisite Defects

Antisite defects, where a boron atom occupies a nitrogen site (B_N) or vice versa (N_B), are another class of intrinsic point defects in h-BN. While these are energetically less favorable than vacancies, they can form under high-energy processing techniques such as ball milling or irradiation (Stefanowicz et al. 2014). DFT calculations indicate that B_N antisites induce deep acceptor levels within the bandgap, significantly affecting the electronic transport properties. Additionally, Frenkel pairs which composed of a vacancy and an associated interstitial (e.g., a displaced nitrogen atom) can be produced under electron irradiation or ion bombardment. These complex defects are known to contribute to the degradation of crystallinity and modify the mechanical and dielectric performance of h-BN (Kumar et al. 2024).

1.2.3. Extrinsic Defects in h-BN

While intrinsic defects in h-BN significantly impact its electronic and optical properties, extrinsic defects originating from foreign atoms introduced during synthesis or post-processing can provide even greater tunability. Among the most studied extrinsic modifications are carbon substitutional impurities and transition metal dopants, particularly Mn, due to their potential to activate otherwise inert h-BN for electronic, optical, and electrochemical applications.

1.2.3.1. Carbon (C) Impurities in h-BN

C atoms can enter the h-BN lattice unintentionally during synthesis, particularly when using carbon-containing precursors, crucibles, or contaminated environments. These impurities may substitute either boron (C_B) or nitrogen (C_N) atoms due to the comparable atomic radii and bonding capabilities, creating localized states in the band structure and breaking the B–N symmetry. First-principles studies have shown that carbon substitution C_N sites is more favorable than at C_B sites, particularly under nitrogen-deficient conditions. C_N defects introduce localized donor-like states, which narrow the bandgap and enhance visible-range PL (Babar et al. 2025). Experimental observations using electron energy loss spectroscopy (EELS) and X-ray photoelectron spectroscopy (XPS) have confirmed the presence of C-related π^* and σ^* states in carbon-doped h-BN, indicating sp^2 hybridization and strong coupling with the BN matrix (Pakdel, Bando, and Golberg 2014). Carbon impurities have also been associated with broad photoluminescence peaks and room-temperature paramagnetism, suggesting the presence of defect-related energy levels and unpaired spins (Mendelson et al. 2021). In electrochemical applications, carbon incorporation has been shown to enhance conductivity and introduce pseudo-capacitive behavior, offering a route to activate h-BN for supercapacitor electrodes (Li et al. 2019). This is particularly important, as pristine h-BN is typically insulating with low charge storage capability.

1.2.3.2. Mn Dopant in h-BN

Doping h-BN with transition metal ions such as Mn has been explored as a strategy to induce magnetic, catalytic, and electrochemical functionalities. Theoretical studies based on DFT suggest that Mn atoms preferentially substitute boron sites (Mn_B) due to favorable formation energies and bonding configurations (Hsu et al. 2023). This substitution creates partially filled d-orbitals that can introduce mid-gap states, enhance spin polarization, and modify the local electronic density of states. Experimentally, Mn doping in h-BN has been achieved through ion implantation, chemical vapor deposition (CVD), and post-synthetic treatment with Mn salts followed by high-temperature annealing. EPR measurements have provided strong evidence for the presence of Mn^{2+} species in doped h-BN, with characteristic hyperfine splitting due to the ^{55}Mn nucleus (I = 5/2), and g-values ranging from 2.002 to 2.005, depending on the local coordination (Keller et al. 2016). The detection of such signals confirms the incorporation of isolated Mn^{2+} centers rather than Mn clusters or oxide phases. PL studies further support the role of Mn dopants in modifying optical behavior. Mn-induced quenching of native PL signals is often observed, attributed to nonradiative recombination channels introduced by the d-orbitals of Mn^{2+} (Yüksel Price, Hardal, Açıkgöz, et al. 2015). Moreover, in the context of electrochemistry, Mn doping has been shown to enhance Faradaic charge storage behavior, likely due to the redox activity of Mn ions and the catalytic activation of adjacent BN lattice sites (Ammar, Bakan-Misirlioglu, et al. 2023). Despite these promising effects, challenges remain in achieving uniform Mn distribution and controlling the oxidation state during synthesis. Overdoping or cluster formation can lead to undesirable secondary phases or degradation of the crystalline quality of h-BN. Moreover, the exceptional chemical and thermal stability of h-BN, while advantageous for many applications, presents a significant challenge for the effective incorporation of transition metal dopants such as Mn into its lattice. This inherent resistance to chemical modification often limits the success of conventional doping techniques. To overcome this limitation, the subsequent methodology section introduces an innovative and cost-efficient strategy that integrates mechanical activation, chemical treatment, and high-temperature processing. This multifaceted approach aims to facilitate the successful incorporation of Mn ions into the h-BN structure by enhancing defect formation and dopant diffusion pathways.

Figure 2 below summarizes the possible intrinsic and extrinsic defects that can form in the structure of h-BN.

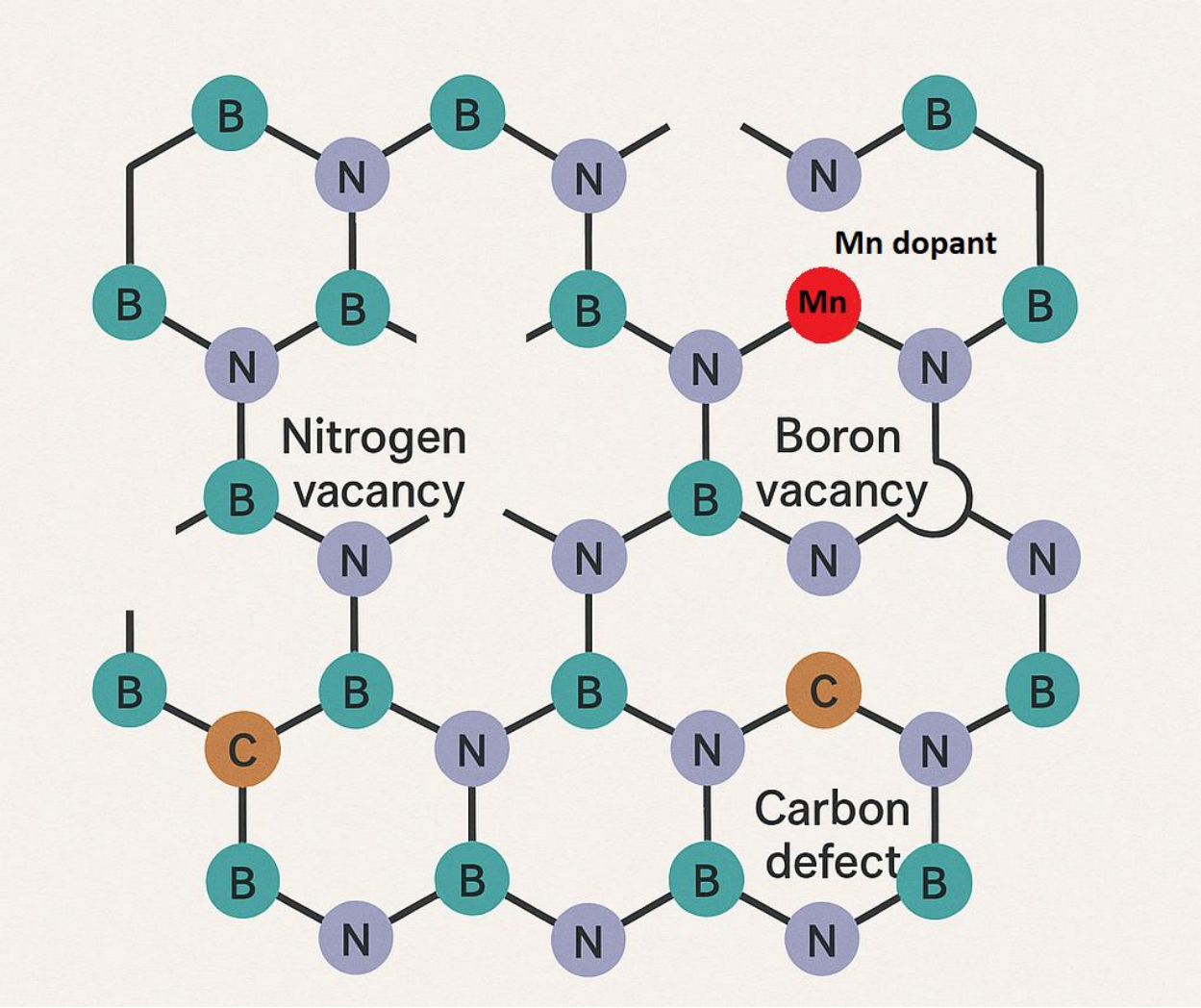

Figure 2: Possible intrinsic and extrinsic defects in h-BN lattice, showing V_N, V_B, C defects, and Mn dopant in the structure of h-BN

1.3. Methodology

This section outlines the experimental and analytical techniques employed to investigate the defect-induced behavior of h-BN materials. The methods were selected to ensure reproducibility, precision, and relevance to the objectives outlined in this chapter. In this research, commercially available h-BN powders were systematically modified through high-energy ball milling to introduce structural defects. The resulting materials were thoroughly characterized using EPR, PL, and Raman spectroscopies to investigate the nature and extent of the induced defect states. Particular attention was given to correlating the type and density of these defects with the electrochemical behavior of h-BN-based electrodes in supercapacitor systems. By establishing a clearer understanding of the role of defect engineering in modulating charge storage mechanisms, this study aims to advance the functional optimization of h-BN for energy storage applications. The findings are anticipated to contribute valuable insights toward the rational design of high-performance electrode materials based on defect-tailored h-BN.

1.3.1. Mechanical Processing

High-energy ball milling was employed as a mechanochemical method to induce structural modifications and facilitate dopant incorporation into the host matrix. Ball milling is a widely used solid-state processing technique that utilizes mechanical forces to reduce particle size, create structural defects, and enhance solid-state reactivity through repeated impact and shear forces generated by colliding milling media. In this study, equal masses of each sample were subjected to milling using a Planetary Micro Mill PULVERISETTE 7 (FRITSCH, Germany). The process was carried out for several hours at a rotational speed of 800 RPM, maintaining a ball-to-powder weight ratio of 10:1. Zirconia (ZrO_2) milling balls with a diameter of 10 mm were used as the grinding medium due to their high hardness and low contamination potential. All milling operations were performed under identical conditions to

ensure consistency across samples and to isolate the effect of processing parameters on structural and functional properties.

1.3.2. Materials and Synthesis

1.3.2.1. Mechanical Induced Defects

To investigate the role of intrinsic point defects, and carbon defects in h-BN, two distinct sample batches were synthesized under controlled conditions to selectively promote the formation of specific defect types namely, carbon impurity-related defects and V_N defects. These tailored modifications enabled a systematic examination of the defect-induced changes in the structural and functional properties of h-BN. .Amorphous h-BN, used as the primary precursor in this study, was sourced from PavTec, Turkey, with a reported purity exceeding 99.98% according to the supplier's technical data sheet. To induce crystallinity and investigate the role of thermal energy in defect formation, the amorphous h-BN powders were subjected to high-temperature annealing under an inert argon atmosphere through two distinct thermal treatment protocols: 1400 °C (denoted as HBN) and 1950 °C (denoted as NHBN), each for a duration of 2 hours. The first treatment at 1400 °C was selected based on the known evaporation point of boron oxide (B_2O_3), a common side product in boron-based ceramics, which fully volatilizes above 1300 °C, thus allowing the formation of phase-pure crystalline h-BN. A second, higher-temperature route at 1950 °C was employed to intensify defect formation within the hexagonal lattice while preserving the structural integrity of h-BN, based on prior literature demonstrating that thermal degradation under inert conditions typically initiates above 2000 °C. To further enhance the concentration and diversity of structural defects, high-energy mechanical ball milling was performed on both thermally treated samples. This mechanical processing step was intended to induce localized lattice distortion and create non-equilibrium defect sites. These combined thermal and mechanical modification strategies were designed to systematically explore the correlation between

synthesis conditions, defect density, and the functional behavior of h-BN in energy storage applications.

Figure 3 below summarizes the aforementioned process.

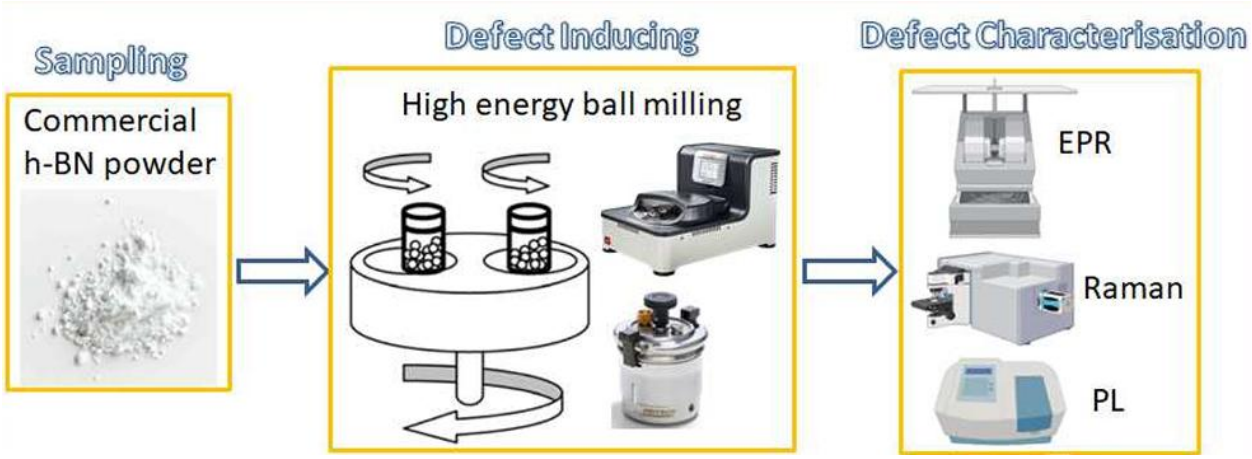

Figure 3: Schematic of the sampling, defect inducing, and defect characterization of intrinsically defective h-BN

1.3.2.2. Mn-doped h-BN synthesis

To address the challenges posed by the exceptional chemical and thermal inertness of h-BN during the doping process, a tailored synthesis route was developed. The procedure begins with a mechanical activation step involving high-energy ball milling, which serves to introduce structural defects and enhance the reactivity of the material. This is followed by a chemical synthesis phase, wherein the precursor materials are dissolved and thoroughly mixed to ensure homogeneous distribution of the dopant species. The final stage involves thermal treatment at elevated temperatures between 700 °C and 900 °C, promoting recrystallization and facilitating the incorporation of Mn ions into the h-BN lattice through diffusion-assisted mechanisms.

First, the commercial h-BN powder obtained from PavTec Turkey is mixed with manganese Nitrate Tetrahdyrate (MAT – $(CH_3COO)_2Mn.4H_2O$), Acros Organics, 99% purity, CAS No.: 6156-78-1. The powder mixture is then placed in a high-energy ball milling device, and ball

milled at 800 rpm for 24 hours in a ball-to-powder ratio of 10:1. The precursor material is then dissolved in methanol (CH_3OH), Sigma Aldrich, 99.8% purity, Cas No.: 67-56-1 to ensure successful dissolving of MAT, and then the mixtures is sonicated at 70 ^oC for 3 hours to maintain a homogeneous mixture and prevent agglomeration of the layers of h-BN. Next, the precursor material is filtered and dried overnight at 90 ^oC, and finally, the precursor material is placed in a high-temperature oven under nitrogen gas flow and heat treated at 700 ^oC to 900 ^oC for 4 to 10 hours, to ensure sufficient recrystallization of the material. Figure 4 below shows the schematic of the synthesis procedure.

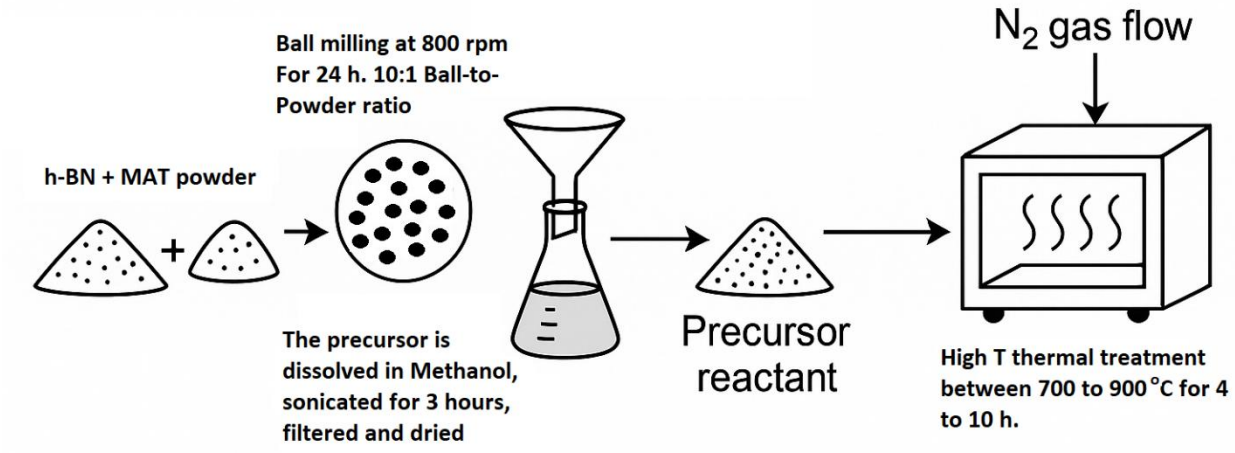

Figure 4: Schematic of the synthesis procedure of Mn doped h-BN, showing the sophisticated process of synthesis combining mechanical, chemical, and thermal processing of the material

1.3.3. Structural Characterization

1.3.3.1. X-ray Diffraction

X-ray diffraction (XRD) was employed to investigate the crystalline structure, phase composition, and structural changes in the synthesized samples. XRD is a nondestructive analytical technique that provides information on the crystallographic arrangement of atoms by measuring the diffraction pattern of X-rays incident on the sample. The diffraction patterns arise due to constructive interference from planes of atoms, governed by Bragg's law $n\lambda = 2d\sin\theta$, where λ is the wavelength of the incident X-ray, d is the interplanar spacing, and θ is the diffraction angle. The XRD patterns were recorded using a Bruker D2 Phaser diffractometer operating with Cu Kα radiation (λ = 1.5405 Å). The measurements were carried out in the 2θ range of 10° to 90°, with a step size of 0.02° and an appropriate scan speed to ensure a sufficient signal-to-noise ratio. The collected diffraction data were analyzed to identify the phase purity, determine crystallite size using the Scherrer equation, and monitor any peak broadening or shifts indicative of strain, defects, or doping-related structural modifications.

For phase identification and structural evaluation, the diffraction data were processed using standard peak-matching software. In addition, Rietveld refinement was carried out using the MAUD software to extract detailed crystallographic parameters, such as lattice constants, phase fractions, atomic positions, and microstrain. The refinement procedure employed a pseudo-Voigt profile function to fit the experimental patterns with reference crystal structures from the crystallography open database COD. The average crystallite size (D) of the samples was initially estimated using the Scherrer equation (1):

$$D = \frac{K\lambda}{\beta Cos\theta} \qquad (1)$$

Where D is the average crystallite size in nm, K is the shape factor, typically taken as 0.9 for spherical crystallites, λ is the X-ray wavelength (0.15406 nm for Cu Kα radiation) ,β is the full width half maximum (FWHM) of the peaks (in radians), and θ is the Bragg angle (half of the 2θ value of the peaks).

To further analyze the effects of crystallite size and lattice strain on peak broadening, Williamson–Hall (W–H) analysis was performed using the relation illustrated in Equation (2):

$$\beta Cos\theta = \frac{K\lambda}{D} + 4\epsilon Sin\theta \qquad (2)$$

Where ϵ represents the microstrain within the lattice.This multi-pronged XRD methodology provided comprehensive insights into the structural evolution of the materials under different doping levels, thermal treatments, and synthesis routes.

1.3.3.2. Scanning Electron Microscopy

The surface morphology and microstructural characteristics of the samples were examined using scanning electron microscopy (SEM), which provides high-resolution imaging by scanning a focused electron beam over the sample surface and detecting emitted secondary electrons, which offer detailed topographical contrast. This technique is particularly valuable for analyzing the shape, texture, and agglomeration of particulate materials. In this study, SEM analysis was performed using a Hitachi HD-2700 microscope, operated at an accelerating voltage of 3 keV. The imaging was conducted over a magnification range of 1,000× to 75,000×, enabling the observation of both macro- and nanoscale features. To minimize charging effects and improve image quality, all samples were coated with a thin conductive layer of gold-palladium (Au–Pd) using a sputter coater prior to measurement. The resulting micrographs provided critical information regarding particle morphology, distribution, and structural changes associated with mechanical and thermal processing steps.

1.3.4. Electronic Characterization

1.3.4.1. Electron Paramagnetic Resonance Spectroscopy

Electron paramagnetic resonance (EPR) spectroscopy was employed to investigate the presence, concentration, and local environment of unpaired electrons and paramagnetic defects in the synthesized materials. EPR is a powerful and highly sensitive characterization technique that detects transitions between magnetic energy levels of unpaired electron spins under an external magnetic field. The fundamental working principle of EPR relies on the Zeeman effect, where unpaired electron spins ($S \neq 0$) experience an energy level splitting in the presence of an external static magnetic field (B_0). When subjected to microwave radiation of frequency (ν), resonance absorption occurs if the energy of the microwave photons matches the energy difference between the spin sublevels. This condition is described by the resonance condition illustrated in Equation (3):

$$h\nu = g\mu_B B_0 \qquad (3)$$

Where: h is Planck's constant, ν is the microwave frequency, g is the spectroscopic g-factor (which depends on the local electronic environment), μ_B is the Bohr magneton, and B_0 is the external magnetic field strength. Deviations in the measured g-factor from the free electron value ($g \approx 2.0023$) provide insights into the nature of the defect or dopant environment, degree of spin-orbit coupling, and ligand field effects (2006b, 2006e, 2006c, 2006d, 2006a).

To fully describe the magnetic interactions experienced by the paramagnetic centers, the system's total energy can be modeled using the spin Hamiltonian formalism, as illustrated in Equation (4):

$$\mathrm{H} = \mu_B B_0 . g . S + SAI + H_{ZFS} + H_{Dipolar} + H_{Exchange} \qquad (4)$$

Where: g is the Zeeman interaction term, describing the interaction between the external magnetic field and the electron spin (S), SAI is the hyperfine interaction term representing the coupling between the electron spin (S) and nearby nuclear spins (I) characterized by the hyperfine coupling tensor (A), H_{ZFS} is the Zero-field splitting (ZFS) term important for

systems with spin S > 1/2 (e.g., transition metal ions like Mn^{2+}) which accounts for spin-spin interactions within the same center even in the absence of a magnetic field, $H_{Dipolar}$ is the dipolar interactions describing spin-spin coupling between different paramagnetic centers, and $H_{Exchange}$ is the exchange interaction term, relevant when electron spins in neighboring atoms interact through exchange coupling.

High-frequency EPR measurements were conducted using a Bruker ELEXSYS E-500 spectrometer operating in Q-band (33.8 GHz) at room temperature, under identical experimental conditions for all samples. Equal masses of powder were loaded into quartz EPR tubes to ensure consistent signal intensities for comparative analysis. Additionally, complementary X-band (9.68 GHz) measurements were carried out using a Bruker EMX-nano spectrometer, also at room temperature, to confirm the reproducibility of spectral features and to enhance spectral resolution for samples with broader or overlapping signals. The obtained spectra were analyzed to identify hyperfine interactions, line broadening effects, and g-factor variations associated with intrinsic or dopant-induced paramagnetic centers. Simulations of the experimental spectra were performed using the EasySpin package (Stoll and Schweiger 2006) (a MATLAB-based EPR simulation toolbox), allowing for detailed fitting of spin Hamiltonian parameters and validation of the spectral assignments.

1.3.4.2. Photoluminescence Spectroscopy

Photoluminescence (PL) spectroscopy was utilized to probe the optical properties and defect-related emission features of the synthesized materials. PL is a non-destructive optical technique that involves the excitation of a sample with a light source and the subsequent measurement of emitted photons as electrons recombine from excited states to lower energy states. The resulting spectra provide insights into band structure, defect levels, and recombination mechanisms within the material. The PL spectra were recorded using an FS5 spectrofluorometer (Edinburgh Instruments), equipped with a 150 W continuous-wave (CW) ozone-free xenon arc lamp as the excitation source. The system features Czerny–Turner monochromators with plane gratings for both excitation and emission paths, offering high

spectral resolution and wavelength selectivity. A PMT-900 photomultiplier tube detector was employed for sensitive photon detection across a broad spectral range. All measurements were carried out at room temperature, and identical instrumental settings were applied to all samples to ensure consistency and comparability of emission intensities. The recorded emission profiles were analyzed to assess defect-related transitions and changes in radiative recombination behavior due to structural modifications or doping.

1.3.4.3. Raman Spectroscopy

Raman spectroscopy was employed to analyze the vibrational modes and structural order of the synthesized materials. This technique is based on inelastic scattering of monochromatic light, typically from a laser source, and provides information about molecular vibrations, phonon modes, and crystal symmetry. Raman spectroscopy is particularly sensitive to lattice defects, dopant incorporation, and disorder in crystalline and nanostructured materials. In this study, Raman spectra were recorded using an inVia Raman spectrometer (Renishaw, UK) equipped with an upright optical microscope for precise sample focusing and spatial resolution. A 532 nm frequency-doubled Nd:YAG solid-state laser was used as the excitation source. To prevent local heating and possible structural degradation of the samples, the laser power was carefully limited to 1% of its maximum output during all measurements. The system was calibrated using a standard silicon reference prior to data collection. The obtained spectra were analyzed to identify characteristic phonon modes, assess defect-induced broadening or shifts, and monitor structural changes resulting from doping or processing treatments.

1.4. Results and Discussions

1.4.1. X-ray Diffraction of Mechanically Induced Defects in h-BN, and Mn:hBN

The crystalline structure, phase composition, and average crystallite size of the samples were investigated using XRD. The corresponding diffractograms for the pristine and ball-milled h-BN samples are shown in Figure 5 below.

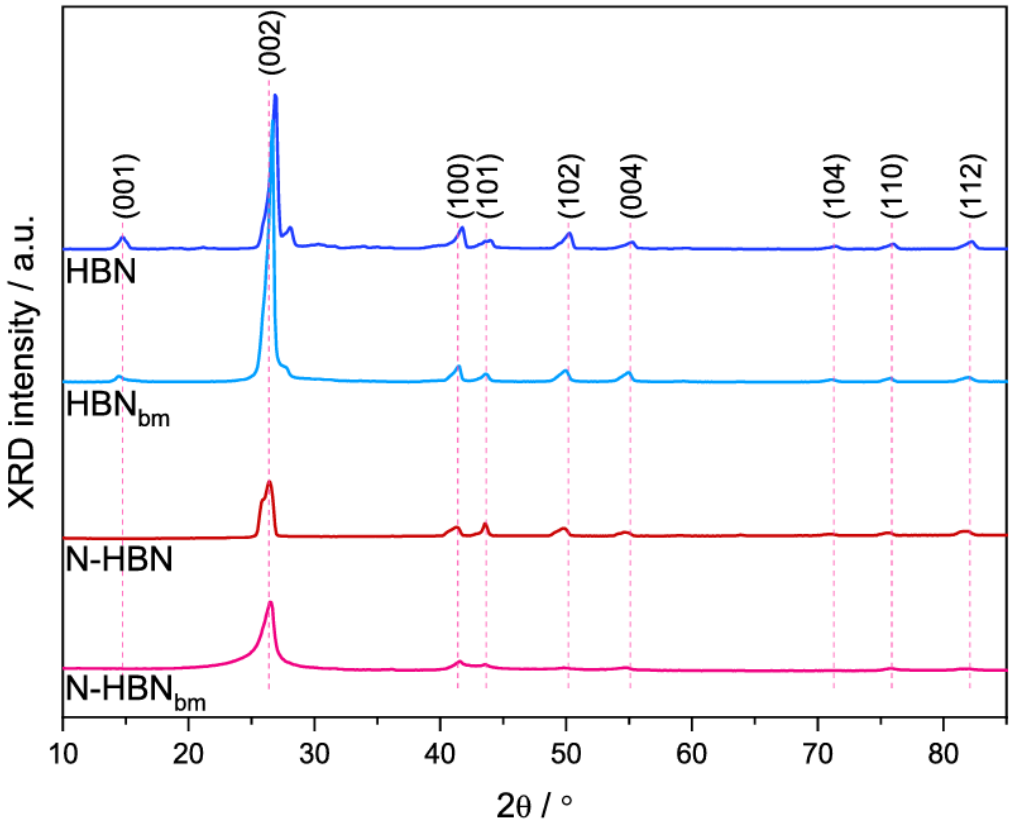

Figure 5: XRD diffractograms of HBN and NHBN samples before and after ball milling, showing the effect of the ball milling process on the crystalline structure of h-BN

Both samples display the characteristic diffraction peaks of h-BN, indexed to the (002), (100), (101), (102), (004), and (110) planes, appearing at approximately 2θ values of 27°, 42°, 44°, 50°, 55°, and 76°, respectively. These reflections are consistent with the standard h-BN reference pattern (JCPDS No. 34-0421) (Nie, Jia, Guo, He, Weng, Li, et al. 2024, Huang et al. 2013). The presence of sharp and well-defined peaks in each sample indicates a relatively high degree of crystallinity. Notably, the HBN and HBN_{bm} samples exhibit sharper

peak profiles than the NHBN sample, implying a lower concentration of defect sites. A weak diffraction peak around $2\theta \approx 14°$ is observed in the HBN and HBN_{bm} samples, which is attributed to the stacking of h-BN layers along the c-axis (Choi et al. 2019). Additionally, a significant difference is noted in the intensity of the (002) reflection between HBN and NHBN samples. Since this peak corresponds to the interlayer spacing along the c-axis of the layered structure, its suppression in NHBN is indicative of a higher density of structural defects (Ji et al. 2012). The (002) peak intensity is further diminished after ball milling, confirming the successful introduction of additional defects in both the HBN_{bm} and $NHBN_{bm}$ samples. To gain deeper insight into the structural ordering and phase composition, Rietveld refinement was performed using Maud software. The refinement utilized crystallographic cards corresponding to space groups P6-m2 for the hexagonal phase and Fmmm for the graphite-like phase. The results of the refinement are presented in Figure 6, Appendix 1, and Table 2.

Table 2: Phase ratio, lattice parameters and D of unmilled and ball-milled h-BN samples

Sample	**Phase**	**Ratio (%)**	**a (nm)**	**b (nm)**	**c (nm)**	**D (nm)**
HBN	Hexagonal	90	2.51	2.51	6.67	30.5
	Graph-like	10	2.5	4.34	3.35	
HBN_{bm}	Hexagonal	93	2.51	2.51	6.64	24.5
	Graph-like	7	2.5	4.32	3.33	
NHBN	Hexagonal	92	2.5	2.5	6.66	32.2
	Graph-like	8	2.48	4.33	3.31	
$NHBN_{bm}$	Hexagonal	95	2.49	2.49	6.74	21.7
	Graph-like	5	2.48	4.33	3.31	

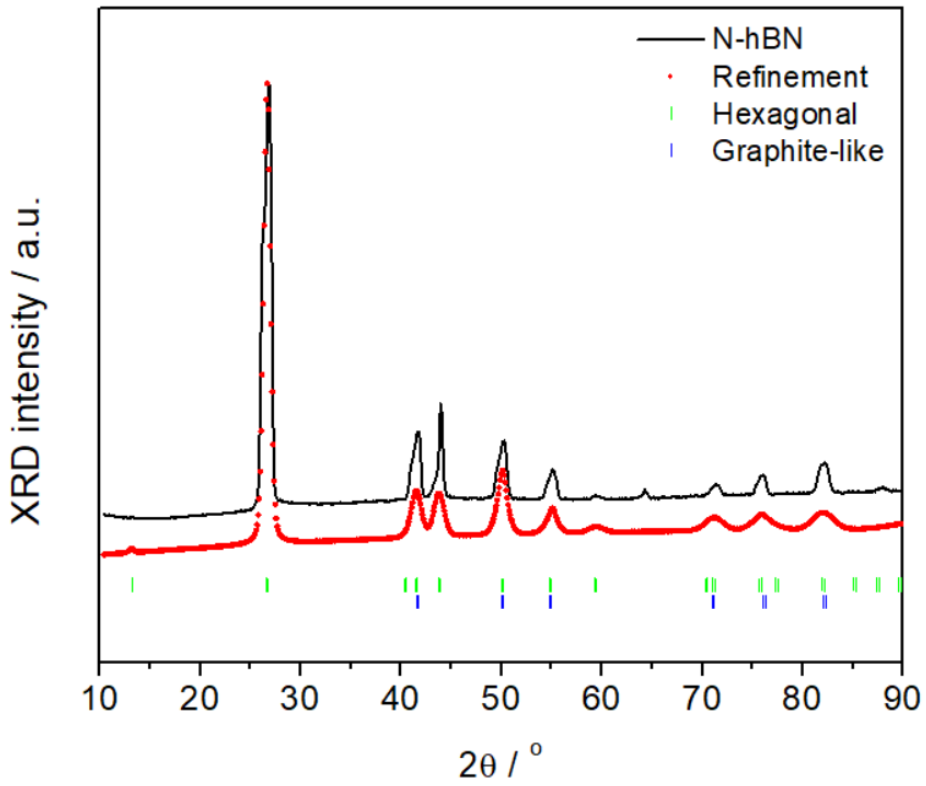

Figure 6: Reitveld refinement of NHBN samples, showing the ratio of each phase in the cysrtal structure of h-BN

The analysis indicates that the hexagonal phase remains dominant in all samples and becomes more prominent following ball milling. Furthermore, the reduction in crystallite size after milling is expected to enhance the surface area-to-volume ratio, which is favorable for electrochemical applications to be discussed in the next chapters. A subtle contraction in lattice parameters was observed for the HBN_{bm} sample, where the c-axis lattice constant decreased from 6.67 nm in the pristine HBN to 6.64 nm after ball milling. This change suggests a possible reduction in interlayer spacing due to strain effects induced by mechanical processing (Shenoy et al. 2021). This structural compression may also point to an increase in defect density and enhanced surface activity. In contrast, the NHBN sample did not exhibit a comparable shift in lattice parameters. Additionally, a notable decrease in the intensity of the graphite-like phase was observed in both HBN and NHBN samples after milling, in agreement with the morphological changes confirmed by SEM analysis to be discussed next. Lastly, the $NHBN_{bm}$ sample exhibited a slightly smaller average crystallite

size compared to HBN_{bm}, a factor that is likely to contribute positively to its electrochemical performance. It is also worth noting that there is a minor peak around 2θ = 65o degrees for NHBN samples. This peak is not associated with any phase of BN. Furthermore, the peak disappears after ball milling NBHN, and it does not appear in any other samples except NHBN. The fact that ball milling led to the disappearance of the peak, and the absence of this peak in HBN samples suggests that this is most likely a mechanically vulnerable crystalline phase that is favored by the heat treatment conditions of NHBN samples, thus disappearing after the ball milling process.

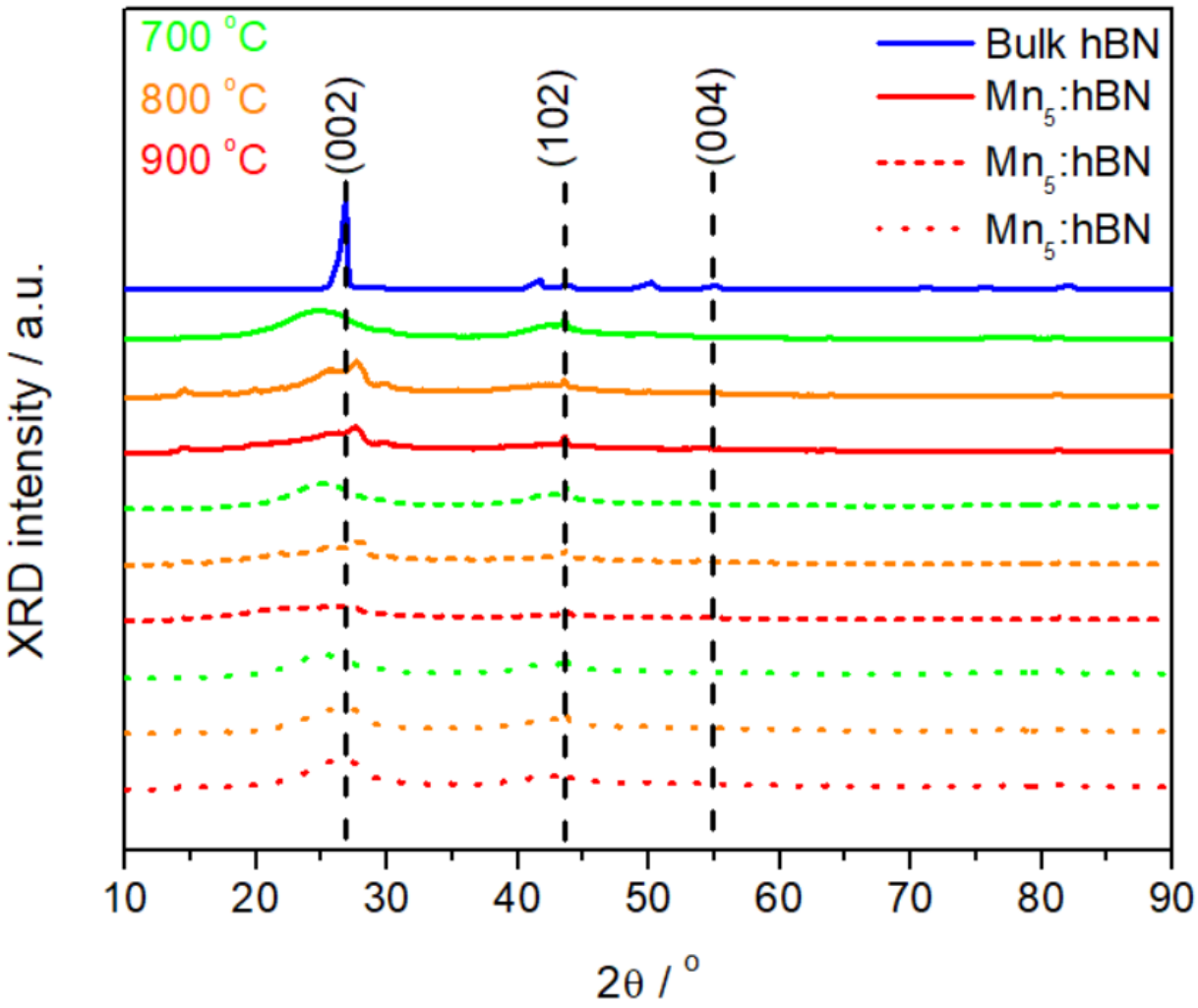

Figure 7: XRD diffractograms of Mn-doped h-BN samples at different heat treatment temperatures, showing the effect of the heat treatment temperature, and the Mn-dopant percentage on the crystal structure of h-BN

To investigate the influence of manganese doping and thermal treatment on the crystallographic structure of h-BN, XRD analysis was performed on bulk h-BN and Mn-doped h-BN samples subjected to different calcination temperatures (700 °C, 800 °C, and 900 °C). The diffraction patterns are presented in Figure 7, where bulk h-BN is shown as a reference (blue curve), and Mn-doped samples with 1, 3, and 5 at.% Mn are plotted with varying line styles and colors according to the calcination temperature. All observed diffraction peaks correspond well to the characteristic reflections of h-BN (JCPDS No. 34-0421), confirming the retention of the hexagonal phase after Mn incorporation. The main diffraction peaks appear at approximately 26.7°, 41.6°, and 55.0°, which correspond to the (002), (102), and (004) planes, respectively. These reflections are consistent across all samples, indicating that the crystal structure of h-BN is preserved even at high Mn doping levels and elevated calcination temperatures. Compared to pristine h-BN, the Mn-doped samples exhibit a noticeable broadening and intensity reduction in the (002) peak. This trend becomes more prominent as the Mn content increases from 1 at.% to 5 at.%, suggesting a reduction in crystallite size and/or an increase in structural disorder due to substitutional or interstitial incorporation of Mn ions. The (002) peak also shows a slight shift to lower 2θ values in the highly doped samples, indicative of possible lattice expansion caused by the ionic size mismatch between Mn^{2+} and the host atoms. Such a shift implies a distortion along the c-axis, which is consistent with Mn incorporation into the layered structure of h-BN. Thermal treatment plays a crucial role in influencing the crystallinity and phase evolution of the doped systems. At 700 °C, all Mn-doped samples exhibit broadened peaks with low intensity, reflecting incomplete crystallization or high defect concentration. Upon increasing the temperature to 800 °C, a significant improvement in peak sharpness and intensity is observed, indicating enhanced crystal ordering and grain growth. However, further increasing the temperature to 900 °C does not yield a substantial increase in crystallinity for the 3% and 5% Mn-doped samples, suggesting that higher dopant concentrations may inhibit full structural recovery even at elevated temperatures.

The average crystallite size results are summarized in table 3 below:

Table 3: Lattice parameters and D of Mn doped h-BN samples calcined at various temperatures

Sample	**a (nm)**	**b (nm)**	**c (nm)**	**D (nm)**
Mn_1:hBN 700 ºC	2.23	2.23	5.11	84.1
Mn_1:hBN 800 ºC	2.21	2.21	5.67	93.1
Mn_1:hBN 900 ºC	2.36	2.36	5.8	108
Mn_3:hBN 700 ºC	2.42	2.42	6.3	88.3
Mn_3:hBN 800 ºC	2.42	2.42	6.4	97.4
Mn_3:hBN 900 ºC	2.43	2.43	6.5	109.9
Mn_5:hBN 700 ºC	2.51	2.51	5.9	98.3
Mn_5:hBN 800 ºC	2.51	2.51	6.5	102.5
Mn_5:hBN 900 ºC	2.51	2.51	6.6	112.5

Importantly, no secondary peaks corresponding to manganese oxides (e.g., MnO, Mn_2O_3, or Mn_3O_4) or other impurity phases are detected within the instrumental resolution. This suggests either successful incorporation of Mn ions into the h-BN matrix or the formation of highly dispersed amorphous phases below the XRD detection limit. The homogeneous distribution of Mn without phase segregation is essential for maintaining the intrinsic properties of h-BN while introducing desirable electronic or magnetic functionalities.The systematic XRD analysis demonstrates that Mn doping up to 5 at.% can be accommodated within the h-BN lattice without disrupting its hexagonal structure. While higher Mn content and lower annealing temperatures introduce structural disorder and reduce crystallinity, thermal treatment at 800 °C appears optimal for balancing dopant incorporation and crystal quality. The absence of secondary phases further confirms the structural integrity of the Mn-doped h-BN system, making it a suitable candidate for defect-engineered functional materials.

1.4.2. Scanning Electron Microscopy Images of Mechanically Induced Defects in h-BN, and Mn:hBN

The structural morphology of the synthesized h-BN samples was examined using SEM. Representative SEM micrographs of both the HBN and NHBN samples, before and after ball milling, are presented in Figure 8.

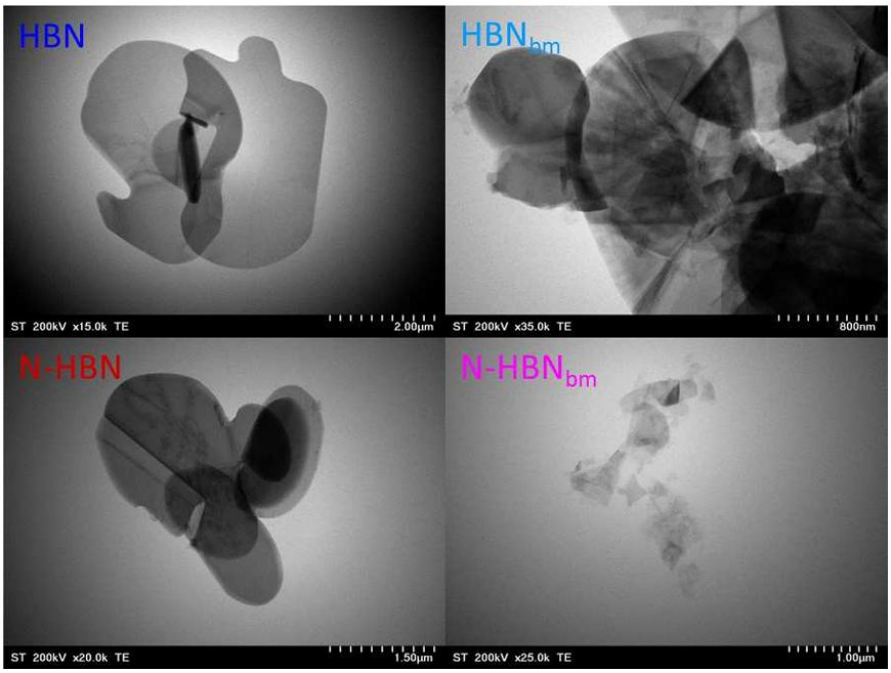

Figure 8: SEM images of HBN and NHBN samples before and after the ball milling process, showing the influence of ball milling on the morphology

All samples exhibit a characteristic nanosheet morphology, which becomes noticeably reduced in lateral dimensions following the milling process. This reduction in sheet size is attributed to the mechanical shearing forces induced by high-energy ball milling. The 2D nanosheet configuration is considered advantageous for electrochemical applications due to its inherently high surface area, which offers a greater number of accessible active sites for redox reactions and facilitates potential surface functionalization (Khan et al. 2016, García-Miranda Ferrari, Rowley-Neale, and Banks 2021). While the formation of two-dimensional layers is typical for h-BN, it is known that under specific synthesis conditions, such as exposure to high mechanical stress or elevated pressure, three-dimensional phases may emerge (Schimpf, Motylenko, and Rafaja 2013). This is evident in the SEM images provided in Appendix 2, where both HBN and NHBN samples exhibit minor 3D features.

These are most likely the result of nanosheet folding, wrinkling, and partial stacking. The presence of these structural deviations is consistent with the phase information derived from the Rietveld refinement analysis discussed in the XRD results section, where such minor 3D phases are also considered.

1.4.3. Raman Analysis of Mechanically Induced Defects in h-BN, and Mn:hBN

h-BN shares a structural resemblance with graphite, as both materials are composed of two-dimensional atomic layers arranged in a hexagonal lattice. However, in contrast to the AB stacking of graphite, h-BN exhibits an AA′AA′ stacking configuration, in which boron atoms in one layer are positioned directly above nitrogen atoms in adjacent layers, and vice versa. A distinguishing feature in the Raman spectrum of h-BN is a prominent in-plane vibrational mode with Γ5+ or E2g symmetry, typically centered around 1364 cm^{-1} (Schimpf, Motylenko, and Rafaja 2013, Reich et al. 2005). This mode originates from the relative in-plane motion of boron and nitrogen atoms within the same layer, and the displacements in adjacent layers occur in a symmetric manner. Due to this symmetry, the longitudinal optical (LO) and transverse optical (TO) modes do not split, as their contributions effectively cancel out.

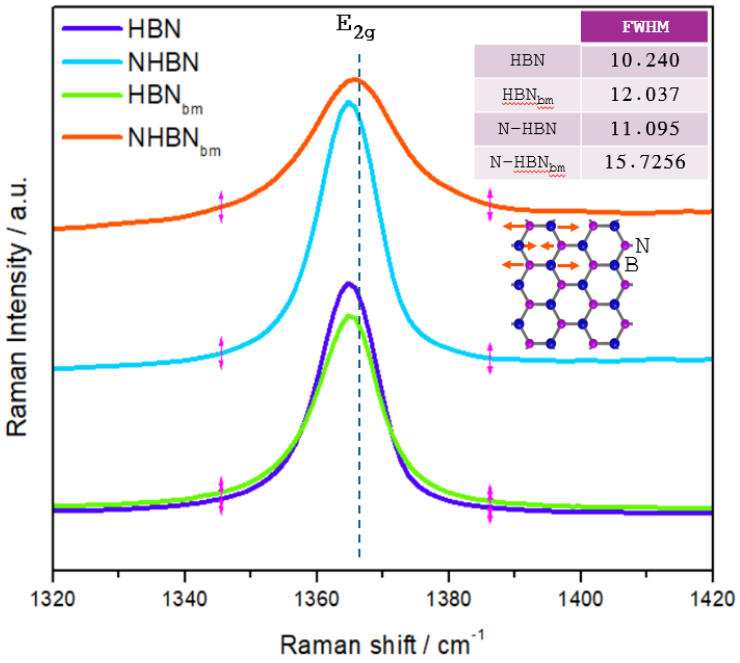

Figure 9: First-order Raman spectra of HBN and NHBN samples, shown before and after the ball-milling process. The E2g vibrational mode of h-BN is illustrated in the top-right corner

Figure 8 illustrates the Raman spectra of the h-BN samples, captured both before and after undergoing high-energy ball milling. The FWHM of the characteristic Raman peak was evaluated to assess the degree of structural order. As shown in Figure 9 and supported by the FWHM analysis, the mechanical milling process introduces notable lattice disorder, which is reflected in the broadening of the Raman peaks. This broadening serves as an indicator of reduced crystallinity and a diminished long-range structural order within the material (Eckmann et al. 2013, Betsch, Park, and White 1991). In h-BN, the characteristic Raman-active E_2g phonon mode typically appears around ~1366 cm^{-1} for bulk, crystalline material. This mode arises from the in-plane vibrations of boron and nitrogen atoms. In well-ordered crystalline h-BN, the phonon lifetime is relatively long due to coherent lattice vibrations over extended distances, resulting in sharp and well-defined Raman peaks. However, broadening of this E_2g peak indicates a reduction in phonon lifetime, which is a direct consequence of increased phonon scattering. This scattering arises from various forms of lattice disorder introduced through the ball milling process.

1.4.4. Electron Paramagnetic Resonance of Mechanically Induced Defects in h-BN, and Mn:hBN

EPR spectroscopy is a highly sensitive technique for probing paramagnetic centers, capable of detecting spin concentrations as low as 10^{12} spins, making it particularly suitable for investigating ionized defect centers in solid-state materials (Toloman et al. 2025, Ammar, Yildirim, et al. 2023, Ammar, Stan, et al. 2023, Aleinawi, Saritas, et al. 2025). The Q-band EPR spectra shown in Figure 10a and 10b reveal distinct signatures for the HBN and NHBN samples.

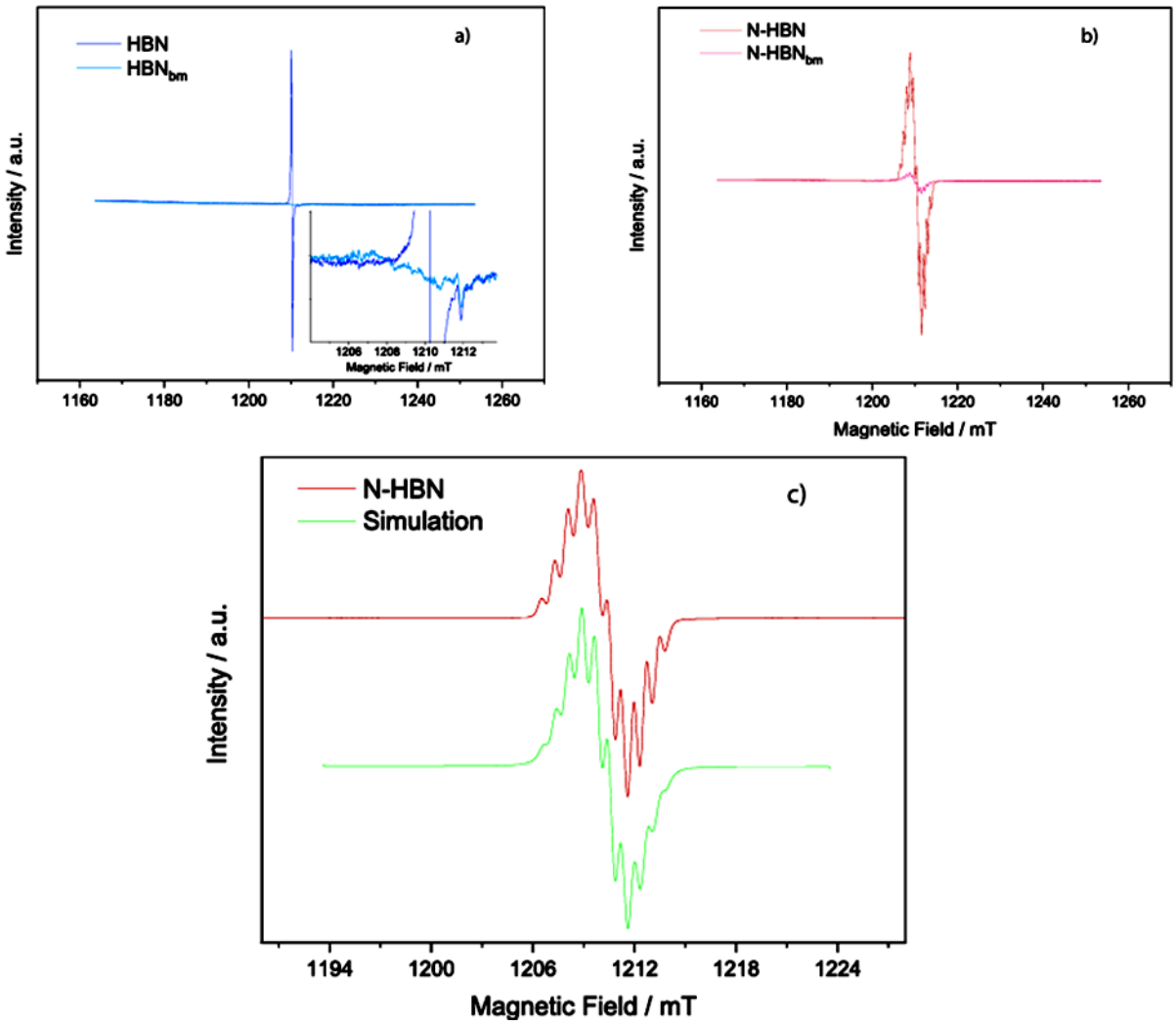

Figure 10: Q-band EPR spectra of the unmilled and ball-milled HBN (a) and NHBN (b) samples. Simulation of the NHBN EPR spectrum (c) reveals that the defect centers are nitrogen and not boron based

The pristine HBN sample exhibits a sharp, intense resonance with a linewidth of approximately 0.2 mT and a g-value of 1.996. This signal does not correspond to typical V_B nor V_N centers, which are usually characterized by complex hyperfine structures (Panich et al. 2005). Instead, we attribute this feature to carbon-related impurity centers, consistent with previous reports where carbon incorporation into h-BN yielded similar EPR responses (Römelt 1966, Moore and Singer 1972). Following high-energy ball milling, this carbon-associated signal vanishes, and a weak, multi-line spectrum emerges, as shown in the inset of Figure 10a. This transition suggests that the carbon impurities were primarily located at

or near the surface, where they formed paramagnetic dangling bonds that were disrupted by mechanical processing. The NHBN sample displays a more intricate EPR pattern as seen in Figure 9b, featuring a well-defined 10-line hyperfine structure. This pattern arises from an unpaired electron localized at a nitrogen vacancy, surrounded by three equivalent ^{11}B atoms. Given the natural abundance of ^{11}B (80.1%), the expected number of hyperfine lines is calculated as illustrated in Equation (5):

$$N = 2I \cdot n + 1 = 10 \qquad (5)$$

where $I(^{11}B) = 3/2$ and $n = 3$ (Römelt 1966). Figure 10c presents a simulated fit of the NHBN spectrum, modeled using two spin systems. The first, with spin $S_1 = 1/2$ and three equivalent ^{11}B nuclei, employs mixed Lorentzian and Gaussian line shapes with linewidths of 0.05 and 0.35 mT, respectively. The second component, assigned to a minor population of paramagnetic impurities, is characterized by a broader linewidth (2.4 and 0.01 mT) and the same spin value ($S_2 = 1/2$). The anisotropic hyperfine interaction (HF_{aniso}) parameters extracted from the simulation are summarized in Appendix 3 for a better overview of the EasySpin fitting parameters.

The g-factor and hyperfine values align with literature reports on singly ionized nitrogen vacancies in h-BN, affirming that V_N centers dominate the paramagnetic defect landscape in NHBN. In contrast, a V_B coordinated with three nitrogen atoms would be expected to exhibit a 7-line hyperfine pattern, which is not observed in this case. Post-ball milling, the overall intensity of the EPR signal in NHBN decreases markedly. This reduction is not due to the annihilation of the defect centers, as confirmed by an increase in photoluminescence intensity after milling. Rather, it suggests that the mechanical energy imparted during milling provides sufficient excitation to release the trapped electrons from the V_N defect states, effectively quenching the EPR-active centers without eliminating the defects themselves.

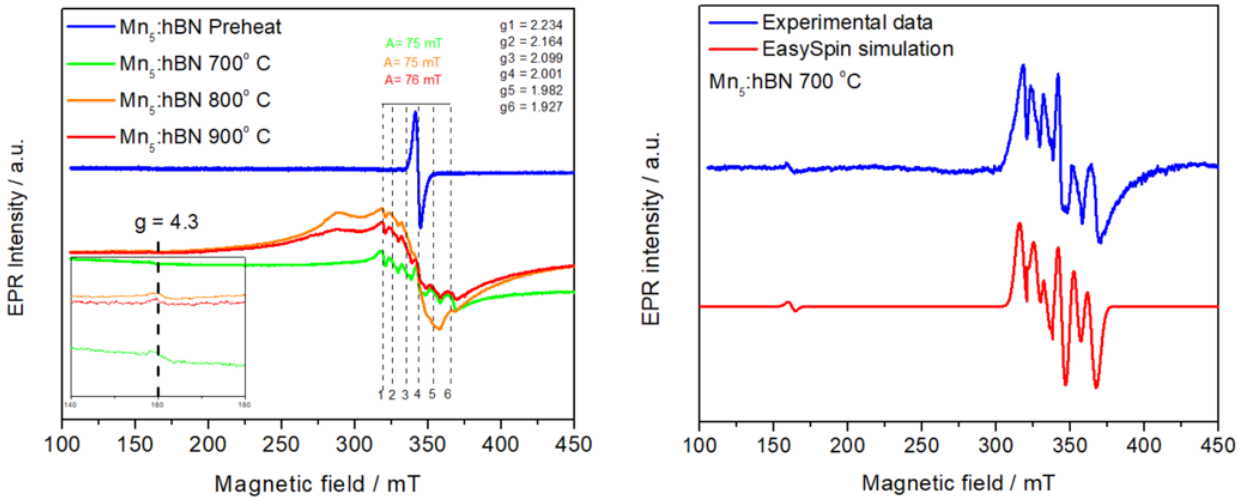

Figure 11: X-band EPR spectra of Mn_5:hBN samples taken at different heat treatment temperatures showing the appearance of hyperfine lines after heat treatment (left), and the EasySpin simulation of the hyperfine lines as a result of Mn^{+2} incorporation into the structure of h-BN

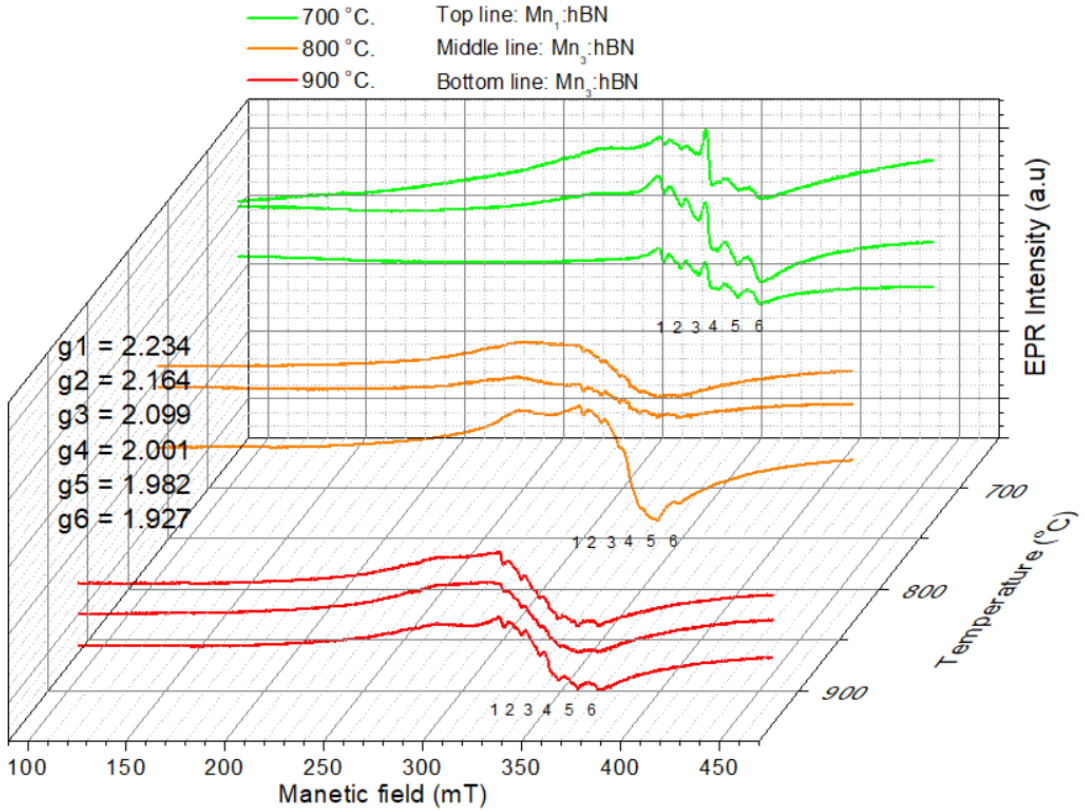

Figure 12: X-band 3D EPR spectra of Mn doped h-BN samples at varying heat treatment temperatures, and varying Mn concentrations showing the sextet hyperfine lines of Mn^{+2} incorporation into the structure of h-BN

Figures 11 and 12 above show the X-band EPR spectra of Mn doped h-BN samples at different heat treatments temperatures, and different Mn dopant concentrations. The EPR analysis of 5% Mn-doped hBN samples subjected to varying thermal treatments revealed significant changes in the local environment and electronic configuration of Mn ions. In the preheated sample, a broad resonance centered around $g \approx 2.001$ was observed, indicative of unsuccessful incorporation of Mn^{2+} into the structure, likely on the surface or within interstitial positions. This low-field signal gradually diminished with increasing annealing temperature, suggesting a thermally driven migration of Mn ions into more ordered lattice sites. Starting from 700 °C and becoming more pronounced at 800 °C and 900 °C, a characteristic six-line hyperfine splitting emerged near $g \approx 2.0$, consistent with the electron-nuclear interaction of Mn^{2+} ($S = 5/2$, $I = 5/2$) in a less distorted, substitutional environment within the hBN lattice. The extracted hyperfine coupling constant ($A \approx 75–76$ mT) obtained from EasySpin simulations shown in Figure 11 (right) aligns well with literature values reported for Mn^{2+} in insulating hosts. EasySpin simulation of the 700 °C sample further supported this interpretation, reproducing the spectral features through a multi-site g-tensor model (Babunts et al. 2023). Overall, the progressive thermal evolution from surface-bound to substitutional Mn sites reflects enhanced dopant incorporation and reduced local structural disorder with increasing annealing temperature.

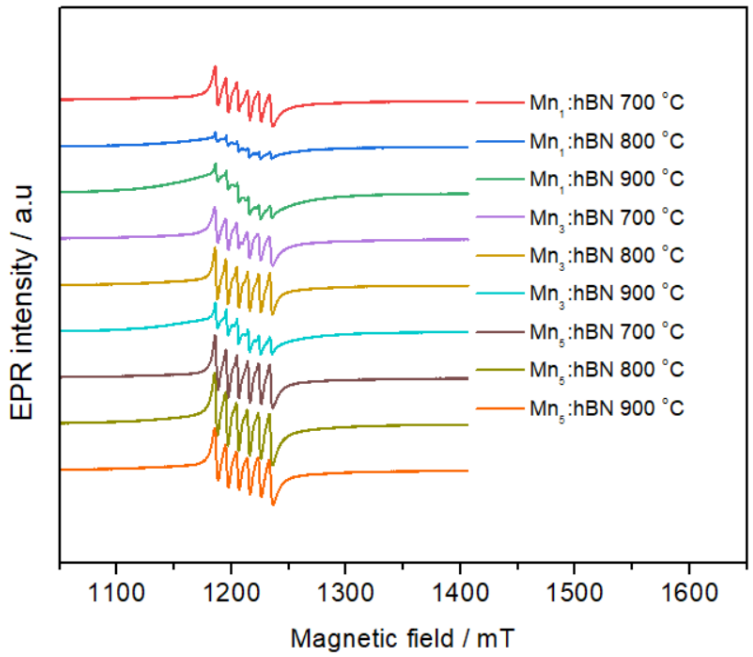

Figure 13: Q-band EPR spectra of spectra of Mn doped h-BN samples at varying heat treatment temperatures, and varying Mn concentrations

The Q-band EPR spectra of Mn-doped hBN samples shown in Figure 13 (Mn_{1-5}:hBN) annealed at different temperatures (700 °C, 800 °C, and 900 °C) provide further insights into the local magnetic environment and electronic configuration of Mn^{2+} ions. All samples exhibit a well-resolved six-line hyperfine splitting pattern in the magnetic field range between 1150 mT and 1300 mT, a hallmark of isolated Mn^{2+} species ($3d^5$, S = 5/2, I = 5/2) with significant electron-nuclear hyperfine interaction. The hyperfine lines remain distinct and regularly spaced across all doping concentrations and annealing temperatures, confirming the presence of paramagnetically isolated Mn^{2+} ions within the hBN lattice. Notably, the intensity and resolution of the hyperfine lines improve with increasing Mn concentration and annealing temperature. For the lower Mn concentrations (Mn_1 and Mn_2), the hyperfine features appear relatively weak and broadened at 700 °C, suggesting either incomplete dopant activation or residual local disorder. As the annealing temperature rises to 800 °C and 900 °C, the signal intensity increases and the line widths become sharper, indicating enhanced dopant incorporation and a reduction in local structural distortions around Mn^{2+} centers. For higher doping levels (Mn_3 to Mn_5), the hyperfine lines are more intense and better resolved, particularly after annealing at 900 °C, implying higher occupancy of substitutional sites within the hBN lattice. This trend aligns with the X-band

EPR observations, reinforcing the conclusion that thermal treatment plays a critical role in promoting the migration of Mn ions into more symmetric and substitutionally favorable positions. The consistent hyperfine coupling observed across all samples (~75–76 mT in X-band) further confirms that the Mn ions predominantly exist in a +2 oxidation state and experience a relatively similar ligand field environment regardless of concentration.

Overall, the Q-band measurements offer enhanced spectral resolution compared to X-band, allowing clearer observation of the Mn^{2+} hyperfine structure and providing additional evidence for successful thermal-driven incorporation of Mn dopants into the hBN framework.

1.4.5. Photoluminescence of Mechanically Induced Defects in h-BN, and Mn:h-BN

PL spectroscopy was employed to investigate the optical properties and defect-related emissions in the h-BN samples, providing complementary insights into their structural disorder. Figure 14 presents the room-temperature PL spectra of both unmilled and ball-milled HBN and NHBN samples, recorded using an excitation wavelength of 380 nm. Although this excitation energy lies well below the intrinsic bandgap energy of h-BN (~210 nm), it effectively probes the sub-bandgap defect states responsible for ultraviolet and visible light emissions. The deconvolution of the PL spectra, represented by the accompanying pie charts, reveals the relative contribution of various emission centers.

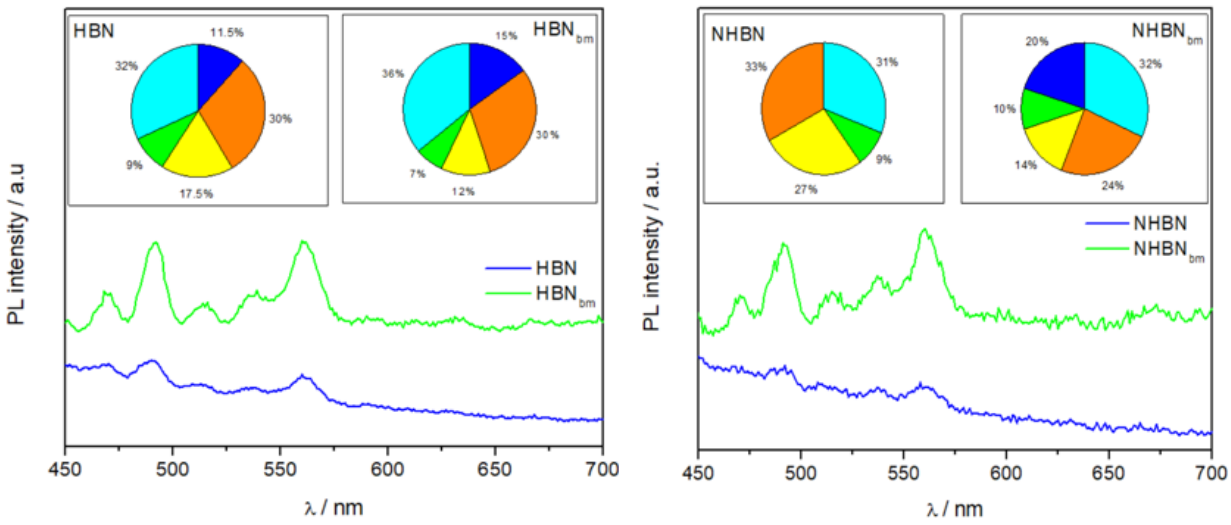

Figure 14: PL spectra of the unmilled and ball-milled HBN (Left) and NHBN (Right) samples. The pie charts show the emissions percentage related to each sample, the emissions were obtained from the area under each peak after deconvolution

Notably, in contrast to the behavior observed in EPR measurements discussed in the previous section, the ball-milled samples of both HBN and NHBN exhibit a pronounced increase in PL intensity across the measured spectral range. This enhancement indicates a substantial rise in defect density following the ball milling process. However, when these PL findings are correlated with EPR results, an interesting distinction emerges: despite the increase in optical defect signatures, the overall EPR signal intensity decreases significantly after milling for both sample types. This inverse trend suggests that the defects responsible for the enhanced PL emissions are predominantly non-paramagnetic and likely exist in charge-neutral or diamagnetic states.

The origin of the PL emissions in h-BN has been extensively discussed in the literature (Stagi et al. 2024, Silly et al. 2007, Nash et al. 2019, Berzina et al. 2016). Emissions in the blue and cyan regions (450–520 nm) are typically attributed to quantum emitters associated with nitrogen vacancies or carbon-related impurities introduced during synthesis or post-processing (Liang et al. 2023). Additionally, emissions in the green (~530 nm), yellow, and orange ranges (560–620 nm) are commonly linked to various intrinsic point defects and complex vacancy configurations within the h-BN lattice (Weston et al. 2018, Castelletto et al. 2020). The combined analysis of PL and EPR data offers a comprehensive understanding of defect evolution in these materials. For pristine h-BN, PL emissions are largely dominated

by carbon-related defect states, which act as luminescent centers in the visible region. In contrast, the PL behavior of NHBN is primarily governed by V_N centers, which are known to act as efficient visible-light-emitting sites. The ball milling process further amplifies the optical activity in both materials by generating a higher density of defect states.

However, the EPR response of the two materials to ball milling differs markedly. In h-BN, the reduced EPR signal intensity after milling likely results from the ionization and subsequent removal or passivation of carbon-based paramagnetic defects from the surface, decreasing the population of detectable unpaired electron centers. In the case of NHBN, two mechanisms appear to contribute to the EPR signal reduction: first is the conversion of paramagnetic nitrogen vacancies into diamagnetic or recombined states, and second is the defect oversaturation, where increased defect–defect interactions lead to significant line broadening and overall signal suppression.

This integrated PL-EPR analysis highlights the complex and sample-dependent dynamics of defect generation, transformation, and annihilation in h-BN systems. While PL spectroscopy sensitively captures the optical activity and relative defect populations, EPR spectroscopy offers a quantitative measure of the paramagnetic defect centers and their evolution under different processing conditions.

Figure 15 below depicts the PL spectra of Mn doped h-BN samples at varying heat treatment temperatures, and different Mn dopant concentrations.

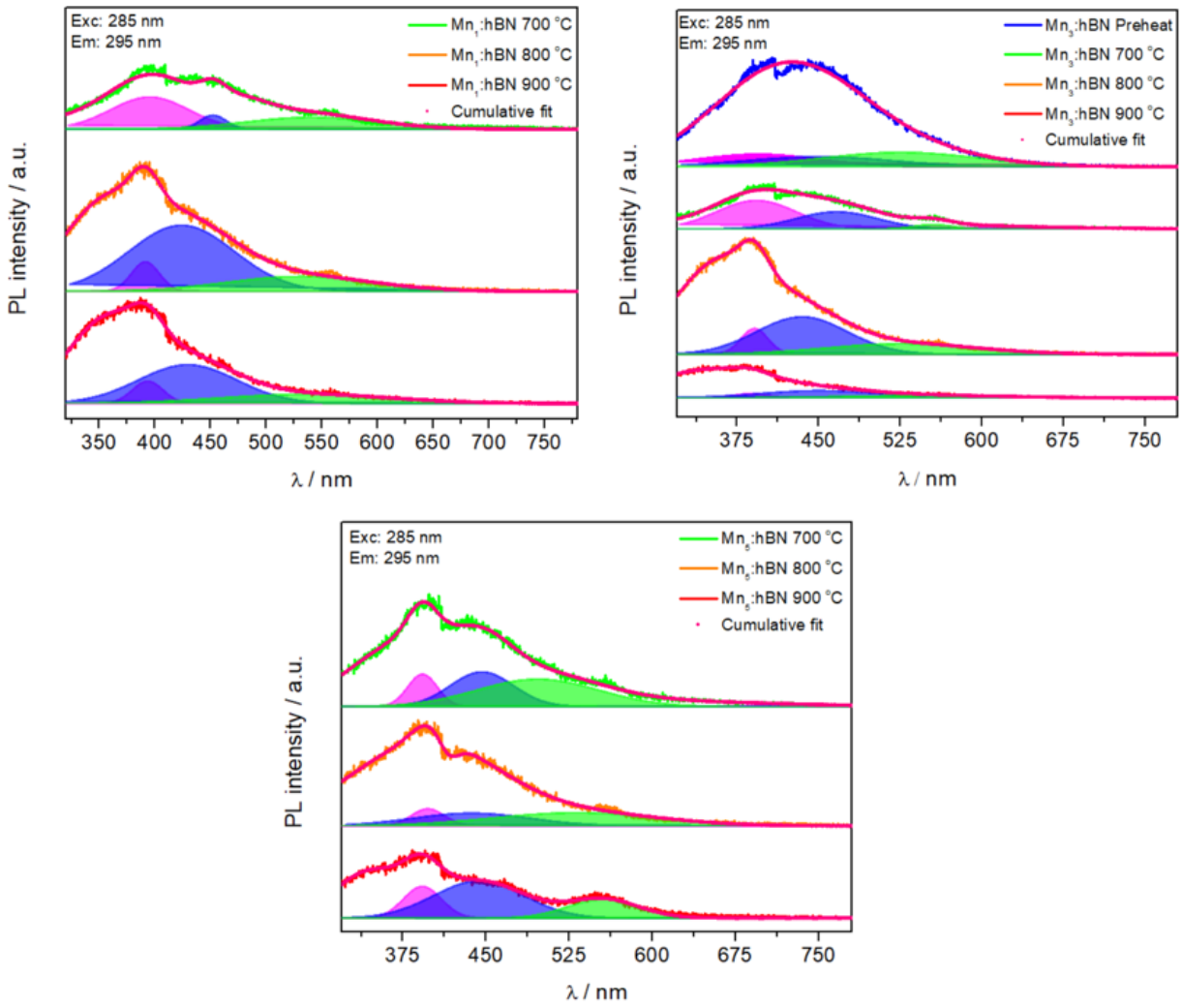

Figure 15: PL spectra of Mn doped h-BN samples at different heat treatment temperautres, and different Mn dopant concentrarions showing the effect of Mn dopant on the shift of the emissions in the visible light range

The influence of Mn dopant concentration and annealing temperature on the optical behavior of h-BN can be clearly discerned from the PL spectra presented in Figure 15, along with the corresponding emission percentage distributions illustrated in Appendix 4. A notable enhancement in blue light emission intensity is observed as both the heat treatment temperature and Mn doping level increase. Although specific reports on Mn-doped h-BN remain scarce in the literature, this trend is consistent with observations from other transition metal ions (TMI)-doped h-BN systems. Previous studies have demonstrated that TMI incorporation introduces additional electronic states within the bandgap of h-BN, thereby facilitating radiative recombination pathways responsible for blue emission (Nie, Jia, Guo,

He, Weng, and Ju 2024). In the context of Mn doping, the presence of Mn ions can create localized energy states that promote such recombination processes. Furthermore, thermal treatment plays a crucial role in modulating defect structures and activating dopant-related luminescent centers, which further amplifies the observed blue emission. This combined effect of doping and thermal processing is consistent with the defect-mediated luminescence mechanisms widely reported for similar doped boron nitride systems.

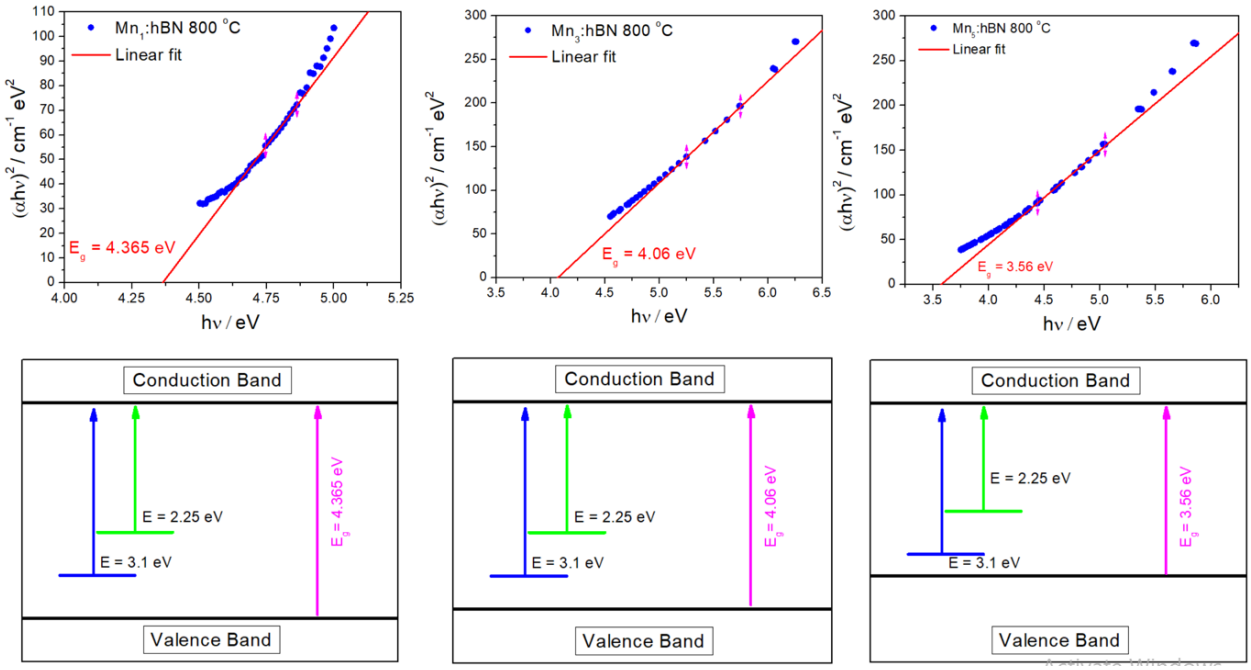

Figure 16: Tauc plots of Mn-doped h-BN samples showing the band gap energy change as a function of increasing Mn dopant concentration, along with an illustration of the energy model

To investigate the influence of Mn doping on the optical bandgap energy of h-BN, Tauc plot analysis was employed to estimate the bandgap values of the synthesized samples, as illustrated in Figure 16. The Tauc method is a widely used optical characterization technique for determining the optical bandgap of semiconducting materials based on UV–Vis absorbance data.

The analysis involves recording the UV–Vis absorbance spectrum of each sample, followed by converting the absorbance data into the absorption coefficient α using the relation illustrated in Equation (6):

$$\alpha = \frac{2.303\ x\ Absorbance}{t} \qquad (6)$$

where t is the thickness of the sample. Subsequently, the Tauc relation is applied, which expresses the relationship between the absorption coefficient and the incident photon energy (hν) as illustrated in Equation (7):

$$(\alpha h\nu)^n = A(h\nu - E_g) \qquad (7)$$

where hν is the photon energy, A is a material-dependent constant, E_g is the optical bandgap energy, and n denotes the nature of the electronic transition (with n = 2 for allowed indirect transitions, commonly used for h-BN).

By plotting $(\alpha h\nu)^n$ vs hν, the bandgap energy is estimated by extrapolating the linear portion of the curve to intersect the photon energy axis (hν), where this intercept corresponds to the optical bandgap of the material. The generated Tauc plots for the Mn-doped h-BN samples revealed distinct variations in bandgap energies with increasing Mn concentration, demonstrating the dopant-induced modulation of the electronic structure of h-BN. The band gap energy seems to be decreasing with increasing the Mn dopant concentration. This observation is crucial for the electrochemical performance to be discussed in Chapter 4. The decrease of band gap energy indicates an improvement of the conductivity of the material, which in turn enhances the electrochemical performance of h-BN as an electrode material in energy storage devices.

1.5. Microstructural and Defect Landscape of h-BN

In this chapter, a comprehensive structural, morphological, optical, and defect analysis of both pristine and Mn-doped h-BN materials has been presented, highlighting the influence of ball milling, Mn dopant concentration, and thermal treatment on the physicochemical properties of h-BN.

XRD analysis confirmed the preservation of the hexagonal phase across all synthesized samples, with no evidence of secondary impurity phases such as manganese oxides, even at high Mn doping levels and elevated calcination temperatures. Rietveld refinement further revealed subtle variations in lattice parameters and average crystallite sizes, with clear trends of crystallite size reduction and increased structural disorder upon ball milling and Mn doping. Notably, the NHBN samples exhibited higher defect densities, as reflected in the suppression and broadening of the (002) reflection, a feature further accentuated after ball milling.

Morphological evaluation by SEM supported these structural findings, showing a marked reduction in lateral sheet size and the appearance of nanoscale wrinkles and folding in milled samples, thus confirming the generation of a more defective and high-surface-area morphology favorable for electrochemical applications.

Raman spectroscopy provided additional evidence of increased lattice disorder following mechanical processing, with significant broadening of the E_2g phonon mode observed in ball-milled samples. The evolution of vibrational features further validated the XRD and SEM observations, indicating disruption of long-range crystalline order due to both doping and milling.

EPR spectroscopy offered valuable insights into the defect landscape, identifying carbon-related impurity centers in pristine h-BN and V_N centers in NHBN. Ball milling led to a notable reduction in paramagnetic signal intensity, suggesting both the annihilation of carbon-based centers and the ionization or passivation of nitrogen vacancies. The successful incorporation of Mn^{2+} ions into the h-BN lattice was confirmed by the appearance of characteristic six-line hyperfine splitting in both X-band and Q-band EPR spectra at elevated annealing temperatures, with hyperfine constants (~75–76 mT) consistent with substitutional Mn^{2+} incorporation.

PL studies demonstrated a substantial increase in blue light emission intensity with rising Mn concentration and annealing temperature, a trend attributed to the introduction of Mn-induced defect states within the bandgap. This increase in blue emission, coupled with reduced EPR-active centers, further supports the conclusion that Mn doping introduces predominantly non-paramagnetic luminescent centers, consistent with reported defect-

mediated recombination mechanisms in TMI-doped h-BN systems. Finally, Tauc plot analysis revealed a progressive narrowing of the optical bandgap with increasing Mn content, suggesting Mn-induced bandgap engineering in h-BN. This bandgap reduction is particularly significant, as it implies enhanced electrical conductivity, a critical factor for improving charge transport in electrochemical applications.

In summary, the systematic modification of h-BN through Mn doping, thermal treatment, and mechanical milling has led to controlled structural disorder, defect engineering, and tunable optical and electronic properties. These modifications are expected to positively influence the electrochemical performance of the synthesized materials, as will be elaborated in Chapter 4.

2. STRUCTURAL DEFECTS IN ZnO STRUCTURE

2.1. Introduction

Transition metal-based electrode materials have been the subject of intensive research in the pursuit of energy storage systems that combine cost-efficiency, rapid charge-discharge capability, high performance, and long operational life (Cui and Meng 2020). Among these, transition metal oxides (TMOs), notably ZnO (Stefan et al. 2024), MnO_2 (Kour, Tanwar, and Sharma 2022), and RuO_2 (Umran and Alibage 2024), have attracted attention due to their inherently high capacitance values and robust electrochemical stability. Despite these strengths, TMO electrodes often face persistent challenges such as relatively low energy density, elevated interfacial resistance, limited mechanical resilience, and increasing environmental considerations. To address these limitations, recent studies have proposed various strategies that significantly enhance the electrochemical performance of TMOs (Zhao et al. 2017, Nasser et al. 2023, Nasser et al. 2022).

Zinc oxide (ZnO), in particular, has emerged as a promising material because of its favorable intrinsic properties. It possesses a wide direct bandgap of approximately 3.44 eV (Zagorac et al. 2022), a high exciton binding energy (~60 meV), and a low power threshold for optical pumping (Teisseyre et al. 2020). ZnO also demonstrates efficient ultraviolet (UV) emission, a notable piezoelectric coefficient (d_{33} = 9.093 pm/V, which increases to 26.7 pm/V in the nanoscale regime) (Nadupalli et al. 2021), and a favorable pyroelectric coefficient, all while being chemically stable and environmentally benign. These qualities render ZnO suitable for various applications including short-wavelength optoelectronics (Khan et al. 2024), photovoltaics (Sharma et al. 2022a), sensing and actuation systems (Srikanth et al. 2021),

supercapacitor electrodes (Ammar et al. 2025), UV light sources, photodetectors, and chemical or biological sensors (Que et al. 2021).

Various synthesis routes have been developed for producing ZnO nanomaterials, each influencing the material's size, shape, and crystalline structure (Noman, Nesrine, and and Petru 2022). These include chemical approaches such as sol–gel, hydrothermal, solvothermal, precipitation, chemical vapor deposition, microemulsion, and microwave-assisted synthesis; physical techniques such as laser ablation, ball milling, and thermal evaporation; and biological (green) methods involving enzymatic or plant-based synthesis. Among these, prominent methods include co-precipitation (Devi and Velu 2016), sol–gel (Arya et al. 2021), ball milling (Amirkhanlou, Ketabchi, and Parvin 2012), hydrothermal (Liu et al. 2022), solvothermal (Kunjara Na Ayudhya et al. 2006), and microwave-assisted techniques (Aleinawi, Ammar, et al. 2025, Aleinawi et al. 2022). Each method yields distinct nanostructural features, thereby influencing application-specific performance. Microwave-assisted synthesis, in particular, stands out due to its rapid reaction kinetics and eco-friendly nature. It enables ZnO nanostructures to be synthesized within minutes, with reduced chemical usage and lower energy demands. Furthermore, it allows fine-tuning of morphology and crystallinity by controlling reaction time, microwave power, and precursor concentration (Aleinawi, Ammar, et al. 2025, Aleinawi et al. 2022). Such process control has led to ZnO-based nanostructures exhibiting high specific capacitance, elevated energy densities, and prolonged cycle life, typically exceeding 1000 charge/discharge cycles—making them highly promising for energy storage devices.

Another critical aspect influencing the electrochemical performance of ZnO-based electrodes is the presence of defect centers (Altaf et al. 2024). Defects, defined as disruptions in the periodic atomic lattice, have a profound impact on physical, chemical, and electronic properties. These include point defects (e.g., vacancies), edge dislocations, and surface irregularities, all of which affect charge storage behavior and ion transport efficiency (Singal et al. 2020). Defect engineering strategies have shown that introducing vacancies and structural distortions can increase specific capacitance by providing additional charge trapping sites and improving ionic/electronic conductivity (Ammar et al. 2021). Oxygen vacancies in particular have been linked to enhanced carrier concentrations and improved

reaction kinetics, as they serve as shallow donors that modulate the electronic structure. These vacancies can also increase interlayer spacing, facilitating faster ion diffusion and promoting pseudocapacitive redox reactions (Wu et al. 2019).

Furthermore, doping strategies are frequently employed to modulate ZnO's defect landscape and electronic structure. Introducing appropriate dopant ions can not only enhance electrical conductivity but also create additional redox-active sites, thereby boosting pseudocapacitance. Surface defects can further enhance electrochemical activity by decreasing charge transfer resistance (Toufani et al. 2020). When combined with functional surface groups, intrinsic defects contribute to improved ion adsorption and migration, ultimately increasing overall storage capacity. Defect-related features are typically characterized using techniques such as PL, Raman spectroscopy, and EPR. Among dopants, Mn is particularly effective in modifying ZnO's structural and functional properties. In addition to contributing beneficial magnetic and electronic characteristics, Mn enhances grain boundary alignment and crystallinity. Studies by Pearton *et al.* (Pearton et al. 2003) and Zheng *et al.* (Zheng, Hu, and Yang 2017) demonstrated that even low levels of Mn doping significantly improve grain growth and atomic alignment, leading to enhanced electrochemical activity. The ionic radius of Mn^{2+} (0.66 Å) closely matches that of Zn^{2+} (0.60 Å), allowing for favorable substitutional doping. This similarity helps minimize lattice strain and supports the formation of stable substitutional defects that can further enhance material performance. While conventional hydrothermal methods have been used extensively to synthesize Mn-doped ZnO, the influence of microwave synthesis parameters, especially microwave power, remains underexplored. The novelty of the present study lies in its integrated approach, combining a binder-free supercapacitor architecture with a systematic exploration of defect engineering via microwave-assisted synthesis and Mn doping. Unlike standard fabrication methods that rely on binders and conductive additives (which often obscure the intrinsic behavior of active materials), our custom-designed, two-point mounting device enables direct assembly of all-in-one supercapacitors. This allows for an unbiased evaluation of the electrochemical performance of the ZnO-based active material. This chapter will mainly focus on the defective structure of h-BN, and the role of the microwave power during synthesis on these defects, while the electrochemical performance will be discussed in details in Chapter 4.

Moreover, the study incorporates precise control of Mn^{2+} concentration and investigates its incorporation into the ZnO lattice using detailed EPR analysis. This not only confirms the oxidation state and substitutional nature of Mn dopants but also provides insights into the interplay between intrinsic defects (e.g., Zn vacancies) and extrinsic dopant-related defects. By correlating defect profiles identified through EPR, PL, Raman, and structural analysis with electrochemical properties, the study offers a comprehensive understanding of structure–function relationships. An additional innovation is the demonstration that microwave power can be used as a tunable parameter to modulate defect density, nanostructure morphology, aspect ratio, and crystallinity. This defect-sensitive approach to synthesis, and its correlation with electrochemical performance in Mn-doped ZnO nanomaterials, fills a critical gap in the existing literature. Thus, the current work provides novel insights into how dopant levels and synthesis energy collectively influence defect chemistry and, by extension, the capacitive behavior of ZnO-based electrode materials.

2.2. Literature Review

2.2.1. General Properties of ZnO

ZnO is a semiconducting metal oxide characterized by a wide, direct bandgap of approximately 3.3 eV (Zhang, Ram, and Stefanakos 2012). It can adopt either a hexagonal wurtzite or a cubic zinc blende crystal structure. However, under ambient conditions, ZnO most commonly forms the thermodynamically stable hexagonal wurtzite phase, as illustrated in Figure 17 below:

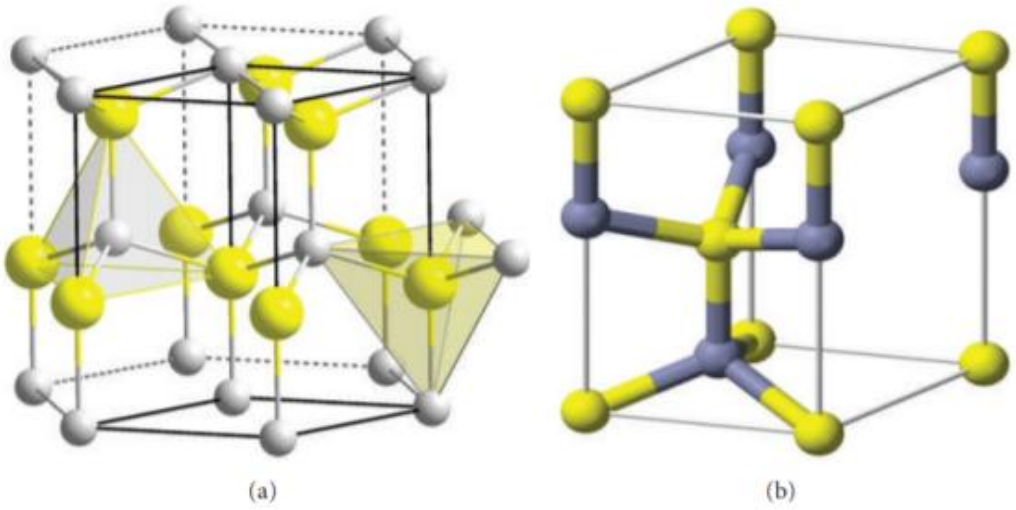

Figure 17: ZnO crystal structure (yellow Zn – grey O) (a) hexagonal wurtzite structure (b) hexagonal wurtzite unit cell, adapted from (Zhang, Ram, and Stefanakos 2012)

Table 4 below shows the major properties of ZnO.

Table 4: General physical and chemical properties of ZnO, adapted from (Sharma et al. 2022b)

Property	Value
Crystal structure	Hexagonal wurtzite at 300 °K
Lattice constants a,b,c	a= 0.32495 nm b= 0.32495 nm c= 0.52069 nm
Melting point	1975 °C
Density	5.66 g/cm^3
Bandgap energy E_g	3.3 eV (direct energy gap)
The effective mass of electrons	0.24
The effective mass of holes	0.59
Refractive index	2.01
Exciton binding energy	60 meV
Dielectric constant	8.656

2.2.2. Intrinsic Defects in ZnO

Native point defects in ZnO include the following:

- Oxygen vacancies V_O.
- Zinc vacancies V_{Zn}.
- Oxygen interstitials O_i.
- Zinc interstitials Zn_i.
- Antisite defects: Zn_O or O_{Zn} (although very rare).

Figure 18 below shows a schematic of the possible intrinsic point defects in ZnO's structure.

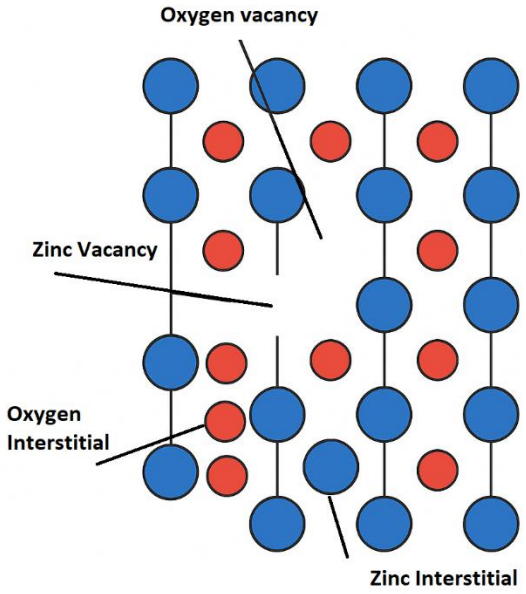

Figure 18: Possible intrinsic point defects in ZnO's structure, showing V_O, V_{Zn}, O_i, and Zn_i in the structure of ZnO

DFT calculations demonstrate that under Zn-rich conditions, V_O and Zn_i possess the lowest formation energies, making them dominant species. Other intrinsic defects like V_Zn and O_i are energetically less favorable. A landmark DFT study quantified formation energies for vacancies, interstitials, and defect complexes, confirming V_O as deep donors and Z_i as highly mobile (Vidya et al. 2011).

V_O is known to produce deep donor levels, while Zn_i produces shallow donors. Interestingly, the interaction between V_O and Zn_i reduce the defect formation energy (Özgür et al. 2005, Kim and Park 2009).

2.2.3. Extrinsic Defects in ZnO

Extrinsic defects refer to foreign atoms intentionally introduced into the ZnO lattice to modify its electronic, optical, magnetic, or catalytic properties. These dopants substitute either Zn^{2+} or O^{2-} lattice sites or occupy interstitial positions, generating new energy levels within the bandgap and interacting with native defects. The selection of dopant species, their oxidation state, ionic radius, and chemical compatibility with the host lattice critically influence the defect structure, crystallinity, and overall performance of ZnO-based materials. Transition metal dopants, such as Mn, Co, Ni, and Fe are of particular interest due to their ability to induce spin-polarized states and magnetic ordering, making doped ZnO a candidate for spintronic applications (Ruf et al. 2016a, D, Selvaraj, and Sundar 2017). Among these, Mn has been extensively explored owing to its half-filled $3d^5$ configuration (Mn^{2+}, S = 5/2), which allows strong exchange interactions and hyperfine splitting observable via EPR. Mn can isovalently substitute Zn^{2+} with minimal lattice strain, but its incorporation often triggers local distortion and promotes the formation or annihilation of intrinsic defects such as V_O and Zn_i. These complex defect interactions significantly impact charge carrier dynamics, band structure modulation, and defect-driven photoluminescence and magnetic behavior (Aleinawi, Ammar, et al. 2025, Aleinawi et al. 2022).

The nature and concentration of extrinsic defects in ZnO are highly sensitive to synthesis conditions. Conventional solid-state or sol-gel methods often result in inhomogeneous dopant distribution and secondary phases. In contrast, techniques like microwave-assisted hydrothermal synthesis offer advantages in terms of rapid nucleation, reduced defect clustering, and enhanced dopant incorporation, making them ideal for tailoring the defect landscape in doped ZnO systems. Therefore, understanding and controlling extrinsic defect formation in ZnO is central to developing advanced functional materials with customized

electrical, magnetic, and catalytic properties. The following sections will explore the specific case of Mn doping in ZnO, its impact on structural and electronic properties, and the role of synthesis parameters, particularly under microwave-assisted conditions, in modulating the defect chemistry of the material. EPR reveals Mn^{2+} hyperfine lines whose intensity and width depend on Mn concentration and microwave power, signaling interactions with vacancy-rich environments. PL shows defect-level emission changes linked to Mn integration and microwave treatment (Romeiro et al. 2013).

ZnO is intrinsically a paramagnetic semiconductor under ambient conditions. However, when doped with TMIs such as Mn, Fe, Cr, Co, or Cu, it can be transformed into a dilute magnetic semiconductor (DMS) as illustrated in Figure 19. These TMIs possess partially filled d or f orbitals, with at least one unpaired electron contributing to the overall magnetic behavior. Upon substitutional doping, for instance, Mn^{4+} can replace Zn^{2+} in the ZnO lattice, introducing unpaired $4s^2$ electrons into the hybridized sp^3 orbitals of the host matrix. This interaction between the magnetic dopant and the ZnO lattice results in the emergence of ferromagnetic or paramagnetic ordering, depending on dopant concentration and synthesis conditions. DMS materials have garnered significant attention for their potential applications in spintronic devices, where control over electron spin, in addition to charge, opens new avenues in next-generation information processing technologies.

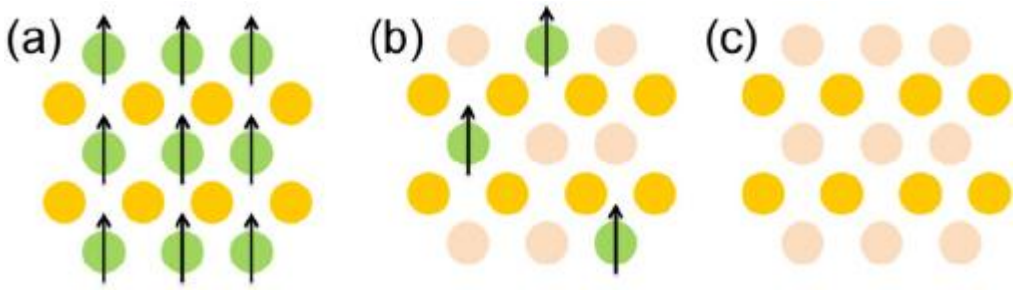

Figure 19: (A) Magnetic semiconductor, (B) DMS, (C) Nonmagnetic semiconductor, adapted from (Sharma et al. 2022b)

2.2.4. Role of the Synthesis Route

The synthesis route of ZnO plays a crucial rule in the formation of intrinsic and extrinsic point defects. Amongst the various synthesis routes, the microwave assisted route is one of the most studied method due to its unique advantages of parameters control, extremely fast reaction time, and simplicity. Furthermore, the microwave assisted hydrothermal method is well known for producing the nanowires or nanorods morphology, which maximizes the ratio between the length to the diameter of the rods aspect raio (AR), which in turn maximizes the specific capacitance of the electrode material. The volumetric heating in the microwave assisted hydrothermal method creates rapid, uniform nucleation, tight control over crystallite size, and excellent dopant distribution, in contrast to the traditional hydrothermal methods (Wojnarowicz, Chudoba, and Lojkowski 2020). On top of that, by varying microwave power or duration, one can tune rod vs. spherical particle formation and induce homogeneous Mn distribution with sharper defect spectral features. In our study, we aim to underline the relation between the microwave power during the synthesis route, and the defective structure of ZnO, which ultimately affects the electrochemical performance which will be discussed in details in later chapters.

2.3. Methodology

2.3.1. Materials and Synthesis

The synthesis was carried out using zinc nitrate hexahydrate (ZNH (Zn(NO3)2·6H2O, Acros Organics, 98% purity, CAS No.: 10196-18-6), hexamethylenetetramine (HMTA - (CH2)6N4, Merck, 99% purity, CAS No.: 100-97-0), the source of Mn was manganese acetate tetrahydrate (MAT - (CH3COO)2Mn·4H2O, Acros Organics, 99% purity, CAS No.: 6156-78-1), and methanol (CH3OH, Sigma Aldrich, 99.8% purity, Cas No.: 67-56-1) as solvent. A solution of 25 mM of ZNH and MTA was prepared by dissolving the precursors in deionized (DI) water and magnetically stirring for 1 hour at 600 rpm to ensure dissolving

of the precursors. The solution was then inserted in a conventional microwave oven, and the synthesis was carried out at different microwave powers of 160, 320, 640, and 800 W. The obtained powders were then filtered using filtration papers, washed thoroughly with DI water and alcohol, and left to dry out in an oven at 80 °C overnight. Mn-doped ZnO was synthesized by following the same steps aforementioned, with the addition of MAT dissolved in methanol to the ZNH and MTA solution, and to ensure sufficient energy for the incorporation of Mn ions into the structure of ZnO, the powder was subjected to an additional heat treatment process at the end of the synthesis. The powder was heated to 400 °C for 4 h in an inert atmosphere, and slowly cooled to room temperature afterward. The synthesized samples are illustrated as ZnO:Mn_x where x indicates the At.% Mn dopant. Figure 20 below shows a schematic of the synthesis procedure.

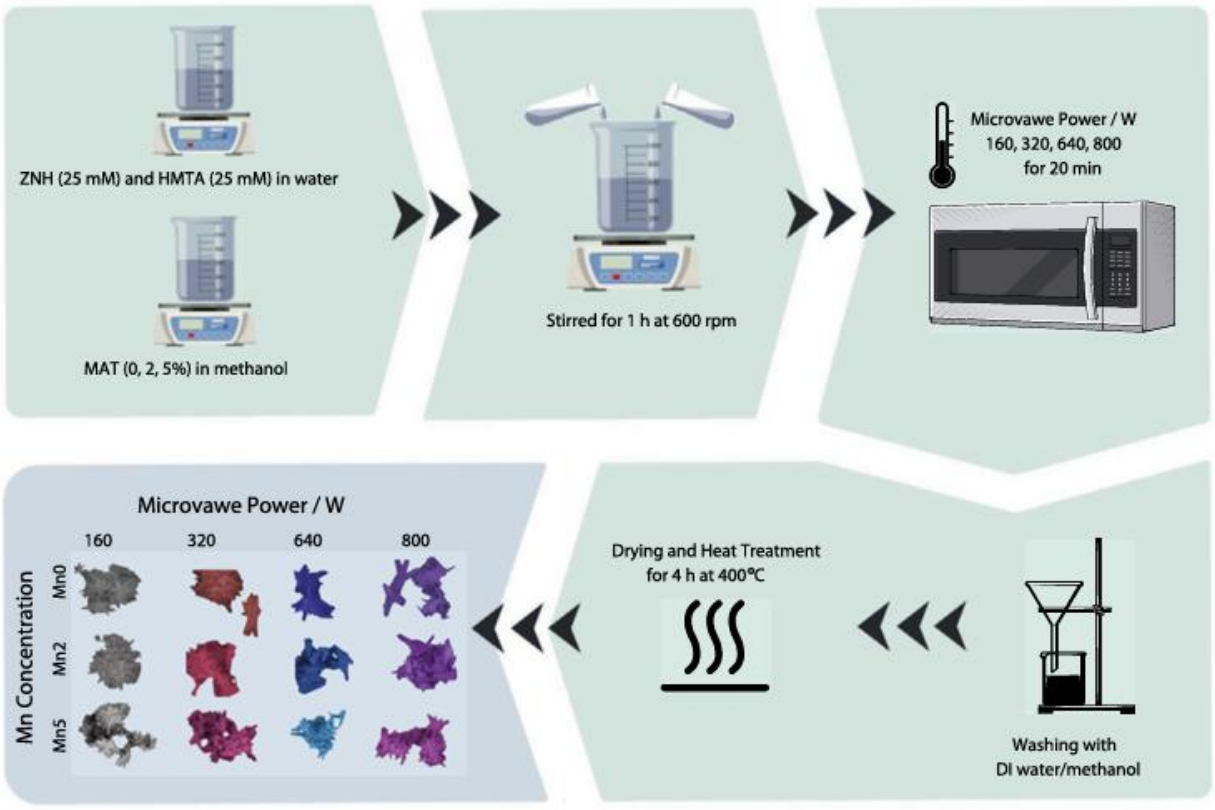

Figure 20: Schematic representation of the microwave-assisted hydrothermal technique used to synthesize ZnO and Mn-doped ZnO nanorods

2.3.2. BET Isotherms for Surface Area Estimation

he Brunauer–Emmett–Teller (BET) method is a widely used technique for determining the specific surface area of porous and nanostructured materials. It is based on the physical adsorption of gas molecules (typically nitrogen) onto the surface of a solid at cryogenic temperatures. By analyzing the resulting adsorption–desorption isotherms, the BET theory allows for the calculation of the surface area through multilayer adsorption modeling. The method assumes that adsorption occurs in layers, that the first layer forms uniformly, and that subsequent layers condense in a manner governed by the equilibrium between adsorption and desorption at each layer. The BET equation is applied to the linear portion of the isotherm at relative pressures (P/P_0) typically ranging between 0.05 and 0.30, where monolayer formation dominates. This calculated monolayer coverage is then used to determine the total specific surface area of the material.

The specific surface area analysis was carried out using N2 adsorption-desorption isotherms using a Micromeritics 3Flex surface characterization analyzer (Micromeritics Instrument Corp., Norcross, GA, USA). Before analysis, the samples were degassed under vacuum at 200 °C for 12 h to remove adsorbed gases and moisture, and the measurements were conducted at 77 K using high-purity nitrogen gas as the adsorbate. The Brunauer-Emmett-Teller (BET) method was applied to calculate the specific surface area from the linear region of the adsorption isotherm (typically at relative pressures *P/P*0 between 0.05 and 0.30).

2.4. Results and Discussions

2.4.1. Scanning Electron Microscopy Images of Mn-doped ZnO

The undoped and Mn-doped ZnO samples synthesized at varying microwave powers were systematically characterized to investigate the combined influence of dopant concentration and microwave irradiation on their morphological and structural attributes. SEM was

employed to evaluate the morphology of the nanostructures, as shown in Figure 21 and Appendix 3.

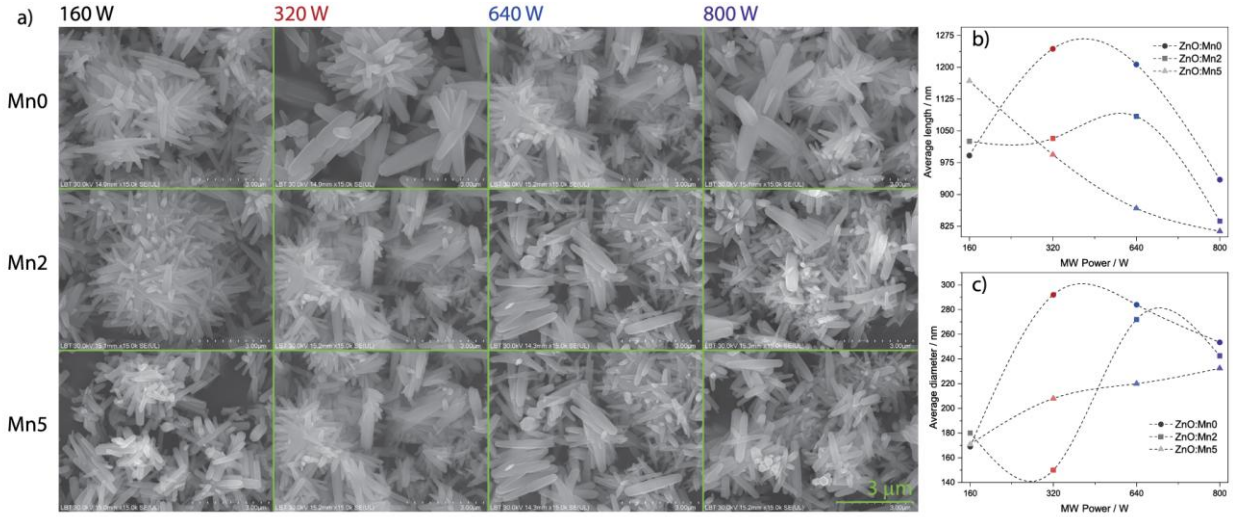

Figure 21: SEM micrographs of the undoped and Mn-doped ZnO materials synthesized at different microwave powers showing the nanorod-shaped structures (a) and the average nanorod length (b), and diameter (c) obtained from the histograms of the SEM images

For the undoped ZnO ($ZnO:Mn_0$), synthesis at a lower microwave power of 160 W resulted in uniformly distributed nanostructures with reduced size. Upon increasing the power to 340 W, notable elongation and an increase in rod diameter were observed. A further increase to 640 W improved both structural uniformity and overall size. However, at the maximum power level of 800 W, structural degradation became evident, with signs of breakage and morphological irregularity. In contrast, the Mn-doped samples exhibited distinct behavior. For $ZnO:Mn_2$ synthesized at 160 W, the morphology showed denser packing and more pronounced clustering compared to the undoped counterpart. Increasing the microwave power to 340 W and 640 W led to a gradual enhancement in structural density and growth. At 800 W, although deformation occurred, it was less severe than in the undoped sample. For the $ZnO:Mn_5$ composition, synthesis at 160 W produced highly aggregated and growth-suppressed morphologies relative to $ZnO:Mn_0$. As the microwave power increased, the morphology became increasingly distorted and uneven. The sample synthesized at 800 W exhibited heavy aggregation and lower aspect ratios, suggesting that excessive Mn doping or high microwave energy may hinder proper crystal growth.

Measurements of the nanorods' length and diameter were extracted from SEM images using the ImageJ software and are summarized in Figure 21 (b and c) and Appendix 3. The average diameter of ZnO:Mn_0 reached a maximum at 340 W, indicating this power level is optimal for rod growth in undoped samples. Interestingly, in Mn-doped samples, this peak diameter shifted to higher microwave power levels, with ZnO:Mn_2 and ZnO:Mn_5 showing maximum diameter at around 640 W. This shift implies a correlation between optimal growth conditions and both dopant concentration and microwave energy. Furthermore, increasing Mn content to 5% led to a general decrease in diameter, suggesting a dopant-induced inhibition of lateral growth.

Overall, the data indicate that lower microwave powers favor higher AR nanorods by promoting elongation while limiting radial expansion. However, these conditions also result in lower nanorod density. Conversely, higher microwave powers enhance density and thickness but may introduce structural degradation, especially at elevated Mn concentrations.

2.4.2. X-ray Diffraction of Mn-doped ZnO

XRD results of the pure and Mn-doped ZnO samples are presented in Figure 22, and Appendix 4.

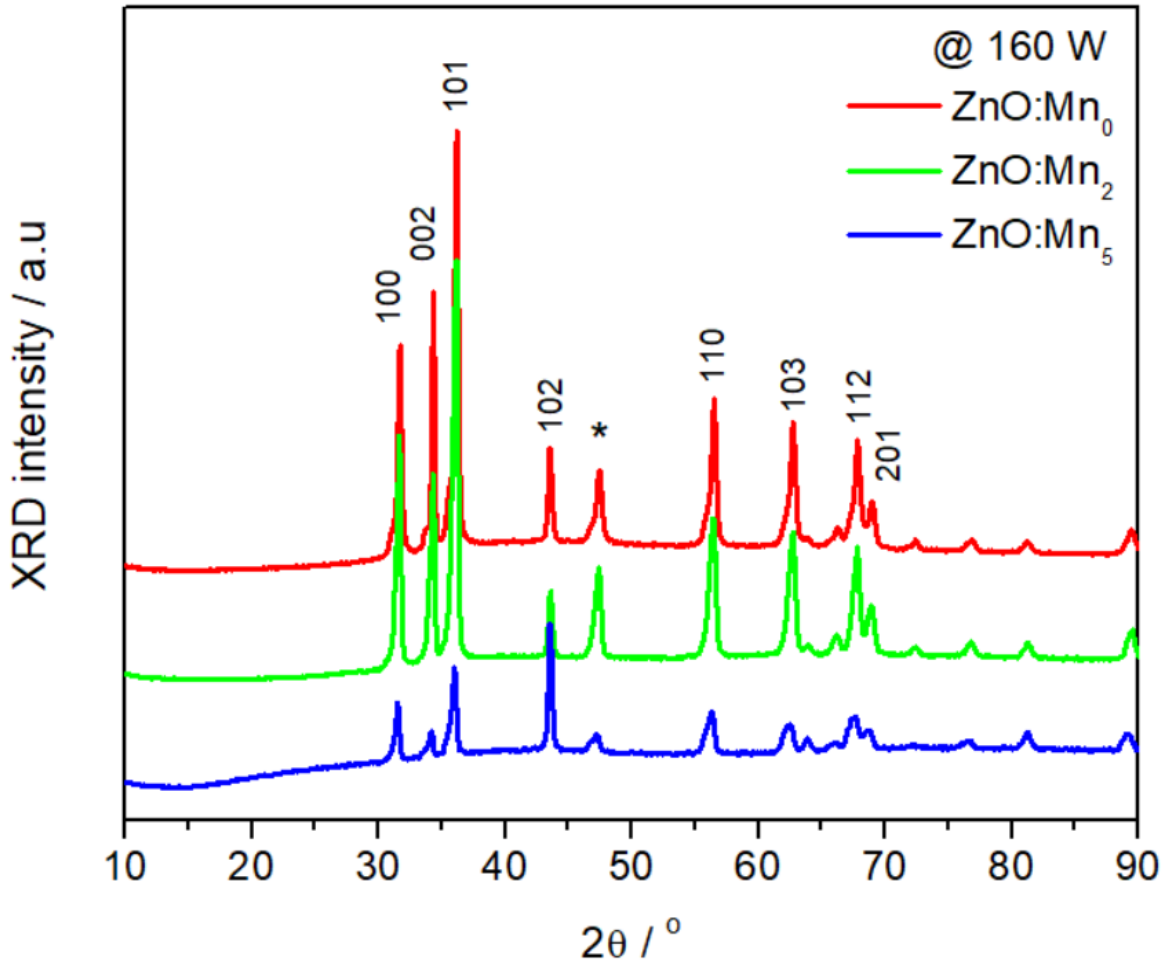

Figure 22: XRD diffractograms of the undoped and Mn-doped ZnO materials synthesized at 160 W microwave power

All patterns reveal distinct reflections corresponding to the hexagonal wurtzite phase of ZnO with space group $P6_3mc$, which is known to be the thermodynamically stable crystalline phase under ambient conditions (Dole et al. 2011). The characteristic diffraction peaks indexed to the (100), (002), (101), (102), (110), (103), (112), and (201) planes were observed at 2θ values of 31.77°, 34.42°, 36.25°, 47.54°, 56.60°, 62.86°, 67.96°, and 69.10°, respectively, consistent with standard JCPDS data (card no. 36-1451).

In addition to the expected wurtzite peaks, a secondary diffraction feature appears at approximately $2\theta \approx 43.5°$, which does not correspond to any planes of the wurtzite ZnO structure. Notably, this peak is also visible in the ZnO:Mn_0 samples, suggesting it is not related to Mn doping. It is therefore attributed to ZnO-related secondary phases, most likely residual elemental zinc or zinc hydroxide ($Zn(OH)_2$), as previously reported in the literature (Wang et al. 2015, Sapkota et al. 2019). Interestingly, the intensity of this impurity peak diminishes progressively with increasing microwave power. This trend is in agreement with previous studies indicating that elevated microwave energies promote the thermal decomposition of $Zn(OH)_2$ into ZnO, thus reducing the presence of hydroxide-related impurities (Tseng et al. 2012). To obtain detailed structural parameters, Rietveld refinement was performed on all XRD datasets (Figure 23 and Appendix 4), and the extracted values for average crystallite size and unit cell volume are compiled in Table 5.

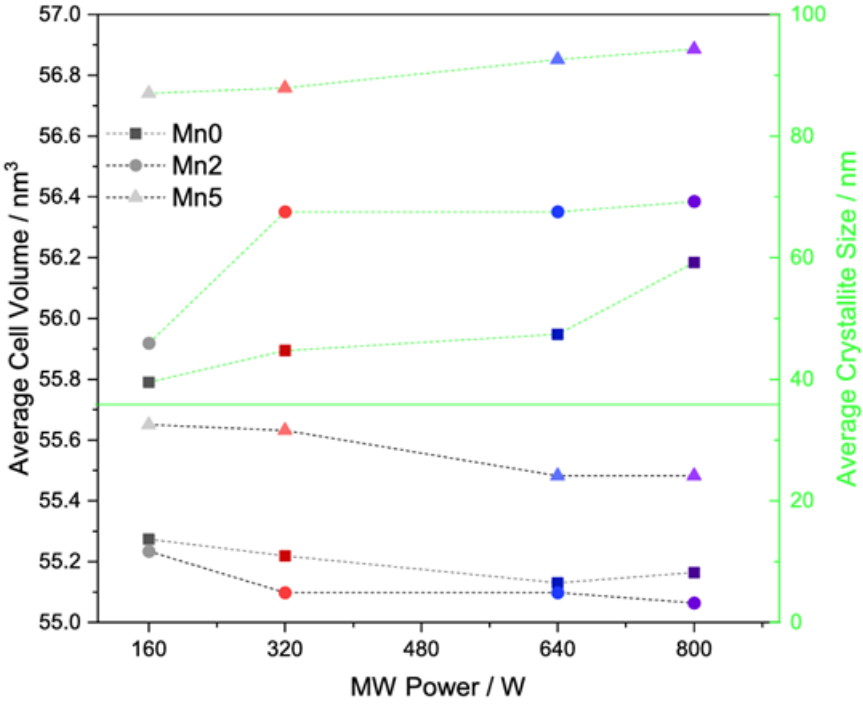

Figure 23: The average crystallite size and the average cell volume of ZnO:Mn samples as a function of the microwave power

Table 5: Lattice parameters and D of Mn doped ZnO samples synthesized at various microwave powers

Sample	a (nm)	b (nm)	c (nm)	D (nm)
ZnO:Mn_0 @ 160 W	3.255	3.255	5.217	39.5
ZnO:Mn_0 @ 320 W	3.254	3.254	5.215	44.7
ZnO:Mn_0 @ 640 W	3.252	3.252	5.213	47.4
ZnO:Mn_0 @ 800 W	3.253	3.253	5.213	59.2
ZnOMn_2 @ 160 W	3.256	3.256	3.21	45.9
ZnOMn_2 @ 320 W	3.252	3.252	5.21	67.5
ZnO:Mn_2 @ 640 W	3.252	3.252	5.21	67.5
ZnO:Mn_2 @ 800 W	3.251	3.251	5.21	69.2
ZnO:Mn_5 @ 160 W	3.262	3.262	5.23	87
ZnO:Mn_5 @ 320 W	3.263	3.263	5.225	87.9
ZnO:Mn_5 @ 640 W	3.263	3.263	5.211	92.6
ZnO:Mn_5 @ 800 W	3.263	3.263	5.211	94.3

The refined lattice parameters suggest a slight distortion upon Mn doping, indicating successful substitution of Zn^{2+} ions by Mn^{2+} within the crystal lattice. A general increase in average crystallite size was observed with both increasing Mn content and higher microwave power, implying that elevated energy input during synthesis promotes grain growth. However, this size enhancement does not directly imply an improvement in crystallinity. The diffraction peaks tend to broaden with increasing Mn doping, which is indicative of enhanced lattice strain and microstructural disorder, particularly noticeable at intermediate Mn concentrations. This peak broadening is attributed to the ionic size mismatch between Mn^{2+} (0.66 Å) and Zn^{2+} (0.60 Å), which introduces localized distortions within the ZnO crystal framework. The average unit cell volume shows a non-monotonic trend: for ZnO:Mn_2 samples, the cell volume decreases slightly compared to the undoped case, despite the larger ionic radius of Mn^{2+}. This counterintuitive behavior is attributed to the microstrain and local lattice compression induced by low-level dopant incorporation and elevated microwave power. Conversely, at higher Mn concentration (ZnO:Mn_5), the unit cell volume increases

again, consistent with the expected expansion of the lattice due to more significant substitution of Zn^{2+} by Mn^{2+}. This may indicate the approach to a solubility threshold, where the lattice can no longer fully accommodate the dopant without inducing phase separation or structural perturbations.

In summary, the XRD analysis demonstrates that both Mn doping and microwave synthesis parameters play crucial roles in tailoring the structural evolution of ZnO. While microwave power enhances crystallite growth and reduces hydroxide impurities, it also amplifies dopant-induced strain, which must be carefully optimized to preserve crystal integrity.

2.4.3. BET Surface Area Analysis of Mn-doped ZnO

BET surface area analysis was performed to evaluate the impact of surface characteristics on the capacitive behavior of the synthesized materials. The BET method enables a reliable estimation of the specific surface area by analyzing nitrogen adsorption–desorption isotherms, thereby providing valuable insight into the number of accessible active sites available for charge storage. As such, BET measurements are instrumental in elucidating the structure–property relationships of electrode materials for supercapacitor applications.

The obtained BET results are presented in Figure 24, where the nitrogen adsorption–desorption isotherms and the linear form of the BET equation are presented.

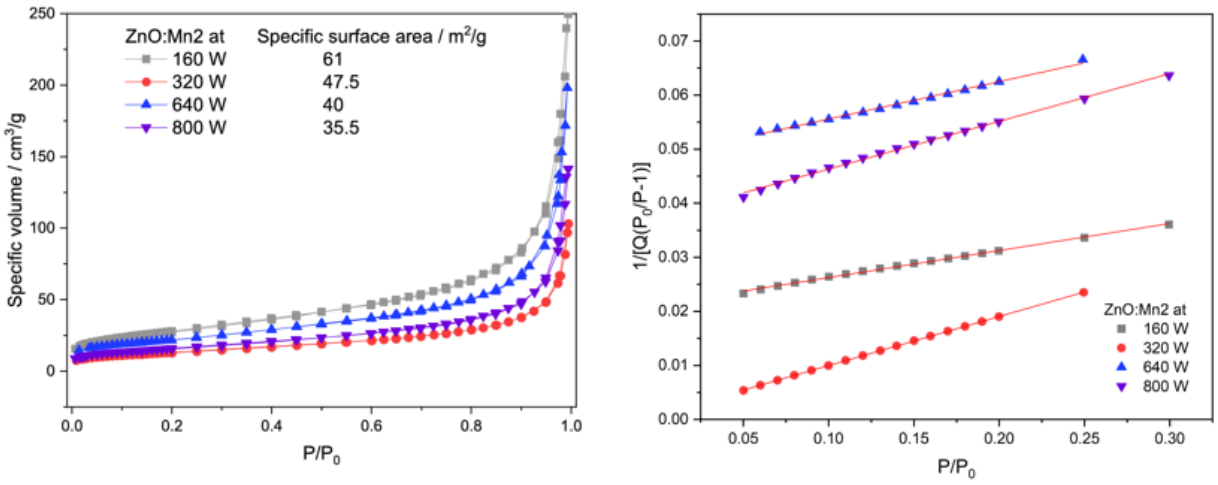

Figure 24: N_2 adsorption-desorption isotherms of the Mn_2:ZnO nanorods synthesized at different microwave powers (left), and linear fit of the N_2 adsorption-desorption isotherms obtained for the Mn_2:ZnO synthesized at differen microwave powers

The BET relation used for surface area estimation is given by Equation (8):

$$\frac{1}{V(\frac{P_0}{P}-1)} = \frac{C-1}{V_m C}.\frac{P_0}{P} + \frac{1}{V_m C} \qquad (8)$$

Where V denotes the volume of nitrogen adsorbed at equilibrium pressure P, is the volume corresponding to monolayer coverage, P_0 is the saturation pressure of the adsorbate, and C is a constant related to the enthalpy of adsorption. The specific surface area was determined from the linear region of the BET plot in the relative pressure range of 0.05-0.3, using the slope and intercept of the equation above.

Among the samples, ZnO:Mn_2 synthesized at 160 W exhibited the highest specific surface area of 61 m²/g. This value systematically decreased with increasing microwave power, suggesting that higher power levels result in lower surface area. This observation aligns well with the morphological data obtained from SEM image analysis, which showed increased aggregation and thicker structures at higher synthesis powers. Although a surface area of 61 m²/g is not exceptionally high, it falls within the typical range reported for Mn-doped ZnO nanowires and is strongly influenced by both the dopant concentration and the morphological evolution of the nanostructures (Biswas et al. 2020, Abdollahi et al. 2011). Despite the relatively modest surface area, Mn-doped ZnO nanowires can still achieve efficient electrochemical performance. This is largely attributed to the fast electron transport enabled

by the direct, vertically aligned configuration of the nanowires. Moreover, their high aspect ratio provides sufficient surface exposure to electrolyte ions, particularly along the nanowire sidewalls, thereby promoting ion diffusion and facilitating Faradaic reactions (Özkan et al. 2020, Lee et al. 2016). These structural features are especially advantageous when the dominant charge storage mechanism in the supercapacitor is governed by diffusion-controlled Faradaic processes, as will be elaborated in the subsequent section discussing the Dunn analysis in Chapter 4.

2.4.4. Raman Analysis of Mn-doped ZnO

Raman spectroscopy was employed to probe the vibrational properties of the synthesized ZnO nanostructures at the molecular level, providing key insights into their lattice dynamics. The acquired spectra, shown in Figure 25 and Appendix 5, confirm the successful formation of both undoped and Mn-doped ZnO under various microwave-assisted synthesis conditions.

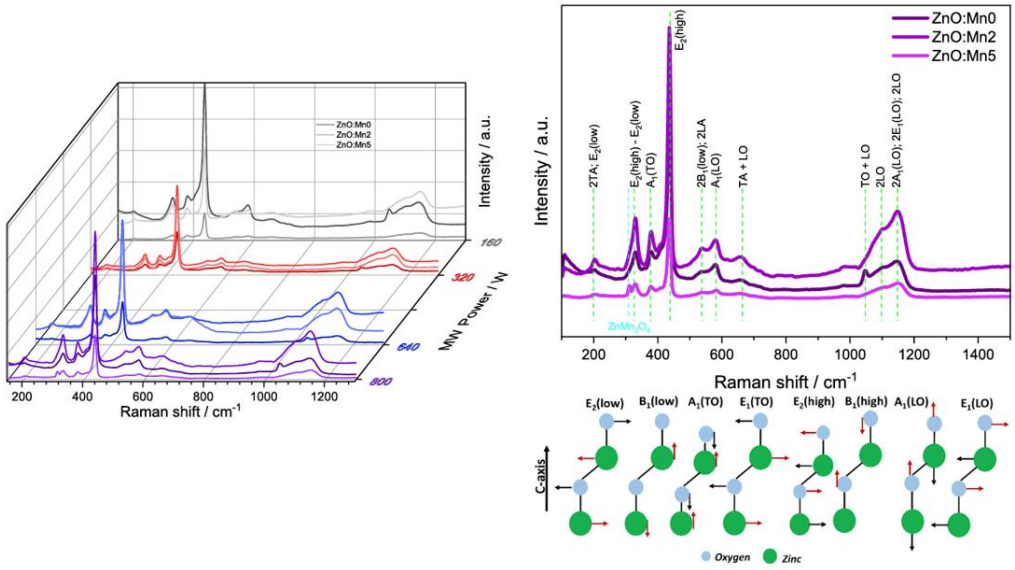

Figure 25: The first-order and second-order Raman spectra of undoped and Mn doped ZnO samples synthesized at different microwave powers, and a comparison between the Raman spectra of the undoped and Mn-doped ZnO synthesized at a microwave power of 800 W, where all the observable Raman modes are indicated together with all possible Raman modes that are ZnO specific

In conventional backscattering geometry, ZnO typically exhibits strong E_2 vibrational modes, which serve as distinct fingerprints of its crystal structure (Ercay et al. 2025, Colak et al. 2024).

In the hexagonal wurtzite phase of ZnO (space group $P6_3mc$), the number of optical phonon modes is dictated by the four atoms per unit cell, resulting in a total of 12 phonon modes, including three acoustic and nine optical modes (Ercay et al. 2025). Among these, the E_2(high) mode, detected around 436 cm^{-1} in Figure 25, is a particularly important marker for the wurtzite ZnO phase and is associated with oxygen atom vibrations perpendicular to the c-axis (Altaf et al. 2024). The E_2(low) mode, often related to Zn vibrations, was not observed in the current spectra; however, a notable feature near 330 cm^{-1} is consistent with the E_2(high) – E_2(low) difference mode, commonly classified as a second-order Raman transition.

Due to the intrinsic polarity of the wurtzite lattice, the A_1 and E_1 modes split into longitudinal optical (LO) and transverse optical (TO) components. In our results, the A_1(TO) mode appears at approximately 379 cm^{-1}, while the A_1(LO) mode is observed near 580 cm^{-1}. The latter becomes particularly prominent when the crystallographic c-axis is aligned parallel to the sample surface. At higher wavenumbers, weak overtone and combination bands emerge. A subtle shoulder around 1105 cm^{-1} is attributed to 2LO scattering processes along the A–L–M direction in the Brillouin zone, and may also be a result of overlapping $2A_1$(LO) and $2E_1$(LO) contributions at the Γ-point. Second-order difference modes generally fall within the range of fundamental one-phonon bands, whereas higher-frequency regions are dominated by two-phonon sum processes and multi-phonon scattering involving LO modes.

Raman spectral analysis of Mn-doped ZnO samples reveals pronounced changes in vibrational behavior, consistent with the incorporation of Mn ions into the ZnO lattice. Such doping can lead to phonon mode shifts, peak broadening, and altered intensities. In some cases, new bands may emerge due to the presence of Mn-related local vibrational modes, activation of Raman-inactive phonons caused by lattice disorder, or the formation of secondary phases like $ZnMn_2O_4$ (Zhang et al. 2015).

As seen in Figure 25, the sample synthesized at 800 W exhibits a weak Raman band near 310 cm^{-1}, which corresponds to vibrations associated with Mn ions in octahedral BO_6 coordination, a structural unit characteristic of $ZnMn_2O_4$. Another feature typical of this

spinel phase—appearing around 670 cm^{-1} and attributed to A_1g symmetry vibrations of oxygen atoms in tetrahedral AO_4 environments—is not resolved in the current spectra, likely due to overlap with the broad TO + LO second-order mode. Notably, the TO + LO mode itself is absent in both doping levels examined, as shown in Figure 25. This suppression is plausibly linked to defect-mediated scattering induced by Mn incorporation, such as the formation of oxygen vacancies or interstitial Zn/Mn species. These defects disrupt phonon propagation, modify dispersion relations, and can selectively weaken or quench particular vibrational modes.

2.4.5. Photoluminescence of Mn-doped ZnO

PL spectroscopy was employed to investigate the defect-related optical emissions in the synthesized ZnO nanostructures and to assess how Mn doping influences these emissions by introducing extrinsic defect states. Figure 26 (a) presents the PL spectra of undoped and Mn-doped ZnO samples synthesized at 160 W, while Appendix 6 includes the corresponding spectra for all other samples prepared under varying microwave powers. To further resolve the emission features, Gaussian deconvolution was performed on each PL spectrum, with the fitting results shown in Appendix 7. A detailed deconvolution of the ZnO:Mn_2 sample identified as the optimal composition in terms of electrochemical performance is provided in Figure 26 (b).

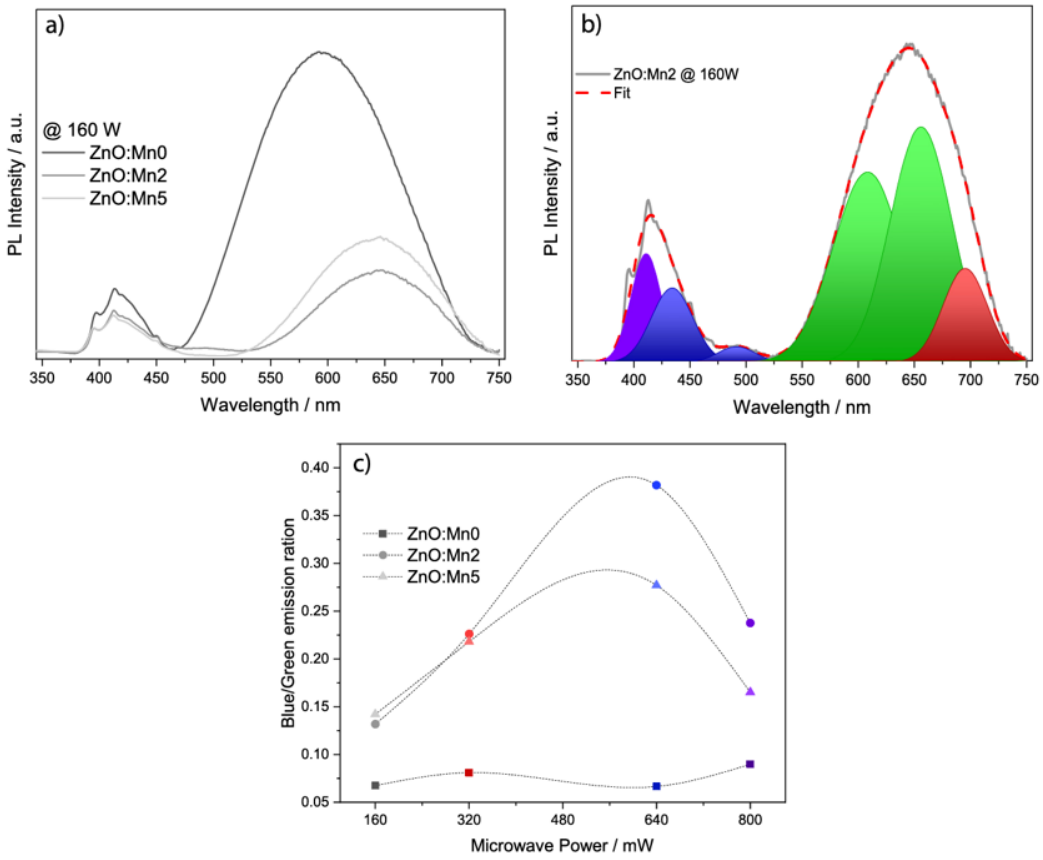

Figure 26: PL emission spectra of undoped and Mn-doped ZnO samples synthesized at 160 W microwave power (a), and the deconvolution of the peaks of ZnO:Mn_2 @160 W showing the different emission maxima at different wavelength (b), as well as the Blue-to-Green emission ratios of all samples (c)

Across all samples, two dominant emission bands are evident in Figure 26 (a). The first, a relatively weak peak around 415 nm, and the second, a broader and more intense band centered near 590 nm in the undoped ZnO. Upon Mn doping, this latter band undergoes a redshift and appears around 640 nm, indicating a significant modification in the defect-related luminescence. Moreover, a marked decrease in overall PL intensity is observed in the doped samples compared to the undoped counterpart. This quenching effect suggests successful incorporation of Mn ions into the ZnO lattice, which introduces extrinsic defect centers that suppress the radiative recombination associated with native defects (Norberg et al. 2004).

As shown in Figure 26 (b), the deconvoluted PL spectrum of the ZnO:Mn_2 sample reveals multiple emission bands corresponding to distinct defect states. The weak violet emission at ~390 nm is attributed to near-band-edge (NBE) recombination. Blue emission bands are generally associated with V_{Zn}, while green and red emissions are linked to transitions involving Zn_i and oxygen-related defects. Specifically, green luminescence originates from Zn_i to V_O complexes, while red emission is typically associated with O_i (Kaftelen et al. 2012).

The deconvolution results in Figure 26 (b) and Appendix 7 demonstrate that Mn doping significantly alters the defect landscape. A notable reduction in blue emission intensity implies that Mn^{2+} ions occupy zinc lattice sites, thereby decreasing the concentration of zinc vacancies. In parallel, a suppression of green and red emissions indicates that Mn also modifies the local environment of oxygen vacancies and interstitials, likely by occupying interstitial sites or altering defect charge states. The redshift observed in the red emission band of the doped samples supports this interpretation and suggests a modified defect state configuration induced by the dopant.

Figure 26 (c) presents the ratio of blue to green emission intensities for all samples. A systematic reduction in intensity is observed across all Mn-doped samples, regardless of the microwave power applied during synthesis. This consistent trend further supports the conclusion that Mn is effectively incorporated into the ZnO lattice, modifying its defect chemistry at each power level.

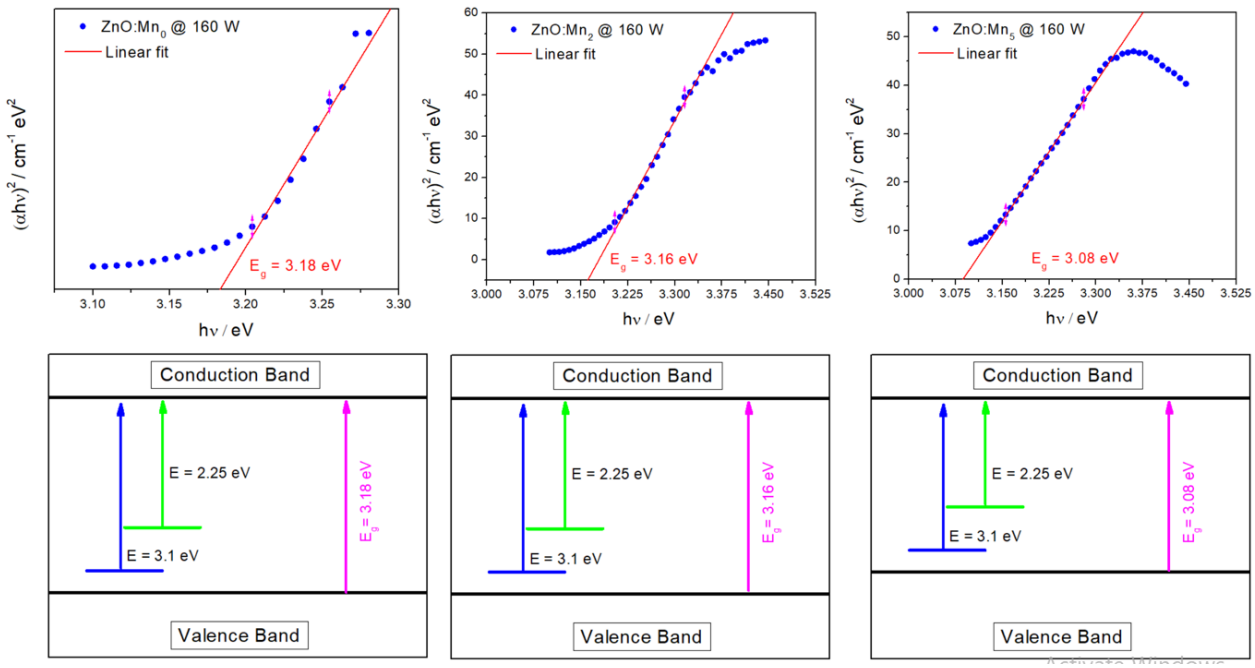

Figure 27: Tauc plots of ZnO:Mn @ 160 W samples showing the band gap energy change as a function of increasing Mn dopant concentration, along with an illustration of the energy model

The optical band gap properties of Mn-doped ZnO nanostructures synthesized at 160 W microwave power were evaluated using Tauc plots as shown in Figure 27 above. The extracted bandgap values reveal a progressive redshift with increasing Mn concentration: 3.18 eV, 3.16 eV, and 3.08 eV, respectively. The sample with the highest bandgap (3.18 eV) corresponds to the ZnO lattice that remains relatively undisturbed, resulting in minimal electronic perturbation. As the Mn content increases, a modest narrowing of the bandgap is observed, suggesting the formation of shallow defect states or the introduction of localized electronic levels near the conduction band. The most doped sample, with an E_g of 3.08 eV, exhibits the greatest redshift, which can be attributed to enhanced lattice distortion, increased carrier–dopant interactions, and the development of band tailing effects. These trends are further illustrated in the accompanying band diagrams, which propose a fixed intrinsic ZnO transition at ~3.1 eV, alongside a sub-band transition at ~2.25 eV attributed to Mn-related states and intrinsic defects such as oxygen vacancies. The gradual shift in the Tauc-derived bandgap values highlights the impact of Mn doping on the electronic structure, indicating a controlled modulation of the optical absorption edge. This bandgap engineering not only supports enhanced visible light absorption but also implies potential benefits for charge

carrier dynamics, which are critically important for the electrochemical performance of these nanostructured materials.

2.4.6. Electron Paramagnetic Resonance of Mn-doped ZnO

The Q-band EPR spectra of undoped and Mn-doped ZnO samples are presented in Figure 28 and Appendix 8. In the undoped ZnO samples, a distinct resonance appears at a g-factor of approximately 1.96, which is commonly attributed to intrinsic point defects, particularly singly ionized zinc vacancies (V_{Zn^-}) (Erdem 2017). The intensity of this signal exhibits a clear dependence on the microwave power applied during synthesis. This trend is attributed to variations in particle size and crystallinity, in line with earlier reports by Erdem *et al.* (Kasap et al. 2019).

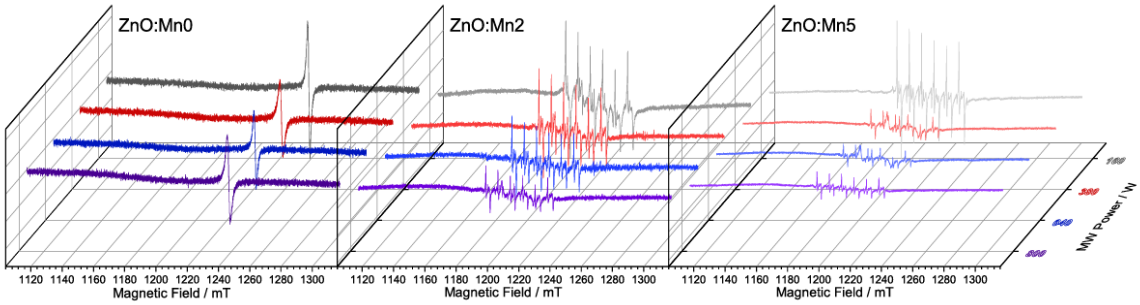

Figure 28: Q-band EPR spectra of ZnO:Mn0, ZnO:Mn2, and ZnO:Mn5 samples synthesized at different microwave powers. The undoped samples present a resonant line at g ≈ 1.96, attributed to intrinsic defects like Zn vacancies, while the Mn-doped ZnO samples display typical anisotropic sextet hyperfine lines of Mn2+ centers

To interpret these observations, a core–shell structural model was considered, suggesting that the g ≈ 1.96 resonance predominantly originates from core-localized defects within the ZnO crystallites. This is supported by comparative data from both EPR and photoluminescence studies (Nadupalli et al. 2021, Parashar et al. 2012), as well as theoretical calculations (Janotti and Walle 2005, Janotti and Van de Walle 2006), which consistently associate the g ≈ 1.96 signal with V_{Zn^-} centers. While V_O is also prevalent intrinsic defects in ZnO, their EPR activity is highly dependent on their charge states. Under ambient

conditions, V_O generally exists as either neutral V_{O^0} or doubly ionized $V_{O^{2-}}$ species, both of which are diamagnetic (Yüksel Price, Hardal, Acikgoz, et al. 2015) and therefore EPR-silent. Our interpretation of the g ≈ 1.96 resonance is further validated by correlative data from structural characterization. Specifically, the ZnO:Mn_0 sample synthesized at 160 W shows the smallest crystallite size and nanorod dimensions (see Figures 21 (b and c) and 23) This supports the size-dependent nature of zinc vacancy-related EPR signals, as smaller crystallites tend to exhibit more pronounced V_{Zn^-} signals, while increased crystallinity and particle size lead to their attenuation.

In Mn-doped ZnO samples, the EPR spectra display a well-resolved anisotropic sextet pattern, characteristic of Mn^{2+} ions substituting Zn^{2+} in the ZnO lattice. These six hyperfine lines arise from electron–nuclear spin interactions involving the Mn nucleus (I = 5/2), with transitions occurring according to the selection rule $\Delta m_S = \pm 1$ (Yüksel Price, Hardal, Acikgoz, et al. 2015). The appearance of this hyperfine structure provides clear evidence for the successful incorporation of Mn^{2+} into substitutional Zn sites. Additionally, the high-frequency Q-band measurement allows for the resolution of zero-field splitting (ZFS), which becomes evident in the EPR spectra. The presence of ZFS features further confirms the non-centrosymmetric environment of Mn^{2+} ions in the wurtzite ZnO lattice (Misra 1996). The observed hyperfine lines remain sharp and well-defined, indicating minimal broadening and suggesting that Mn ions are uniformly distributed within the lattice rather than forming clusters or secondary phases (Lorenz et al. 2014).

Simulation of the EPR data yields the following parameters: g ≈ 2.0019, hyperfine coupling constant A = 220 MHz, axial ZFS parameter D = 720 MHz, and rhombic ZFS parameter E = 22 MHz. These values are in excellent agreement with previously reported literature for Mn^{2+} in ZnO, further corroborating the substitutional nature of the doping (Ankiewicz et al. 2009).

Notably, the strongest Mn^{2+}-related EPR signal is observed in the sample synthesized at 160 W, suggesting that lower microwave powers enhance the incorporation of Mn ions into the ZnO lattice. This could be due to improved dopant solubility and reduced defect clustering at lower energy input levels, which promote uniform substitutional doping and suppress secondary phase formation.

2.5. Microwave-Driven Structural and Defect Engineering in Mn-Doped ZnO Nanostructures

Comprehensive structural and spectroscopic investigation was conducted to elucidate the influence of Mn doping and microwave-assisted synthesis on the morphological, crystallographic, and defect-related properties of ZnO nanostructures.. SEM analysis confirmed that microwave power critically affects the growth and uniformity of ZnO nanorods, with low power favoring higher aspect ratios and high power promoting aggregation and thickening. Mn doping was found to suppress radial growth and introduce morphological distortions at high concentrations, indicating a dopant-dependent growth mechanism. XRD and Rietveld refinement revealed that all samples retained the hexagonal wurtzite ZnO phase. However, Mn incorporation introduced lattice strain, peak broadening, and non-monotonic changes in unit cell volume. The observed changes were attributed to the substitutional replacement of Zn^{2+} by larger Mn^{2+} ions and the associated local structural distortions. Increasing microwave power facilitated grain growth and reduced hydroxide-related impurities, yet also amplified dopant-induced microstrain at higher Mn concentrations. BET analysis showed that Mn_2:ZnO synthesized at 160 W possessed the highest specific surface area (61 m^2/g), which decreased systematically with higher synthesis powers due to increased nanorod aggregation. Despite moderate surface areas, the aligned nanorod morphology and structural integrity remained favorable for electrochemical applications. Raman spectroscopy confirmed the presence of key ZnO phonon modes and revealed subtle spectral modifications due to Mn doping, such as mode shifts and peak broadening. The emergence of weak Mn-related vibrational bands, including those tentatively assigned to $ZnMn_2O_4$, suggest localized structural changes and possible secondary phase evolution under extreme synthesis conditions. Photoluminescence spectroscopy further validated the successful doping process by showing a redshift and quenching of visible emissions, particularly in the green and red regions. These spectral features correspond to alterations in oxygen- and zinc-related defect states and suggest Mn-induced modulation of intrinsic defect chemistry.

Finally, Q-band EPR measurements provided direct evidence of Mn^{2+} substitutional doping, as indicated by the characteristic sextet hyperfine structure. Intrinsic Zn vacancies (VZn^{-}), identified by a $g \approx 1.96$ resonance, were found to diminish with increasing crystallite size, supporting a core-localized defect model. The strongest Mn^{2+} EPR signals were observed at 160 W, aligning with PL and XRD findings and indicating enhanced dopant incorporation under moderate microwave energy.

Together, these results demonstrate that controlled Mn doping and careful tuning of microwave synthesis power can effectively modulate the structural, optical, and electronic properties of ZnO nanostructures. The optimal conditions identified as moderate Mn content (2%) and low to intermediate microwave powers (160–340 W) yield materials with favorable morphological uniformity, enhanced defect control, and high surface area, making them promising candidates for next-generation electrochemical energy storage applications.

3. STRUCTURAL ENGINEERING OF Mn:ZnO-hBN NANOCOMPOSITES

3.1. Introduction

h-BN has garnered significant interest in energy device research due to its high thermal stability, electrical insulation, and chemical inertness. However, its intrinsic low electronic conductivity limits its effectiveness as an electrode material in supercapacitors (Kumar et al. 2019). To overcome this, h-BN is frequently employed as a supporting platform for conductive and redox-active moieties, but the synergy between h-BN and electrified components remains underexplored, particularly in the context of metal-doped composites. ZnO, a wide-bandgap semiconductor with high charge mobility and environmental friendliness, has been extensively studied in supercapacitor electrodes (Shaheen et al. 2021, Kumar et al. 2022, Altaf et al. 2022). Mn-doping of ZnO further enhances electrochemical performance by introducing midgap states and increasing pseudocapacitive behavior. For instance, Mn-doped ZnO synthesized via microwave-assisted methods demonstrates improved charge–discharge rates, reduced bulk resistance, and enhanced cycle stability (Aleinawi, Ammar, et al. 2025). Similarly, Mn-doped ZnO integrated with reduced graphene oxide (rGO) achieves specific capacitances up to ~487 $F\,g^{-1}$ at 2 $A\,g^{-1}$, indicating the profound impact Mn substitution can have on ZnO's energy storage capabilities (Ahmed, Chib, and Arya 2025). Recent work by Özel *et al.* (2024) employed sol–gel synthesis to fabricate h-BN doped ZnO nanoparticles (1–10 wt%). They observed a four-fold increase in dielectric constant at 1 kHz (from ~12 to ~55 with 10 wt% h-BN), attributed to enhanced interfacial polarization between ZnO and h-BN (Ozel et al. 2024). This demonstrates that h-BN can significantly alter ZnO’s interface properties, critical for charge storage

applications. However, dielectric enhancement does not necessarily translate into improved electrochemical performance. Bridging this gap requires coupling the dielectric properties imparted by h-BN with redox-active components that can support faradaic reactions.

A composite of Mn-doped ZnO embedded within an h-BN matrix could synergize the interfacial polarization benefits of h-BN with Mn-ZnO's pseudocapacitive redox activity through the following:

1- Enhanced Capacitance: Mn-doped ZnO provides reversible redox sites, while the h-BN layer enhances surface polarization and stability, potentially improving both electric double-layer and pseudocapacitance, where h-BN provides the high active surface area for the EDLC, and Mn-doped ZnO provides active sites for Faradaic redox reactions that increase the psuedocapacitive behavior.
2- Improved Structural Stability: h-BN's mechanical robustness may buffer volumetric changes during cycling, enhancing electrode longevity, and its incredible thermal and chemical stability can further enhance the stability of the device.
3- Optimized Morphology and Interface: h-BN's platelet structure could promote uniform Mn-ZnO nanoparticle distribution, maximizing active surface area, a strategy validated in both ZnO/h-BN dielectric composites and Mn-ZnO/rGO studies (Ahmad et al. 2014).

Herein, we propose the development of a Mn:ZnO-hBN nanocomposite via a combination of sophisticated synthesis techniques that combine mechanical processing, chemical enhancements, and thermal treatment, aiming to recrystallize the composite material. The main goal of such development is to enhance both pseudocapactive and EDLC properties of the composite material, enhance the capacitive stability of the material, and optimize the structural architecture of the developed composite material.

This chapter will focus on the systemically characterization of the composite material through advanced characterization techniques such as EPR, PL, and Raman spectroscopy which provides a deep understanding of the electronic properties of the developed composite material, and XRD, and SEM which gives a clear picture of the structure and morphology of the composite material.

The effect on the electrochemical properties and performance of the developed nanocomposite as a supercapacitor electrode material will be analyzed in details in Chapter 4.

3.2. Literature Review

3.2.1. Structural and Electrochemical Insights

The incorporation of Mn dopant into the ZnO lattice has been shown to modulate the optical bandgap and reduce the crystallite size. This effect was demonstrated by Raha *et al.*, as illustrated in Figure 29 below (Rahal et al. 2025).

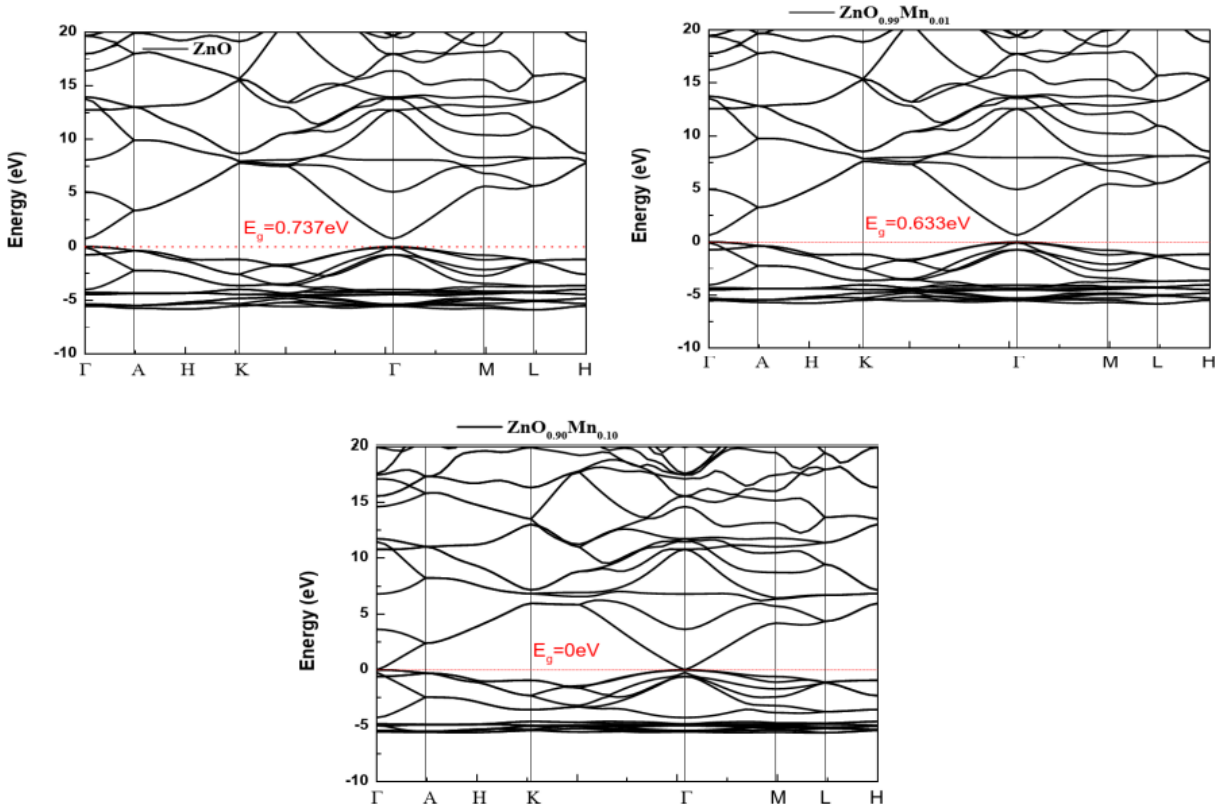

Figure 29: The band structures of ZnO, Mn_1ZnO, and $Mn_{10}ZnO$, showing the effect of Mn dopant on the optical bandgap properties of ZnO, adapted from (Rahal et al. 2025)

The bandgap energy of ZnO systematically decreases with increasing Mn doping concentration, approaching near-zero values at approximately 8% Mn content. At this critical concentration, the material exhibits metallic behavior characterized by a vanishing bandgap ($E_g \approx 0$ eV), indicating a transition from semiconducting to metallic electronic properties.

Regarding the electrochemical performance, Pravin *et al.* demonstrated a 2.4-fold enhancement in specific capacitance for Mn-doped ZnO thin films compared to undoped ZnO, utilizing the spray pyrolysis synthesis technique (151 F/g to 360 F/g respectively) (More et al. 2021a). In comparison, ZnO/reduced graphene oxide (ZnO/rGO) composites have achieved even higher values, with specific capacitance reaching up to 487 F g^{-1} and a capacitive retention of approximately 81% after 5,000 charge–discharge cycles (Ahmed, Chib, and Arya 2025). These findings underscore the substantial influence of both dopant incorporation and conductive matrix integration on the electrochemical behavior of ZnO-based materials. However, we have demonstrated superior electrochemical stability, achieving capacitance retention exceeding 90% after 5,000 cycles, thereby outperforming ZnO/rGO benchmarks in terms of long-term cycling durability in our work (Aleinawi, Ammar, et al. 2025). Detailed electrochemical performance comparisons and stability analyses will be presented in Chapter 4.

3.2.2. Electrochemical Performance of h-BN Composites

While numerous studies have explored the electrochemical performance of h-BN composites, the majority have focused primarily on h-BN/carbon-based hybrid systems. For example, Shams *et al.* reported a specific capacitance of approximately 116 F/g at 1 A/g using a liquid-phase exfoliated h-BN functionalized with sodium thiosulfate (STS), achieving ~87% capacitance retention after 3,000 cycles. The enhanced performance was attributed to improved dispersion and electronic conductivity imparted by the STS treatment (Baby et al. 2025). In a subsequent study employing a hydrothermal synthesis route, the same group achieved a significantly higher capacitance of 361.6 F/g at 3 A/g, with 85% retention after 5,000 cycles. This improvement was ascribed to the introduction of polyethylene glycol

(PEG), which effectively inhibited agglomeration and promoted better electrode–electrolyte interface dynamics (Shams, Bindhu, Murali, Ramesh, Al Souwaileh, et al. 2025). Similarly, Ashwini *et al.* developed in-situ grown h-BN-based heterostructures that exhibited a specific capacitance ranging from ~800 F/g at low scan rates to ~100 F/g at higher rates, alongside an exceptional cycling stability over 20,000 cycles. These results suggest a transition toward battery-type behavior, driven by improved electron diffusion kinetics (Alegaonkar, Alegaonkar, and Pardeshi 2020).

3.2.3. Unexplored Mn:ZnO-hBN Nanocomposite

Although direct studies on Mn:ZnO-hBN for supercapacitor use are currently lacking, the independent advantages suggest strong hybrid potential: Mn-ZnO provides redox pseudocapacitance, enhanced conductivity, and cycling stability. While h-BN enables interfacial polarization, structural stability, and high thermal/chemical resilience. Mn:ZnO-hBN nanocomposite could therefore deliver hybrid capacitance by combining pseudocapacitance (from Mn-ZnO) and interfacial/stabilizing effects (from h-BN). It can also provide enhanced stability: h-BN platelets can buffer structural strain during repeated cycles. h-BN may act as a scaffold to distribute Mn-ZnO nanoparticles evenly, which is a strategy proven in ZnO/rGO systems.

No peer-reviewed study has yet combined Mn-doped ZnO with h-BN for electrochemical energy storage. Herein, we aim to explore the synthesis strategies through combining sophisticated techniques to ultimately develop the composite material, provide a detailed analysis through advanced techniques such as EPR, PL, Raman, XRD, and SEM. Later in Chapter 4 we aim to determine the specific capacitance, rate performance, cycling stability up to 5000 cycles, and impedance to understand internal resistance and ion diffusion.

3.3. Methodology

3.3.1. Materials and Synthesis

The synthesis procedure of the Mn_2:ZnO-hBN nanocomposite follows a similar approach to the Mn:hBN synthesis detailed in Chapter 1 (materials and synthesis section), with a few key modifications. Specifically, following the ball milling and filtration steps, an additional stage is incorporated. Namely, the microwave-assisted hydrothermal treatment described in Chapter 2. This integration enhances the synthesis pathway by facilitating the uniform growth of Mn-doped ZnO on the hBN matrix. A schematic representation of the Mn_2:ZnO-hBN nanocomposite synthesis process is presented in Figure 30 below.

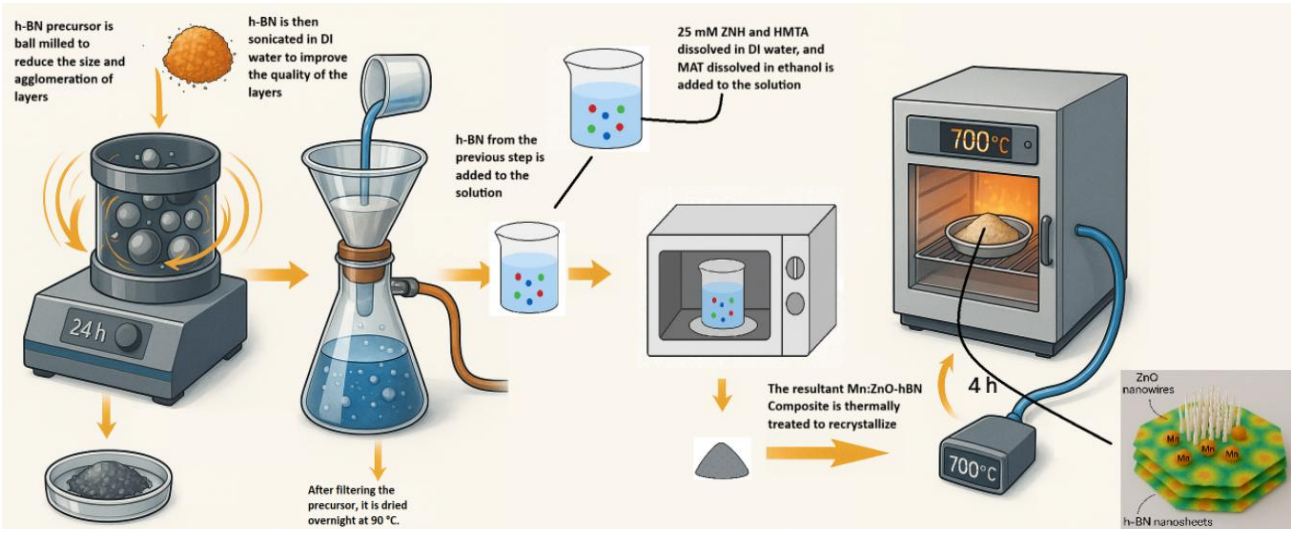

Figure 30: Schematic of the synthesis procedure of Mn_2:ZnO-hBN nanocomposites, revealing the sophisticated method of mechanical, chemical, and thermal processing combined together in this developed advanced synthesis technique

The synthesis process begins with high-energy ball milling of h-BN powder at 800 rpm for 24 hours. This step serves to reduce the lateral size of the h-BN layers while simultaneously introducing structural defects that facilitate subsequent integration with Mn-doped ZnO nanowires. Following ball milling, the h-BN powder is dispersed in deionized (DI) water and subjected to ultrasonic treatment at 80 °C for 3 hours to enhance exfoliation and improve layer quality. In parallel, a separate solution is prepared by dissolving zinc nitrate

hexahydrate (ZNH) and hexamethylenetetramine (HMTA) in DI water to achieve a 25 mM concentration. Manganese acetate tetrahydrate (MAT) is then dissolved in methanol and added to the precursor solution. The mixture is magnetically stirred for 1 hour to ensure homogeneity, after which the pre-treated h-BN dispersion is introduced. The resulting suspension is transferred to a conventional microwave system and irradiated at 160 W for 20 minutes under controlled conditions to facilitate nucleation and growth of the Mn:ZnO phase on the h-BN substrate. The product is subsequently filtered, dried, and subjected to a thermal annealing step at 700 °C for 10 hours to induce crystallization and enhance structural integration within the composite.

3.4. Results and Discussions

3.4.1. Scanning Electron Microscopy Images of the Nanocomposite

The morphology of the nanocomposite Mn_2:ZnO-hBN samples is illustrated in the SEM image in Figure 31 below, along with a schematic representation of the developed composite morphology.

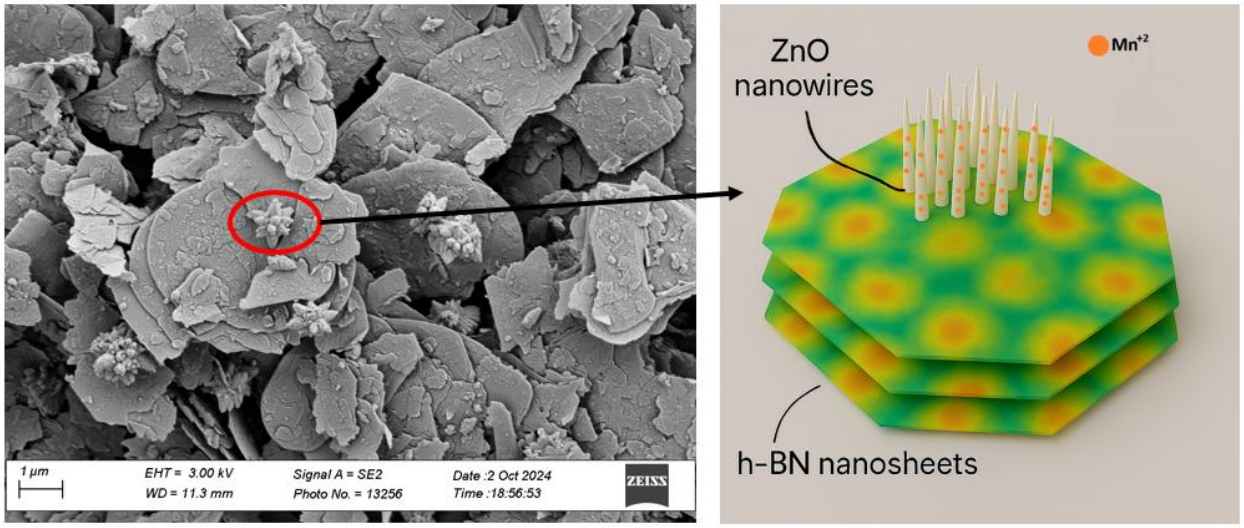

Figure 31: SEM image of the Mn_2ZnO:hBN nanocomposite showing both morphologies of h-BN discussed in chapter 1, and MnZnO discuseed in chapter 2 (left), and a schematic of the morphology (right)

The presented images clearly demonstrate the distinct morphologies of the materials. The layered structure of h-BN, as discussed in Chapter 1, remains evident, while the MnZnO nanorods, detailed in Chapter 2, appear to grow atop the h-BN layers in the form of clustered nanowire assemblies, often resembling nanoflowers. These nanoflower-like formations contribute significantly to increasing the active surface area, which is advantageous for enhancing electrochemical reaction sites. The influence of these MnZnO nanorods on the electrochemical performance will be thoroughly analyzed in the Dunn analysis section of Chapter 4. Additionally, the role of the sonication process during synthesis should be highlighted, as it appears to have improved the structural quality and dispersion of the h-BN layers, as evident in the provided images.

3.4.2. X-ray Diffraction of the Nanocomposite

The crystalline structure and phase composition of the synthesized hBN-MnZnO nanocomposites with varying ZnO content (5 wt.%, 10 wt.%, and 20 wt.%) were characterized by XRD. Figure 32 presents the corresponding XRD patterns for the 5:95, 10:90, and 20:80 Mn_2ZnO:hBN samples.

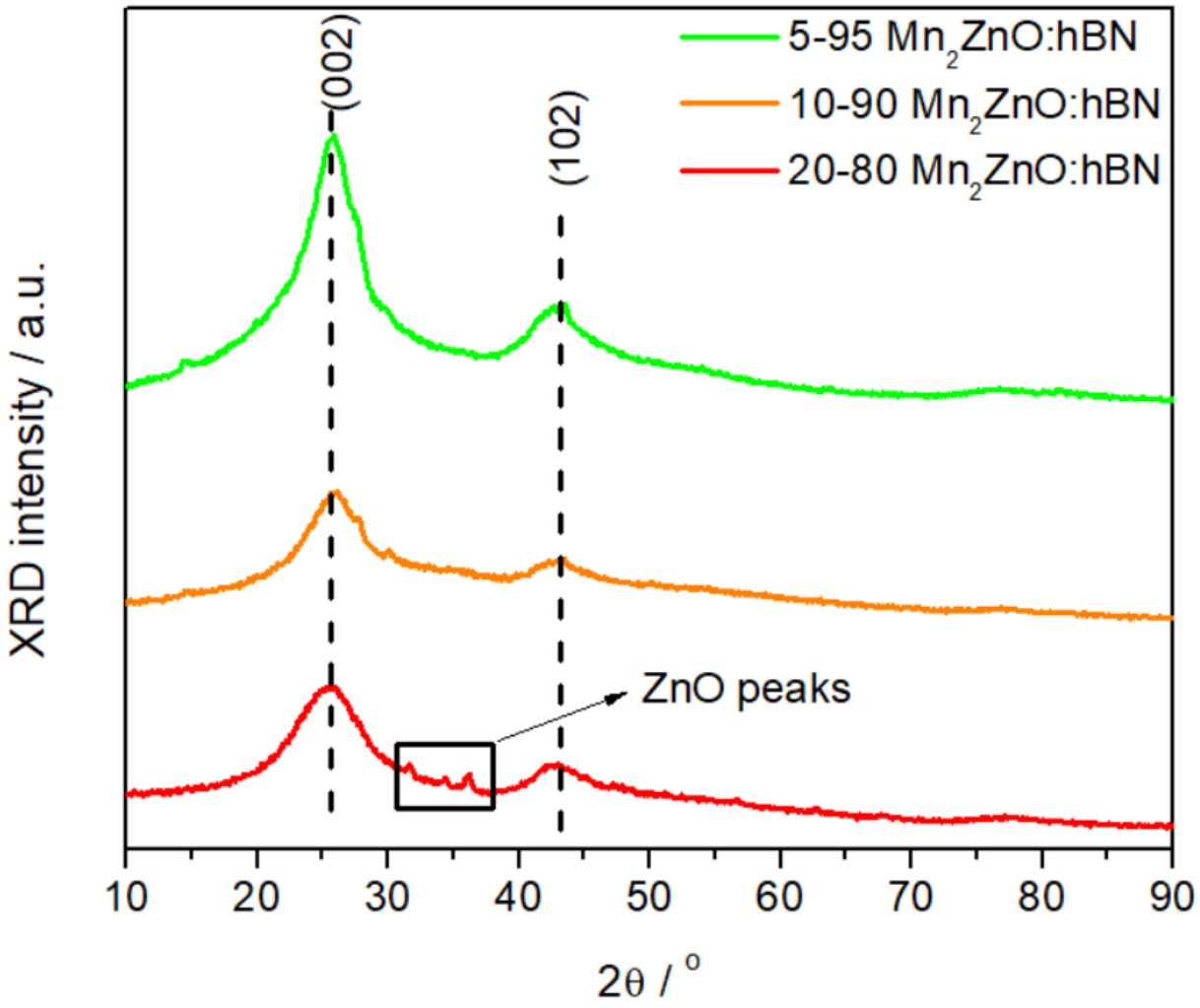

Figure 32: XRD diffractograms of Mn_2:ZnO-hBN nanocomposites at different concentrations showing the development of the crystalline structure as a result of introducing ZnO into the structure of h-BN

All three samples display two dominant diffraction peaks centered at approximately $2\theta \approx 27°$ and 43°, corresponding to the (002) and (102) crystallographic planes of h-BN, as indexed to the standard JCPDS card No. 34-0421 (Zhi et al. 2009). The high intensity and sharpness of these peaks in the 95:05 and 90:10 samples suggest a relatively high crystallinity of the h-BN phase at lower ZnO loadings.

Upon increasing the ZnO content to 20 wt.% (80:20 sample), additional diffraction features emerge in the 2θ range between 30° and 40°. These additional peaks can be assigned to the characteristic reflections of the hexagonal wurtzite ZnO phase (JCPDS No. 36-1451), including the (100), (002), and (101) planes (Özgür et al. 2005). The appearance and

intensification of ZnO-related peaks with increasing ZnO concentration confirm the successful incorporation and crystallization of the Mn-doped ZnO nanostructures within the composite matrix. Notably, the intensity of the (002) h-BN peak shows a decreasing trend with increasing ZnO content. This reduction is attributed to the relative dilution of h-BN within the composite and possible partial coverage of the h-BN surface by ZnO nanoparticles, which may reduce the effective diffraction volume of h-BN. Additionally, the broadening of the ZnO peaks in the 80:20 sample suggests a nanoscale crystallite size and the presence of Mn-doping-induced lattice distortions. The absence of detectable ZnO peaks in the 95:05 and 90:10 samples indicates either the low crystallinity or insufficient quantity of ZnO to produce distinct diffraction signals detectable under the current measurement conditions. This observation is consistent with previous studies on ZnO-hBN composites, where the ZnO phase becomes XRD-visible only beyond a certain threshold concentration.

Overall, the XRD results confirm the successful synthesis of Mn:ZnO-hBN nanocomposites with tunable ZnO content, where both the phase composition and the relative crystallinity are strongly dependent on the ZnO loading.

3.4.3. Electron Paramagnetic Resonance of the Nanocomposite

EPR spectroscopy was conducted in both X-band and Q-band frequencies to investigate the paramagnetic centers and Mn^{2+} ion incorporation within the Mn_2:ZnO-hBN nanocomposites at varying ZnO loadings. The recorded EPR spectra are presented in Figure 33 below.

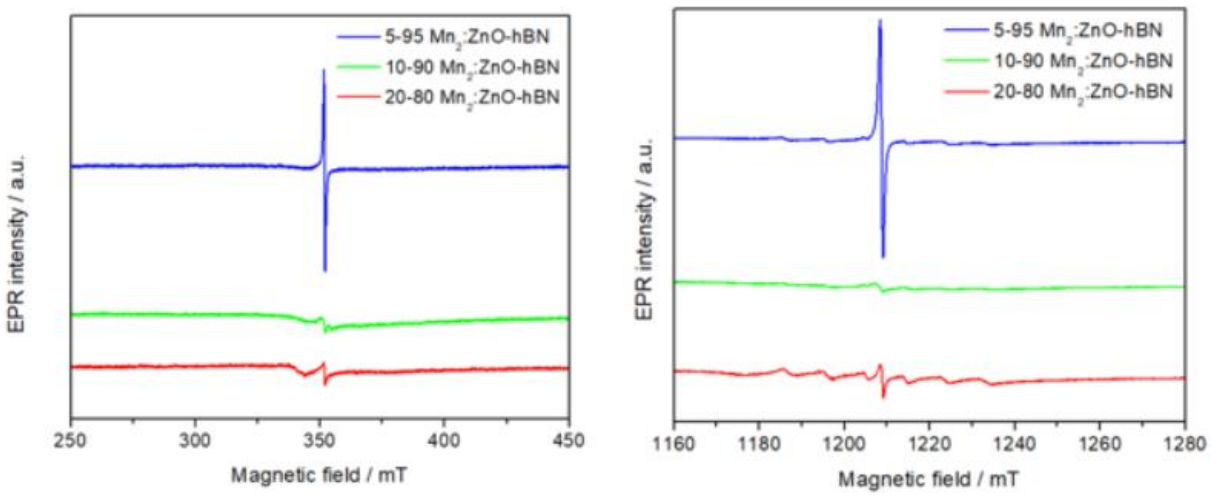

Figure 33: X-band EPR spectrum (left) and Q-band EPR spectrum (right) of Mn_2:ZnO-hBN nanocomposites showing the effect of the ZnO:hBN concentration's on the electronic structure of the nanocomposite

The X-band spectra (left panel) reveal a single dominant and sharp resonance signal centered around 350 mT for all samples, with the strongest intensity observed in the 5-95 Mn_2:ZnO-hBN composite (blue curve). This signal corresponds to a g-factor of approximately 2.004, which is commonly associated with defect-related paramagnetic centers, such as V_N, V_O in h-BN or ZnO matrix. Notably, the characteristic six-line hyperfine splitting typically observed for isolated Mn^{2+} ions in ZnO is absent in the X-band spectra of all three samples. The lack of resolved hyperfine structure may be attributed to several factors, including low Mn^{2+} concentration, strong dipole–dipole interactions, line broadening due to clustering, or overlap with dominant defect-related signals from the h-BN matrix (Bououdina et al. 2014). As the ZnO content increases from 5 wt.% to 20 wt.%, a systematic decrease in overall X-band signal intensity is observed. This trend suggests a dilution of defect-related paramagnetic centers associated with h-BN, likely due to the increasing mass fraction of ZnO in the composite. Furthermore, the observed line broadening in the higher ZnO-loaded samples (10-90 and 20-80) may indicate enhanced magnetic interactions between Mn^{2+} ions or increased structural disorder within the ZnO phase (Petit et al. 2004).

The Q-band spectra (right panel), recorded at a higher frequency (~34 GHz), provide enhanced spectral resolution and improved sensitivity to hyperfine features. The 5-95 Mn_2:ZnO-hBN sample again shows a sharp and intense resonance signal around 1220 mT, corresponding to the same $g \approx 2.004$ paramagnetic defect center observed in the X-band.

However, even at Q-band resolution, no clear Mn^{2+} hyperfine sextet is detected, further supporting the conclusion that the Mn^{2+} concentration is below the EPR detection threshold for hyperfine splitting or that strong spin-spin interactions and inhomogeneous broadening dominate the Mn environment in these samples (Petit et al. 2006). Similar to the X-band observations, the Q-band spectra also show a notable decrease in signal intensity with increasing ZnO content, indicating that the total population of EPR-active defect sites decreases as more ZnO is incorporated into the composite. This reduction aligns with the dilution of h-BN, which is known to host prominent paramagnetic defect centers contributing to $g \approx 2.004$ signals (Zhi 2006).

3.4.4. Photoluminescence of the Nanocomposite

The PL analysis of Mn_2:ZnO-hBN nanocomposites displays a distinct difference from both pristine and Mn doped h-BN discussed in Chapter 1 as shown in Figure 34 below.

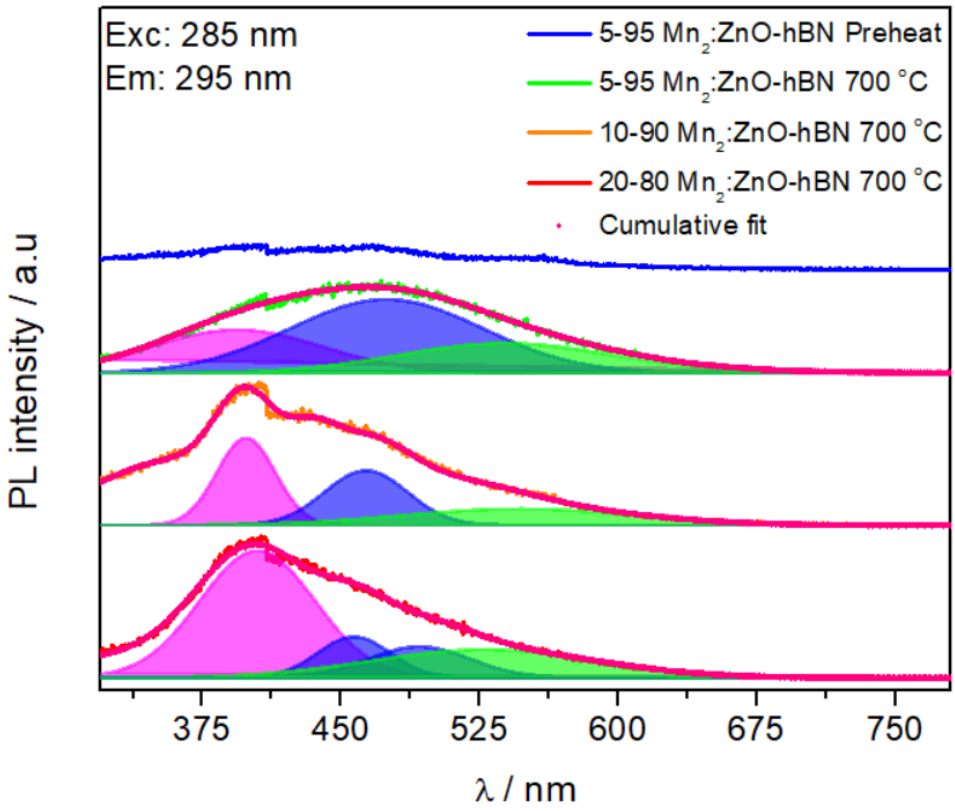

Figure 34: PL spectra of Mn_2:ZnO-hBN nanocomposites along with the deconvolution of the peaks showing the effect of ZnO on the optical properties of h-BN

A pronounced feature observed in all post-annealed samples is the enhanced UV near-band-edge (NBE) emission centered in the range of 370–400 nm, which is attributed to the radiative recombination of free excitons in the ZnO wurtzite lattice (Vanheusden et al. 1996, Özgür et al. 2005). This emission is almost negligible in the preheated 5-95 Mn_2:ZnO-hBN sample (blue curve), indicating the absence of significant crystalline ZnO phase prior to annealing. However, following thermal treatment at 700 °C, the samples containing higher ZnO concentrations (10% and 20%) exhibit a substantial increase in NBE intensity. This trend is most prominent in the 20-80 Mn_2:ZnO-hBN composite, where the UV emission intensity reaches its maximum.

This clear enhancement of the NBE emission with increasing ZnO content confirms the successful crystallization of ZnO nanoparticles within the hBN matrix and highlights the ZnO contribution to the optical properties of the composite system. The improved UV emission can also be linked to reduced non-radiative recombination sites due to better crystal quality in higher ZnO-loaded samples. Moreover, the Mn-doping within the ZnO lattice may

additionally contribute to the modulation of carrier recombination dynamics, though no secondary Mn-related peaks are prominently detected in this spectral region (Janotti and Van de Walle 2009).

In addition to the UV NBE peak, broad visible emissions ranging from 450 nm to 700 nm are observed across all samples, with increasing intensity for samples containing higher ZnO content as depicted in Appendix 11. Deconvolution of the PL spectra reveals multiple defect-related bands. These visible emissions are typically associated with intrinsic ZnO defects such as V_o, Zn_i, O_i. The relative intensity of these defect emissions also increases with ZnO concentration, suggesting that higher ZnO loadings introduce more defect sites within the nanocomposite.

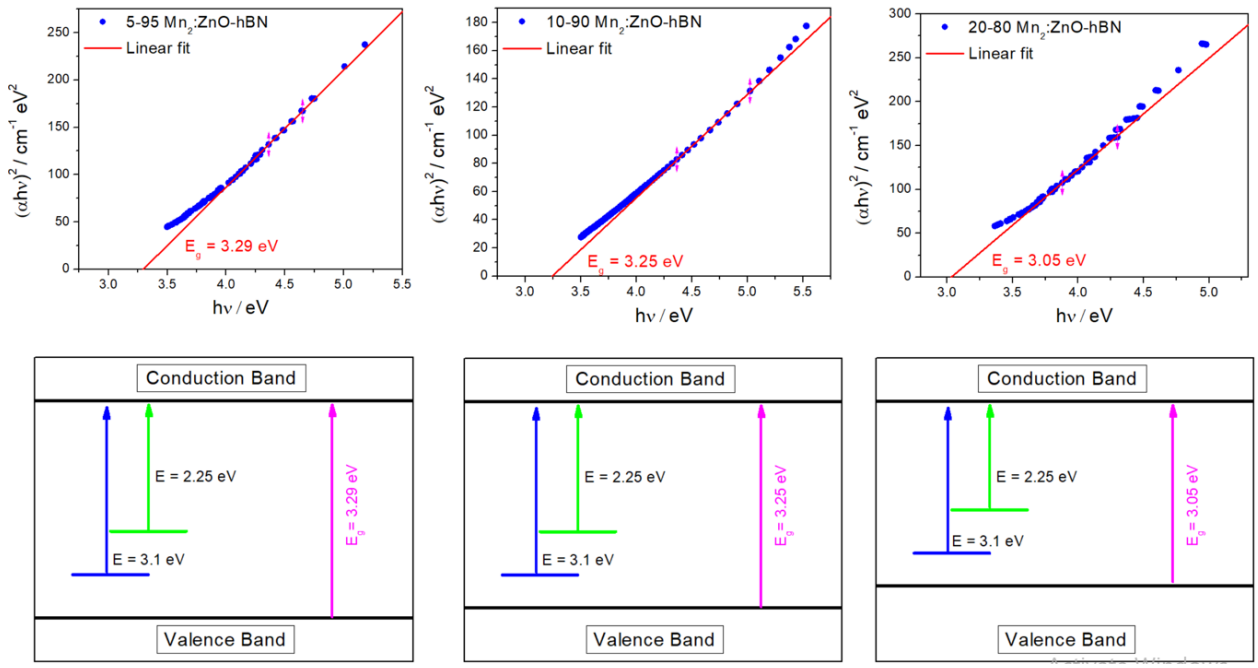

Figure 35: Tauc plots of Mn_2:ZnO-hBN samples showing the band gap energy change as a function of increasing the concentration of ZnO in the nanocomposite structure

The effect of ZnO content on the optical band gap energy of the synthesized nanocomposites is illustrated in Figure 35, which presents the corresponding Tauc plots. The band gap values were determined using the same methodology outlined previously in Chapter 1. A clear and progressive reduction in the optical band gap energy is observed with increasing ZnO concentration within the hBN matrix. This band gap narrowing is particularly significant for

the higher ZnO-loaded samples, highlighting the influence of ZnO incorporation on the electronic structure of the composite system. The observed decrease in band gap energy is expected to play a pivotal role in enhancing the electrochemical behavior of the materials, a topic that will be discussed in detail in the Chapter 4.

3.5. Crystallographic and Defect Modulation in Mn:ZnO–h-BN Nanocomposite Systems

This chapter presented a detailed structural and optical characterization of the Mn_2:ZnO-hBN nanocomposites synthesized with varying ZnO concentrations. The collective results clearly demonstrate the successful integration of Mn-doped ZnO nanostructures onto the h-BN matrix, with a tunable composition-dependent evolution of morphological, crystallographic, electronic, and optical properties. SEM imaging revealed the formation of hierarchical architectures where MnZnO nanorods, often assembling into nanoflower-like clusters, are uniformly distributed over the layered h-BN substrate. This tailored morphology is expected to enhance the electrochemically active surface area, creating more accessible reaction sites for charge storage. XRD analysis confirmed the coexistence of both h-BN and ZnO phases within the composites. At lower ZnO concentrations, the h-BN crystallinity remains dominant, while higher ZnO loadings promoted the appearance and growth of the hexagonal wurtzite ZnO phase. The observed peak broadening and intensity shifts suggest a nanoscale crystallite size and Mn-induced lattice distortions within the ZnO domains. EPR spectroscopy, conducted at both X-band and Q-band frequencies, provided insight into the local magnetic environment and defect structures. A dominant $g \approx 2.004$ signal was observed across all samples, indicative of paramagnetic defect centers primarily originating from the h-BN matrix and ZnO-related defects such as nitrogen and oxygen vacancies. The absence of well-resolved Mn^{2+} hyperfine splitting in both frequency regimes suggests either a low substitutional Mn^{2+} concentration, strong spin-spin interactions, or broadening effects due to site disorder. Photoluminescence measurements further validated the structural observations by showing a pronounced increase in near-band-edge UV emission with increasing ZnO

content, directly correlating with improved ZnO crystallinity. Simultaneously, enhanced visible-range defect-related emissions were observed, reflecting the increasing defect density introduced by higher ZnO incorporation. The Tauc plot analysis highlighted a progressive narrowing of the optical band gap energy as a function of ZnO concentration. This band gap modulation, induced by both compositional changes and Mn doping effects, is anticipated to play a significant role in facilitating enhanced charge transport and electrochemical activity.

In summary, the results of this chapter provide strong evidence that controlled ZnO incorporation and Mn doping effectively engineer the structural and electronic properties of the h-BN-based nanocomposites. Table below summarizes the critical parameters obtained from the advanced characterization techqniues for the difference samples highlighted in the previous chapters. These tailored characteristics set the foundation for the improved electrochemical performance will be discussed Chapter 4.

Table 6: Characterization parameters of the various materials systems discussed in the previous chapters

Sample	**g factor**	**E_g (eV)**	**D (nm)**
Mn_1:h-BN at 800 ºC	2.0019	4.365	93
Mn_3:h-BN at 800 ºC	2.0019	4.06	98
Mn_5:h-BN at 800 ºC	2.0019	3.56	103
ZnO:Mn_0 at 160 W	2.0021	3.18	40
ZnO:Mn_2 at 160 W	2.0021	3.16	46
ZnO:Mn_5 at 160 W	2.0021	3.08	87
5-95 Mn_2:ZnO-hBN	2.0020	3.29	98
10-90 Mn_2:ZnO-hBN	2.0020	3.25	88
20-80 Mn_2:ZnO-hBN	2.0020	3.05	84

4. ASSESSING THE ELECTROCHEMICAL PERFORMANCE OF h-BN, ZnO:Mn, AND Mn:ZnO-hBN

4.1. Introduction

Defect-engineered h-BN has recently garnered significant attention as a promising electrode material for supercapacitor applications. While pristine h-BN exhibits excellent thermal and chemical stability, its wide bandgap and intrinsically poor electrical conductivity limit its electrochemical activity in its unprocessed form. However, introducing structural defects—such as vacancies, edge disruptions, and substitutional impurities—can significantly enhance its charge storage capabilities by increasing the density of active sites and facilitating ion diffusion pathways. The most effective way to evaluate the influence of these defect states is through direct electrochemical testing in supercapacitor configurations, where their contribution to performance metrics can be quantitatively assessed.

Traditional non-defective h-BN shows a negligible electrochemical response; however, its electrochemical performance can be a drastically improved by combining it with conductive nanomaterials in a composite form. Methods such as ball milling are widely employed to introduce controlled defects while simultaneously reducing particle size, thereby enhancing surface accessibility. For instance, Bongu *et al.* demonstrated a high-performing composite system incorporating h-BN, graphene, and MoS_2, achieving a specific capacitance of 392 F/g, along with an energy density of 16.4 Wh/kg and power density of 501 W/kg in a symmetric supercapacitor device (Bongu, Arsalan, and Alsharaeh 2024). These improvements were attributed to the synergistic effects of increased surface area, improved electrical conductivity, and defect-enhanced redox activity. Such results highlight the

transformative potential of defect-rich h-BN-based composites to rival traditional carbon-based materials in energy storage applications.

In parallel, metal oxide nanostructures, particularly ZnO and its doped variants have also shown significant promise as electrode materials for supercapacitors due to their high theoretical capacitance, favorable redox activity, and environmental stability. ZnO-based composites have demonstrated high specific capacitance and energy density, along with good cycling stability over 1000 cycles (Guo et al. 2016), making them suitable candidates for advanced energy storage systems. A critical factor underpinning these electrochemical improvements is the presence of defect centers, such as oxygen vacancies and grain boundaries, which significantly influence the material's surface chemistry and electrical transport properties (Toloman et al. 2025, Ben Gouider Trabelsi et al. 2024). These structural imperfections can enhance ionic conductivity, reduce charge transfer resistance (Toufani et al. 2020), and serve as active sites for faradaic reactions—thereby boosting the overall electrochemical performance (Singal et al. 2020, Sahu et al. 2024). Moreover, defect centers are known to modulate the electronic structure of ZnO by acting as shallow donors. Oxygen vacancies, in particular, can increase carrier concentration, improve electrical conductivity, and expand interlayer spacing to facilitate rapid ion transport and enhanced redox kinetics (Wu et al. 2019). Strategies such as doping with transition metals, e.g., Mn have been employed to further improve the performance of ZnO-based electrodes. Mn doping not only introduces new defect states but also induces redox activity, enabling pseudocapacitive behavior while tuning the bandgap to enhance electrical conductivity. The incorporation of dopants can simultaneously promote defect formation and modify surface chemistry to create more favorable conditions for electrochemical charge storage (Gao et al. 2021).

Given these complementary attributes, the combination of Mn-doped ZnO nanostructures with defect-engineered h-BN in a single composite offers a highly promising yet largely unexplored pathway for developing next-generation supercapacitor electrodes. While extensive research has been conducted on individual systems, defect-modified h-BN and doped ZnO, there is a noticeable gap in the literature regarding the integration of these two materials into a unified composite architecture. The synergistic interaction between Mn-induced redox activity in ZnO nanorods and the high surface area and defect-mediated ion

accessibility of h-BN can be expected to deliver enhanced electrochemical properties, such as higher specific capacitance, improved energy and power densities, and superior cycling stability. Furthermore, the use of ball milling and microwave-assisted hydrothermal synthesis can facilitate intimate contact between the components and promote uniform growth of Mn:ZnO on the h-BN substrate, ensuring efficient charge transfer and structural coherence.

In conclusion, the design of a Mn:ZnO-hBN nanocomposite represents a novel and promising approach to supercapacitor electrode development. It leverages the strengths of both material systems, defect-rich h-BN and doped ZnO, and addresses their respective limitations through composite engineering. Further exploration and experimental validation of such a system could contribute significantly to the field of high-performance, hybrid energy storage devices. In this chapter, the electrochemical performance of each individual system will be thoroughly examined, followed by an in-depth analysis of the electrochemical behavior of the combined systems in the form of composite materials.

4.2. Literature Review

4.2.1. Electrochemical Performance of h-BN

Despite its high thermal stability and chemical inertness, pristine h-BN exhibits poor electrochemical activity due to its limited conductivity. However, introducing defects such as vacancies, edge distortions, or substitutional impurities can significantly enhance its electrochemical performance by creating additional active sites and improving ionic transport. Shams *et al.* demonstrated that sodium thiosulfate (STS) functionalization of h-BN improves dispersibility and electrical conductivity, leading to a specific capacitance of ~116 F/g at 1 A/g with 87% retention over 3000 cycles (Shams, Bindhu, Murali, Ramesh, Souwaileh, et al. 2025). Later, a hydrothermal synthesis involving polyethylene glycol (PEG) led to a capacitance of 361.6 F/g and 85% retention after 5000 cycles (Shams, Bindhu, Murali, Ramesh, Al Souwaileh, et al. 2025). Another study by Ashwini *et al.* reported

heterostructures formed via in-situ assembly of h-BN with conductive materials, exhibiting specific capacitances up to ~800 F/g and robust cycling performance over 20,000 cycles (Alegaonkar, Alegaonkar, and Pardeshi 2020). These studies establish the critical role of defect engineering and composite formation in unlocking h-BN's electrochemical potential. The combination with carbon-based or metal-based materials is often necessary to overcome its intrinsic limitations. However, these studies explored only composites formed of h-BN combined with carbon based materials as shown in Figure 36 below.

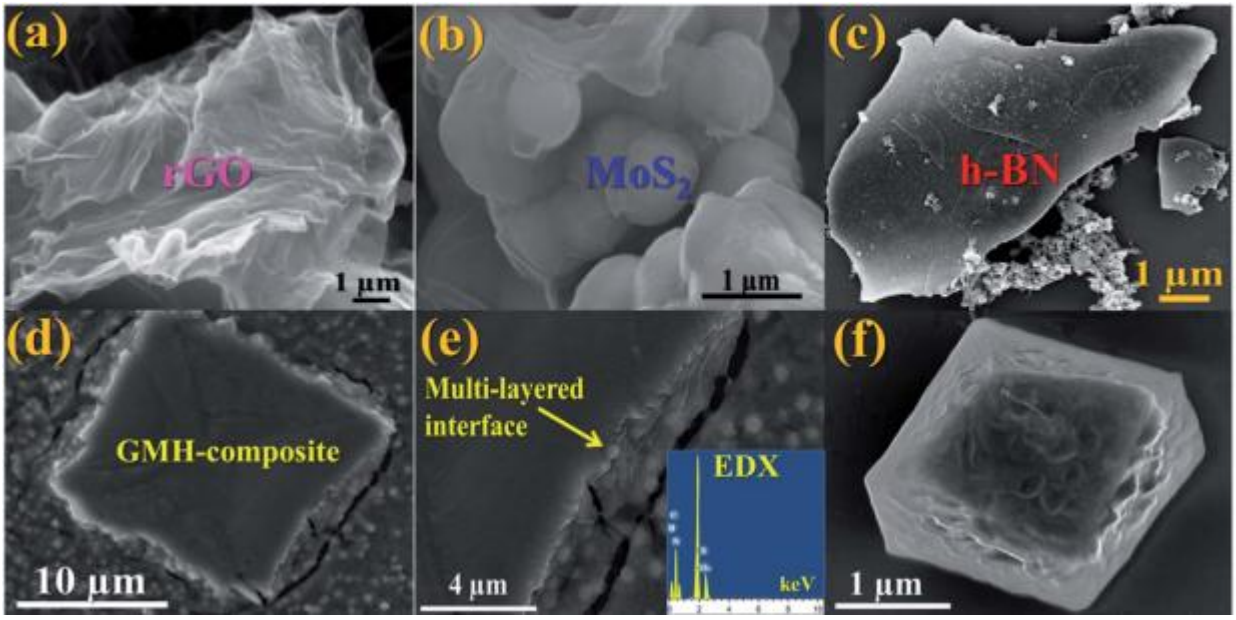

Figure 36: SEM images of the upper panel showing individual 2D layers of (a) rGO, (b) MoS2, and (c) h-BN. Lower panel: (d) rGO–MoS_2–h-BN composite, (e) sandwiched layers (inset: EDX spectrum revealing the elemental composition), (f) a smaller block of the blend, adapted from (Alegaonkar, Alegaonkar, and Pardeshi 2020)

4.2.2. Electrochemical Performance of Mn-doped ZnO

ZnO is a well-known semiconducting metal oxide with a notable pseudocapacitive behavior. However, its electrochemical performance is often hindered by low conductivity and limited specific capacitance. To overcome these limitations, doping ZnO with TMIs, particularly Mn, has been a widely adopted strategy. Pravin *et al.* demonstrated that Mn doping in ZnO thin films synthesized via spray pyrolysis enhanced the specific capacitance from 151 F/g

(undoped) to 360 F/g due to improved charge storage and redox activity of Mn ions (More et al. 2021b). Similarly, Khan *et al.* reported that Mn doping not only enhanced electrochemical performance but also improved the structural and morphological characteristics of ZnO nanostructures, leading to better cycling stability and charge/discharge rates (Khan et al. 2017). Mn ions, possessing multiple oxidation states ($Mn^{2+}/Mn^{3+}/Mn^{4+}$), introduce additional redox activity, which contributes significantly to pseudocapacitance in the electrode material (Chen, Ding, et al. 2015).

4.2.3. Unexplored Potential of Mn:ZnO-hBN Nanocomposites

Despite extensive studies on h-BN composites and Mn-doped ZnO individually, there is a noticeable gap in the literature regarding their combination into a single composite system. Integrating Mn-doped ZnO nanorods with defect-engineered h-BN is expected to offer a synergistic benefit, combining the pseudocapacitive behavior and enhanced conductivity of Mn:ZnO with the high surface area, structural stability, and ion-accessibility of h-BN. Such a composite is likely to overcome the conductivity limitations of h-BN and address the stability concerns of ZnO under prolonged cycling. To date, no peer-reviewed studies have systematically explored this composite system, indicating a promising avenue for novel electrode development in supercapacitor research.

4.3. Methodology

4.3.1. Two-Electrode Supercapacitor Configuration

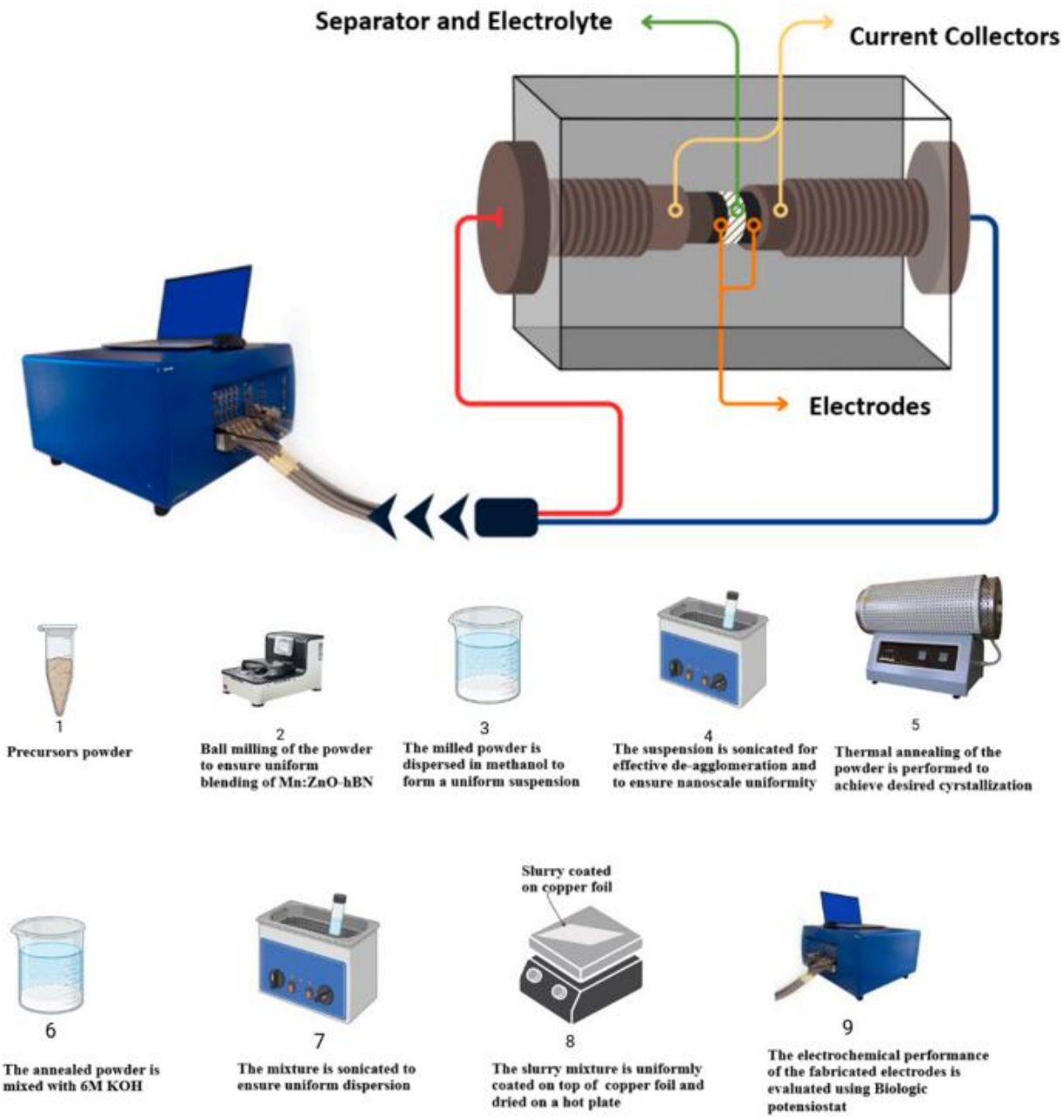

Figure 37: Schematic of the double electrode symmetric supercapacitor configuration used to measure the electrochemical properties of the supercapacitor devices

The double electrode configuration was used to study the synergy between the electrode materials and between the electrode and electrolyte, as shown in Figure 37 above. To accurately analyze the electrodes, symmetric SC devices have been used for all materials. The electrode material was mixed with Polyvinylidene Fluoride (PVDF) as a binder and dissolved in a 6 M Potassium Hydroxide (KOH) solution. To ensure a homogeneous slurry, the mixture was dissolved in a sonicator at 70 °C. The slurry was coated on top of two electrodes and left to dry on a hot plate at 90 °C. Finally, the electrodes were separated with a glass fiber separator and wetted with a few drops of 6 M KOH, which was used as the electrolyte. The total mass of the electrode material used in the study is 25 mg, either coated on top of Cu foil electrodes with 1.5 x 1.5 cm area, or on top of a stainless steel bolt with 15 mm diameter, yielding a mass loading of 2.5 mg/cm2. This mass loading was chosen to maintain consistency with the literature while ensuring robust electrochemical performance. The SC devices were then connected to a Biologic VMP300 multichannel po tentiostat. Several different methodologies were used for the analysis, such as cyclic voltammetry (CV) that involves subjecting the working electrodes to a linearly changing voltage, to study the redox behavior, the specific capacitance of the SC devices, and the electrochemical stability. Electrochemical impedance spectroscopy (PEIS) under potentiostatic conditions, and galvanostatic cycling with potential limitation (GCPL).

4.4. Results and Discussions

4.4.1. Cylic Voltammetry, Specific Capacitance and Working Mechanism Analysis

The CV of the undoped ball-milled h-BN samples discussed in Chapter 1 is displayed in Figure 38 below.

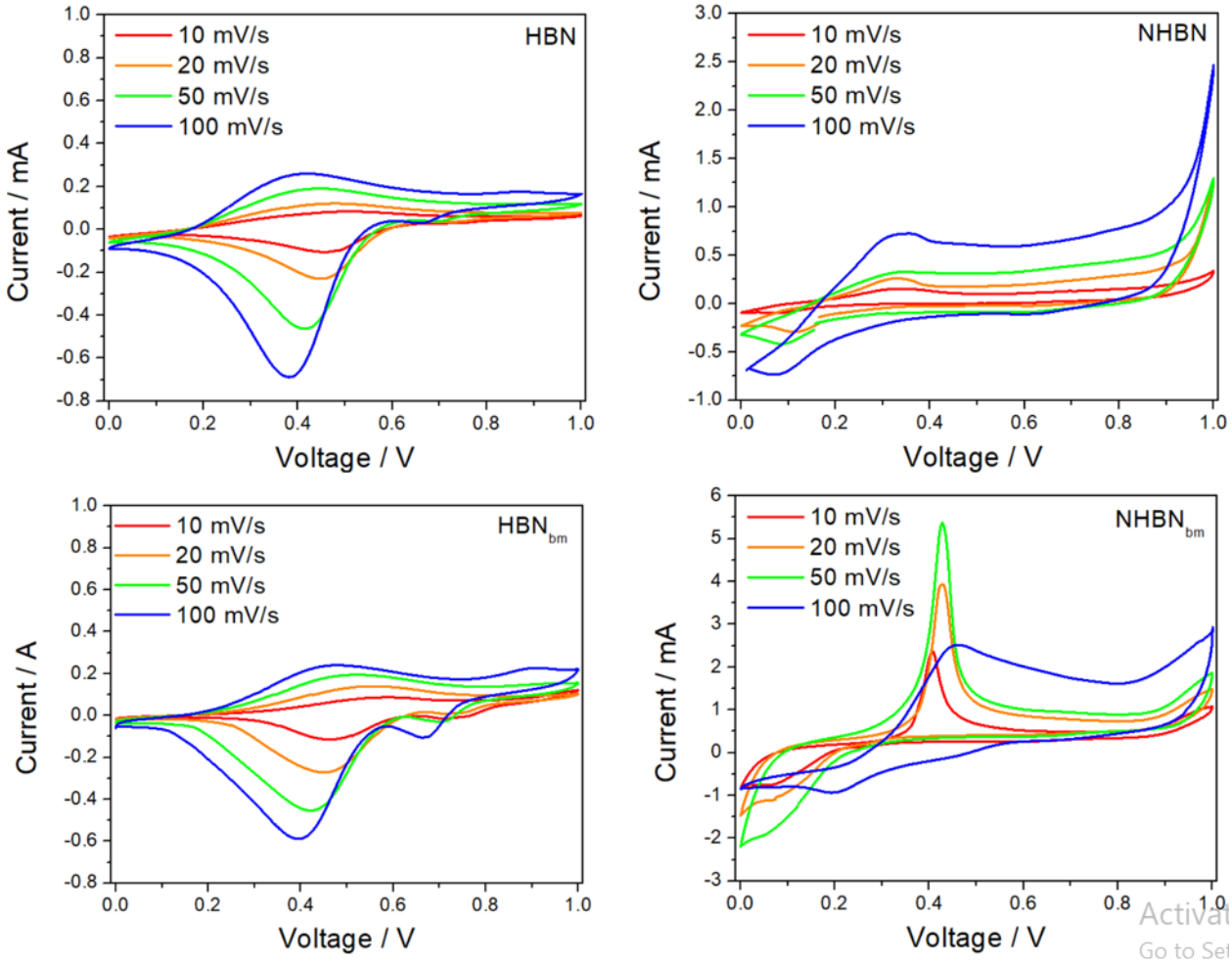

Figure 38: CV graphs of unmilled, and ball-milled h-BN samples with carbon defects (HBN – top), and V_N (NHBN – bottom), showing the effect of the ball milling process on the current response

The NHBN samples exhibited a significantly higher current response compared to the HBN samples, which can be directly attributed to the increased defect density and complexity, as evidenced by the EPR, PL, and Raman characterization results discussed earlier. This

enhanced defect landscape facilitates improved charge storage and electron transport during electrochemical cycling.

Interestingly, the ball-milled NHBN samples displayed a distinct electrochemical behavior. At a high scan rate of 100 mV/s, the CV curves revealed minor redox features. However, when the scan rate was reduced to 50 mV/s, a prominent oxidation peak emerged at approximately 0.4 V. This behavior is primarily attributed to ion diffusion limitations at higher scan rates, where the restricted time window does not permit complete electrochemical reactions, thereby favoring surface-controlled reduction processes (Zhang et al. 2023). Furthermore, NHBN samples display strong oxidation peaks, while HBN samples display strong reduction peaks. This variation of electrochemical behavior is understood from the effect of C-doping on the structure of h-BN which introduces midgap states that tend to increase the reduction reactions in h-BN (Chatterjee et al. 2025). In general, The pseudocapacitive behavior associated with Faradaic redox reactions can be attributed to the defect-engineered h-BN structure, which includes V_N and carbon substitutional defects. Although pristine h-BN is electrically insulating and typically shows electric double-layer capacitance (EDLC) only, the introduction of structural defects significantly alters its electronic structure and surface reactivity. While the precise redox mechanism in defective h-BN is still under investigation, a general reaction pathway in alkaline electrolytes (e.g., KOH) can be proposed as follows:

$$\equiv BN\_defect + OH^- \rightleftharpoons \equiv BN\_defect–OH + e^-$$

Here, ≡BN_defect represents a defect site (either a nitrogen-vacancy or carbon substitution) that can undergo reversible surface hydroxylation or electron transfer reactions.

To quantitatively evaluate the capacitive performance, the CV curves were analyzed to calculate the specific capacitance at various scan rates by using the relation illustrated in Equation (9):

$$C_S = \frac{A}{2mk\Delta V} \qquad (9)$$

Where C_s is the specific capacitance in F/g, A is the area enclosed under CV curves in mA.V, m is the active mass of the electrode materials in g, k is the scan rate in mV/s, and V is the voltage window in V.

Figure 39 presents the variation of specific capacitance as a function of scan rate for all samples.

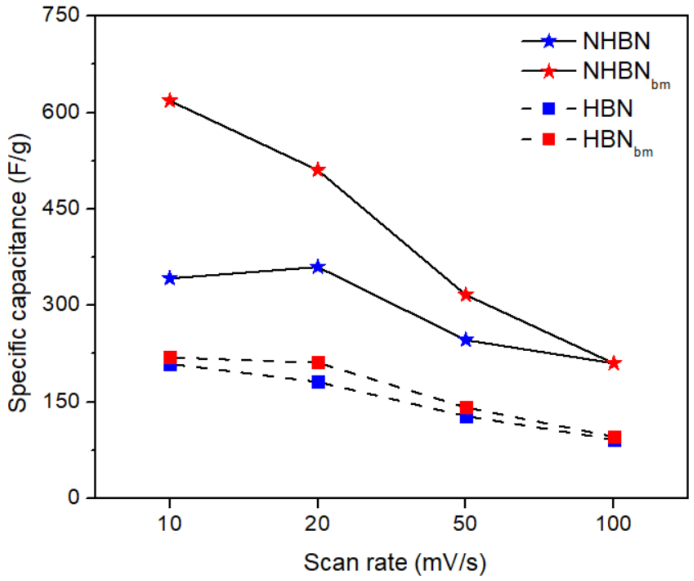

Figure 39: Specific capacitance of unmilled and ball-milled h-BN samples at varying scan rates, showing the effect of ball-milling on the specific capacitance of the electrodes

As expected, all samples showed a general increase in specific capacitance with decreasing scan rate, which is a typical behavior for supercapacitor electrodes. This trend reflects the enhanced ion accessibility and prolonged time for electrochemical reactions at lower scan rates. For the un-milled NHBN sample, the highest specific capacitance was recorded at 20 mV/s. However, a notable decline in capacitance was observed when the scan rate was further reduced to 10 mV/s. This behavior suggests either ion diffusion saturation at 20 mV/s or possible electrolyte decomposition at lower scan rates (Patra et al. 2021). In contrast, the ball-milled NHBN samples did not exhibit this drop in capacitance at low scan rates. Instead, they maintained and even improved their capacitance, indicating that the introduction of additional defect sites via ball milling effectively eliminated the diffusion saturation barrier observed in the un-milled samples. The ball-milled NHBN sample reached a maximum specific capacitance of 615 F/g at a scan rate of 10 mV/s, highlighting the substantial impact

of defect engineering on electrochemical performance. To gain deeper insight into the charge storage mechanism, the Dunn method was employed (Raavi et al. 2023). The Dunn Equation (10) is expressed as:

$$I(V) = k_1 v + k_2 \sqrt{v} \qquad (10)$$

Where k_1 and k_2 are the capacitive and diffusive currents respectively, and v is the scan rate.

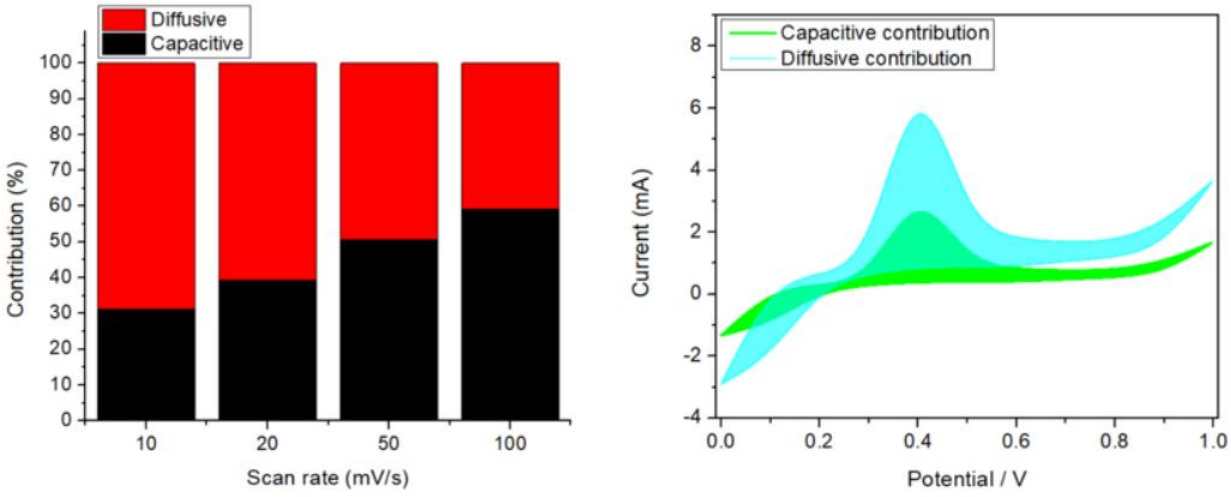

Figure 40: Dunn method showing the working mechanism of $NHBN_{bm}$ at 10 mV/s scan rate (right) and the contribution of the diffusive and capacitive working mechanism of $NHBN_{bm}$ samples at 10 mV/s scan rate (left)

The relative contributions of each mechanism can be quantified by analyzing the slope and intercept of a Dunn plot. The analysis of the Dunn plots, presented in Figure 40 allowed for quantification of the relative contributions of capacitive and diffusive processes. Figure 40 (right) shows the separation of capacitive and diffusive currents at 10 mV/s, while Figure 40 (left) illustrates the percentage contribution of each mechanism across different scan rates. The results reveal a clear increase in the diffusion-controlled Faradaic contribution as the scan rate decreases. This indicates that the introduction of additional defect sites through ball milling significantly enhances the material's redox-active behavior, providing more electrochemically accessible sites for charge storage reactions.

Under CV, ZnO demonstrates a predominantly pseudocapacitive behavior, diverging from the classic rectangular profiles associated with EDLCs. In EDLC systems, charge storage

arises from the non-faradaic, physical adsorption of electrolyte ions at the electrode–electrolyte interface, typically producing featureless rectangular CV curves due to the rapid electrostatic ion accumulation (Gogotsi and Penner 2018). By contrast, ZnO, as a transition metal oxide, undergoes reversible faradaic redox reactions, reflected in the appearance of distinct anodic and cathodic peaks in the CV profiles. These peaks result from ion intercalation and redox kinetics that are inherently slower and more diffusion-limited compared to the nearly instantaneous ion adsorption processes of EDLCs (Bhojane 2022). The faradaic reactions in ZnO are governed by ion diffusion-controlled kinetics, contributing to the diffusive charge storage behavior observed in CV measurements. The synthesis route plays a crucial role in tailoring the capacitive response of ZnO electrodes by influencing defect density and distribution (Zhang et al. 2018). For example, ZnO:Mn_0 @ 800 W displays defect-induced facilitation of ion transport, as indicated by minor but observable redox peaks. In contrast, ZnO:Mn_0 @ W exhibits a more rectangular-like CV shape, indicative of suppressed faradaic activity. Although synthesis parameters generally enhance the faradaic properties of ZnO by introducing defects that aid ion transport, careful control over defect concentration is essential. Excessive defect generation can hinder performance by increasing internal resistance or blocking active sites (Najib et al. 2020). Furthermore, Mn doping acts as an additional strategy to enhance pseudocapacitive behavior by providing new electrochemically active sites and improving electronic conductivity.

Figure 41 and Appendix 12 illustrate the CV responses of the supercapacitor devices tested across five scan rates (10, 20, 50, 100, and 200 mV/s), while Figure 42 presents the specific capacitance variation as a function of scan rate for all undoped and Mn-doped ZnO samples synthesized at different microwave powers. The variation in microwave power and Mn doping concentration was designed to modulate defect density and electrochemically active surface area.

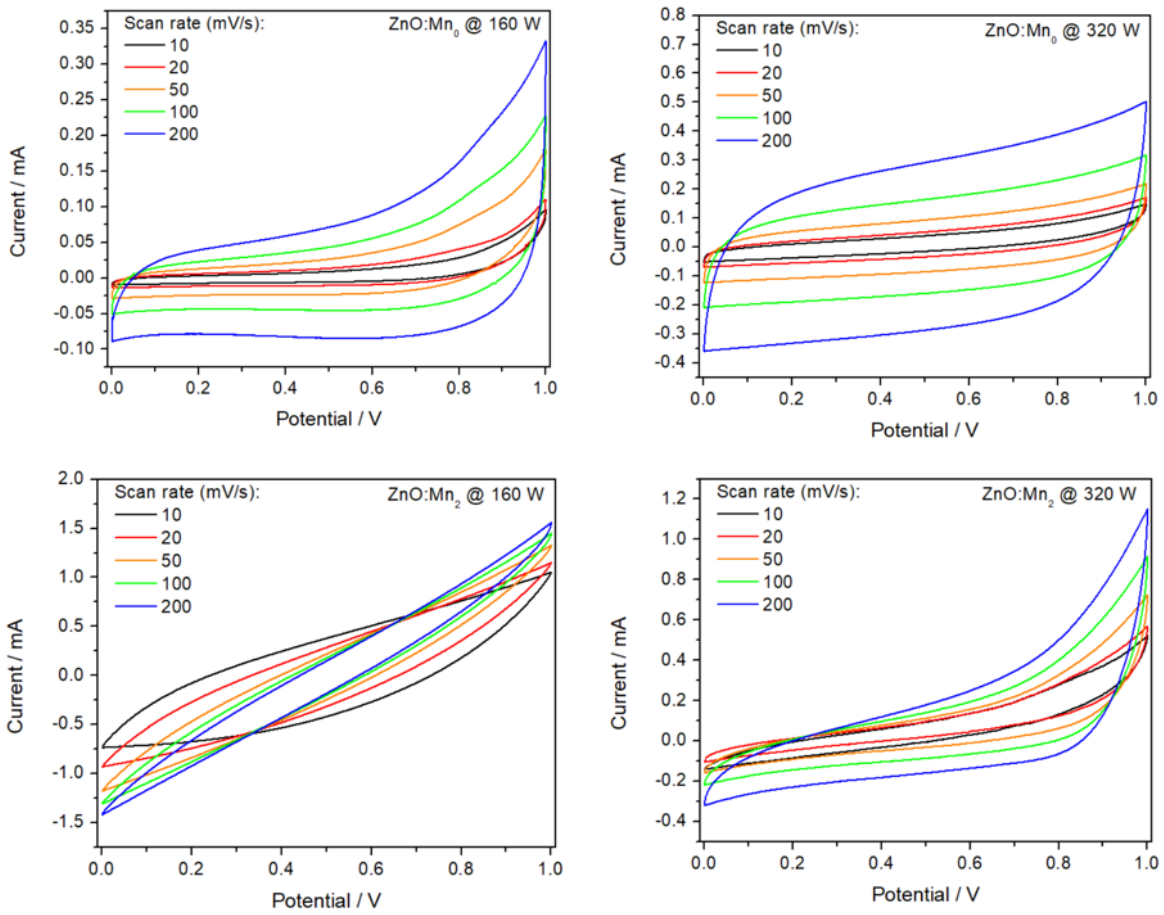

Figure 41: CV of ZnO:Mn_0 and ZnO:Mn_2 @ 160 and 320 W microwave power, showing the effect of the synthesis microwave power on the behavior of the supercapacitor device

Undoped ZnO typically exhibits prominent redox features, particularly @160 W the increase in Mn doping concentration from 2% to 5% resulted in nearly a twofold increase in peak current, suggesting enhanced pseudocapacitive behavior via improved ion diffusion pathways. This improvement highlights the critical role of Mn dopants in facilitating redox activity. However, at higher dopant levels or synthesis powers, the trade-off between defect density and charge transfer resistance becomes apparent.

For instance, in ZnO:Mn_5 @ 320 W, although redox peaks became more pronounced, the increasing defect concentration began to impede ion transport, leading to reduced peak currents and specific capacitance values. This indicates the onset of excessive defect-induced resistance that adversely affects charge storage efficiency. Similarly, ZnO:Mn_0 @ 640 W shows moderate pseudocapacitive characteristics, with minor redox peaks, while doping at

this power level (ZnO:Mn_2 and ZnO:Mn_5) led to further increases in peak definition and overall capacitance. At 800 W synthesis power, Mn doping had a more profound impact. The ZnO:Mn_2 sample exhibited highly defined redox peaks, reflecting an increase in faradaic reaction sites and improved ion diffusion kinetics. Nevertheless, at 5% Mn doping, a decline in electrochemical performance was observed, attributable to excessive structural distortion and elevated internal resistance.

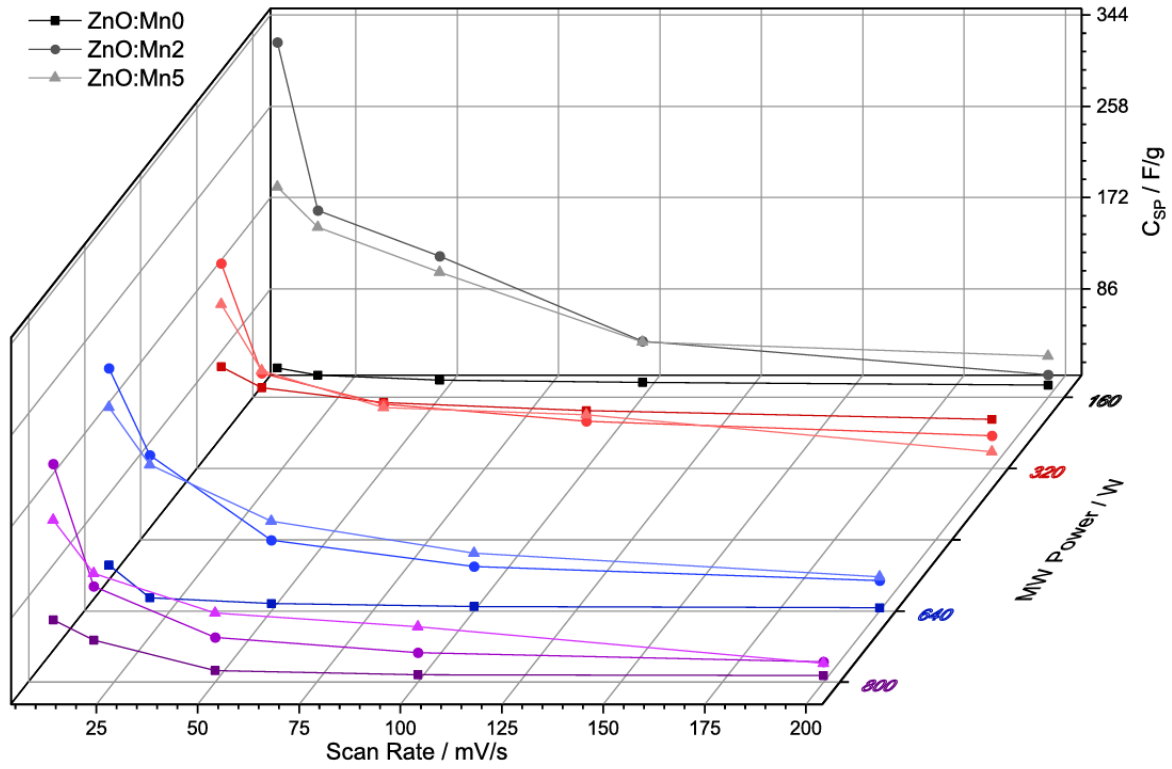

Figure 42: Specific capacitance of ZnO:Mn samples synthesized at various microwave powers, showing the effect of the synthesis conditions on the electrochemical performance of the device

Quantitative analysis of the CV curves enabled the calculation of Cs for all samples, as shown in Figure 42. Among all tested conditions, ZnO:Mn_2 consistently exhibited the highest Cs, followed by ZnO:Mn_5 and undoped ZnO. This trend emphasizes the role of moderate Mn doping in optimizing the balance between charge carrier density and structural integrity. The observed enhancement at 2% Mn is likely due to the generation of additional redox-active centers without compromising the crystallinity and morphology of the ZnO nanostructures. In contrast, higher doping levels (5% Mn) introduced excessive defects, reducing

crystallinity as confirmed by XRD and causing morphological deterioration, as seen in SEM images.

To further elucidate the charge storage mechanism and quantify the relative contributions of capacitive and diffusion-controlled processes, the Dunn method was employed. The results, presented in Figure 43, reveal a noticeable increase in the diffusive contribution for ZnO:Mn_2 compared to undoped ZnO across all synthesis powers, except at 800 W.

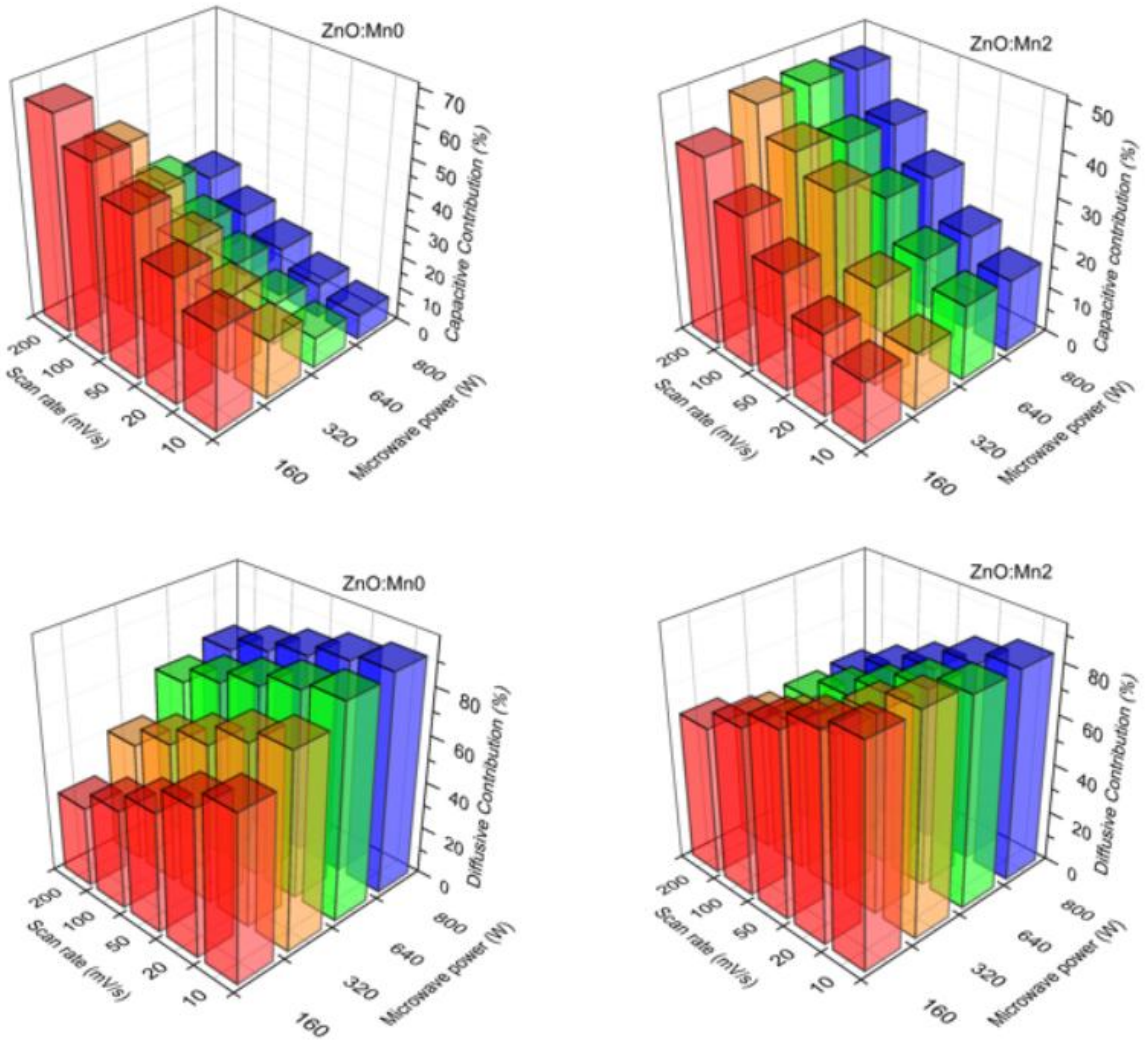

Figure 43: 3D representation of Dunn technique's capacitive and diffusive contributions for ZnO:Mn_0 and ZnO:Mn_2 samples at various microwave powers

At a low scan rate (10 mV/s), where ion diffusion time is sufficient, the contribution from diffusion-controlled processes was maximized. Specifically, ZnO:Mn_2 exhibited higher

diffusive contributions at 160, 320, and 640 W compared to the corresponding undoped ZnO samples, highlighting the beneficial role of Mn doping in enhancing faradaic charge storage. However, for the 800 W samples, undoped ZnO surprisingly displayed a higher diffusive contribution (~90%) than ZnO:Mn2 (~85%). This reduction for ZnO:Mn_2 at 800 W can be attributed to morphological degradation, particularly a decrease in aspect ratio as indicated by SEM histograms, which limited ion transport and reduced the efficacy of faradaic processes. The enhanced diffusive behavior in Mn-doped ZnO electrodes stems largely from the multivalent nature of Mn ions ($Mn^{2+}/Mn^{3+}/Mn^{4+}$), which introduces additional redox centers that participate in fast and reversible electron transfer reactions during charging and discharging cycles. These redox transitions extend charge storage beyond surface ion adsorption, enabling bulk and near-surface faradaic reactions (Rashid et al. 2021). Moreover, Mn incorporation promotes the formation of oxygen vacancies within the ZnO lattice, thereby enhancing electrical conductivity and providing additional active sites for redox interactions with the electrolyte (Dillip et al. 2016, Das et al. 2023). These oxygen vacancies not only improve charge transport kinetics but also act as ion diffusion channels, further amplifying the material's pseudocapacitive performance.

The electrochemical behavior of Mn:h-BN and Mn:ZnO–h-BN nanocomposites exhibits a hybrid charge storage mechanism, integrating characteristics observed in both individual Mn-doped ZnO and h-BN systems. The CV responses of these materials, presented in Figures 44 and 45, along with the detailed plots in Appendix 13, reveal this combined behavior.

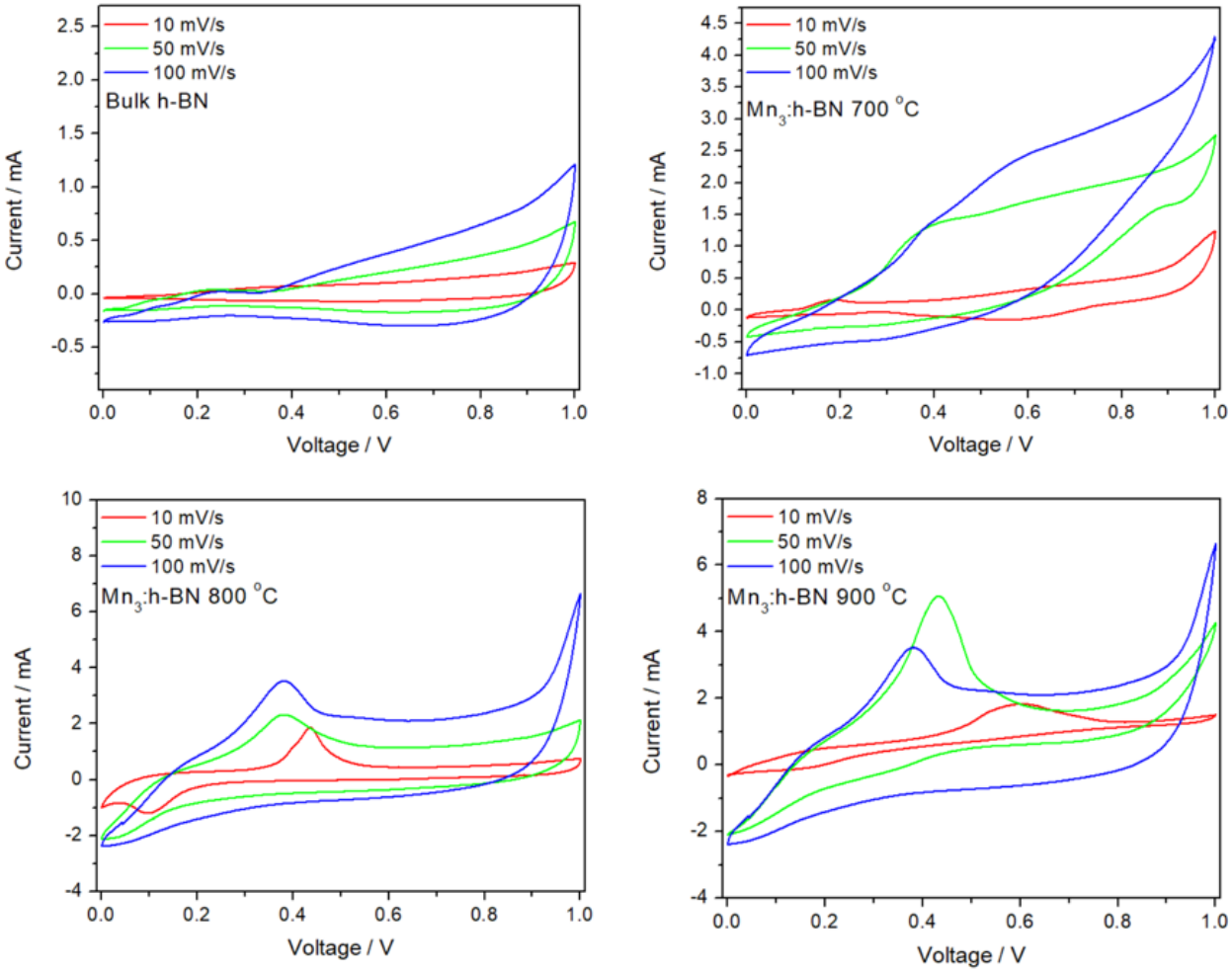

Figure 44: CV plots of Mn_3:h-BN samples at various heat treatment temperatures, showing the effect of Mn dopant incorporation in the structure of h-BN on the working mechanism of the supercapacitor devices

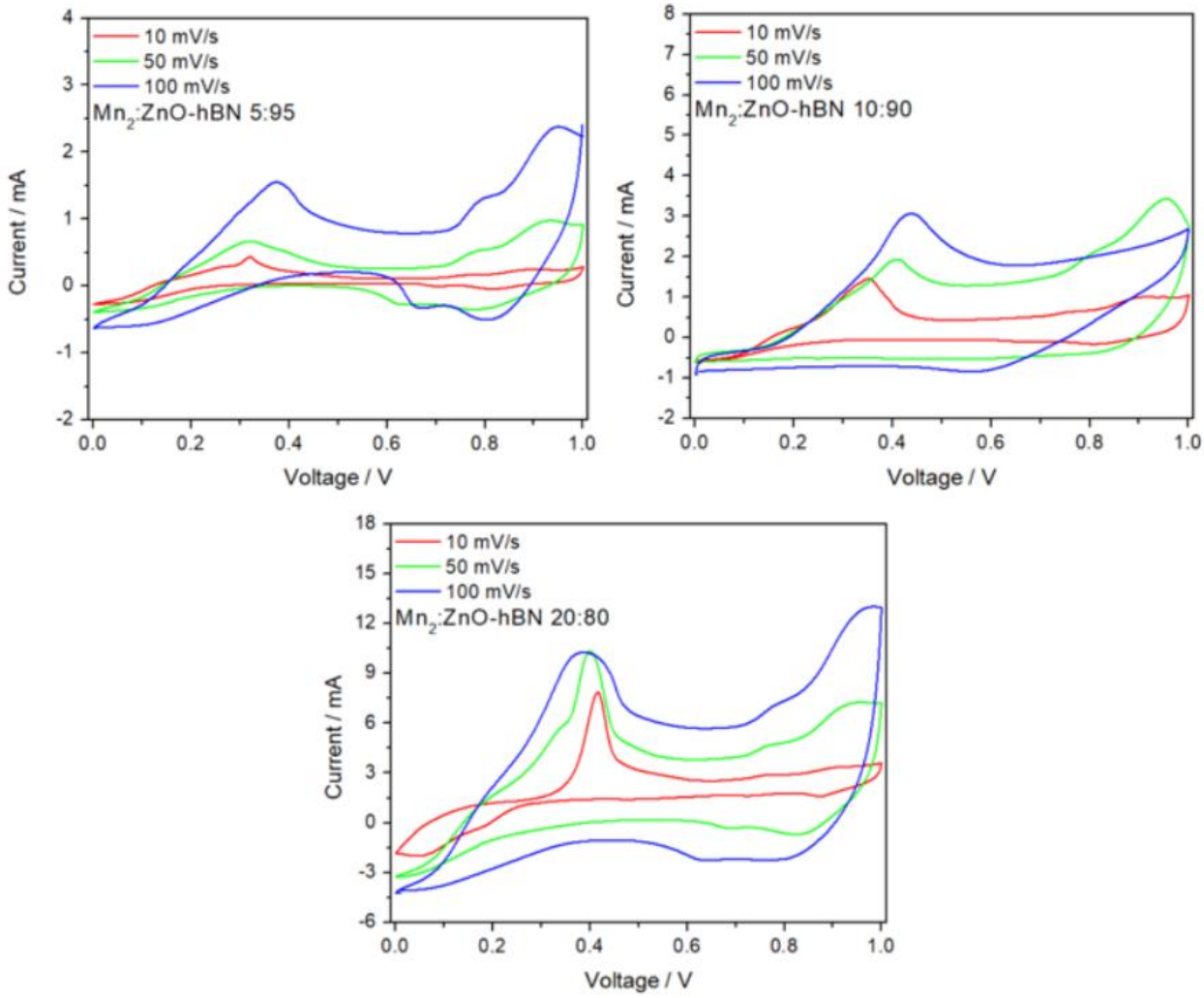

Figure 45: CV graphs of Mn_2:ZnO-hBN nanocomposites samples showing the effect of increasing the concentration of ZnO phase on the current response of the supercapacitor devices

The Mn-doped h-BN samples exhibited relatively modest changes in their CV profiles following thermal treatment at 700 °C. While no significant alterations in the overall curve shape were observed compared to the untreated samples, a noticeable increase in current density occurred. This enhancement is likely attributed to improved electrical conductivity and surface activation induced by the moderate thermal exposure. However, as the annealing temperature was raised to 800 °C and 900 °C, the electrochemical behavior of the Mn-doped h-BN changed considerably. Distinct and well-defined oxidation peaks became evident in the CV curves, indicating the onset of faradaic redox reactions that were previously absent

or considerably suppressed in the bulk and lower-temperature-treated samples. This suggests that higher thermal energy facilitates defect formation and activates additional electrochemically active sites within the h-BN structure. The Mn:ZnO–h-BN nanocomposites demonstrated a similar but more pronounced temperature-dependent evolution in their electrochemical response. Post-annealing at elevated temperatures resulted in a substantial increase in current response during CV measurements, reflecting enhanced charge storage capability. This improvement can be attributed to the synergistic interaction between the Mn-doped ZnO nanostructures and the defect-engineered h-BN matrix. The Mn dopants introduced additional redox-active sites, while the defective h-BN provided an extended surface area and facilitated faster ion diffusion pathways. The pseudocapacitive nature of the nanocomposites became particularly evident after thermal treatments at 800 °C and 900 °C, where intensified and broadened redox peaks were observed. These results collectively demonstrate that both Mn doping and composite formation with h-BN, when combined with controlled high-temperature annealing, significantly enhance the faradaic contribution and ion transport kinetics of the electrode materials. This strategy effectively tunes the electrochemical performance of the system, making it highly suitable for advanced supercapacitor applications.

The specific capacitance of Mn-doped h-BN and the ZnO-hBN nanocomposites is shown in Figures 46 and 47.

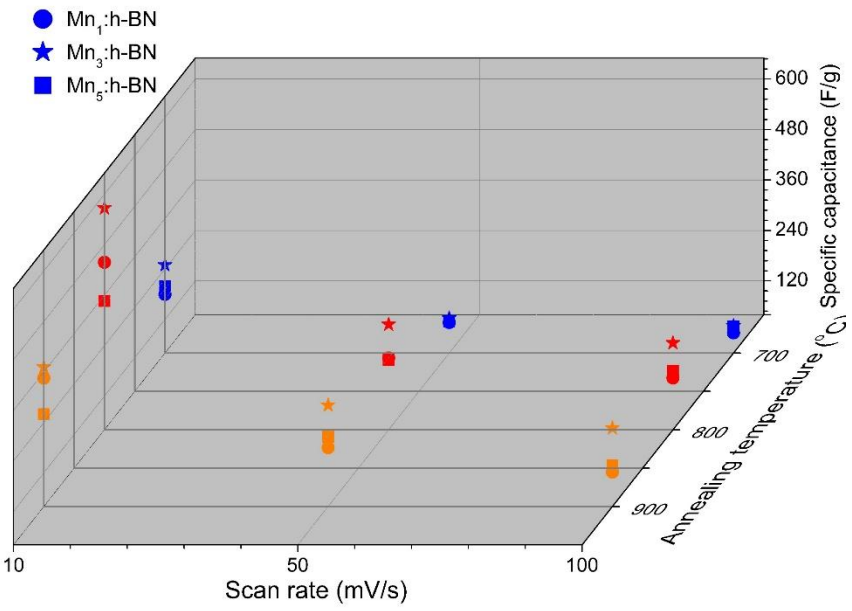

Figure 46: 3D representation of the specific capacitance Mn:h-BN samples at different heat treatment temperatures showing the effect of Mn-dopant incorporation in the structure of h-BN

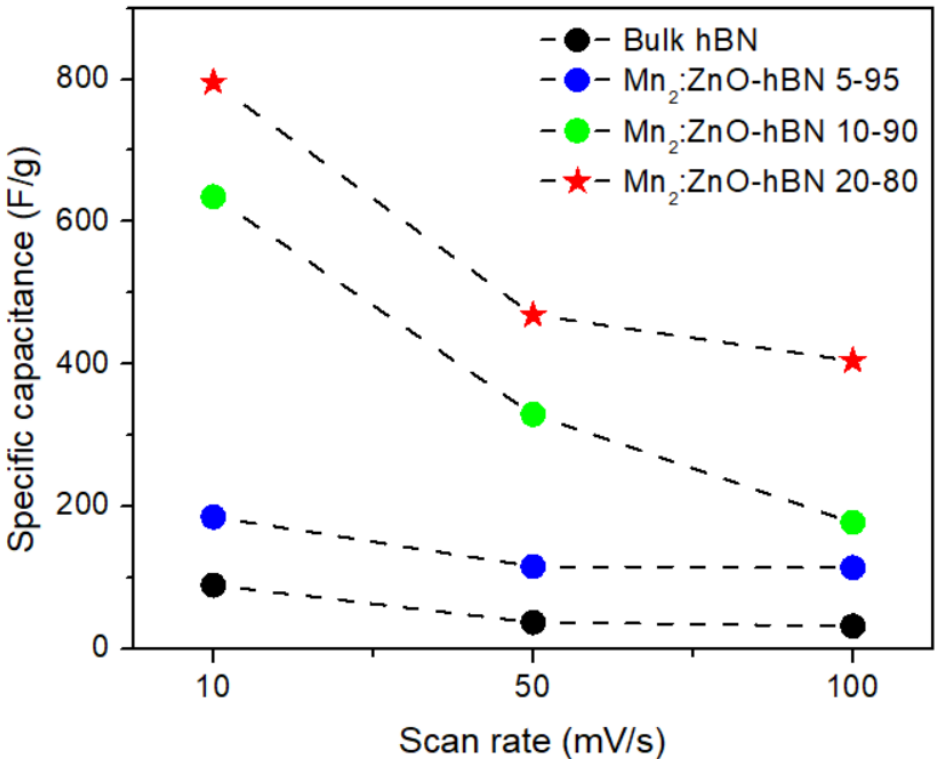

Figure 47: Specific capacitance of the nanocomposites, showing the effect of ZnO to h-BN concentration on the electrochemical performance of the supercapacitor devices

The Mn-doped h-BN samples exhibited a marked enhancement in specific capacitance compared to pristine bulk h-BN. Among the various heat treatment conditions, samples annealed at 800 °C demonstrated the highest electrochemical performance. This temperature appears to provide an optimal balance—facilitating the effective incorporation of Mn ions into the h-BN lattice while avoiding the excessive microstrain and structural distortions observed at higher annealing temperatures, such as 900 °C. The successful doping at this intermediate temperature likely contributes to the creation of additional redox-active sites and improved electrical conductivity without compromising the structural integrity of the material. For the Mn:ZnO–h-BN nanocomposites, the composition with a 20:80 ZnO-to-h-BN weight ratio delivered the most favorable electrochemical performance. This particular configuration achieved a remarkable specific capacitance of up to 800 F/g, surpassing all other tested composite formulations. The superior performance of this system can be attributed to the synergistic effects between the Mn-doped ZnO nanostructures and the defect-rich h-BN matrix. The ZnO component provides abundant faradaic reaction sites, while the high h-BN content enhances ion transport pathways and contributes to structural stability during cycling. These findings underscore the critical role of both compositional design and thermal processing in optimizing electrode performance. The strategic combination of Mn-doped ZnO with h-BN in a nanocomposite architecture not only maximizes the density of active sites but also ensures efficient ion diffusion and electronic conductivity, offering a promising pathway for high-performance supercapacitor electrodes.

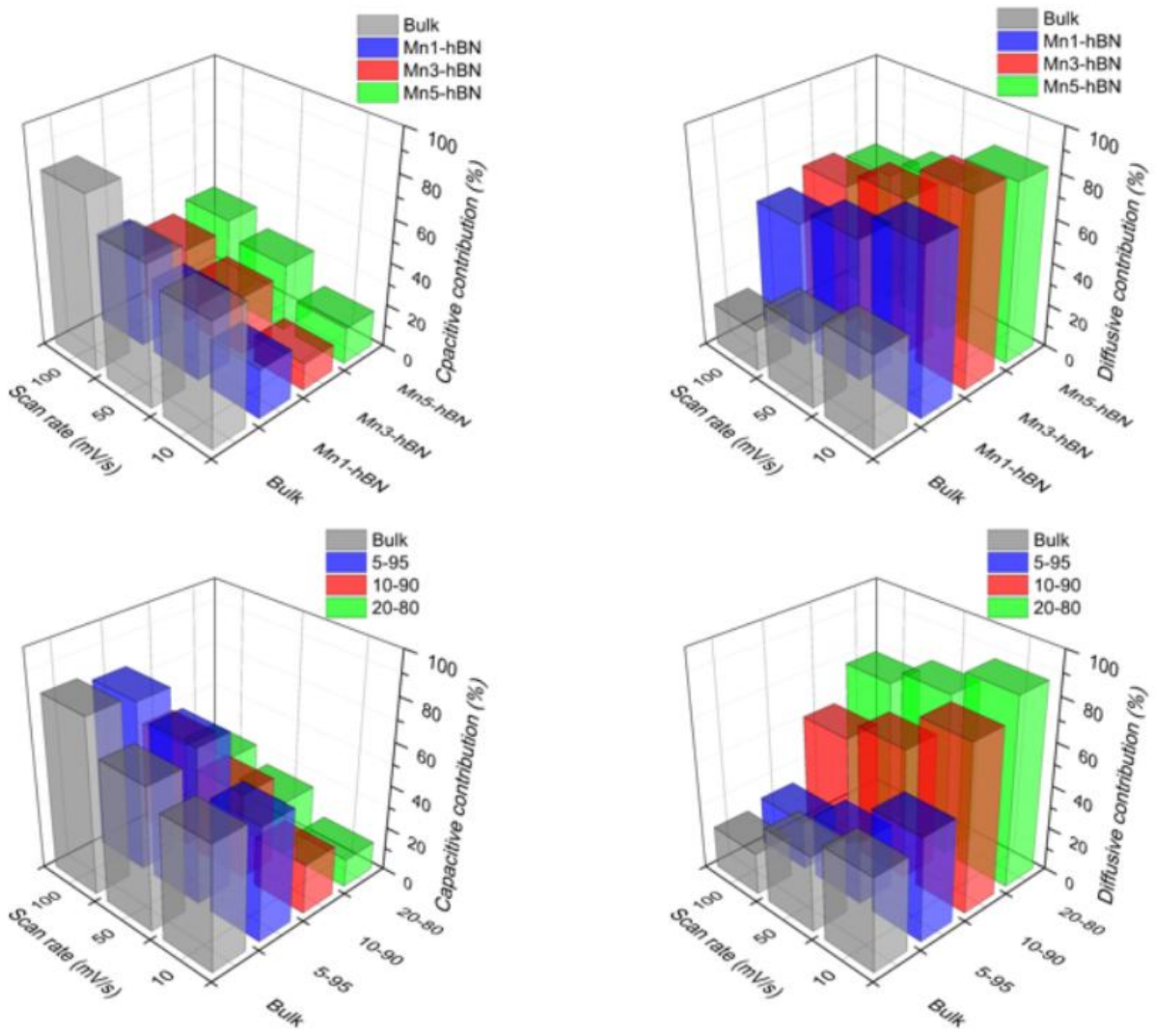

Figure 48: 3D representation of Mn-doped h-BN and Mn:ZnO-hBN nanocomposites Dunn technique's capacitive and diffusive contributions, showing the working mechanism of the supercapacitor devices

The charge storage mechanisms governing the performance of the Mn-doped h-BN and Mn:ZnO-hBN nanocomposite-based supercapacitor devices are illustrated in Figure 48. The bulk h-BN samples primarily exhibit EDLC-dominated behavior, characterized by non-faradaic charge storage resulting from the physical adsorption of electrolyte ions at the electrode–electrolyte interface. However, the introduction of Mn dopants into the h-BN lattice induces a notable shift toward pseudocapacitive charge storage. This transition is attributed to the creation of additional electrochemically active sites by Mn ions, which facilitate surface and near-surface faradaic redox reactions within the h-BN structure.

Consequently, the Mn-doped h-BN electrodes demonstrate an enhanced contribution from faradaic processes compared to their undoped counterparts. This pseudocapacitive contribution becomes even more significant in the Mn:ZnO-hBN nanocomposite systems. The presence of ZnO, a well-known pseudocapacitive material, further amplifies the diffusive-controlled charge storage mechanism. The synergistic effect between Mn-doped ZnO and the defective h-BN matrix leads to a dominant pseudocapacitive response, characterized by higher current densities and larger specific capacitance values, as discussed in the preceding sections. Importantly, the inherent structural stability of h-BN provides a robust framework that accommodates the increased faradaic activity without compromising long-term performance. This balance between high pseudocapacitive contribution and structural integrity will be further demonstrated in GCPL section to be discussed later in this chapter.

4.4.2. Impedance and Z-fit Analysis

Figure 49 presents the EIS plots for both unmilled and ball-milled h-BN samples. A clear distinction in impedance behavior is observed between the HBN and NHBN samples, which can be directly attributed to the differing defect types and concentrations within their structures. The HBN samples exhibit a relatively small semicircular arc in the high-frequency region of the Nyquist plot, followed by a near-vertical straight line in the low-frequency region. The high-frequency semicircle corresponds to the charge transfer resistance and inherent internal resistance of the material. In contrast, the low-frequency linear region reflects a diffusion-controlled process, characterized by the so-called Warburg impedance (Nishikata, Ichihara, and Tsuru 1995), which arises from ion diffusion limitations within the electrode material.

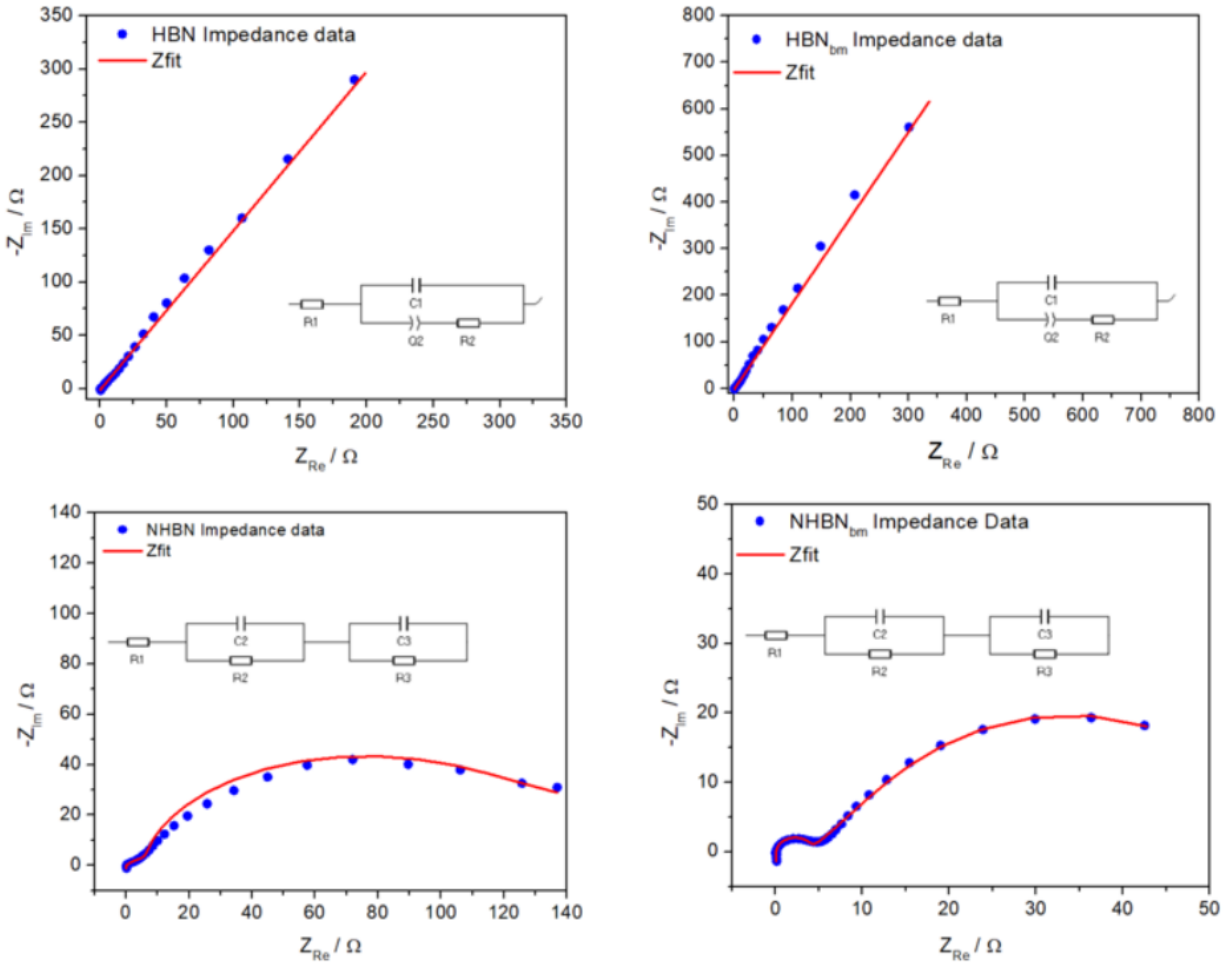

Figure 49: EIS plots of unmilled and ball-milled HBN (top) and NHBN (bottom) samples, along with the equivalent circuits obtained from the Zfit shown in the red line

In comparison, the NHBN samples display a significantly different impedance response, marked by the presence of two distinct semicircles. This dual semicircle behavior indicates multiple charge storage and transport processes, likely originating from the higher density of electrochemically active defect sites associated with nitrogen vacancies in the NHBN structure. The difference between the HBN and NHBN samples is particularly evident in the low-frequency region, where the nature and concentration of defects distinctly influence the ion transport mechanism and overall device behavior. This observation is consistent with the findings from the Dunn analysis, which also highlighted the influence of defects on charge storage mechanisms. To gain deeper insight into these impedance characteristics, equivalent circuit modeling was performed using Z-fit analysis, with the derived circuits and fitted component values summarized in Appendix 14. The presence of nitrogen vacancies in the

NHBN samples provides additional active sites for faradaic redox reactions, which explains the appearance of two semicircles and the overall lower resistance, especially after the ball milling process. Conversely, the HBN samples exhibited an increase in Warburg impedance following ball milling, as shown in Appendix 14. This increase can be attributed to the further hindrance of ion diffusion, likely caused by the introduction or amplification of a secondary phase within the h-BN structure specifically, the presence of carbon-related impurities, which act as barriers to efficient ion transport.

The EIS responses of the Mn-doped ZnO samples are presented in Figure 50 and Appendix 15.

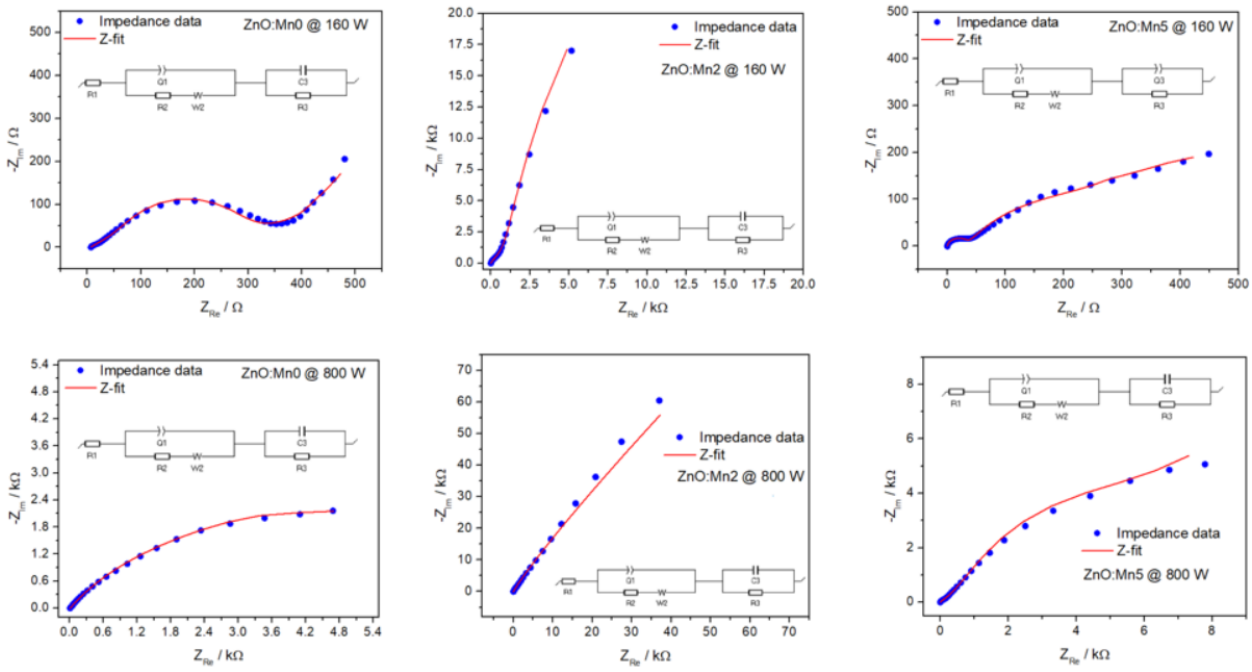

Figure 50: EIS plots of ZnO:Mn_0 and ZnO:Mn_2 samples synthesized at 160 and 800 W microwave power, along with the equivalent circuits obtained from the Zfit shown in red line

All impedance spectra exhibit characteristic features indicative of multiple charge transfer processes within the supercapacitor devices. Specifically, the Nyquist plots display a combination of elements corresponding to the electrode-electrolyte interfacial resistance (R_s), charge transfer resistance (R_{ct}), and a diffusion-controlled process, as evidenced by the linear Warburg region observed at low frequencies. To gain a more quantitative understanding of these processes, Z-fit modeling was performed on the EIS data. The

resulting equivalent circuit models and the corresponding fitted resistance values are summarized in Appendix 16.

Among all the tested samples, ZnO:Mn2 exhibited the lowest Rs, suggesting improved ionic conductivity at the electrode surface. However, this sample simultaneously showed the highest R_{ct}, which may appear counterintuitive but can be explained by structural changes induced by Mn doping. At lower doping concentrations, Mn^{2+} ions effectively substitute for Zn^{2+} ions within the ZnO crystal lattice, as confirmed by EPR measurements. This substitution disrupts the concentration and distribution of oxygen vacancies, leading to an increase in charge transfer resistance due to reduced carrier mobility and fewer available conduction pathways. At higher Mn doping levels, as seen in the ZnO:Mn_5 samples, this effect becomes less pronounced. The increase in Mn concentration appears to mitigate the disruption of oxygen vacancies, likely by altering defect chemistry or promoting the formation of alternative conduction pathways. This behavior aligns with previous studies reporting similar trends in Mn-doped ZnO systems, where dopant concentration plays a crucial role in balancing ionic and electronic conductivity (Oo et al. 2009, Motevalizadeh, Shohany, and Ebrahimizadeh Abrishami 2016).

Figures 51 and 52, along with the detailed data presented in Appendix 16, display the EIS plots for both the Mn-doped h-BN samples and the Mn:ZnO-hBN nanocomposites. For the nanocomposite systems, a clear trend is observed: the overall resistance decreases with increasing ZnO content relative to h-BN within the composite structure. This reduction in resistance is expected, as the introduction of ZnO, especially in its Mn-doped form, enhances the electronic conductivity and provides additional pathways for ion diffusion. ZnO's inherent pseudocapacitive properties, combined with the increased surface area and higher density of electrochemically active sites from Mn doping, contribute to improved charge transfer kinetics and reduced R_s across the electrode–electrolyte interface. Specifically, as the ZnO to h-BN ratio increases, the diameter of the high-frequency semicircle in the Nyquist plots diminishes, indicating a lowering of charge R_{ct}. Simultaneously, the low-frequency, suggests improved ion diffusion within the electrode material. These observations confirm that the incorporation of ZnO not only facilitates better electronic conduction but also enhances electrolyte accessibility to active sites. In contrast, the Mn-doped h-BN samples

exhibit higher overall impedance compared to the nanocomposites, as expected from the intrinsically insulating nature of h-BN. However, doping h-BN with Mn ions does reduce its R_{ct} compared to undoped bulk h-BN, likely due to the introduction of localized defect states and additional redox-active centers that facilitate faradaic reactions.

Furthermore, the effect of Mn doping on both systems is evident in the EIS profiles. The presence of Mn enhances pseudocapacitive behavior by promoting charge storage through faradaic redox mechanisms, as reflected by reduced R_{ct} and improved low-frequency behavior in both Mn-doped h-BN and the ZnO-hBN nanocomposites. The synergistic combination of Mn-doped ZnO and defect-rich h-BN in the nanocomposites leads to a significant overall reduction in Rs and R_{ct}, optimizing the charge transport properties. These impedance results align well with the CV and specific capacitance data discussed previously, confirming that increasing ZnO content and controlled Mn doping in the nanocomposite architecture effectively enhance both ionic and electronic conductivity, thereby improving overall supercapacitor performance.

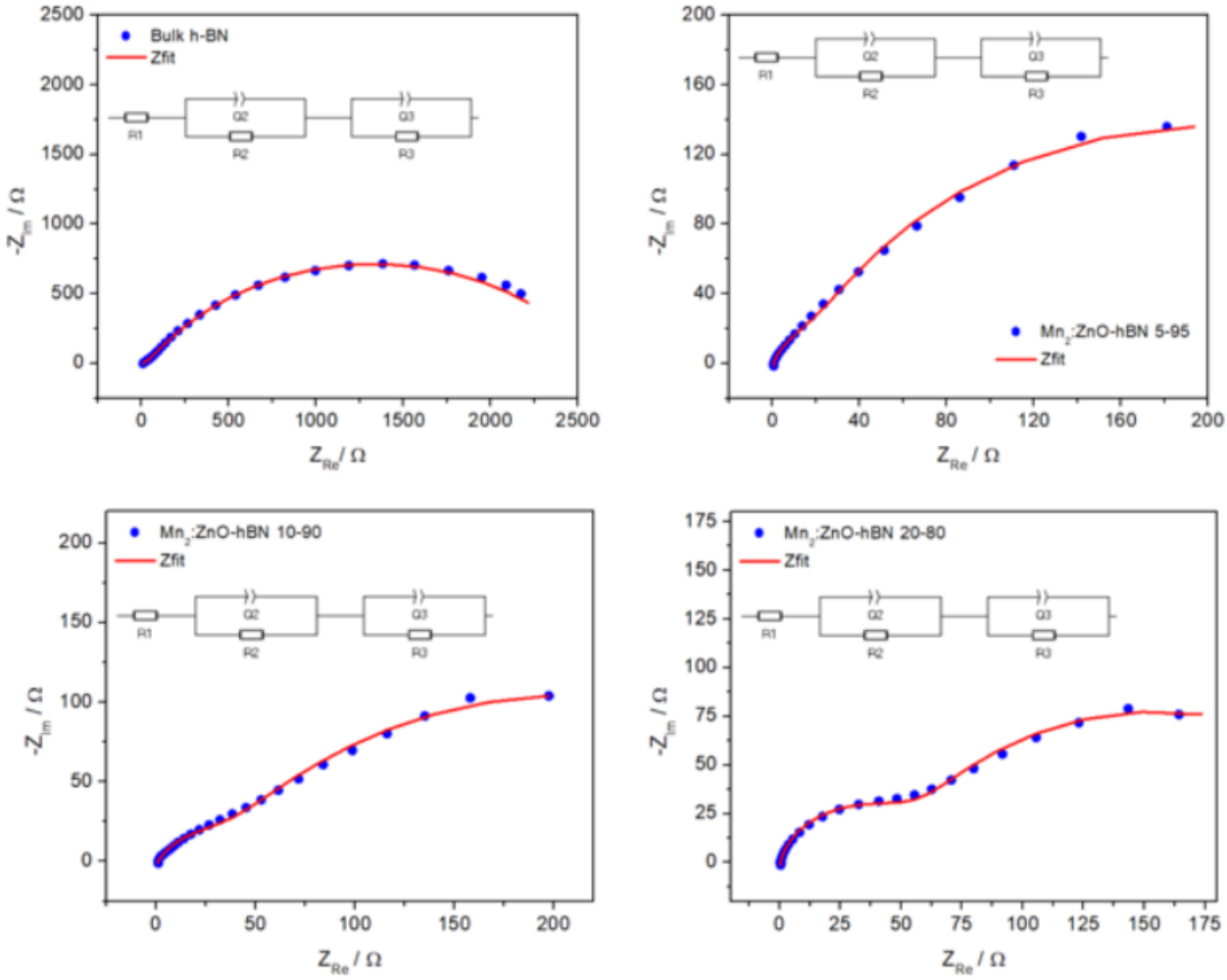

Figure 51: EIS plots of bulk h-BN, and Mn:ZnO-HBN nanocomposites, along with the equivalent circuits obtained from the Z-fit shown in red line

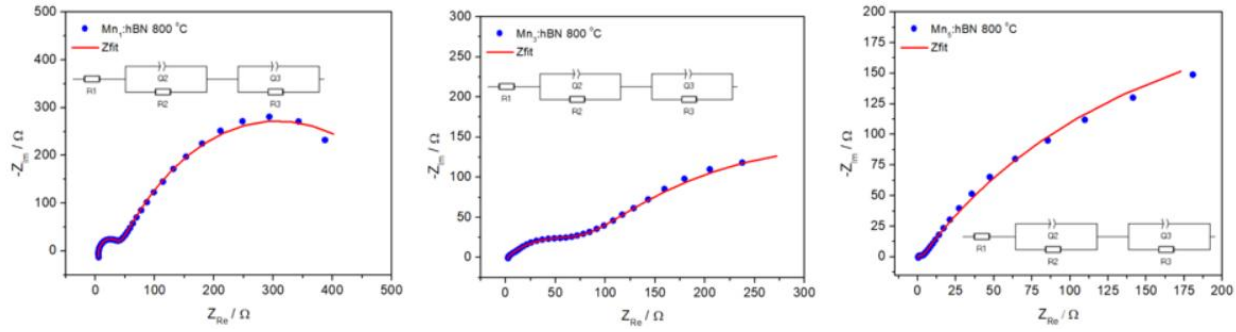

Figure 52: EIS plots of Mn:h-BN samples heat treated at 800 ^{o}C, along with the equivalent circuits obtained from the Z-fit shown in red line

4.4.3. GCPL Analysis of Stability and Ragone Plots

Figure 53 displays the GCPL curves of supercapacitor devices fabricated using HBN and NHBN electrode materials, both before and after ball milling, tested within a potential window of 0 to +1 V at current densities of 0.5 and 1 A/g.

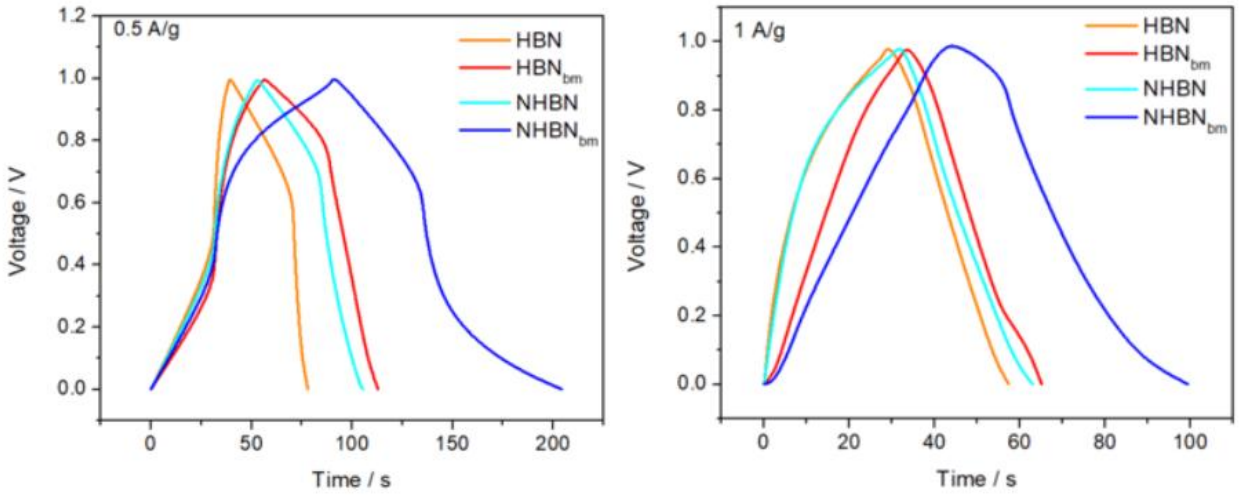

Figure 53: GCPL plot of unmilled and ball-milled h-BN samples at 0.5 A/g (left) and 1 A/g (right) current densities

All samples exhibit noticeable deviations from the ideal symmetric triangular shape typically associated with EDLCs. This non-linear behavior reflects the strong pseudocapacitive contribution arising from faradaic redox processes occurring at the electrode-electrolyte interface. These findings are in agreement with the previously discussed Dunn analysis, which confirmed a dominant pseudocapacitive mechanism in these materials. The deviation from ideal GCD behavior is especially pronounced at the lower current density of 0.5 A/g. This is expected, as lower current densities allow more time for ion diffusion and charge transfer, enabling faradaic reactions to proceed more thoroughly. Among all tested configurations, $NHBN_{bm}$ sample exhibited the longest discharge time, followed by HBN_{bm}, indicating enhanced specific capacitance after mechanical treatment. These results highlight the positive impact of ball milling, which likely increased the number of electrochemically active sites and improved ion transport pathways by introducing structural defects and reducing particle size. It is important to note, however, that specific capacitance values obtained from GCPL measurements can sometimes underestimate the total charge storage capability in defect-rich materials where pseudocapacitive processes dominate. This is

because GCD analysis primarily reflects the contribution from EDLC, while CV, especially when analyzed using the Dunn method, provides a more comprehensive evaluation of both capacitive and diffusion-controlled mechanisms. Figure 54 presents the cycling stability performance of the samples over 5000 continuous charge–discharge cycles.

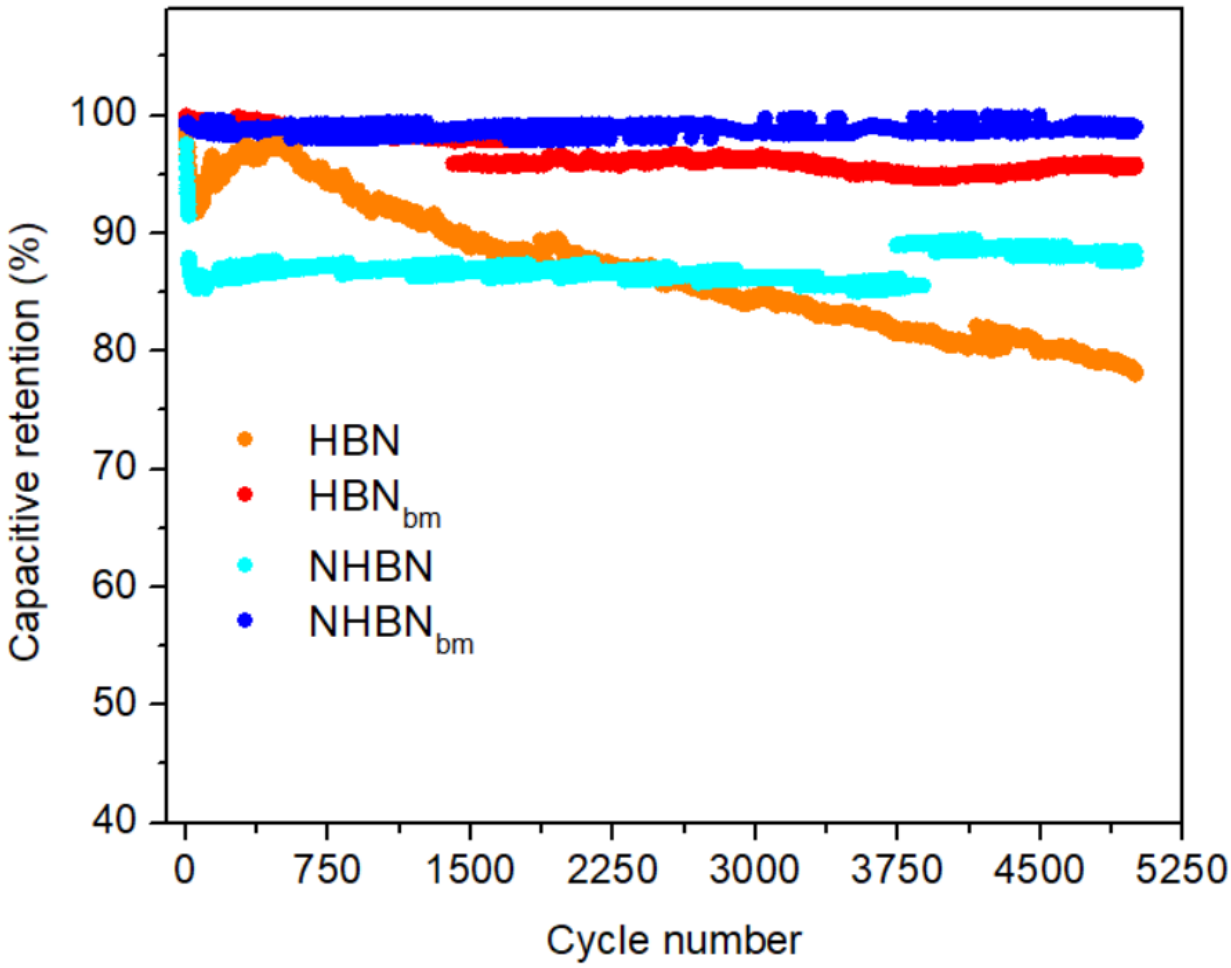

Figure 54: Capacitive retention of unmilled and ball-milled h-BN samples as a function of the cycle number, displaying the cycling stability of the samples

A significant improvement in capacitance retention is observed for the ball-milled samples, with both NHBNbm and HBNbm maintaining over 95% of their initial capacitance values. This remarkable stability can be attributed to several factors, including enhanced electrode–electrolyte contact due to the reduced particle size, improved ion diffusion kinetics, and the introduction of structural disorder that increases accessible active sites without compromising material integrity. These findings collectively demonstrate that ball milling

serves as an effective post-synthesis modification technique for improving both the capacitance and the long-term cycling durability of h-BN-based supercapacitor electrodes.

Figure 55 presents GCPL profiles of the undoped and Mn-doped ZnO samples synthesized at varying microwave powers. Among these, the ZnO:Mn_2 samples generally exhibit a more defined and symmetric triangular GCPL shape, indicative of efficient charge storage and superior charge transfer kinetics within the device. The geometry of the GCD curves provides critical insight into the dominant energy storage mechanism, correlating well with the Dunn analysis results discussed previously.

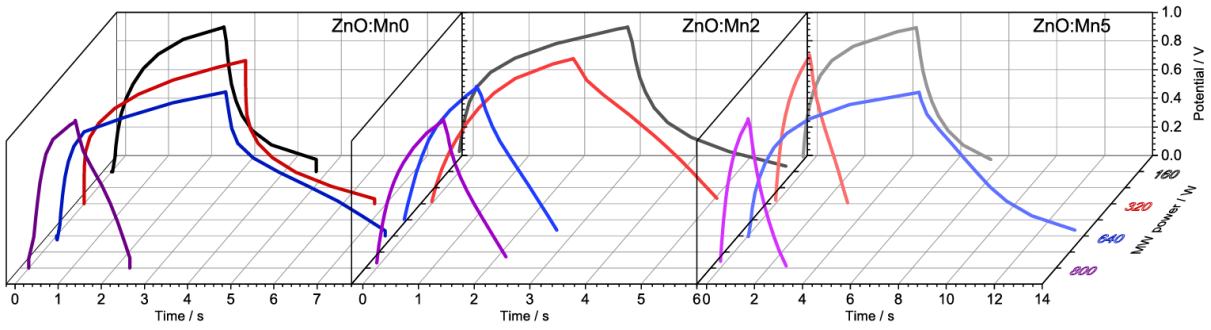

Figure 55: GCPL profiles of Mn doped ZnO samples synthesized at different microwave powers taken at 0.5 A/g current density

Notably, slight deviations from the ideal triangular shape manifesting as semi-triangular curves are observed in the ZnO:Mn_2 samples @ 160 W and 320 W. This behavior suggests a greater contribution from diffusion-controlled pseudocapacitive processes, driven by faradaic redox reactions, in addition to the conventional EDLC mechanism. This increased diffusion-controlled behavior appears to positively impact overall device performance, as reflected by the higher specific capacitance observed in the ZnO:Mn_2 @160 W samples. Beyond the GCD profiles, the long-term cycling stability of the supercapacitor devices was assessed over 5000 continuous charge–discharge cycles. The results, shown in Figure 56.

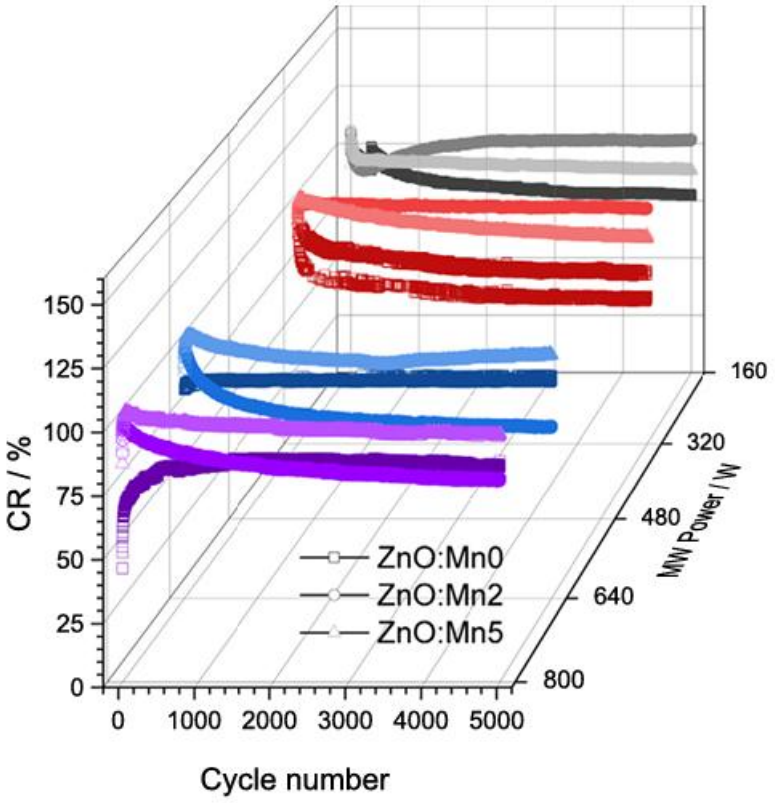

Figure 56: Capacitive retention of Mn-doped ZnO samples synthesized at different microwave powers, showing the cycling stability of the samples

While all samples maintained a reasonable level of stability, with capacitance retention exceeding 70%, a distinct trend emerged in relation to Mn doping levels and synthesis power. Specifically, the ZnO:Mn_2 samples demonstrated enhanced stability at lower microwave powers (160 W and 320 W), whereas the ZnO:Mn_5 samples exhibited improved retention at higher synthesis powers (640 W and 800 W). This behavior is likely linked to the influence of Mn dopant concentration on the structural and morphological evolution of the ZnO nanostructures. At lower doping levels and synthesis powers, Mn incorporation appears to promote the formation of structurally stable nanorod morphologies, while higher doping levels may necessitate elevated energy input during synthesis to achieve microstructures (such as nanoflowers) with improved mechanical and electrochemical stability (Jangu et al. 2023). Although the ~70% retention observed in this study may appear modest when

compared to certain literature reports, it is important to highlight that these ZnO-based electrodes were synthesized via a low-temperature, scalable microwave-assisted hydrothermal process without the use of conductive additives or carbon-based supports. Such simplified, binder-free architectures, while offering processing advantages and structural simplicity, often exhibit lower cycling durability compared to composite or carbon-enhanced systems. Comparable retention values have been reported in similar systems, such as the 68% retention after 5000 cycles reported by Hassan *et al.* (Hassan, Hossain, and Sahajwalla 2022).

Figure 57 presents the GCPL profiles of Mn-doped h-BN samples subjected to different annealing temperatures, alongside Mn:ZnO-hBN composite samples with varying ZnO-to-h-BN weight ratios.

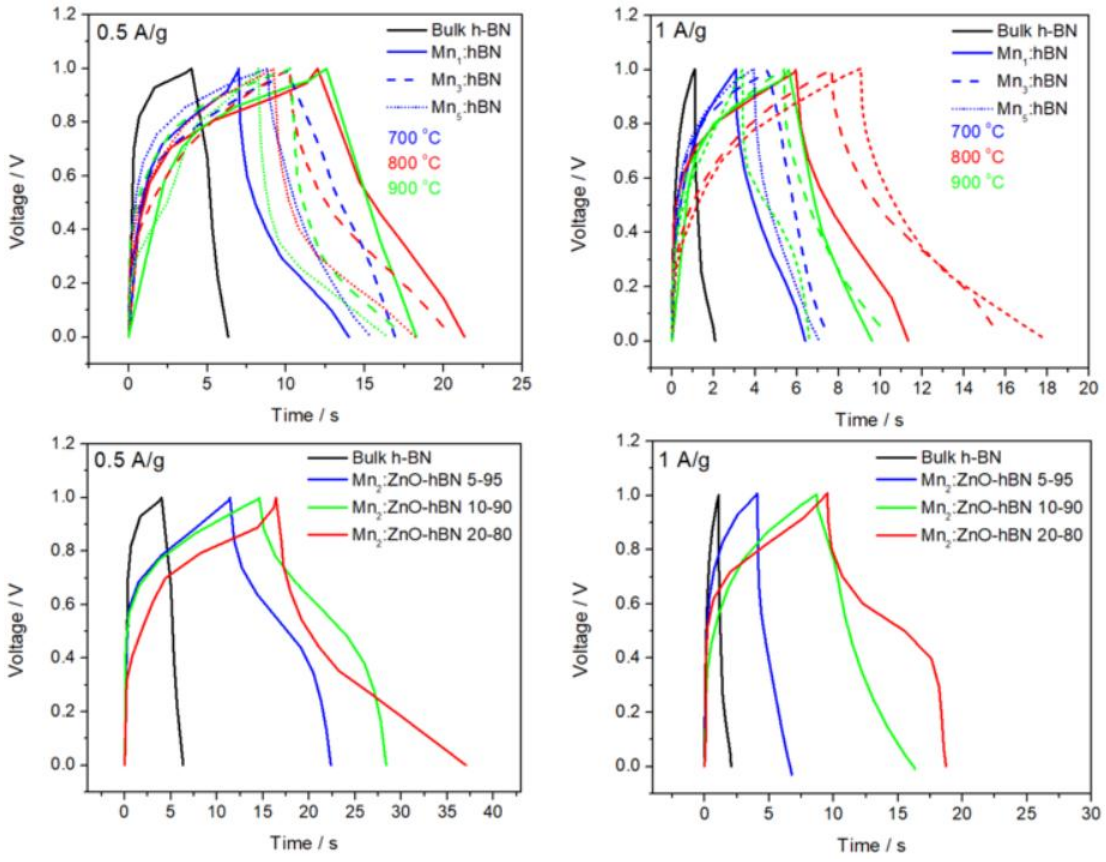

Figure 57: GCPL plots of Mn-doped h-BN samples heat-treated at different temperatures (top), and Mn:ZnO-hBN nanocomposites with different ZnO to h-BN concentrations (bottom), taken at 0.5 and 1 A/g current densities

Among the Mn-doped h-BN samples, those annealed at 800 °C exhibit noticeably superior electrochemical performance, as evidenced by longer discharge times. This enhancement is particularly pronounced in samples doped with 3 wt% Mn. The improved performance at this temperature can be attributed to more effective Mn incorporation into the h-BN lattice, which optimizes the electronic and structural properties. In contrast, samples treated at 700 °C likely suffer from incomplete Mn integration, limiting their structural and electrochemical enhancements. On the other hand, samples annealed at 900 °C show reduced performance, which is attributed to the development of microstrains and possible defect clustering induced by excessive thermal stress. Regarding the doping concentration, the 3 wt% Mn samples appear to offer an optimal balance: they introduce sufficient Mn to induce beneficial structural modifications in h-BN without reaching the oversaturation effects observed in the 5 wt% Mn samples, where excessive doping may disrupt structural integrity and impede ion diffusion pathways.

Figure 58 and Appendix 18 illustrate the capacitive retention of both Mn-doped h-BN samples and Mn:ZnO-hBN nanocomposites over extended charge-discharge cycles. Both material systems demonstrate significantly improved stability compared to their undoped bulk h-BN counterparts. This enhancement can be primarily attributed to the synergistic effect of Mn doping and ZnO incorporation, both of which contribute to increased defect density, improved conductivity, and enhanced structural stability within the electrode material.

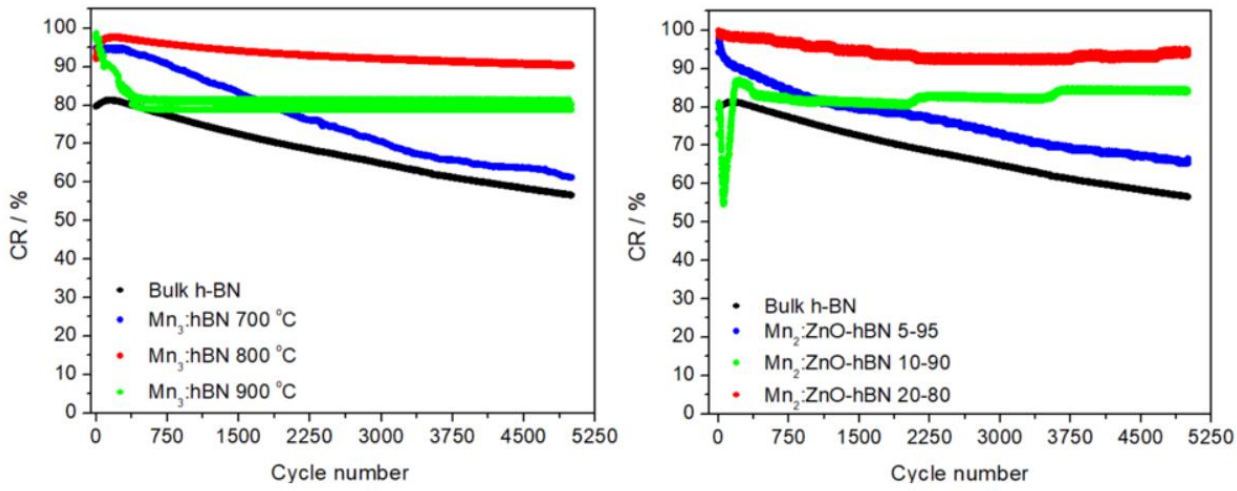

Figure 58: Capacitive retention of Mn_3:h-BN (left), and Mn:ZnO-hBN nanocomposites (right) showing the cycling stability of the samples

For the Mn-doped h-BN samples, the improved retention is largely due to the role of Mn ions in modulating the electronic structure of h-BN, introducing defect sites that facilitate more efficient charge storage and transfer during repeated cycling. The optimal performance observed at specific Mn concentrations aligns with the results from the GCPL analysis, further reinforcing the importance of controlled doping levels. In the case of the Mn:ZnO-hBN nanocomposites, the increase in ZnO-to-h-BN ratio appears to have a positive correlation with capacitive retention. This improvement is likely due to several factors. First, the presence of ZnO nanostructures enhances the overall electrical conductivity of the composite, which mitigates R_s build-up during prolonged cycling. Second, ZnO provides additional active sites for charge storage, contributing to improved electrochemical reversibility. Third, the ZnO nanostructures may act as a mechanical buffer, minimizing the structural degradation of the h-BN framework under repetitive ion intercalation and deintercalation processes. Furthermore, the hierarchical architecture formed in higher ZnO content samples likely promotes better electrode–electrolyte interface contact, facilitating more efficient ion transport. However, it is important to note that beyond an optimal concentration, excessive ZnO content could potentially lead to reduced performance due to increased diffusion path lengths or aggregation effects. Nevertheless, within the investigated concentration range, the trend shows that increasing the ZnO content enhances the long-term electrochemical stability of the supercapacitor devices. Overall, these results demonstrate the critical role of both Mn doping and ZnO hybridization in improving the cyclic durability and

stability of h-BN-based supercapacitors, offering promising pathways for the development of next-generation, high-performance energy storage devices.

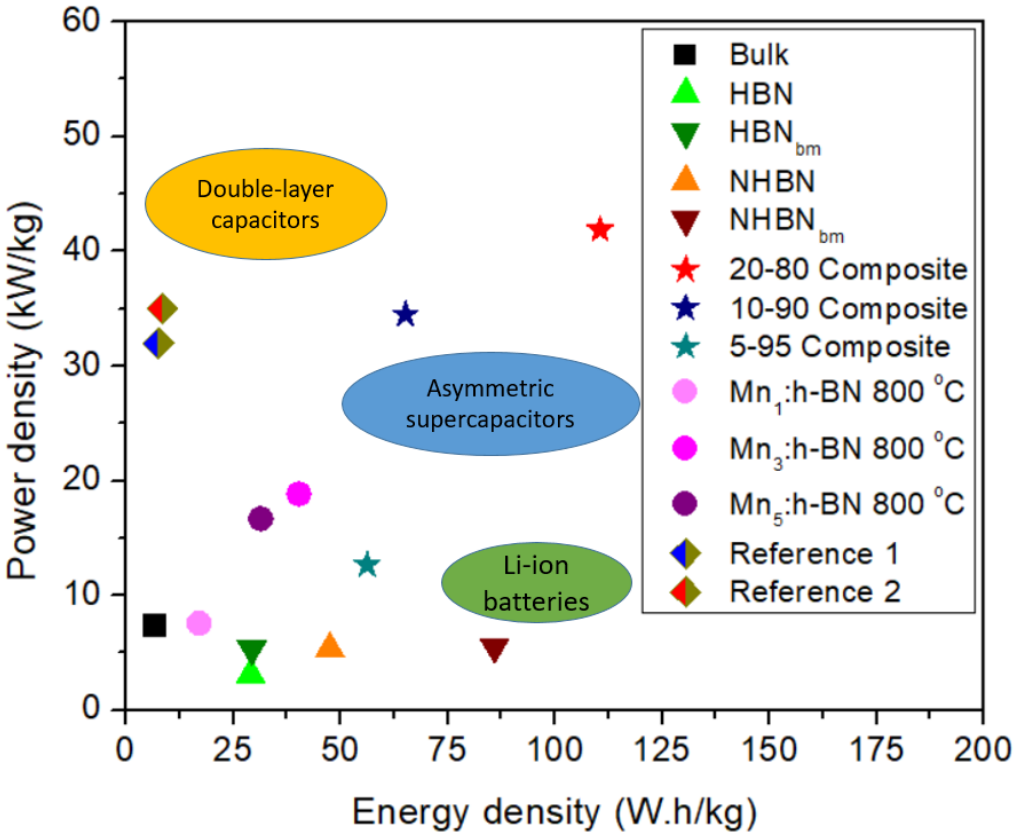

Figure 59: Ragone plot summarizing the overall performance of energy density and power density of bulk h-BN, ball milled h-BN, Mn-doped h-BN, and Mn:ZnO-hBN nanocomposites, comparing them to similar materials systems from literature that combined h-BN with rGO (Reference 1), and h-BN with WS_2 composites (Reference 2) (Krishnamoorthy and Singh 2025, Althubaiti et al. 2022)

Figure 59 presents a comprehensive Ragone plot summarizing the energy density and power density performance of various supercapacitor systems developed and discussed throughout this thesis. The evaluated systems include pristine bulk h-BN, ball-milled h-BN, Mn-doped h-BN, and Mn:ZnO–hBN nanocomposites. For benchmarking purposes, two reference systems utilizing h-BN in combination with reduced graphene oxide (rGO), and with WS_2 composites (References 1 and 2) are also included to highlight the comparative advantages of composite designs (Krishnamoorthy and Singh 2025, Althubaiti et al. 2022). The energy

density and power density were calculated by using the relation illustrated in Equations (11) and (12):

$$E_D = \frac{1}{2} C V^2 \qquad (11)$$

$$P_D = \frac{E_D}{t} \qquad (12)$$

Where E_D is the energy density in W.h/kg, P_D is the power density in kW/kg, C is the specific capacitance in F/g, V is the voltage in V, and t is the discharge time in s.

Among all the studied materials, bulk h-BN exhibited the lowest energy and power density values, registering approximately 9 Wh/kg and 7 kW/kg, respectively. These values are expected given the inherently low electrical conductivity and limited electrochemical activity of pristine h-BN. Upon applying a ball milling process, a modest reduction in power density was observed, dropping to around 5 kW/kg. This decrease is likely due to structural disruptions and increased R_s introduced by mechanical deformation. However, the energy density improved significantly, reaching up to 85 Wh/kg. This enhancement can be attributed to the introduction of structural defects and increased surface area, which facilitated greater ion accessibility and improved charge storage capability. These values approach the lower range of typical lithium-ion batteries, indicating a notable improvement for a non-carbon-based dielectric material. Mn-doped h-BN samples demonstrated further enhancement, with energy density values reaching 48 Wh/kg and power density increasing to 18 kW/kg. The presence of Mn dopants introduced redox-active centers into the h-BN framework, promoting pseudocapacitive behavior and enabling more efficient faradaic charge storage. Although a substantial improvement over the undoped and ball-milled samples, the performance of Mn-doped h-BN remains inferior to that of h-BN/carbon composites. These carbon-rich systems—such as h-BN/rGO composites—typically exhibit exceptionally high power densities due to their large specific surface area and conductive pathways, which favor fast ion transport and efficient double-layer charge storage. However, they generally lack the contribution from redox mechanisms, resulting in limited energy density. Moreover, such systems underutilize the chemical stability and faradaic potential of h-BN. In contrast, the Mn:ZnO–hBN nanocomposite samples developed in this work displayed the highest overall performance, achieving energy densities up to 110 Wh/kg and power densities as high as

40 kW/kg. This superior performance can be attributed to the synergistic integration of Mn-doped ZnO nanostructures with the defect-engineered h-BN matrix. The ZnO component contributes abundant pseudocapacitive activity through reversible faradaic reactions involving the Mn^{2+}/Mn^{3+} and Zn^{2+}/Zn^{0} redox couples, while the h-BN framework offers mechanical robustness, chemical stability, and enhanced ion diffusion pathways due to its defect-rich morphology. Furthermore, the composite design effectively balances fast charge–discharge capability with deep charge storage, resulting in excellent performance across both energy and power domains. The inclusion of Mn not only boosts redox activity but also induces oxygen vacancies in ZnO, improving electronic conductivity and facilitating efficient charge transfer. The microwave-assisted hydrothermal synthesis method used here ensures uniform dispersion of active components and scalable fabrication, further supporting the practical viability of the developed nanocomposites.

Overall, the Mn:ZnO–hBN system represents a significant advancement in the development of high-performance, binder-free electrode materials. It surpasses the performance of conventional h-BN and even h-BN/carbon composites by leveraging both EDLC and pseudocapacitive mechanisms, offering an ideal platform for next-generation energy storage devices that demand both high power and high energy density.

4.5. Electrochemical Enhancement through Mn Doping and Composite Integration

This chapter has comprehensively evaluated the electrochemical performance of various h-BN based systems, including pristine, ball-milled, Mn-doped h-BN, and Mn:ZnO–hBN nanocomposites, with a focus on their application as electrode materials for supercapacitor devices. Through a multi-faceted investigation involving CV, GCD, EIS, and Dunn method analysis, the interplay between defect engineering, dopant incorporation, and structural optimization has been systematically unraveled.

Pristine h-BN, while chemically stable, demonstrated limited electrochemical activity due to its inherently insulating nature. Ball milling introduced structural disorder and defect sites, modestly improving its capacitance and enabling pseudocapacitive behavior. Mn doping significantly enhanced redox activity by creating electrochemically active sites such as nitrogen vacancies and substitutional defects, which facilitated faradaic reactions and improved charge transport properties. Notably, optimal doping conditions, both in terms of concentration and annealing temperature, were shown to be critical for maximizing performance without compromising structural integrity. The most remarkable advancements were achieved with the development of Mn:ZnO–hBN nanocomposites. These hybrid materials synergistically combined the pseudocapacitive redox activity of Mn-doped ZnO with the chemical stability and ion diffusion pathways of defect-engineered h-BN. This integration resulted in the highest recorded energy and power densities in this study (110 Wh/kg and 40 kW/kg, respectively) demonstrating superior performance even in comparison to reference carbon-based h-BN composites. The enhanced electrochemical behavior was further supported by excellent cycling stability, confirming the robustness and reversibility of the charge storage mechanisms. The Ragone plot provided a holistic comparison of the energy and power capabilities of each system and confirmed that the Mn:ZnO–hBN nanocomposites successfully bridge the gap between high energy and high power requirements, an area where many traditional supercapacitor systems fall short. Importantly, these results were achieved without the use of conductive additives or carbon-based supports, highlighting the potential of these materials for lightweight, scalable, and environmentally benign energy storage applications.

In conclusion, this work demonstrates that the strategic integration of transition metal doping and nanostructured composite design within the h-BN framework offers a powerful route for the development of next-generation supercapacitor electrodes. The insights gained from this study not only advance the understanding of defect-mediated charge storage in dielectric materials but also open new avenues for the rational design of multifunctional electrode architectures that meet the growing demands for high-performance, sustainable energy storage technologies.

5. CONCLUSIONS AND FUTURE OUTLOOKS

This dissertation has introduced a novel defect and composition-driven materials design strategy that transforms isulating h-BN into a high-performance electrode candidate for supercapacitor devices. By leveraging systematic structural defect engineering, Mn doping, and composite integration with Mn-doped ZnO, this work addresses a critical limitation in the field: the electrochemical inactivity of pristine h-BN.

The systematic EPR investigation across all studied systems revealed a distinct evolution in defect chemistry. In the case of h-BN, the dominant intrinsic defects are V_N, which are clearly identified by a ten-line hyperfine structure in the EPR spectrum, consistent with coupling to nearby boron nuclei. These V_N centers emerge most prominently after thermal activation, reflecting their paramagnetic nature and crucial role in enhancing electrochemical activity. In contrast, a separate sharp signal at g = 2.004 was attributed to carbon-related impurities, most likely substitutional carbon atoms, introduced during synthesis or processing. For undoped ZnO, the dominant paramagnetic species is the singly ionized oxygen vacancy V_O^+, detected as a broad resonance centered around g = 1.96, characteristic of ZnO nanostructures with high surface area. Upon Mn doping, the ZnO defect profile shifts significantly: Mn^{2+} ions substitute for Zn^{2+}, giving rise to a well-resolved six-line hyperfine structure centered at g = 2.00. This confirms successful incorporation of isolated Mn^{2+} ions, and the suppression or modification of oxygen-related defects. In the Mn:ZnO-hBN nanocomposites, EPR results reveal a coexistence of both nitrogen vacancy signals from h-BN and Mn^{2+} hyperfine structures from ZnO, indicating that both types of paramagnetic defects are retained. The spectra also show some line broadening and slight g-shifts, suggesting possible electronic

interactions across the ZnO/h-BN interface. This combination of defects enhances redox activity and charge storage by creating a hybrid network of active sites.

The primary contribution of this thesis lies in developing a comprehensive defect model for h-BN, highlighting the synergistic role of both intrinsic (V_N, V_B) and extrinsic (carbon substitution, Mn^{2+} doping) defect centers. The model is substantiated through advanced spectroscopic techniques, especially Q- and X-band EPR which confirmed the formation of paramagnetic nitrogen vacancies and substitutional Mn^{2+} incorporation, evidenced by well-resolved sextet hyperfine structures under optimized annealing conditions. In terms of structural modification, the work demonstrates that high-energy ball milling and annealing at 800 °C can reproducibly tune crystallite size, defect density, and phase purity. Notably, ball-milled, nitrogen-deficient h-BN ($NHBN_{bm}$) achieved a 3-fold improvement in specific capacitance (~615 F/g at 10 mV/s), revealing the role of V_N in enhancing pseudocapacitive behavior. Mn doping of h-BN further enabled the introduction of redox-active sites and bandgap narrowing (from 5.85 eV to ~4.2 eV), verified by Tauc analysis. These modifications led to a further boost in performance, with Mn-doped h-BN achieving ~566 F/g specific capacitance at 1 A/g, and >92% retention over 5,000 cycles, validating its electrochemical reversibility and robustness. A significant advancement was achieved through the synthesis of Mn:ZnO–hBN nanocomposites, which combined the faradaic redox activity of ZnO:Mn with the ion-accessible architecture of h-BN. These nanocomposites delivered the highest performance metrics in this study—~795 F/g specific capacitance, 110 Wh/kg energy density, and 41.8 kW/kg power density—all obtained without any carbon-based conductive additives. The hybrid material also exhibited excellent cycling stability (>90% after 5000 cycles), confirmed by impedance analysis and Ragone plotting.

Chapter 1 established a foundational understanding of how intrinsic point defects, such as nitrogen and boron vacancies, antisites, and interstitials, as well as extrinsic defects like carbon impurities and Mn dopants, affect the structural and electronic properties of h-BN. Using XRD, EPR, PL, and Raman analyses, it was shown that controlled thermal annealing and high-energy ball milling generate defect-rich h-BN with enhanced surface activity and localized electronic states. Furthermore, the successful substitution of Mn^{2+} ions into the h-

BN lattice, as confirmed by EPR hyperfine splitting, added significant redox functionality to the material.

Chapter 2 investigated the synthesis and characterization of Mn-doped ZnO nanorods using a microwave-assisted hydrothermal method. The study revealed that microwave power and Mn concentration jointly govern crystal growth, surface area, and defect density. The introduction of Mn into ZnO was shown to improve charge transport and defect-mediated pseudocapacitance, making ZnO:Mn a promising component for composite systems.

Chapter 3 extended the defect-engineering approach by combining ZnO:Mn with h-BN to produce Mn:ZnO–hBN nanocomposites. The structural, optical, and electronic characterizations revealed synergistic interactions between the two materials. The presence of h-BN provided a robust and high-surface-area matrix, while the ZnO:Mn phase contributed redox-active sites and improved conductivity. These effects were further supported by narrowing of the bandgap and enhancement in PL emission profiles.

Chapter 4 evaluated the electrochemical performance of all material systems using CV, GCPL, and EIS in symmetric two-electrode configurations. The results confirmed a stepwise improvement in specific capacitance, energy density, and stability.

Looking forward, this research opens several pathways for further development:

Atomic-level control of defect configurations via plasma treatment, or ion implantation could enable precise tailoring of electronic and electrochemical properties. In situ/operando characterization (e.g., operando EPR, synchrotron XRD) may provide real-time insights into the dynamics of charge storage and defect evolution under operational conditions. Hybrid systems integrating h-BN-based materials with 2D conductors like graphene, MXenes, or CNTs may lead to next-generation electrodes with unprecedented energy and power densities. Scalability and device integration, including flexible substrates or microsupercapacitor architectures, could bridge the gap between lab-scale materials and real-world applications. Computational modeling and machine learning can be employed to predict optimal defect types and dopant configurations for targeted performance metrics.

In conclusion, this thesis provides a robust materials design framework that combines structural defect engineering, transition metal doping, and composite formation to enhance

the electrochemical utility of h-BN. These findings contribute both to the fundamental understanding of defect chemistry in 2D materials and to the development of practical, high-performance energy storage devices.

6. BIBLIOGRAPHY

2006a. "Basic Principles of Paramagnetic Resonance." In *Electron Paramagnetic Resonance*, 1-35.

2006b. "Hyperfine (A) Anisotropy." In *Electron Paramagnetic Resonance*, 118-157.

2006c. "Isotropic Hyperfine Effects in EPR Spectra." In *Electron Paramagnetic Resonance*, 58-84.

2006d. "Magnetic Interaction between Particles." In *Electron Paramagnetic Resonance*, 36-57.

2006e. "Zeeman Energy (g) Anisotropy." In *Electron Paramagnetic Resonance*, 85-117.

Abdollahi, Yadollah, Abdul Abdullah, Zulkarnain Zainal, and Nor Yusof. 2011. "Synthesis and Characterization of Manganese Doped ZnO Nanoparticles." *Int. J. Basic Appl. Sci.* 11.

Ahmad, Mukhtar, Ejaz Ahmed, Waqar Ahmed, Abdelbary Elhissi, Z. L. Hong, and N. R. Khalid. 2014. "Enhancing visible light responsive photocatalytic activity by decorating Mn-doped ZnO nanoparticles on Graphene." *Ceramics International* 40:100087-10095. doi: 10.1016/j.ceramint.2014.03.184.

Ahmed, Aamir, Anoop Chib, and Sandeep Arya. 2025. "High performance Mn doped ZnO loaded rGO electrode and its practical application as an electrode for self-charging supercapacitor device." *Journal of Energy Storage* 105:114783. doi: 10.1016/j.est.2024.114783.

Ahmed, Aamir, Anoop Singh, and Sandeep Arya. 2025. "High performance Mn doped ZnO loaded rGO electrode and its practical application as an electrode for self-charging supercapacitor device." *Journal of Energy Storage* 105:114783. doi: https://doi.org/10.1016/j.est.2024.114783.

Alaş, Melis Ö, Ahmet Güngör, Rükan Genç, and Emre Erdem. 2019. "Feeling the power: robust supercapacitors from nanostructured conductive polymers fostered with Mn2+ and carbon dots." *Nanoscale* 11 (27):12804-12816. doi: 10.1039/C9NR03544C.

Alegaonkar, Ashwini P., Prashant S. Alegaonkar, and Satish K. Pardeshi. 2020. "Electrochemical performance of a self-assembled two-dimensional heterostructure of rGO/MoS2/h-BN." *Nanoscale Advances* 2 (4):1531-1541. doi: 10.1039/D0NA00021C.

Aleinawi, Mohamad Hasan, Ameen Uddin Ammar, Merve Buldu-Akturk, Nur Selin Turhan, Shankari Nadupalli, and Emre Erdem. 2022. "Spectroscopic Probing Of Mn-Doped ZnO Nanowires Synthesized via a Microwave-Assisted Route." *The Journal of Physical Chemistry C* 126 (8):4229-4240. doi: 10.1021/acs.jpcc.2c00009.

Aleinawi, Mohamad Hasan, Ameen Uddin Ammar, Duygu Şentürk, Lucian Barbu-Tudoran, Oluwatosin Johnson Ajala, Defne Eşkin, Feray Bakan Misirlioglu, Arpad Mihai Rostas, and Emre Erdem. 2025. "Microwave-tuned Mn-doped ZnO for all-in-one supercapacitors: Correlating defect chemistry with electrochemical behavior." *Journal of Colloid and Interface Science* 698:138012. doi: https://doi.org/10.1016/j.jcis.2025.138012.

Aleinawi, Mohamad Hasan, Eminenur Saritas, Maria Stefan, Ameen Uddin Ammar, Abdalla Hroub, Feray Bakan Misirlioglu, Amelia Bocirnea, Sergiu Macavei, Septimiu Tripon, Emre

Erdem, and Rostas Arpad Mihai. 2025. "Supercapacitor devices based on multiphase MgTiO3 perovskites doped with Mn2+ ions." *Materials Chemistry and Physics* 329:130016. doi: https://doi.org/10.1016/j.matchemphys.2024.130016.

Altaf, Cigdem Tuc, Tuluhan Olcayto Colak, Arpad Mihai Rostas, Crina Socaci, Mihaela Diana Lazar, Lucian Barbu Tudoran, Mohamad Hasan Aleinawi, Feray Bakan Misirlioglu, Ipek Deniz Yildirim, Emre Erdem, Nurdan Demirci Sankir, and Mehmet Sankir. 2024. "Zinc oxide nanoflake/reduced graphene oxide nanocomposite-based dual-acting electrodes for solar-assisted supercapacitor applications††Electronic supplementary information (ESI) available. See DOI: https://doi.org/10.1039/d4ya00253a." *Energy Advances* 3 (8):1965-1976. doi: https://doi.org/10.1039/d4ya00253a.

Altaf, Cigdem Tuc, Ozlem Coskun, Alihan Kumtepe, Arpad Mihai Rostas, Igor Iatsunskyi, Emerson Coy, Emre Erdem, Mehmet Sankir, and Nurdan Demirci Sankir. 2022. "Photo-supercapacitors based on nanoscaled ZnO." *Scientific Reports* 12 (1):11487. doi: 10.1038/s41598-022-15180-z.

Althubaiti, Nada, Yasmin Mussa, Bongu Chandra Sekhar, Zahra Bayhan, Muhammad Arsalan, Abdel Rahman Soliman, and Edreese Alsharaeh. 2022. "Reduced graphene oxide/hexagonal boron nitride-based composite as a positive electrode in asymmetric supercapacitors." *Journal of Materials Science* 57:1-15. doi: 10.1007/s10853-022-07525-w.

Amirkhanlou, Sajjad, Mostafa Ketabchi, and Nader Parvin. 2012. "Nanocrystalline/nanoparticle ZnO synthesized by high energy ball milling process." *Materials Letters* 86:122-124. doi: https://doi.org/10.1016/j.matlet.2012.07.041.

Ammar, Ameen Uddin, Mohamad Hasan Aleinawi, Maria Stefan, Ahmet Gungor, Adriana Popa, Dana Toloman, Karlo Maškarić, Eminenur Saritas, Lucian Barbu-Tudoran, Sergiu Macavei, Marin Senila, Emre Erdem, and Arpad Mihai Rostas. 2025. "Lithium-induced defect centers in nanorod-shaped zinc oxide for supercapacitor applications." *Electrochimica Acta* 519:145806. doi: https://doi.org/10.1016/j.electacta.2025.145806.

Ammar, Ameen Uddin, Feray Bakan-Misirlioglu, Mohamad Hasan Aleinawi, Giorgia Franzo, Guglielmo Guido Condorelli, Fatma Nur Tuzluca Yesilbag, Yasar Ozkan Yesilbag, Salvo Mirabella, and Emre Erdem. 2023. "All-in-one supercapacitors with high performance enabled by Mn/Cu doped ZnO and MXene." *Materials Research Bulletin* 165:112334. doi: https://doi.org/10.1016/j.materresbull.2023.112334.

Ammar, Ameen Uddin, Manuela Stan, Adriana Popa, Dana Toloman, Sergiu Macavei, Cristian Leostean, Alexandra Ciorita, Emre Erdem, and Arpad Mihai Rostas. 2023. "All-in-one supercapacitor devices based on nanosized Mn4+-doped WO3." *Journal of Energy Storage* 72:108599. doi: https://doi.org/10.1016/j.est.2023.108599.

Ammar, Ameen Uddin, Ipek Deniz Yildirim, Mohamad Hasan Aleinawi, Merve Buldu-Akturk, Nur Selin Turhan, Shankari Nadupalli, Arpad Mihai Rostas, and Emre Erdem. 2023. "Multifrequency EPR spectroscopy study of Mn, Fe, and Cu doped nanocrystalline ZnO." *Materials Research Bulletin* 160:112117. doi: https://doi.org/10.1016/j.materresbull.2022.112117.

Ammar, Ameen Uddin, Ipek Deniz Yildirim, Feray Bakan, and Emre Erdem. 2021. "ZnO and MXenes as electrode materials for supercapacitor devices." *Beilstein Journal of Nanotechnology* 12:49-57. doi: https://doi.org/10.3762/bjnano.12.4.

Ankiewicz, Amélia, Wolfgang Gehlhoff, Joana Martins, Angela Pereira, Sergio Pereira, Axel Hoffmann, E. Kaidashev, Andreas Rahm, Michael Lorenz, Marius Grundmann, Maria Carmo, Tito Trindade, and Nikolai Sobolev. 2009. "Magnetic and structural properties of transition metal doped zinc-oxide nanostructures." *physica status solidi (b)* 246:766-770. doi: 10.1002/pssb.200880581.

Arenal, R., A. C. Ferrari, S. Reich, L. Wirtz, J. Y. Mevellec, S. Lefrant, A. Rubio, and A. Loiseau. 2006. "Raman Spectroscopy of Single-Wall Boron Nitride Nanotubes." *Nano Letters* 6 (8):1812-1816. doi: 10.1021/nl0602544.

Arya, Sandeep, Prerna Mahajan, Sarika Mahajan, Ajit Khosla, Ram Datt, Vinay Gupta, Sheng-Joue Young, and Sai Oruganti. 2021. "Review—Influence of Processing Parameters to Control Morphology and Optical Properties of Sol-Gel Synthesized ZnO Nanoparticles." *ECS Journal of Solid State Science and Technology* 10. doi: 10.1149/2162-8777/abe095.

Attaccalite, C., M. Bockstedte, A. Marini, A. Rubio, and L. Wirtz. 2011. "Coupling of excitons and defect states in boron-nitride nanostructures." *Physical Review B* 83 (14):144115. doi: 10.1103/PhysRevB.83.144115.

Azevedo, S., J. Kaschny, Caio de Castilho, and F. Mota. 2009. "Electronic structure of defects in a boron nitride monolayer." *The European Physical Journal B* 67:507-512. doi: 10.1140/epjb/e2009-00043-5.

Babar, Rohit, Ádám Ganyecz, Igor A. Abrikosov, Gergely Barcza, and Viktor Ivády. 2025. "Carbon-contaminated topological defects in hexagonal boron nitride for quantum photonics." *npj 2D Materials and Applications* 9 (1):33. doi: 10.1038/s41699-025-00559-z.

Babunts, Roman A., Yulia A. Uspenskaya, Nikolai G. Romanov, Sergei B. Orlinskii, Georgy V. Mamin, Elena V. Shornikova, Dmitri R. Yakovlev, Manfred Bayer, Furkan Isik, Sushant Shendre, Savas Delikanli, Hilmi Volkan Demir, and Pavel G. Baranov. 2023. "High-Frequency EPR and ENDOR Spectroscopy of Mn2+ Ions in CdSe/CdMnS Nanoplatelets." *ACS Nano* 17 (5):4474-4482. doi: 10.1021/acsnano.2c10123.

Baby, Bindhu, Murali Adhigan, Ramesh Redrouthu, Abdullah Al, and Sung Soo Han. 2025. "High-Performance Boron Nitride/Graphene Oxide Composites Modified with Sodium Thiosulfate for Energy Storage Applications." *Nanoscale Advances* 7. doi: 10.1039/D4NA00937A.

Behzad, Somayeh, and Raad Chegel. 2024. "Tunability of electronic and thermoelectric properties of hexagonal boron nitride with carbon impurities under magnetic field: Tight binding investigation." *Journal of Molecular Graphics and Modelling* 127:108679. doi: https://doi.org/10.1016/j.jmgm.2023.108679.

Ben Gouider Trabelsi, Amira, Ramzi Nasser, Fatemah Alkallas, Abeer Saqr, B. El-Gammal, Ji-Ming Song, and Habib Elhouichet. 2024. "Corrigendum to “Tuning the electrochemical properties of ZnO through chromium doping and its suitability for supercapacitor application” [J. Energy Storage 87 (2024) 111487]." *Journal of Energy Storage* 91:111962. doi: 10.1016/j.est.2024.111962.

Berzina, Baiba, Valdis Korsaks, Laima Trinkler, Anatolijs Sarakovskis, Jurgis Grube, and Stefano Bellucci. 2016. "Defect-induced blue luminescence of hexagonal boron nitride." *Diamond and Related Materials* 68. doi: 10.1016/j.diamond.2016.06.010.

Betsch, Regis J., Hong Lee Park, and William B. White. 1991. "Raman spectra of stoichiometric and defect rutile." *Materials Research Bulletin* 26 (7):613-622. doi: https://doi.org/10.1016/0025-5408(91)90104-T.

Bhojane, Prateek. 2022. "Recent advances and fundamentals of Pseudocapacitors: Materials, mechanism, and its understanding." *Journal of Energy Storage* 45:103654. doi: https://doi.org/10.1016/j.est.2021.103654.

Biswas, Bharati, Moushumi Purkayastha, Ekta Tiwari, Shanku Denrah, Mitali Sarkar, Gopala Darbha, and Tapas Pal Majumder. 2020. "Study of the photocatalytic activity of Mn-doped ZnO nanocomposites depending on their morphology and structure with the variation of manganese concentration." *Surfaces and Interfaces* 23:100902. doi: 10.1016/j.surfin.2020.100902.

Bongu, C. S., M. Arsalan, and E. H. Alsharaeh. 2024. "2D Hybrid Nanocomposite Materials (h-BN/G/MoS(2)) as a High-Performance Supercapacitor Electrode." *ACS Omega* 9 (13):15294-15303. doi: 10.1021/acsomega.3c09877.

Bououdina, M., K. Omri, M. El-Hilo, Abdelfattah El Amiri, O. M. Lemine, A. Alyamani, Hassan Lassri, and El Mir Lassaad. 2014. "Structural and magnetic properties of Mn-doped ZnO nanocrystals." *Physica E: Low-dimensional Systems and Nanostructures* 56:107–112. doi: 10.1016/j.physe.2013.08.024.

Cassabois, G., P. Valvin, and B. Gil. 2016. "Hexagonal boron nitride is an indirect bandgap semiconductor." *Nature Photonics* 10 (4):262-266. doi: 10.1038/nphoton.2015.277.

Castelletto, Stefania, Faraz A. Inam, Shin-ichiro Sato, and Alberto Boretti. 2020. "Hexagonal boron nitride: a review of the emerging material platform for single-photon sources and the spin–photon interface." *Beilstein Journal of Nanotechnology* 11:740-769. doi: https://doi.org/10.3762/bjnano.11.61.

Chatterjee, Arka, Abhijit Biswas, Addis S. Fuhr, Tanguy Terlier, Bobby G. Sumpter, Pulickel M. Ajayan, Igor Aharonovich, and Shengxi Huang. 2025. "Room-temperature high-purity single-photon emission from carbon-doped boron nitride thin films." *Science Advances* 11 (25):eadv2899. doi: doi:10.1126/sciadv.adv2899.

Chen, Dongchang, Dong Ding, Xiaxi Li, Gordon Henry Waller, Xunhui Xiong, Mostafa A. El-Sayed, and Meilin Liu. 2015. "Probing the Charge Storage Mechanism of a Pseudocapacitive MnO2 Electrode Using in Operando Raman Spectroscopy." *Chemistry of Materials* 27 (19):6608-6619. doi: 10.1021/acs.chemmater.5b03118.

Chen, Yin-Chung, Shang-Chin Lee, Te-Huan Liu, and Chien-Cheng Chang. 2015. "Thermal conductivity of boron nitride nanoribbons: Anisotropic effects and boundary scattering." *International Journal of Thermal Sciences* 94:72-78. doi: https://doi.org/10.1016/j.ijthermalsci.2015.02.005.

Cheng, Yuang, Yang Chen, Bingchen Lv, Zhiming Shi, Yuanyuan Yue, Yuping Jia, Ke Jiang, Xiaoyu Wei, Dabing Li, Shanli Zhang, and Xiaojuan Sun. 2024. "Enhanced p-type conductivity of hexagonal boron nitride by an efficient two-step doping strategy." *Optical Materials Express* 14. doi: 10.1364/OME.523859.

Chernozatonskii, Leonid A., Victor A. Demin, and Stefano Bellucci. 2016. "Bilayered graphene/h-BN with folded holes as new nanoelectronic materials: modeling of structures and electronic properties." *Scientific Reports* 6 (1):38029. doi: 10.1038/srep38029.

Choi, Christopher S., David S. Ashby, Danielle M. Butts, Ryan H. DeBlock, Qiulong Wei, Jonathan Lau, and Bruce S. Dunn. 2019. "Achieving high energy density and high power density with pseudocapacitive materials." *Nature Reviews Materials* 5:5-19.

Colak, Tuluhan, Çiğdem Tuç Altaf, Fatma Tuzluca, Yasar Yesilbag, Ipek Yıldırım, Emre Erdem, Feray Bakan Misirlioglu, Nurdan Sankir, and Mehmet Sankir. 2024. "Photo-supercapacitors based on zinc oxide/MXene paper dual acting electrodes." *Journal of Energy Storage* 86:111274. doi: 10.1016/j.est.2024.111274.

Cui, Mingjin, and Xiangkang Meng. 2020. "Overview of transition metal-based composite materials for supercapacitor electrodes." *Nanoscale Advances* 2 (12):5516-5528. doi: https://doi.org/10.1039/d0na00573h.

D, Guruvammal, Sathish Selvaraj, and S. Sundar. 2017. "Structural, optical and magnetic properties of Co doped ZnO DMS nanoparticles by microwave irradiation method." *Journal of Magnetism and Magnetic Materials* 452. doi: 10.1016/j.jmmm.2017.12.097.

Das, Abinash, Dongyu Liu, Riu Riu Wary, Andrey S. Vasenko, Oleg V. Prezhdo, and Ranjith G. Nair. 2023. "Mn-Modified ZnO Nanoflakes for Optimal Photoelectrochemical Performance Under Visible Light: Experimental Design and Theoretical Rationalization." *The Journal of Physical Chemistry Letters* 14 (43):9604-9611. doi: 10.1021/acs.jpclett.3c02730.

Dean, C. R., A. F. Young, I. Meric, C. Lee, L. Wang, S. Sorgenfrei, K. Watanabe, T. Taniguchi, P. Kim, K. L. Shepard, and J. Hone. 2010. "Boron nitride substrates for high-quality graphene electronics." *Nature Nanotechnology* 5 (10):722-726. doi: 10.1038/nnano.2010.172.

Devi, P. Geetha, and A. Sakthi Velu. 2016. "Synthesis, structural and optical properties of pure ZnO and Co doped ZnO nanoparticles prepared by the co-precipitation method." *Journal of Theoretical and Applied Physics* 10 (3):233-240. doi: 10.1007/s40094-016-0221-0.

Dillip, Gowra Raghupathy, Arghya Narayan Banerjee, Veettikkunnu Chandran Anitha, Borelli Deva Prasad Raju, Sang Woo Joo, and Bong Ki Min. 2016. "Oxygen Vacancy-Induced Structural, Optical, and Enhanced Supercapacitive Performance of Zinc Oxide Anchored Graphitic Carbon Nanofiber Hybrid Electrodes." *ACS Applied Materials & Interfaces* 8 (7):5025-5039. doi: 10.1021/acsami.5b12322.

Dole, B. N., V. D. Mote, V. R. Huse, Y. Purushotham, M. K. Lande, K. M. Jadhav, and S. S. Shah. 2011. "Structural studies of Mn doped ZnO nanoparticles." *Current Applied Physics* 11 (3):762-766. doi: https://doi.org/10.1016/j.cap.2010.11.050.

Eckmann, A., J. Park, H. Yang, D. Elias, A. S. Mayorov, G. Yu, R. Jalil, K. S. Novoselov, R. V. Gorbachev, M. Lazzeri, A. K. Geim, and C. Casiraghi. 2013. "Raman fingerprint of aligned graphene/h-BN superlattices." *Nano Lett* 13 (11):5242-6. doi: 10.1021/nl402679b.

Ercay, Egehan, Serra Ersoy, Mucahid Ozcan, Feray Bakan Misirlioglu, Ahmet Gungor, Andrew Ozarowski, Figen Kaya, Arpad Mihai Rostas, Cengiz Kaya, and Emre Erdem. 2025. "Enhancing ZnO-based supercapacitors through carbon-induced defect centers." *MRS Bulletin* 50 (5):572-584. doi: 10.1557/s43577-024-00845-z.

Erdem, Emre. 2017. "Defect induced p-type conductivity in zinc oxide at high temperature: electron paramagnetic resonance spectroscopy." *Nanoscale* 9 (31):10983-10986. doi: 10.1039/C7NR03988C.

Gao, Yanjun, Shaohua Zhang, Xiangyang Li, Lijie Li, Lixia Bao, Niu Zhang, Jiong Peng, and Xin Li. 2021. "Synergistically optimizing electronic structure and reducing ions transport resistance by oxygen functional groups and defects in carbon for superior sodium capture and potassium storage capability." *Carbon* 181:323-334. doi: https://doi.org/10.1016/j.carbon.2021.05.039.

García-Miranda Ferrari, A., S. J. Rowley-Neale, and C. E. Banks. 2021. "Recent advances in 2D hexagonal boron nitride (2D-hBN) applied as the basis of electrochemical sensing platforms." *Anal Bioanal Chem* 413 (3):663-672. doi: 10.1007/s00216-020-03068-8.

Gogotsi, Yury, and Reginald M Penner. 2018. Energy storage in nanomaterials–capacitive, pseudocapacitive, or battery-like? : ACS Publications.

Guo, Hongxuan, Jianhua Gao, Nobuyuki Ishida, Mingsheng Xu, and Daisuke Fujita. 2014. "Characterization of two-dimensional hexagonal boron nitride using scanning electron and scanning helium ion microscopy." *Applied Physics Letters* 104 (3):031607. doi: 10.1063/1.4862819.

Guo, Yanzhen, Binbin Chang, Ting Wen, Chunmei Zhao, Hang Yin, Yannan Zhou, Yonggang Wang, Baocheng Yang, and Shouren Zhang. 2016. "One-pot synthesis of graphene/zinc oxide by microwave irradiation with enhanced supercapacitor performance." *RSC Advances* 6 (23):19394-19403. doi: 10.1039/C5RA24212F.

Hassan, Kamrul, Rumana Hossain, and Veena Sahajwalla. 2022. "Recycled ZnO-fused macroporous 3D graphene oxide aerogel composites for high-performance asymmetric supercapacitors." *Journal of the American Ceramic Society* 105 (12):7467-7478. doi: https://doi.org/10.1111/jace.18697.

Hsu, Chou-Yi, Shelesh Krishna Saraswat, Abdelmajeed Adam Lagum, Alaa M. Al-Ma'abreh, Farzad Molani, Tariq J. Al-Musawi, A. M. A. Mohamed, and Mustafa M. Kadhim. 2023. "Study the single-atom Mn-doped catalysts on boron nitride sheet surface as cathode for oxygen reduction reaction in proton-exchange membrane fuel cells." *Sustainable Chemistry and Pharmacy* 33:101115. doi: https://doi.org/10.1016/j.scp.2023.101115.

Huang, Caijin, Cheng Chen, Xinxin Ye, Weiqing Ye, Jinli Hu, Chao Xu, and Xiaoqing Qiu. 2013. "Stable colloidal boron nitride nanosheet dispersion and its potential application in catalysis." *Journal of Materials Chemistry A* 1 (39):12192-12197. doi: 10.1039/C3TA12231J.

Jaffe, Gabriel R., Keenan J. Smith, Kenji Watanabe, Takashi Taniguchi, Max G. Lagally, Mark A. Eriksson, and Victor W. Brar. 2023. "Thickness-Dependent Cross-Plane Thermal Conductivity Measurements of Exfoliated Hexagonal Boron Nitride." *ACS Applied Materials & Interfaces* 15 (9):12545-12550. doi: 10.1021/acsami.2c21306.

Jangu, Surendra, Sudhir Kumar, Kilingaru Nadumane Deepika, Chacko Jacob, and Debabrata Pradhan. 2023. "Effect of Microwave Power and Cu Doping on MnO2 Nanostructures and Its Supercapacitor Performance." *ACS Applied Electronic Materials* 5 (6):3078-3092. doi: 10.1021/acsaelm.3c00152.

Janotti, Anderson, and Chris Van de Walle. 2009. "Fundamentals of Zinc Oxide As a Semiconductor." *Reports on Progress in Physics* 72:126501. doi: 10.1088/0034-4885/72/12/126501.

Janotti, Anderson, and Chris G. Van de Walle. 2006. "New insights into the role of native point defects in ZnO." *Journal of Crystal Growth* 287 (1):58-65. doi: https://doi.org/10.1016/j.jcrysgro.2005.10.043.

Janotti, Anderson, and Chris Walle. 2005. "Oxygen vacancies in ZnO." *Applied Physics Letters* 87:122102. doi: 10.1063/1.2053360.

Ji, C., V. I. Levitas, H. Zhu, J. Chaudhuri, A. Marathe, and Y. Ma. 2012. "Shear-induced phase transition of nanocrystalline hexagonal boron nitride to wurtzitic structure at room temperature and lower pressure." *Proc Natl Acad Sci U S A* 109 (47):19108-12. doi: 10.1073/pnas.1214976109.

Jungwirth, Nicholas R., and Gregory D. Fuchs. 2017. "Optical Absorption and Emission Mechanisms of Single Defects in Hexagonal Boron Nitride." *Physical Review Letters* 119 (5):057401. doi: 10.1103/PhysRevLett.119.057401.

Kaftelen, Hülya, Kasim Ocakoglu, Ralf Thomann, Suyan Tu, Stefan Weber, and Emre Erdem. 2012. "EPR and photoluminescence spectroscopy studies on the defect structure of ZnO nanocrystals." *Physical Review B* 86 (1):014113. doi: 10.1103/PhysRevB.86.014113.

Kasap, Sibel, Ismet I. Kaya, Sergej Repp, and Emre Erdem. 2019. "Superbat: battery-like supercapacitor utilized by graphene foam and zinc oxide (ZnO) electrodes induced by structural defects." *Nanoscale Advances* 1 (7):2586-2597. doi: 10.1039/C9NA00199A.

Keller, Katharina, Michal Zalibera, Mian Qi, Vanessa Koch, Julia Wegner, Henrik Hintz, Adelheid Godt, Gunnar Jeschke, Anton Savitsky, and Maxim Yulikov. 2016. "EPR characterization of Mn(ii) complexes for distance determination with pulsed dipolar spectroscopy." *Physical Chemistry Chemical Physics* 18 (36):25120-25135. doi: 10.1039/C6CP04884F.

Khan, Aamar F., Dale A. C. Brownson, Edward P. Randviir, Graham C. Smith, and Craig E. Banks. 2016. "2D Hexagonal Boron Nitride (2D-hBN) Explored for the Electrochemical Sensing of Dopamine." *Analytical Chemistry* 88 (19):9729-9737. doi: 10.1021/acs.analchem.6b02638.

Khan, Rajwali, Naveed Ur Rahman, Muhammad Faisal Hayat, Djamel Ghernaout, Alsamani A. M. Salih, Ghulam Abbas Ashraf, Abdus Samad, Muhammad Adil Mahmood, Nasir Rahman, Mohammad Sohail, Shahid Iqbal, Sherzod Abdullaev, and Alamzeb Khan. 2024. "Unveiling cutting-edge developments: architectures and nanostructured materials for application in optoelectronic artificial synapses." *Nanoscale* 16 (31):14589-14620. doi: 10.1039/D4NR00904E.

Khan, Shakeel, Sammia Shahid, Waqas Bashir, Sadia Kanwal, and Ahsan Iqbal. 2017. "Synthesis, characterization and evaluation of biological activities of manganese-doped zinc oxide nanoparticles." *Tropical Journal of Pharmaceutical Research* 16:2331-2339. doi: 10.4314/tjpr.v16i10.17.

Kim, Yong-Sung, and Chul Hong Park. 2009. "Rich Variety of Defects in ZnO via an Attractive Interaction between O Vacancies and Zn Interstitials: Origin of n-Type Doping." *Physical review letters* 102:086403. doi: 10.1103/PhysRevLett.102.086403.

Kour, Simran, Shweta Tanwar, and A. L. Sharma. 2022. "A review on challenges to remedies of MnO2 based transition-metal oxide, hydroxide, and layered double hydroxide composites for supercapacitor applications." *Materials Today Communications* 32:104033. doi: https://doi.org/10.1016/j.mtcomm.2022.104033.

Krishnamoorthy, Dhamodharan, and Abhishek Kumar Singh. 2025. "Two-dimensional exfoliated hexagonal boron nitride-WS2 nanosheets emerge as an efficient positive electrode for high performance hybrid supercapacitor applications." *Diamond and Related Materials* 152:111976. doi: https://doi.org/10.1016/j.diamond.2025.111976.

Kumar, R. Dhilip, S. Nagarani, S. Balachandran, Chidambaram Brundha, S. Hari Kumar, R. Manigandan, Mohanraj Kumar, V. Sethuraman, and Soo Hyung Kim. 2022. "High performing hexagonal-shaped ZnO nanopowder for Pseudo-supercapacitors applications." *Surfaces and Interfaces* 33:102203. doi: https://doi.org/10.1016/j.surfin.2022.102203.

Kumar, Rajesh, Sumanta Sahoo, Ednan Joanni, Rajesh Kumar Singh, Ram Manohar Yadav, Rajiv Kumar Verma, Dinesh Pratap Singh, Wai Kian Tan, Angel Pérez del Pino, Stanislav A. Moshkalev, and Atsunori Matsuda. 2019. "A review on synthesis of graphene, h-BN and MoS2 for energy storage applications: Recent progress and perspectives." *Nano Research* 12 (11):2655-2694. doi: 10.1007/s12274-019-2467-8.

Kumar, Sunny, Vikash Mishra, Kolla Lakshmi Ganapathi, Muralidhar Miryala, M. S. Rao, and Tejendra Dixit. 2024. "Letters: Ab-initio Investigations into Frenkel Defects in Hexagonal Boron Nitride for Quantum Optoelectronic Applications." *IEEE Transactions on Nanotechnology*. doi: 10.1109/TNANO.2024.3354460.

Kunjara Na Ayudhya, Sirachaya, Parawee Tonto, Okorn Mekasuwandumrong, Varong Pavarajarn, and Piyasan Praserthdam. 2006. "Solvothermal Synthesis of ZnO with Various Aspect Ratios Using Organic Solvents." *Crystal Growth & Design* 6 (11):2446-2450. doi: 10.1021/cg050345z.

Lee, Young-Woo, Byung-Sung Kim, John Hong, Juwon Lee, Sangyeon Pak, Hyun-Sik Jang, Dongmok Whang, SeungNam Cha, Jung Inn Sohn, and Jong Min Kim. 2016. "A pseudo-capacitive chalcogenide-based electrode with dense 1-dimensional nanoarrays for enhanced energy density in asymmetric supercapacitors." *Journal of Materials Chemistry A* 4 (26):10084-10090. doi: 10.1039/C6TA03337G.

Li, H., L. Xue, Zhu Wang, and H. Liu. 2023. "Point vacancy defects in hexagonal boron nitride studied by first-principles." *JJAP Conference Proceedings* 9:011104-011104. doi: 10.56646/jjapcp.9.0_011104.

Li, Tianli, Xiuyan Jiao, Ting You, Fang Dai, Panpan Zhang, Feng Yu, Lu Hu, Liwen Ding, Lei Zhang, Zubiao Wen, and Yuping Wu. 2019. "Hexagonal boron nitride nanosheet/carbon nanocomposite as a high-performance cathode material towards aqueous asymmetric supercapacitors." *Ceramics International* 45 (4):4283-4289. doi: https://doi.org/10.1016/j.ceramint.2018.11.101.

Liang, Haidong, Yuan Chen, Leyi Loh, Nicholas Cheng, Yifeng Chen, Chengyuan Yang, Zhepeng Zhang, Kenji Watanabe, Takashi Taniguchi, Su Quek, Michel Bosman, Goki Eda, and Andrew Bettiol. 2023. *Blue Quantum Emitters in hexagonal Boron Nitride*.

Liu, Guang, Tiandong Zhang, Yu Feng, Yongquan Zhang, Changhai Zhang, Yue Zhang, Xubin Wang, Qingguo Chi, Qingguo Chen, and Qingquan Lei. 2020. "Sandwich-structured polymers with electrospun boron nitrides layers as high-temperature energy storage dielectrics." *Chemical Engineering Journal* 389:124443.

Liu, Wei, Shuzhong Wang, Jinlong Wang, Baoquan Zhang, Lu Liu, Hui Liu, and Jianqiao Yang. 2022. "Supercritical hydrothermal synthesis of nano-zinc oxide: Process and mechanism."

Ceramics International 48 (16):22629-22646. doi: https://doi.org/10.1016/j.ceramint.2022.05.094.
Liu, Yuanyue, Xiaolong Zou, and Boris I. Yakobson. 2012. "Dislocations and Grain Boundaries in Two-Dimensional Boron Nitride." *ACS Nano* 6 (8):7053-7058. doi: 10.1021/nn302099q.
Lorenz, Michael, Rolf Böttcher, Stefan Friedländer, Andreas Pöppl, Daniel Spemann, and Marius Grundmann. 2014. "Local lattice distortions in oxygen deficient Mn-doped ZnO thin films, probed by electron paramagnetic resonance." *Journal of Materials Chemistry C* 2 (25):4947-4956. doi: 10.1039/C4TC00407H.
Maciaszek, Marek, Lukas Razinkovas, and Audrius Alkauskas. 2022. "Thermodynamics of carbon point defects in hexagonal boron nitride." *Physical Review Materials* 6 (1):014005. doi: 10.1103/PhysRevMaterials.6.014005.
Mendelson, Noah, Dipankar Chugh, Jeffrey R. Reimers, Tin S. Cheng, Andreas Gottscholl, Hu Long, Christopher J. Mellor, Alex Zettl, Vladimir Dyakonov, Peter H. Beton, Sergei V. Novikov, Chennupati Jagadish, Hark Hoe Tan, Michael J. Ford, Milos Toth, Carlo Bradac, and Igor Aharonovich. 2021. "Identifying carbon as the source of visible single-photon emission from hexagonal boron nitride." *Nature Materials* 20 (3):321-328. doi: 10.1038/s41563-020-00850-y.
Misra, S. K. 1996. "Interpretation of Mn2+ EPR spectra in disordered Materials." *Applied Magnetic Resonance* 10 (1):193-216. doi: 10.1007/BF03163109.
Moore, A. W., and L. S. Singer. 1972. "Electron spin resonance in carbon-doped boron nitride." *Journal of Physics and Chemistry of Solids* 33 (2):343-356. doi: https://doi.org/10.1016/0022-3697(72)90016-9.
More, Pravin, Amol Salunkhe, Yuraj Navale, and Dr Vikas Patil. 2021a. "Facile Synthesis and Electrochemical Investigation of Undoped and Mn-Doped ZnO Electrodes for the Energy Storage Application." *Macromolecular Symposia* 400:2100050. doi: 10.1002/masy.202100050.
More, Pravin, Amol Salunkhe, Yuraj Navale, and Vikas Patil. 2021b. "Facile Synthesis and Electrochemical Investigation of Undoped and Mn-Doped ZnO Electrodes for the Energy Storage Application." *Macromolecular Symposia* 400 (1):2100050. doi: https://doi.org/10.1002/masy.202100050.
Motevalizadeh, L., B. Shohany, and Majid Ebrahimizadeh Abrishami. 2016. "Effects of Mn doping on electrical properties of ZnO thin films." *Modern Physics Letters B* 30:1650024. doi: 10.1142/S021798491650024X.
Mousavi, S. A., and A. Montazeri. 2023. "Predicting mechanical properties of defective h-BN nanosheets using Data-Driven models." *Computational Materials Science* 228:112380. doi: https://doi.org/10.1016/j.commatsci.2023.112380.
Nadupalli, Shankari, Sergej Repp, Stefan Weber, and Emre Erdem. 2021. "About defect phenomena in ZnO nanocrystals." *Nanoscale* 13 (20):9160-9171. doi: 10.1039/D1NR00943E.
Najib, Sumaiyah, Feray Bakan, Nazrin Abdullayeva, Rahim Bahariqushchi, Sibel Kasap, Giorgia Franzò, Mehmet Sankir, Nurdan Demirci Sankir, Salvo Mirabella, and Emre Erdem. 2020. "Tailoring morphology to control defect structures in ZnO electrodes for high-performance supercapacitor devices." *Nanoscale* 12 (30):16162-16172. doi: 10.1039/D0NR03921G.
Nash, David J., Katerina L. Chagoya, Alan Felix, Fernand E. Torres-Davila, Tao Jiang, Duy Le, Laurene Tetard, Talat S. Rahman, and Richard G. Blair. 2019. "Analysis of the fluorescence of mechanically processed defect-laden hexagonal boron nitride and the role of oxygen in catalyst deactivation." *Advances in Applied Ceramics* 118 (4):153-158. doi: 10.1080/17436753.2019.1584482.
Nasser, Ramzi, Xiao-Lu Wang, Jian Tiantian, Habib Elhouichet, and Ji-Ming Song. 2022. "Hydrothermal design of CoMoO4@CoWO4 core-shell heterostructure for flexible all-

solid-state asymmetric supercapacitors." *Journal of Energy Storage* 51:104349. doi: https://doi.org/10.1016/j.est.2022.104349.

Nasser, Ramzi, Hao Zhou, Amira Ben Gouider Trabelsi, Fatemah Homoud AlKallas, Habib Elhouichet, and Ji-Ming Song. 2023. "Engineering preparation of the nanocomposite containing CoWO4 nanodots and its high electrochemical activities." *Journal of Energy Storage* 68:107763. doi: https://doi.org/10.1016/j.est.2023.107763.

Nie, Lunshuai, Kai Jia, Hongguang Guo, Jiaqin He, Zhehui Weng, and Haidong Ju. 2024. *Effect of Tb3+ and Ce3+ co-doping on the structural stability and photoluminescence properties of hexagonal boron nitride phosphors*.

Nie, Lunshuai, Kai Jia, Hongguang Guo, Jiaqin He, Zhehui Weng, Yizhou Li, and Haidong Ju. 2024. "Effect of Tb and Ce Co-doping on the Structure and Photoluminescence Properties of Hexagonal Boron Nitride Phosphors." *Journal of Fluorescence* 35:2215-2225. doi: 10.1007/s10895-024-03663-3.

Nishikata, A., Y. Ichihara, and T. Tsuru. 1995. "An application of electrochemical impedance spectroscopy to atmospheric corrosion study." *Corrosion Science* 37 (6):897-911. doi: https://doi.org/10.1016/0010-938X(95)00002-2.

Noman, Muhammad Tayyab, Amor Nesrine, and Michal and Petru. 2022. "Synthesis and applications of ZnO nanostructures (ZONSs): a review." *Critical Reviews in Solid State and Materials Sciences* 47 (2):99-141. doi: 10.1080/10408436.2021.1886041.

Norberg, Nick, Kevin Kittilstved, James Amonette, Ravi Kukkadapu, Dana Schwartz, and Daniel Gamelin. 2004. *Synthesis of Colloidal Mn2+:ZnO Quantum Dots and High-TC Ferromagnetic Nanocrystalline Thin Films*.

Oo, Hlaing, Laxmikant Saraf, Mark Engelhard, Vaithiyalingam Shutthanandan, L. Bergman, J. Huso, and Matthew McCluskey. 2009. "Suppression of conductivity in Mn-doped ZnO thin films." *Journal of Applied Physics* 105:013715-013715. doi: 10.1063/1.3063730.

Ozel, Cihan, Cevher Kursat Macit, Turan Gurgenc, Fatih Biryan, Ezgi Gurgenc, and Stefano Bellucci. 2024. "Enhancing dielectric properties of ZnO nanopowders with 2D hBN doping: production, structural, morphological and dielectric characterization." *Applied Physics A* 130 (4):232. doi: 10.1007/s00339-024-07380-3.

Özgür, Ü., Ya. I. Alivov, C. Liu, A. Teke, M. A. Reshchikov, S. Doğan, V. Avrutin, S.-J. Cho, and H. Morkoç. 2005. "A comprehensive review of ZnO materials and devices." *Journal of Applied Physics* 98 (4). doi: 10.1063/1.1992666.

Özkan, Selda, Nhat Truong Nguyen, Imgon Hwang, Anca Mazare, and Patrik Schmuki. 2020. *Highly Conducting Spaced TiO$_2$ Nanotubes Enable Defined Conformal Coating with Nanocrystalline Nb$_2$O$_5$ and High Performance Supercapacitor Applications*.

Pakdel, Amir, Yoshio Bando, and Dmitri Golberg. 2014. "Nano boron nitride flatland." *Chemical Society Reviews* 43 (3):934-959. doi: 10.1039/C3CS60260E.

Panich, A. M., A. I. Shames, N. Froumin, C. C. Tang, and Y. Bando. 2005. "Magnetic resonance study of multiwall boron nitride nanotubes." *Physical Review B* 72 (8):085307. doi: 10.1103/PhysRevB.72.085307.

Parashar, S. K. S., B. Murty, Sergej Repp, S. Weber, and Emre Erdem. 2012. "Investigation of intrinsic defects in core-shell structured ZnO nanocrystals." *Journal of Applied Physics* 111:113712. doi: 10.1063/1.4725478.

Paszkowicz, W., J. B. Pelka, M. Knapp, T. Szyszko, and S. Podsiadlo. 2002. "Lattice parameters and anisotropic thermal expansion of hexagonal boron nitride in the 10–297.5 K temperature range." *Applied Physics A* 75 (3):431-435. doi: 10.1007/s003390100999.

Patra, Abhinandan, Namsheer K, Jeena Jos, Surjit Sahoo, Brahmananda Chakraborty, and Chandra Rout. 2021. "Understanding the charge storage mechanism of supercapacitors: in situ/operando spectroscopic approaches and theoretical investigations." *Journal of Materials Chemistry A* 9. doi: 10.1039/D1TA07401F.

Pearton, S. J., D. P. Norton, K. Ip, Y. W. Heo, and T. Steiner. 2003. "Recent progress in processing and properties of ZnO." *Superlattices and Microstructures* 34 (1):3-32. doi: https://doi.org/10.1016/S0749-6036(03)00093-4.

Petit, L., T. C. Schulthess, A. Svane, W. M. Temmerman, Z. Szotek, and A. Janotti. 2006. "Valency configuration of transition metal impurities in ZnO." *Journal of Electronic Materials* 35 (4):556-561. doi: 10.1007/s11664-006-0099-8.

Petit, Leon, T. Schulthess, A. Svane, Zdzislawa Szotek, W. Temmerman, and Anderson Janotti. 2004. "Electronic structure of transition-metal impurities in p-type ZnO." *Physical Review B* 73:045107. doi: 10.1103/PhysRevB.73.045107.

Ponce, Sofía Carolina Godoy, Yathrib Ajaj, Sadek H. Ali, Anupam Yadav, Mandeep Kaur, Shaima Haithem Zaki, Jamal K. Abbas, Hussam Bdali Abdulridui, and Ayodele Lasisi. 2024. "Investigation of hexagonal boron nitride monolayer with pores as an anode material for sodium-ion batteries." *Diamond and Related Materials* 145:111100. doi: https://doi.org/10.1016/j.diamond.2024.111100.

Que, Miaoling, Chong Lin, Jiawei Sun, Lixiang Chen, Xiaohong Sun, and Yunfei Sun. 2021. "Progress in ZnO Nanosensors." *Sensors* 21 (16):5502.

Raavi, Rachana, Suresh Archana, Pattubala Adinarayana Reddy, and Perumal Elumalai. 2023. "Performances of dual carbon multi-ion supercapacitors in aqueous and non-aqueous electrolytes." *Energy Advances* 2 (3):385-397. doi: 10.1039/D2YA00271J.

Rahal, Abdelghani, Idris Bouchama, M. A. Ghebouli, Faisal Katib Alanazi, B. Ghebouli, M. Fatmi, T. Chihi, Talal M. Althagafi, and Khatir Khettab. 2025. "Experimental investigation of structural and optical properties of Mn-doped ZnO thin films deposited by pneumatic spray technique." *Scientific Reports* 15 (1):7086. doi: 10.1038/s41598-025-90425-1.

Rashid, Abdul Rasheed, Abdul Ghafoor Abid, Sumaira Manzoor, Abeer Mera, Tahani I. Al-Muhimeed, Abeer A. AlObaid, Syed Nasir Shah, Muhammad Naeem Ashiq, Muhammad Imran, and Muhammad Najam-Ul-Haq. 2021. "Inductive effect in Mn-doped ZnO nanoribon arrays grown on Ni foam: A promising key for boosted capacitive and high specific energy supercapacitors." *Ceramics International* 47 (20):28338-28347. doi: https://doi.org/10.1016/j.ceramint.2021.06.251.

Reich, S., A. C. Ferrari, R. Arenal, A. Loiseau, I. Bello, and J. Robertson. 2005. "Resonant Raman scattering in cubic and hexagonal boron nitride." *Physical Review B* 71 (20):205201. doi: 10.1103/PhysRevB.71.205201.

Romeiro, Fernanda, Juliane Marinho, Anielle Christine Silva, Nilo Cano, Noelio Dantas, and Renata Lima. 2013. "Photoluminescence and Magnetism in Mn2+-Doped ZnO Nanostructures Grown Rapidly by the Microwave Hydrothermal Method." *The Journal of Physical Chemistry C* 117:26222–26227. doi: 10.1021/jp408993y.

Römelt, G. 1966. "Paramagnetische Elektronenresonanz thermisch und durch Strahlung erzeugter Zentren in Bornitrid." *Zeitschrift für Naturforschung A* 21 (11):1970-1975. doi: doi:10.1515/zna-1966-1122.

Ruf, Thomas, Sergej Repp, Joanna Urban, Ralf Thomann, and Emre Erdem. 2016a. "Competing effects between intrinsic and extrinsic defects in pure and Mn-doped ZnO nanocrystals." *Journal of Nanoparticle Research* 18. doi: 10.1007/s11051-016-3408-z.

Ruf, Thomas, Sergej Repp, Joanna Urban, Ralf Thomann, and Emre Erdem. 2016b. "Competing effects between intrinsic and extrinsic defects in pure and Mn-doped ZnO nanocrystals." *Journal of Nanoparticle Research* 18 (5):109. doi: 10.1007/s11051-016-3408-z.

Sahu, Ghrutanjali, Annu Balhara, Laxmidhar Besra, Divya Nechiyil, K. Sudasrshan, Jyoti Prakash, Santosh Gupta, and Sriparna Chatterjee. 2024. "Defect enriched luminescent MXene-derived TiO2 for supercapacitors." *Inorganic Chemistry Communications* 170:113462. doi: 10.1016/j.inoche.2024.113462.

Sapkota, Kamal Prasad, Insup Lee, Md. Abu Hanif, Md. Akherul Islam, and Jae Ryang Hahn. 2019. "Solar-Light-Driven Efficient ZnO–Single-Walled Carbon Nanotube Photocatalyst for the Degradation of a Persistent Water Pollutant Organic Dye." *Catalysts* 9 (6):498.

Schimpf, C., M. Motylenko, and D. Rafaja. 2013. "Quantitative description of microstructure defects in hexagonal boron nitrides using X-ray diffraction analysis." *Materials Characterization* 86:190-199. doi: https://doi.org/10.1016/j.matchar.2013.09.011.

Shaheen, Irum, Khuram Ahmad, Camila Zequine, R. Gupta, Andrew Thomas, and Mohammad Malik. 2021. "Facile ZnO-based nanomaterial and its fabrication as a supercapacitor electrode: synthesis, characterization and electrochemical studies." *RSC Advances* 11. doi: 10.1039/d1ra04341b.

Shams, Shamsiya, B. Bindhu, Adhigan Murali, R. Ramesh, Abdullah Al Souwaileh, and Sung Soo Han. 2025. "Hydrothermal engineering of polyethylene glycol-assisted boron nitride/hematite nanohybrid composites for high-performance supercapacitors." *RSC Advances* 15 (20):16035-16049. doi: 10.1039/D5RA02227D.

Shams, Shamsiya, B. Bindhu, Adhigan Murali, R. Ramesh, Abdullah Al Souwaileh, and Sung Soo Han. 2025. "High-performance boron nitride/graphene oxide composites modified with sodium thiosulfate for energy storage applications." *Nanoscale Advances* 7 (7):1803-1813. doi: 10.1039/D4NA00937A.

Sharma, Dhirendra Kumar, Sweta Shukla, Kapil Kumar Sharma, and Vipin Kumar. 2022a. "A review on ZnO: Fundamental properties and applications." *Materials Today: Proceedings* 49:3028-3035. doi: https://doi.org/10.1016/j.matpr.2020.10.238.

Sharma, Dhirendra, Sweta Shukla, Kapil Sharma, and Vipin Kumar. 2022b. "A review on ZnO: Fundamental properties and applications." *Materials Today: Proceedings* 49:3028-3035. doi: 10.1016/j.matpr.2020.10.238.

Shen, Yi, and Shuze Zhu. 2023. "Machine learning mechanical properties of defect-engineered hexagonal boron nitride." *Computational Materials Science* 220:112030. doi: https://doi.org/10.1016/j.commatsci.2023.112030.

Shenoy, Manjula, A. Sakunthala, B. Vidhya, Swaminathan Rajesh, Nandhakumar Raju, Senthil Kumar Parthasarathi, M. Sasikumar, Kadarkarai Govindan, Saravanakumar Tamilarasan, Thangavelu Selvaraju, Suryakanth J, and M. V. Reddy. 2021. "Visible light sensitive hexagonal boron nitride (hBN) decorated Fe2O3 photocatalyst for the degradation of methylene blue." *Journal of Materials Science: Materials in Electronics* 32:1-18. doi: 10.1007/s10854-020-05215-4.

Silly, Mathieu, P. Jaffrennou, J. Barjon, Jean-Sébastien Lauret, François Ducastelle, A. Loiseau, Brigitte Attal-Tretout, and E. Rosencher. 2007. "Luminescence properties of hexagonal boron nitride : Cathodoluminescence and photoluminescence spectroscopy measurements." *Physical Review B* 75:085205. doi: 10.1103/PhysRevB.75.085205.

Singal, Shobhita, Akanksha Joshi, Anuj Kumar Tomar, Vikrant Sahu, Gurmeet Singh, and Raj Kishore Sharma. 2020. "Vacancies and edges: Enhancing supercapacitive performance metrics of electrode materials." *Journal of Energy Storage* 31:101614. doi: https://doi.org/10.1016/j.est.2020.101614.

Singha, Shib Shankar, Siddheswar Rudra, Suchanda Mondal, Mukul Pradhan, Arpan Kumar Nayak, Biswarup Satpati, Prabir Pal, Kaustuv Das, and Achintya Singha. 2020. "Mn incorporated MoS2 nanoflowers: A high performance electrode material for symmetric supercapacitor." *Electrochimica Acta* 338:135815. doi: https://doi.org/10.1016/j.electacta.2020.135815.

Srikanth, K. S., Adil Wazeer, P. Mathiyalagan, Shrikant Vidya, Kapil Rajput, and Himmat Singh Kushwaha. 2021. "25 - Piezoelectric properties of ZnO." In *Nanostructured Zinc Oxide*, edited by Kamlendra Awasthi, 717-736. Elsevier.

Stagi, Luigi, Luca Malfatti, Alessia Zollo, Stefano Livraghi, Davide Carboni, Daniele Chiriu, Riccardo Corpino, Pier Carlo Ricci, Antonio Cappai, Carlo Maria Carbonaro, Stefano

Enzo, Abbas Khaleel, Abdulmuizz Adamson, Christel Gervais, Andrea Falqui, and Plinio Innocenzi. 2024. "Phosphorescence by Trapping Defects in Boric Acid Induced by Thermal Processing." *Advanced Optical Materials* 12 (13):2302682. doi: https://doi.org/10.1002/adom.202302682.

Stefan, Maria, Berfu Kocabas, Ahmet Güngör, Dana Toloman, Arpad Mihai Rostas, Ramona Crina Suciu, Sergiu Macavei, Iolanda Ganea, Ioana Perhaita, Septimiu Tripon, Cristian Leostean, Emre Erdem, and Adriana Popa. 2024. "Manganese-doped Zinc Oxide recycled from spent alkaline batteries for photocatalysis and supercapacitor applications." *Journal of Energy Storage* 99:113419. doi: https://doi.org/10.1016/j.est.2024.113419.

Stefanowicz, W., R. Adhikari, T. Andrearczyk, B. Faina, M. Sawicki, J. A. Majewski, T. Dietl, and A. Bonanni. 2014. "Experimental determination of Rashba spin-orbit coupling in wurtzite n-GaN:Si." *Physical Review B* 89 (20):205201. doi: 10.1103/PhysRevB.89.205201.

Stoll, Stefan, and Arthur Schweiger. 2006. "EasySpin, a comprehensive software package for spectral simulation and analysis in EPR." *Journal of Magnetic Resonance* 178 (1):42-55. doi: https://doi.org/10.1016/j.jmr.2005.08.013.

Teisseyre, Henryk, D. Jarosz, Lucja Marona, Agata Bojarska, Vitalii Ivanov, Piotr Perlin, and Tomasz Czyszanowski. 2020. "Homoepitaxial ZnO/ZnMgO Laser Structures and Their Properties." *physica status solidi (a)* 218:2000344. doi: 10.1002/pssa.202000344.

Thirumurugan, Arun, N. Chidhambaram, S. Jasmine Jecintha Kay, N. Dineshbabu, Ranjith Kumar Poobalan, V. S. Manikandan, Shanmuga Sundar Dhanabalan, and Carolina Venegas Abarzúa. 2024. "Chapter 10 - Hexagonal boron nitride for microelectronics, nanoelectronics, and nanophotonics." In *Hexagonal Boron Nitride*, edited by Kalim Deshmukh, Mayank Pandey and Chaudhery Mustansar Hussain, 269-294. Elsevier.

Toledo, José, Daniel Jesus, M. Kianinia, Alexandre Leal, Cristiano Fantini, Luiz Cury, Gustavo Sáfar, I. Aharonovich, and Klaus Krambrock. 2018. "Electron paramagnetic resonance signature of point defects in neutron-irradiated hexagonal boron nitride." *Physical Review B* 98. doi: 10.1103/PhysRevB.98.155203.

Toloman, Dana, Ahmet Gungor, Adriana Popa, Maria Stefan, Sergiu Macavei, Lucian Barbu-Tudoran, Ana Varadi, Ipek Deniz Yildirim, Ramona Suciu, Ion Nesterovschi, Maria Mihet, Emre Erdem, and Arpad Mihai Rostas. 2025. "Morphological impact on the supercapacitive performance of nanostructured ZnO electrodes." *Ceramics International* 51 (1):353-365. doi: https://doi.org/10.1016/j.ceramint.2024.10.466.

Toufani, Maryam, Sibel Kasap, Ali Tufani, Feray Bakan, Stefan Weber, and Emre Erdem. 2020. "Synergy of nano-ZnO and 3D-graphene foam electrodes for asymmetric supercapacitor devices." *Nanoscale* 12 (24):12790-12800. doi: 10.1039/D0NR02028A.

Tran, Toan Trong, Kerem Bray, Michael J. Ford, Milos Toth, and Igor Aharonovich. 2016. "Quantum emission from hexagonal boron nitride monolayers." *Nature Nanotechnology* 11 (1):37-41. doi: 10.1038/nnano.2015.242.

Tseng, Chun-Chieh, Yu-Hsien Chou, Chung-Ming Liu, Yih-Ming Liu, Ming-Der Ger, and Youn-Yuen Shu. 2012. "Microwave-assisted hydrothermal synthesis of zinc oxide particles starting from chloride precursor." *Materials Research Bulletin* 47 (1):96-100. doi: https://doi.org/10.1016/j.materresbull.2011.09.027.

Umran, Haider M., and Ahmed A. Alibage. 2024. "Current research on transition metal oxide materials used to improve super-capacitor performance." *AIP Conference Proceedings* 3091 (1). doi: 10.1063/5.0204701.

Vanheusden, K., C. H. Seager, W. L. Warren, D. R. Tallant, and J. A. Voigt. 1996. "Correlation between photoluminescence and oxygen vacancies in ZnO phosphors." *Applied Physics Letters* 68 (3):403-405. doi: 10.1063/1.116699.

Vidya, R., P. Ravindran, H. Fjellvåg, B. G. Svensson, E. Monakhov, M. Ganchenkova, and R. M. Nieminen. 2011. "Energetics of intrinsic defects and their complexes in ZnO investigated

by density functional calculations." *Physical Review B* 83 (4):045206. doi: 10.1103/PhysRevB.83.045206.
Wang, Chan, Kuan Hu, Ying Liu, Ming-Rong Zhang, Zhiwei Wang, and Zhou Li. 2021. Flexible Supercapacitors Based on Graphene/Boron Nitride Nanosheets Electrodes and PVA/PEI Gel Electrolytes. *Materials* 14 (8). doi:10.3390/ma14081955.
Wang, Mingsong, Lingxia Jiang, Eui Jung Kim, and Sung Hong Hahn. 2015. "Electronic structure and optical properties of Zn(OH)2: LDA+U calculations and intense yellow luminescence." *RSC Advances* 5 (106):87496-87503. doi: 10.1039/C5RA17024A.
Watanabe, Kenji, Takashi Taniguchi, and Hisao Kanda. 2004. "Direct-bandgap properties and evidence for ultraviolet lasing of hexagonal boron nitride single crystal." *Nature Materials* 3 (6):404-409. doi: 10.1038/nmat1134.
Weston, L., Darshana Wickramaratne, Mažena Mackoit Sinkevičienė, Audrius Alkauskas, and Chris Van de Walle. 2018. "Native point defects and impurities in hexagonal boron nitride." *Physical Review B* 97. doi: 10.1103/PhysRevB.97.214104.
Wojnarowicz, J., T. Chudoba, and W. Lojkowski. 2020. "A Review of Microwave Synthesis of Zinc Oxide Nanomaterials: Reactants, Process Parameters and Morphoslogies." *Nanomaterials (Basel)* 10 (6). doi: 10.3390/nano10061086.
Wong, Dillon, Jairo Velasco Jr, Long Ju, Juwon Lee, Salman Kahn, Hsin-Zon Tsai, Chad Germany, Takashi Taniguchi, Kenji Watanabe, and Alex Zettl. 2015. "Characterization and manipulation of individual defects in insulating hexagonal boron nitride using scanning tunnelling microscopy." *Nature nanotechnology* 10 (11):949-953.
Wu, Qi-Long, Shi-Xi Zhao, Le Yu, Xiao-Xiao Zheng, Yi-Feng Wang, Lü-Qiang Yu, Ce-Wen Nan, and Guozhong Cao. 2019. "Oxygen vacancy-enriched MoO3−x nanobelts for asymmetric supercapacitors with excellent room/low temperature performance." *Journal of Materials Chemistry A* 7 (21):13205-13214. doi: 10.1039/C9TA03471D.
Wu, Xin, and Qiang Han. 2020. "Thermal conductivity of monolayer hexagonal boron nitride: From defective to amorphous." *Computational Materials Science* 184:109938. doi: https://doi.org/10.1016/j.commatsci.2020.109938.
Xu, Youli, Shuling Shen, Long Li, Shuning Xiao, Jing Li, Zhihong Tang, and Junhe Yang. 2022. "Site-selective doping induced synergistic effect of midgap states and aspect ratio-related charge transfer in Ag2S-ZnS heterostructure toward H2 photoproduction." *Journal of Alloys and Compounds* 908:164631. doi: https://doi.org/10.1016/j.jallcom.2022.164631.
Yüksel Price, Berat, Gökhan Hardal, Muhammed Acikgoz, Sergej Repp, and Emre Erdem. 2015. "Effects of MnO doping on the electronic properties of zinc oxide: 406 GHz electron paramagnetic resonance spectroscopy and Newman superposition model analysis." *Journal of Applied Physics* 118. doi: 10.1063/1.4935085.
Yüksel Price, Berat, Gökhan Hardal, Muhammed Açıkgöz, Sergej Repp, and Emre Erdem. 2015. "Effects of MnO doping on the electronic properties of zinc oxide: 406 GHz electron paramagnetic resonance spectroscopy and Newman superposition model analysis." *Journal of Applied Physics* 118 (17). doi: 10.1063/1.4935085.
Zagorac, Dejan, Jelena Zagorac, Milan Pejić, Branko Matović, and Johann Christian Schön. 2022. "Band Gap Engineering of Newly Discovered ZnO/ZnS Polytypic Nanomaterials." *Nanomaterials* 12 (9):1595.
Zembilgotov, A. G., N. A. Pertsev, U. Böttger, and R. Waser. 2005. "Effect of anisotropic in-plane strains on phase states and dielectric properties of epitaxial ferroelectric thin films." *Applied Physics Letters* 86 (5):052903. doi: 10.1063/1.1855389.
Zhang, Changyong, Di He, Jinxing Ma, Wangwang Tang, and T. David Waite. 2018. "Faradaic reactions in capacitive deionization (CDI) - problems and possibilities: A review." *Water Research* 128:314-330. doi: https://doi.org/10.1016/j.watres.2017.10.024.
Zhang, Huanhuan, Yanyan Liu, Kang Sun, Shuqi Li, Jingjing Zhou, Shuling Liu, Huijuan Wei, Baozhong Liu, Lixia Xie, Baojun Li, and Jianchun Jiang. 2023. "Applications and theory

investigation of two-dimensional boron nitride nanomaterials in energy catalysis and storage." *EnergyChem* 5 (6):100108. doi: https://doi.org/10.1016/j.enchem.2023.100108.

Zhang, Tong, Huijuan Yue, Hailong Qiu, Kai Zhu, Lijie Zhang, Yingjin Wei, Fei Du, Gang Chen, and Dong Zhang. 2015. "Synthesis of graphene-wrapped ZnMn2O4 hollow microspheres as high performance anode materials for lithium ion batteries." *RSC Advances* 5 (120):99107-99114. doi: 10.1039/C5RA16667E.

Zhang, Yangyang, Manoj Ram, and Elias Stefanakos. 2012. "Synthesis, Characterization, and Applications of ZnO Nanowires." *Journal of Nanomaterials* 2012. doi: 10.1155/2012/624520.

Zhao, Changtai, Chang Yu, Mengdi Zhang, Huawei Huang, Shaofeng Li, Xiaotong Han, Zhibin Liu, Juan Yang, Wei Xiao, and Jianneng Liang. 2017. "Ultrafine MoO2-Carbon microstructures enable ultralong-life power-type sodium ion storage by enhanced pseudocapacitance." *Advanced Energy Materials* 7 (15):1602880.

Zheng, Shuanghao, Weiwei Lei, Jieqiong Qin, Zhong-Shuai Wu, Feng Zhou, Sen Wang, Xiaoyu Shi, Chenglin Sun, Ying Chen, and Xinhe Bao. 2018. "All-solid-state high-energy planar asymmetric supercapacitors based on all-in-one monolithic film using boron nitride nanosheets as separator." *Energy Storage Materials* 10:24-31.

Zheng, Tianxu, Yaobo Hu, and Shengwei Yang. 2017. "Effect of grain size on the electrochemical behavior of pure magnesium anode." *Journal of Magnesium and Alloys* 5 (4):404-411. doi: https://doi.org/10.1016/j.jma.2017.09.003.

Zhi, Chunyi. 2006. "Engineering of electronic structure of boron-nitride nanotubes by covalent functionalization." *Phys. Rev. B* 74. doi: 10.1103/PhysRevB.74.153413.

Zhi, Chunyi, Yoshio Bando, Chengchun Tang, Hiroaki Kuwahara, and Dimitri Golberg. 2009. "Large-Scale Fabrication of Boron Nitride Nanosheets and Their Utilization in Polymeric Composites with Improved Thermal and Mechanical Properties." *Advanced Materials* 21 (28):2889-2893. doi: https://doi.org/10.1002/adma.200900323.

7. APPENDIX A:
Supporting Graphs

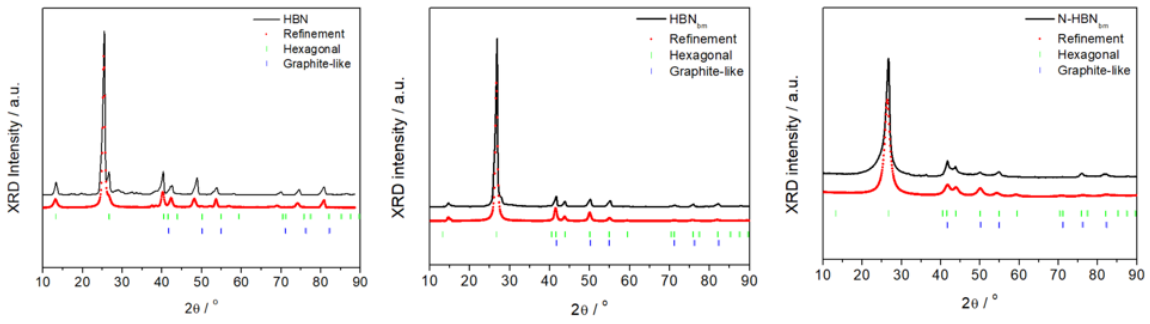

Appendix 1: Reitveld refinement of HBN, HBN_{bm}, and $NHBN_{bm}$ samples revealing the effect of ball-milling on the crystal structure of h-BN

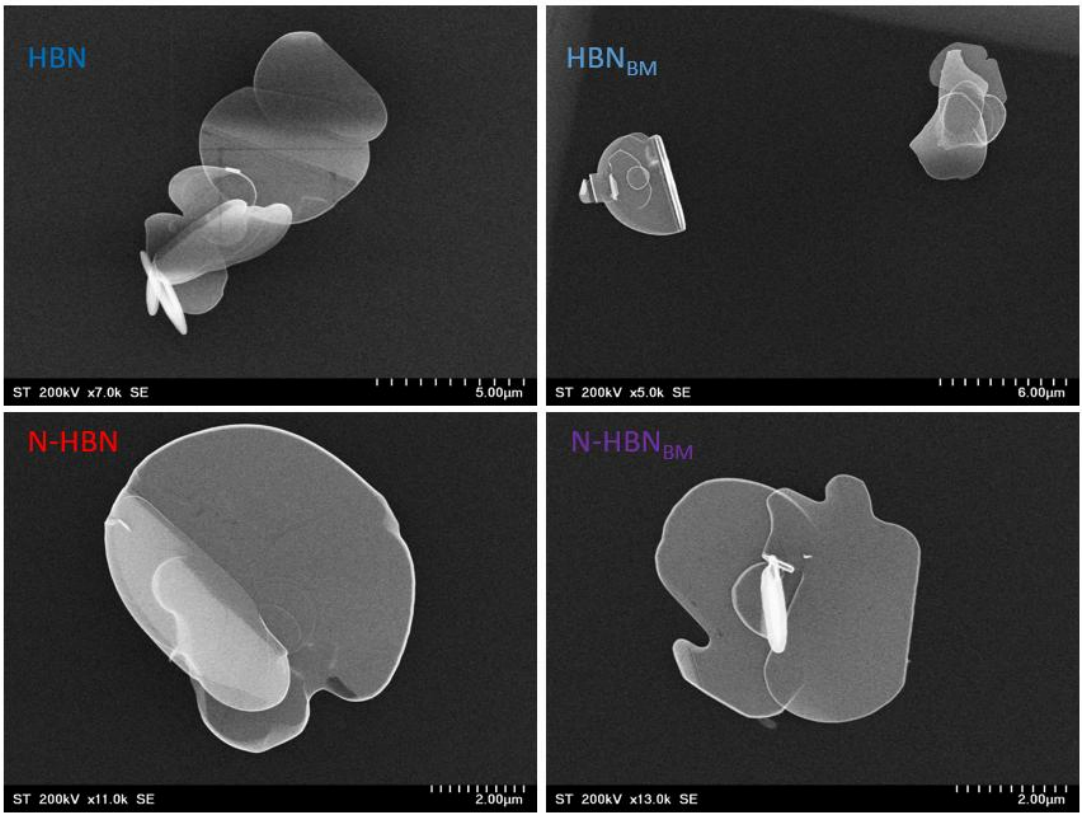

Appendix 2: SEM images of HBN and NHBN samples before and after the ball milling process, showing the morphological changes after the ball milling process

Appendix 3: EasySpin fit parameters of the hyperfine lines of V_N in the structure of h-BN

Signal	**Spin**	**g-value**	**HF_{Aniso} / MHz**			**Lw/mT**
			A1	A2	A3	
Sys1	½	2.0031	23	20.5	20.8	[0.05 0.35]
Sys2	½	2.003	-	-	-	[2.4 0.01]

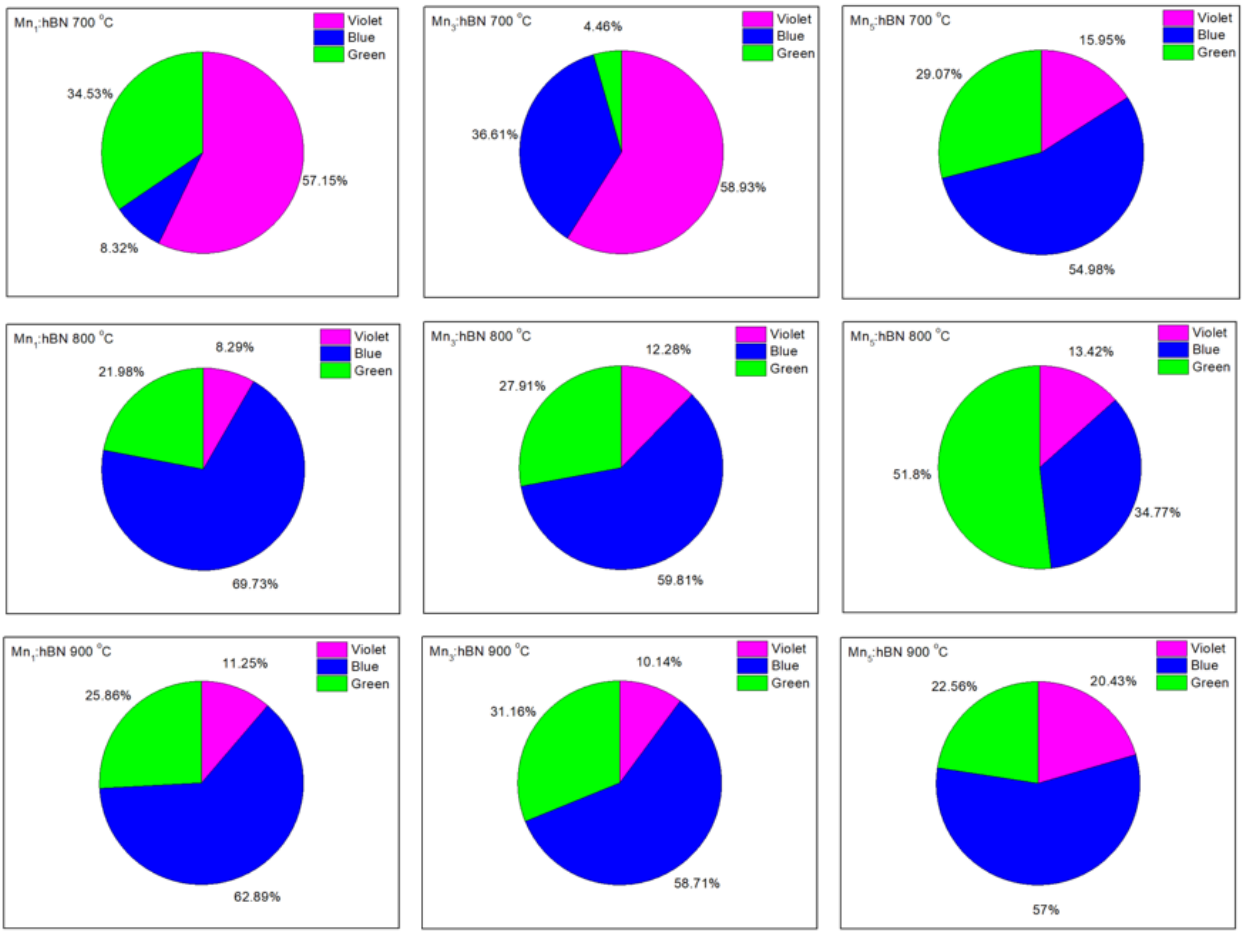

Appendix 4: The percentage of various emissions in the visible light range of Mn-doped h-BN samples obtained from the deconvolution of the PL peaks

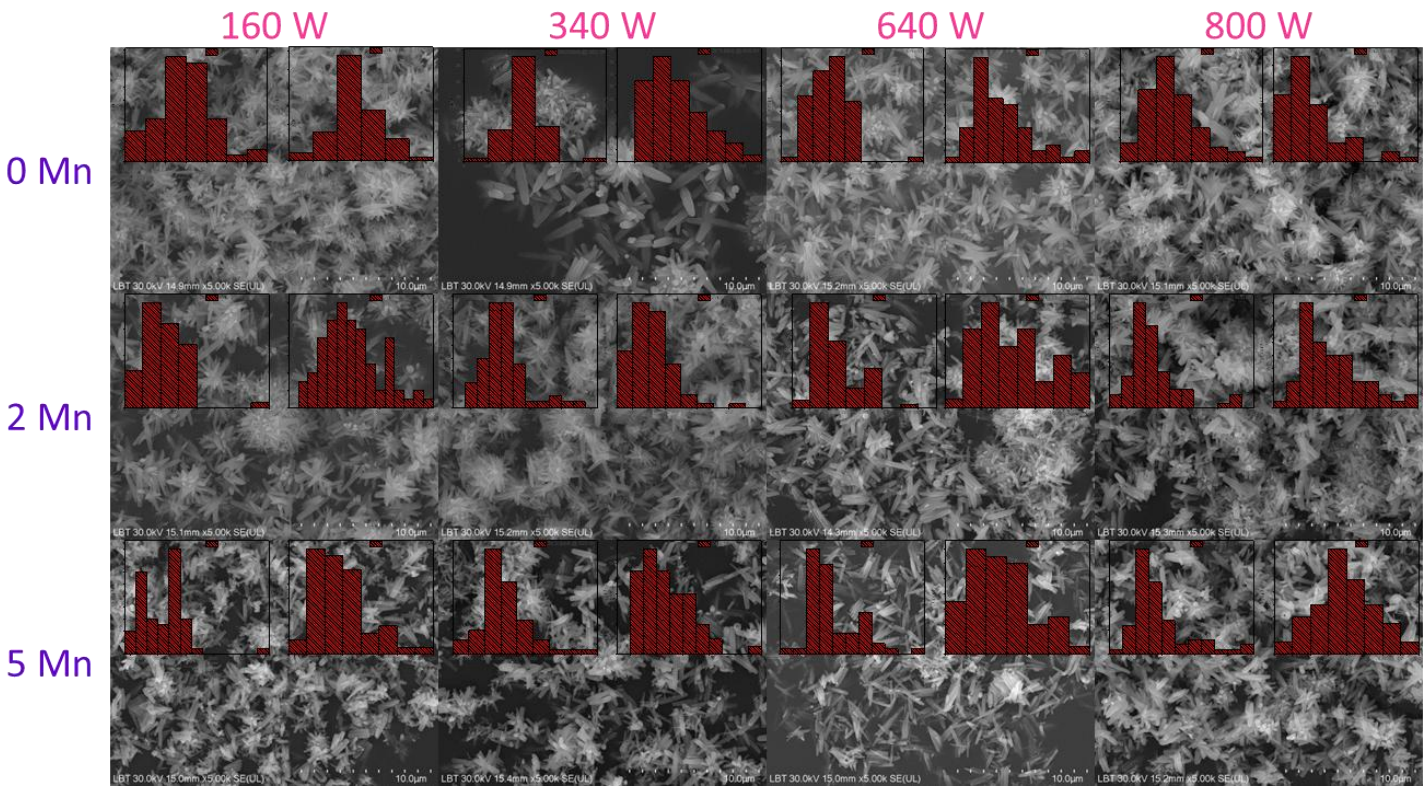

Appendix 5: SEM micrographs together with the length abd diameter size distributions of the undoped and Mn-doped ZnO samples synthesized at differen microwave powers

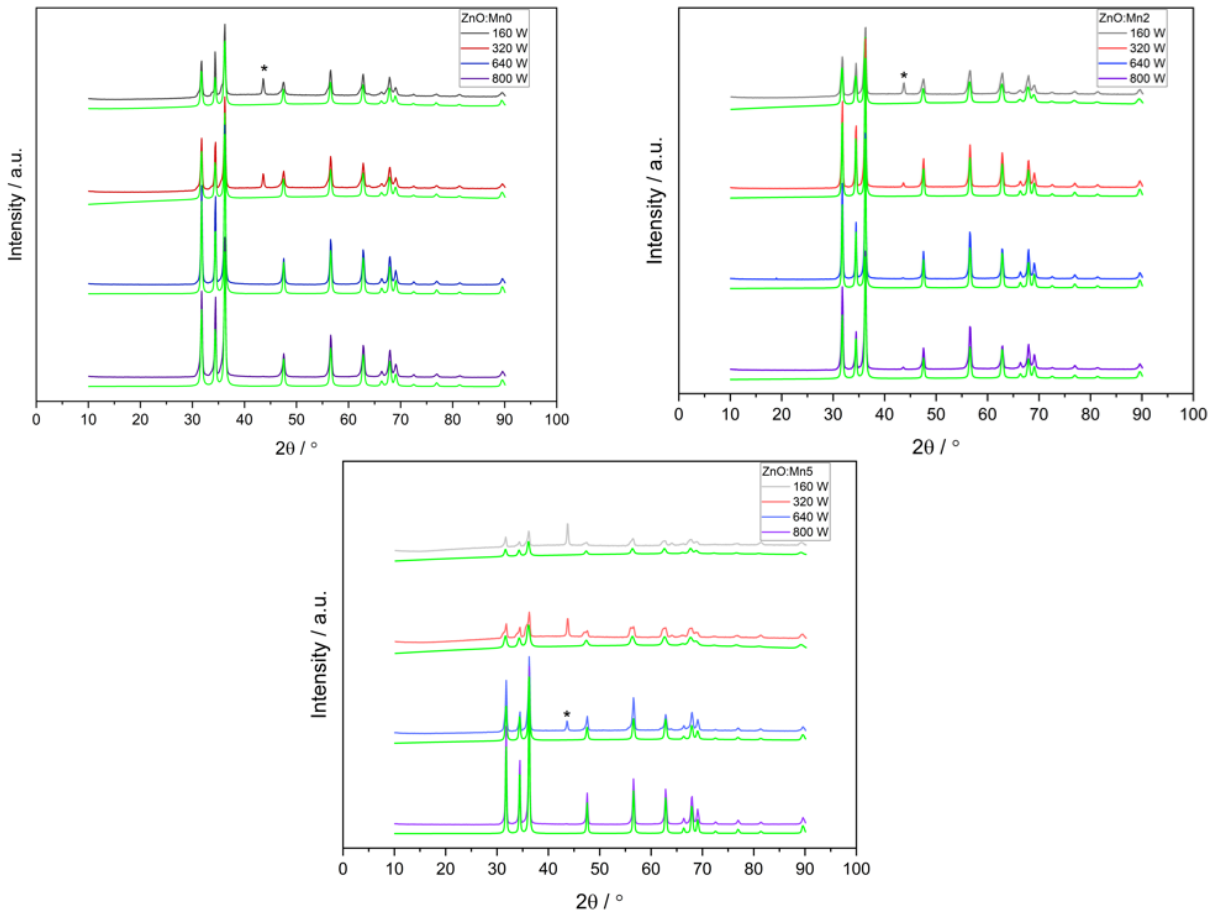

Appendix 6: XDR results together with the Rietveld analysis of the undoped and Mn-doped ZnO samples, synthesized at different microwave powers

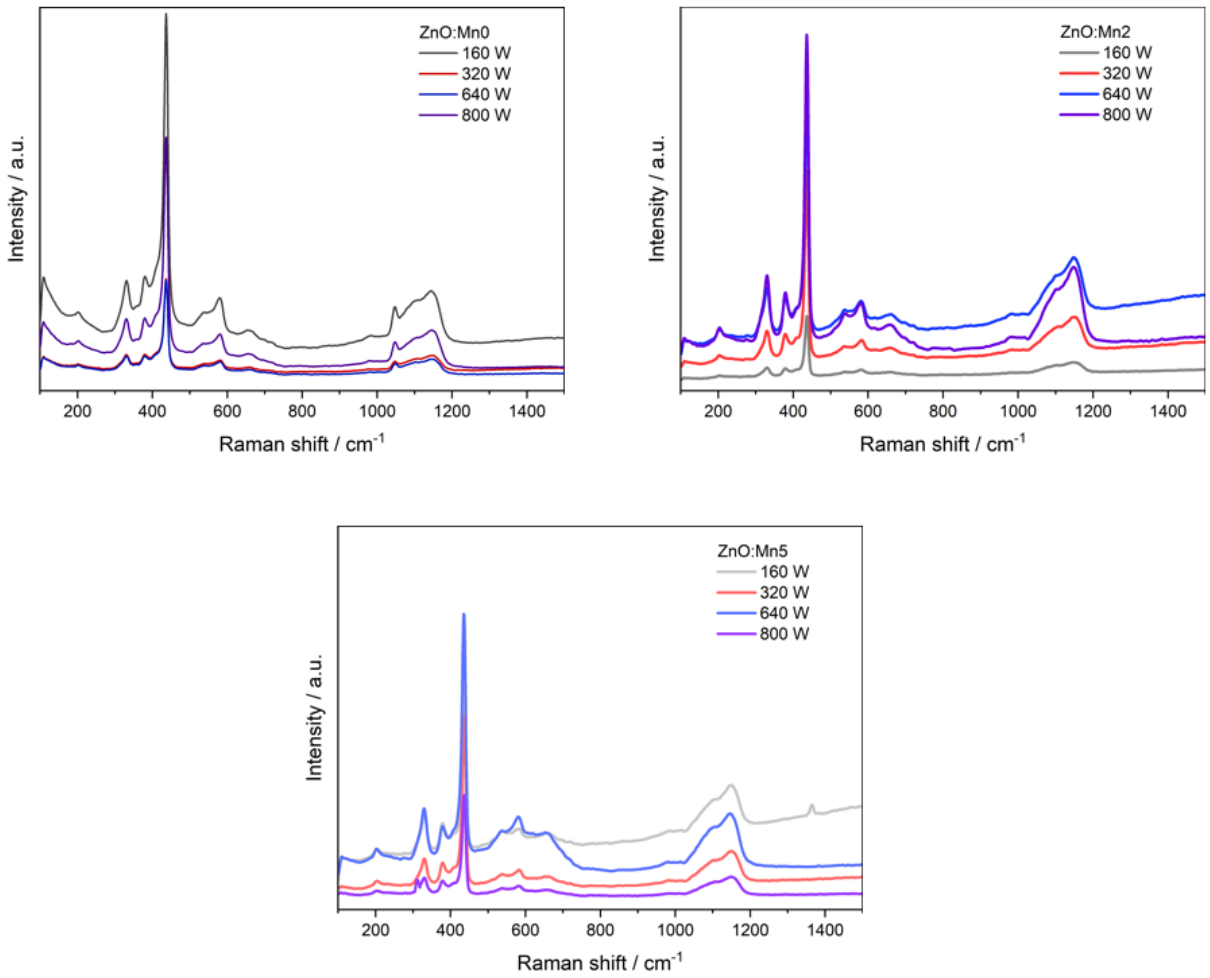

Appendix 7: Raman spectra of the undoped and Mn-doped ZnO samples synthesized at different MW powers

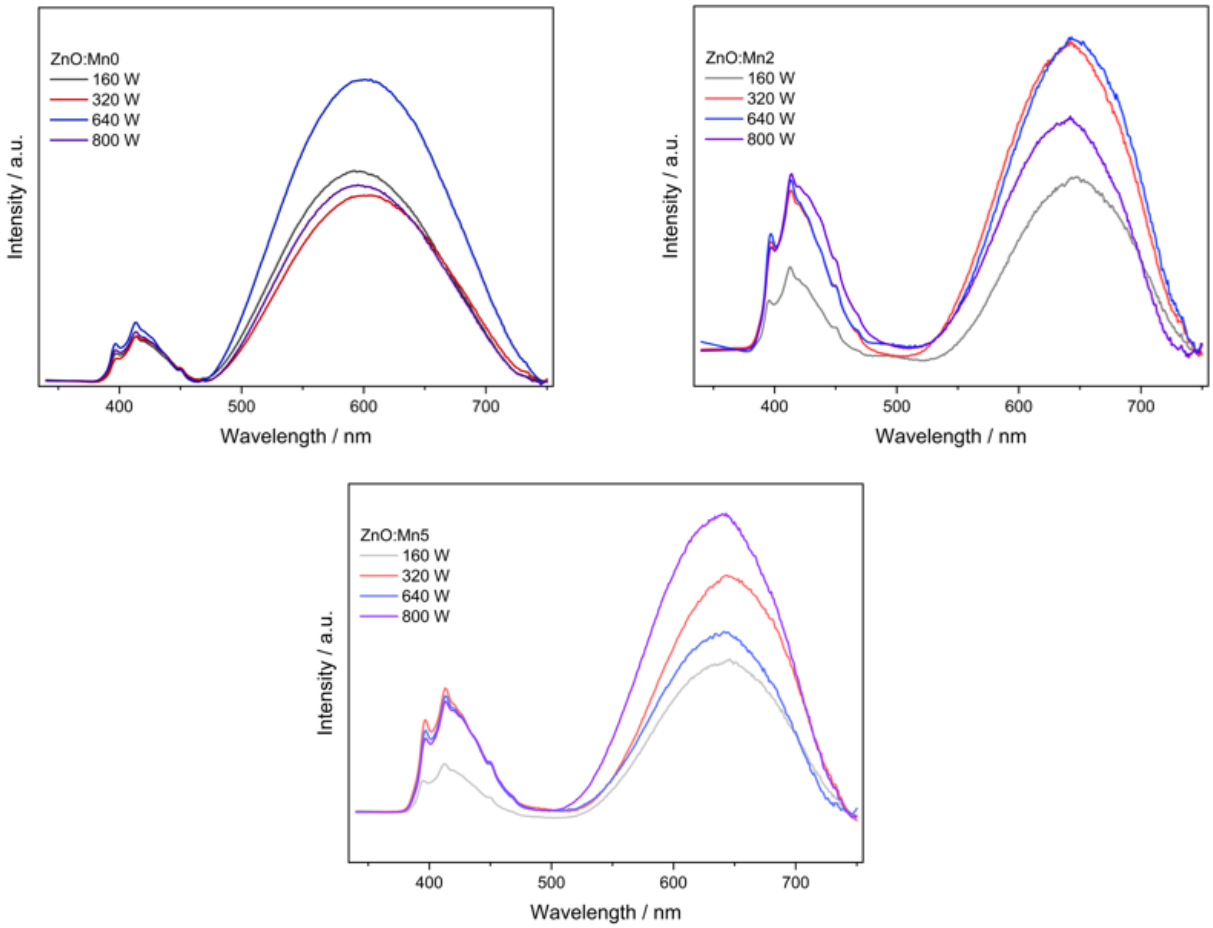

Appendix 8: PL spectra of the undoped and Mn-doped ZnO synthesized at different microwave powers, showing the effect of the microwave power during synthesis on the optical properties of Mn-doped ZnO

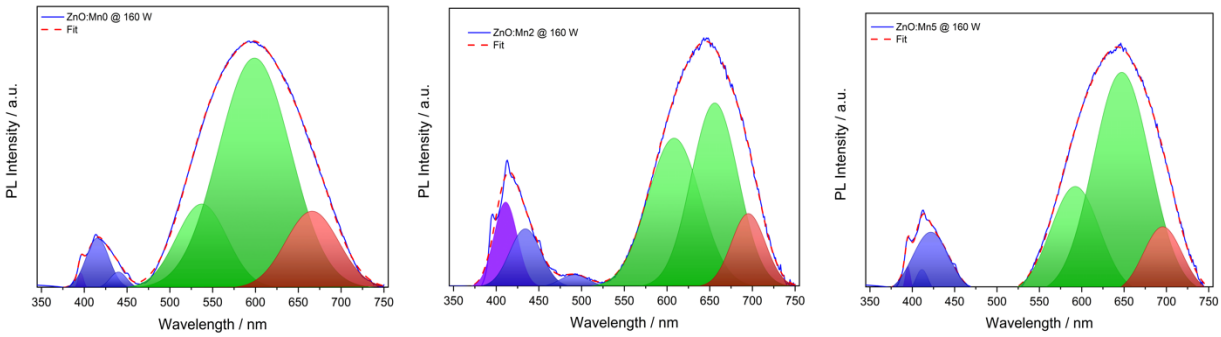

Appendix 9: Gaussian deconvolution results of the undoped and Mn-doped ZnO samples PL spectra, synthesized at 160 W microwave power

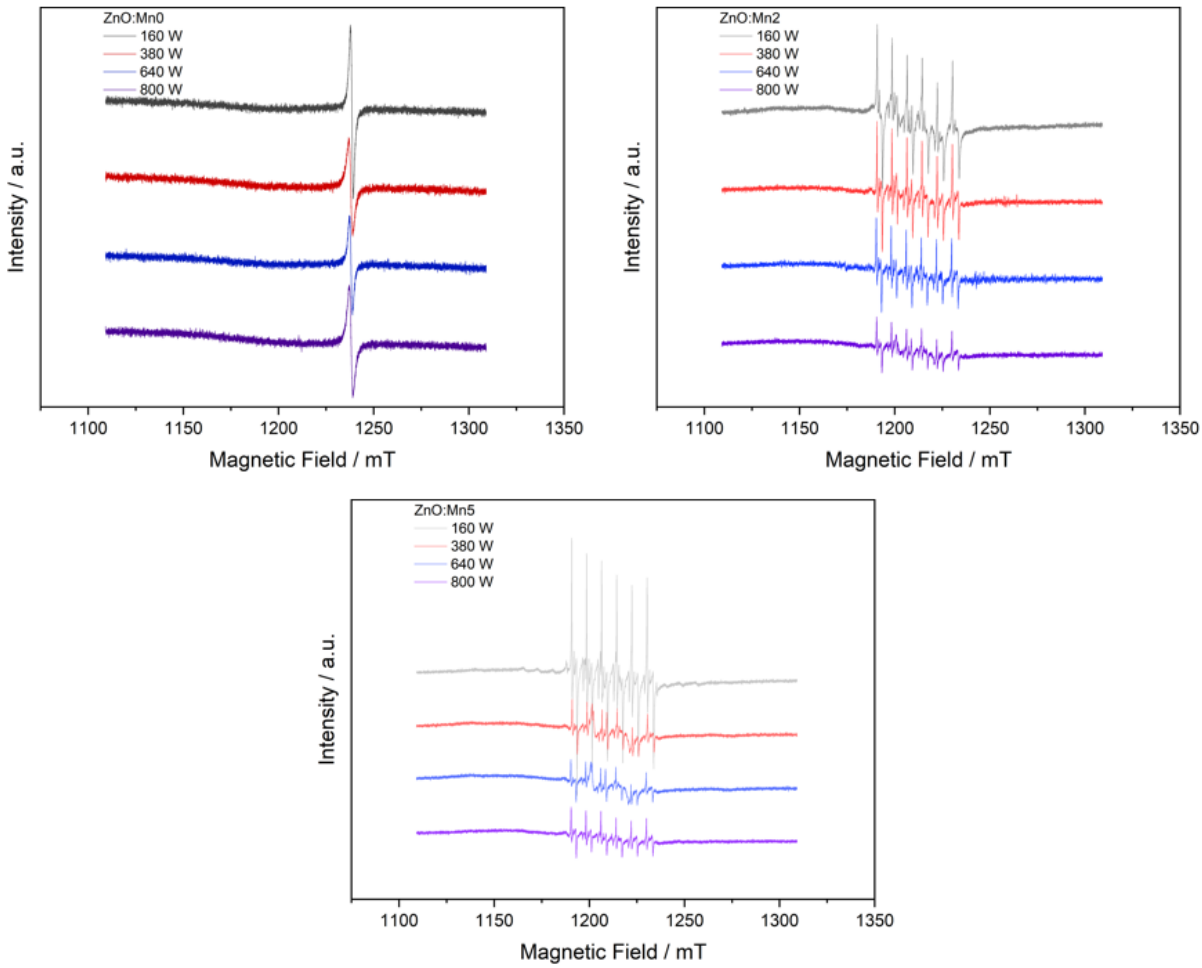

Appendix 10: EPR spectra of the undoped and Mn-doped ZnO samples synthesized at different MW powers, showing the development of sextet hyperfine lines associated witn Mn^{+2} incorporation in the structure of ZnO

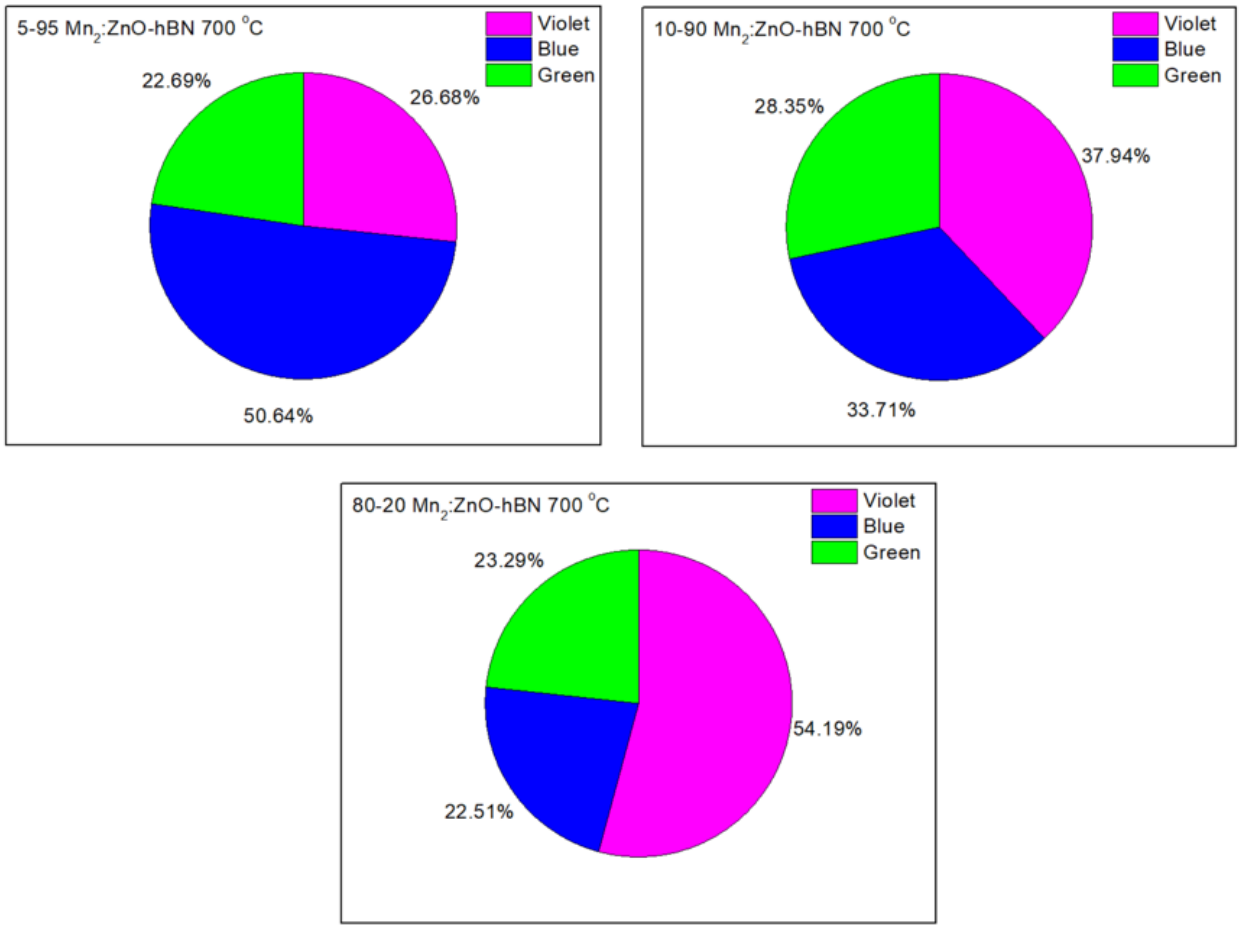

Appendix 11: The percentage of various emissions in the visible light range of Mn:ZnO-hBN nanocomposites, obtained from the PL peaks deconvolution

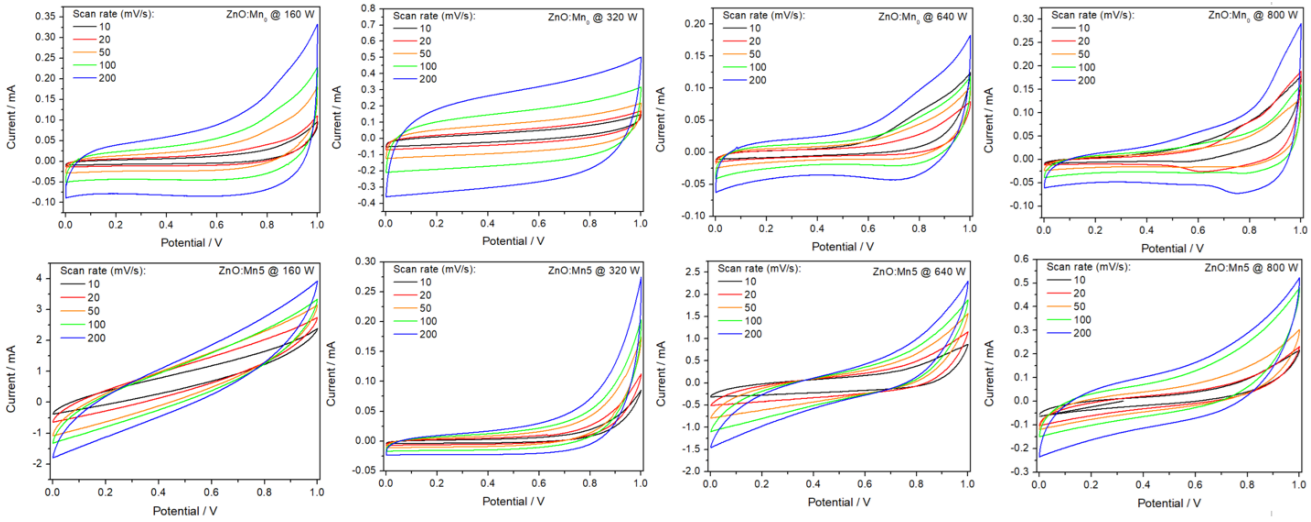

Appendix 12: CV graphs of Mn-doped ZnO samples synthesized at different microwave powers, taken at different scan rates.

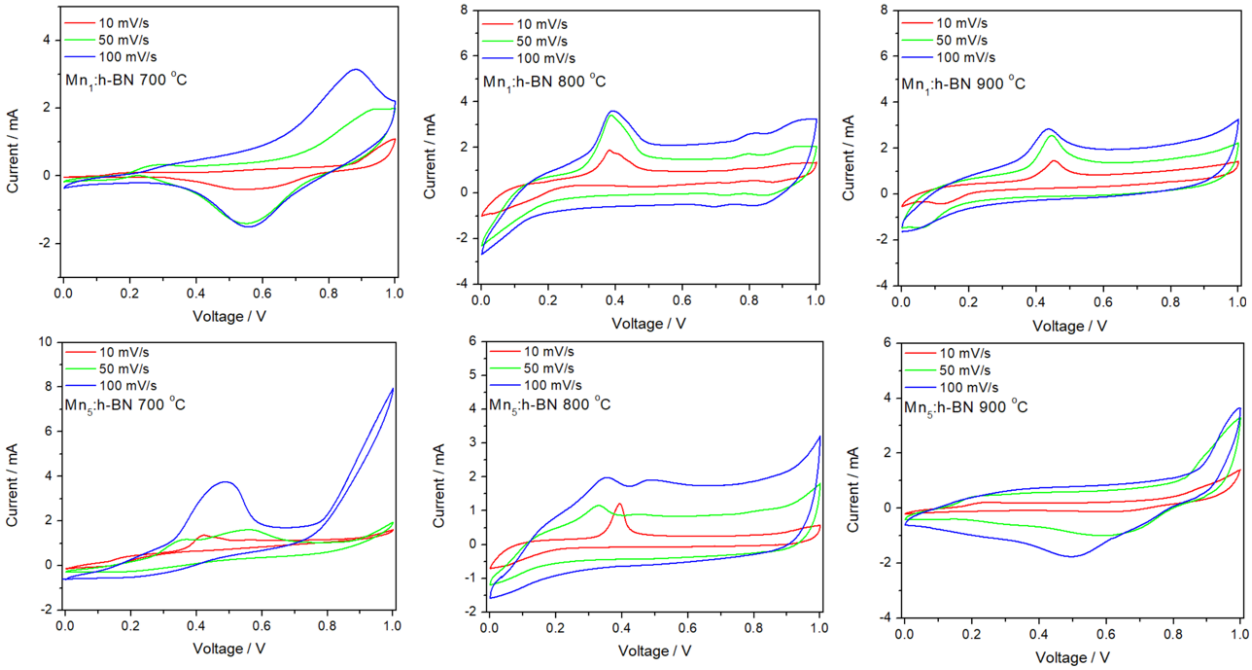

Appendix 13: CV graphs of 1% and 5% Mn-doped h-BN samples, taken at different scan rates

Appendix 14: Zfit equivalent circuit's components for ball-milled h-BN samples

HBN_{bm}		**$NHBN_{bm}$**	
R1 (Ω)	0.023	**R1 (Ω)**	0.034
Q1 (Ω)	0.012	**Q1 (Ω)**	0.104
R2 (Ω)	12.15	**R2 (Ω)**	3.63
C3 (F)	0.691	**C3 (F)**	0.231
R3 (Ω)	157.6	**R3 (Ω)**	9.66

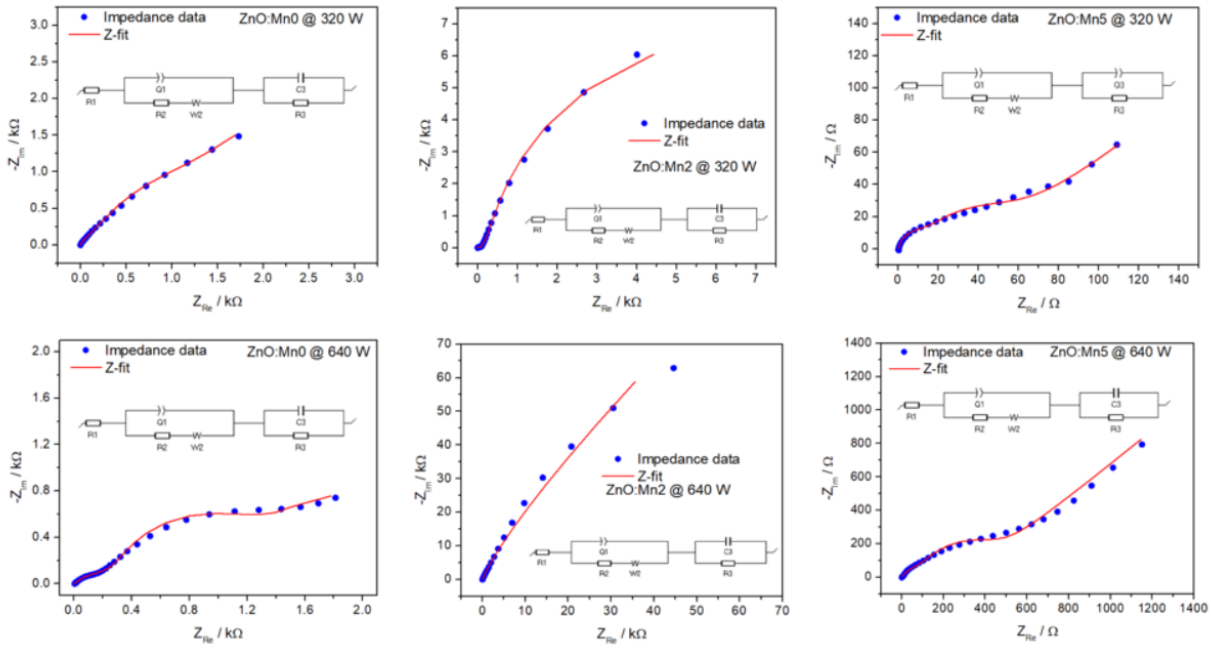

Appendix 15: EIS plots of ZnO:Mn_0 and ZnO:Mn_2 samples synthesized at 320 and 640 W microwave power, along with the equivalent circuits obtained from the Zfit shown in red line

Appendix 16: Zfit equivalent circuit's components for Mn doped-ZnO samples synthesized at different microwave powers

Sample	**R1 / Ω**	**Q1 / mΩ**	**R2 (Ω)**	**W2 / $\Omega/s^{-\frac{1}{2}}$**	**C3** / mF	**R3 / Ω**
ZnO:Mn0 @ 160 W	5.473	1.54	229.8	391	0.120	146.9
ZnO:Mn0 @ 320 W	0.853	0.658	109	215	0.722	405
ZnO:Mn0 @ 640 W	5.26	0.290	306	46.11	1.55	718
ZnO:Mn0 @ 800 W	5.14	0.124	1053	34	0.748	860
ZnO:Mn2 @ 160 W	0.4665	0.295	1691	243.6	4.665	265
ZnO:Mn2 @ 320 W	0.291	0.105	550	25.6	0.202	290
ZnO:Mn2 @ 640 W	0.2775	0.507	531	134	0.081	18.91
ZnO:Mn2 @ 800 W	0.712	0.601	996	148	0.165	130
ZnO:Mn5 @ 160 W	0.296	0.295	332	58.54	58.54	165
ZnO:Mn5 @ 320 W	0.333	0.751	408	187	1.865	255
ZnO:Mn5 @ 640 W	0.264	0.255	136.6	217	0.775	225.4
ZnO:Mn5 @ 800 W	0.280	0.180	72.09	117	1.5	1080

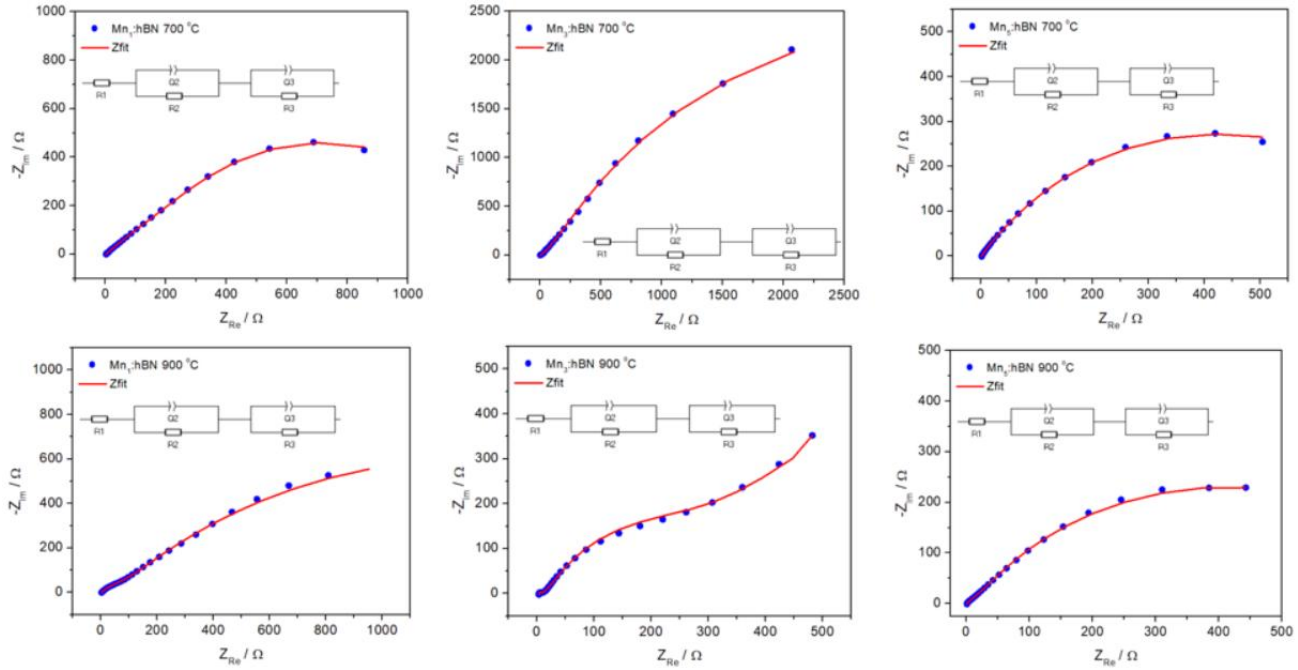

Appendix 17: EIS plots of 1% (top) and 5% (bottom) Mn-doped h-BN samples heat treated at different temperatures

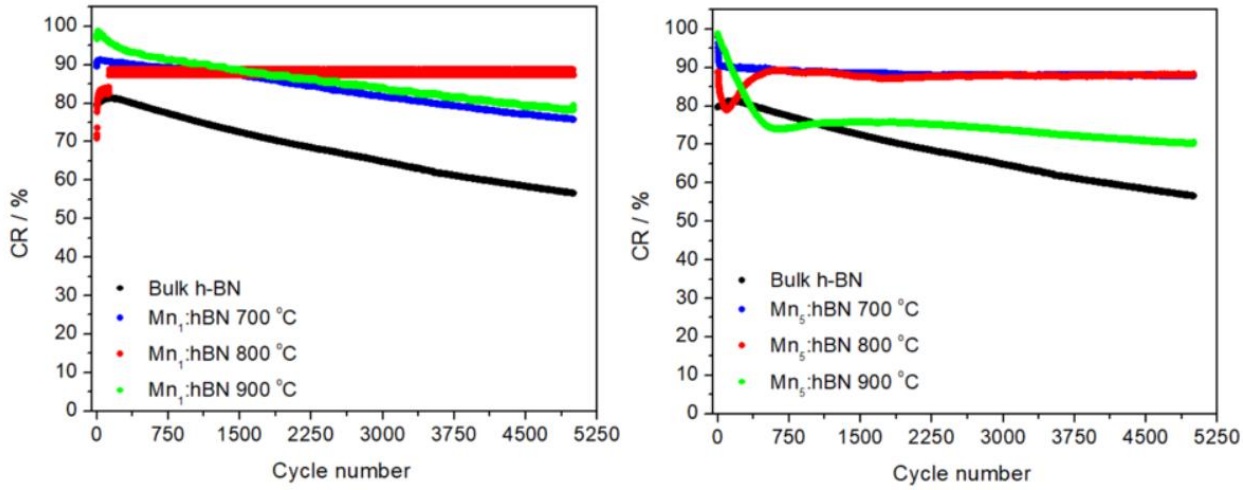

Appendix 18: Capacitive retention graphs of 1% (left) and 5% (right) Mn-doped h-BN samples, showing the cycling stability of the supercapacitor devices

8. APPENDIX B:
Publications and conferences

Peer Reviewed Publications:

1. **M.H. Aleinawi**, Ameen Uddin Ammar, Duygu Şentürk, Lucian Barbu-Tudoran, Oluwatosin Johnson Ajala, Defne Eşkin, Feray Bakan-Misirlioglu, Arpad Mihai Rostas, Emre Erdem, Microwave-tuned Mn-doped ZnO for all-in-one supercapacitors: Correlating defect chemistry with electrochemical behavior. Journal of Colloid and Interface Science, **2025**. 698: p. 138012.
2. **M. H. Aleinawi**, Eminenur Saritas, Maria Stefan, Ameen Uddin Ammar, Abdalla Hroub, Feray Bakan Misirlioglu, Amelia Bocirnea, Sergiu Macavei, Septimiu Tripon, Emre Erdem, Rostas Arpad Mihai, Supercapacitor devices based on multiphase MgTiO3 perovskites doped with Mn2+ ions. Materials Chemistry and Physics, **2025**. 329: p. 130016.
3. **M. H. Aleinawi**, Maria Stefan, Eminenur Saritas, Abdalla Hroub, Feray Bakan-Misirlioglu, Sergiu Macavei, Lucian Barbu Tudoran, Kuray Dericiler, Burcu Saner Okan, Emre Erdem, Arpad Mihai Rostas, Synergy between MgO and TiO2 doped with Mn2+ ions for supercapacitor applications. Next Energy, **2025**. 8: p. 100238.
4. Ameen Uddin Ammar, **M. H. Aleinawi**, Maria Stefan, Ahmet Gungor, Adriana Popa, Dana Toloman, Karlo Maškarić, Eminenur Saritas, Lucian Barbu-Tudoran, Sergiu Macavei, Marin Senila, Emre Erdem, Arpad Mihai Rostas, Lithium-Induced Defect Centers in Nanorod-Shaped Zinc Oxide for Supercapacitor Applications. Electrochemical Acta, **2025**. 519: p. 145806.
5. Cigdem Tuc Altaf, Tuluhan Olcayto Colak, Arpad Mihai Rostas, Crina Socaci, Mihaela Diana Lazar, Lucian Barbu Tudoran, **M. H. Aleinawi**, Feray Bakan Misirlioglu, Ipek Deniz Yildirim, Emre Erdem, Nurdan Demirci Sankir, Mehmet Sankir, Zinc oxide nanoflake/reduced graphene oxide nanocomposite-based dual-acting electrodes for solar-assisted supercapacitor applications. Energy Advances, **2024**. 3(8): p. 1965-1976.
6. Abdalla Hroub, **M. H. Aleinawi**, Maria Stefan, Maria Mihet, Alexandra Ciorita, Feray Bakan-Misirlioglu, Emre Erdem, Arpad Mihai Rostas, Vanadium-doped magnesium oxide nanoparticles as electrodes in supercapacitor devices. Journal of Alloys and Compounds, **2023**. 958: p. 170442.
7. Merve Buldu-Akturk, Namik Kemal Gozuacik, **M. H. Aleinawi**, Arpad Mihai Rostas, Sedat Alkoy, Ebru Mensur, Emre Erdem, Elucidating the capacitive behavior of Gd-doped BNT-BKT-BT electrodes in All-in-One supercapacitor devices. Physica Scripta, **2023**. 98(10): p. 105933.

8. Ameen Uddin Ammar, Ipek Deniz Yildirim, **M. H. Aleinawi**, Merve Buldu-Akturk, Nur Selin Turhan, Shankari Nadupalli, Arpad Mihai Rostas, Emre Erdem, Multifrequency EPR spectroscopy study of Mn, Fe, and Cu doped nanocrystalline ZnO. Materials Research Bulletin, **2023**. 160: p. 112117.
9. Ameen Uddin Ammar, Feray Bakan-Misirlioglu, **M. H. Aleinawi**, Giorgia Franzo, Guglielmo Guido Condorelli, Fatma Nur Tuzluca Yesilbag, Yasar Ozkan Yesilbag, Salvo Mirabella, Emre Erdem All-in-one supercapacitors with high performance enabled by Mn/Cu doped ZnO and MXene. Materials Research Bulletin, **2023**. 165: p. 112334.
10. Ammar, A.U., **M.H. Aleinawi**, and E. Erdem, Hydrogen Electrical Vehicles, in Hydrogen Electrical Vehicles. **2023**. p. 1-10.
11. **M. H. Aleinawi**, Ameen Uddin Ammar, Merve Buldu-Akturk, Nur Selin Turhan, Shankari Nadupalli, Emre Erdem ,Spectroscopic Probing Of Mn-Doped ZnO Nanowires Synthesized via a Microwave-Assisted Route. The Journal of Physical Chemistry C, **2022**. 126(8): p. 4229-4240.

Attended Conferences:

1. 4th International Symposium on Characterization (ISC23) – Sakarya University – Sakarya – 16 to 18 November **2024. Oral presentation**: "Defects study of h-BN performance in supercapacitor devices."
2. 18th International Nanoscience & Nanotechnology Conference (NANO TR 18) – KOÇ University – Istanbul – 26 to 28 August **2024. Poster**: "Exploring the morphological effect of ZnO nanostructures on the diffusive/pseudocapacitive behavior as supercapacitor electrode materials."
3. EFSUN workshop – Gebze Technical University – Kocaeli – 12 June **2024. Poster**: "Exploring the morphological effect of ZnO nanostructures on the diffusive/pseudocapacitive behavior as supercapacitor electrode materials."
4. EFSUN workshop – Sabanci University Faculty of Engineering and Natural Science – Istanbul – 16 May **2024. Oral presentation**: "Piezoelectric Nanogenerators Based on ZnO NWs."
5. 3rd International Symposium on Characterization (ISC23) – Sabanci University (SUNUM) – Istanbul – 6 to 8 September **2023. Poster**: "Investigation of Specific Capacitance Properties of ZnO Nanowires and ZnO Nanoparticles."
6. 17th International Nanoscience & Nanotechnology Conference (NANO TR 17) – Izmir Institute of Technology – Izmir – 27 to 29 August **2023. Oral presentation**: "Exploring the Capacitive and Piezoelectric Properties of Tunable Structured ZnO Nanomaterials."
7. NANOSİS Platformu workshop (2. NANOSİS Çalıştayı) – Sabanci University (SUNUM) – Istanbul – 3 May **2023. Poster**: Nanosis project.
8. 2nD International Natural Science, Engineering and Material Technologies conference NEM 2022 – İğneada / Kırklareli – 15 to 17 September **2022. Oral presentation**: "Utilization of Piezoelectric Effect in Zinc Oxide Nanowires as a Nanogenerator."
9. Helmholtz-SESAME Soft X-ray Beamline for SESAME (HESEB) workshop – University of Istanbul – Istanbul – 8 and 9 September **2022. Workshop** participation.
10. NANOSİS Platformu workshop (1. NANOSİS Çalıştayı) – Sabanci University (SUNUM) – Istanbul – 6 April **2022. Poster**: Nanosis project.